Preface

It is a pleasure and honor to welcome you to the 2nd International Symposium on Noninvasive Functional Source Imaging within the Human Brain and Heart in Zagreb, Croatia. The goal of this series of biannual international NFSI symposia is to promote the research and use of noninvasive functional imaging techniques both in basic and clinical applications while preserving a strong emphasis on data analysis and evaluation of emerging modeling strategies. The symposium is aimed in gathering scientists of differing backgrounds involved in a multidisciplinary approach to assess brain and heart functions in health and disease.

The first NFSI symposium started as First Austrian Symposium on Noninvasive Magnetic and Electrical Source Imaging within the Human Heart and Brain and was held in Graz, in September of 1997. In addition to MEG/MCG and EEG/ECG, the NFSI-99 includes also fMRI and TMS, the other two major functional imaging techniques. The use of different noninvasive techniques and especially their multi-modal integration is likely to provide better understanding and deeper insight into brain and heart functions and connectivity than any of the techniques by itself. The ultimate goal is the real-time noninvasive brain and heart functional anatomy with a spatio-temporal resolution that exceeds the resolution of any of individual techniques.

In order to pursue not only scientific but also an educational mission with this symposium, distinguished speakers such as G.-L. Romani, R. Savoy, R. Ilmoniemi, and A. van Oosterom were invited to give tutorial lectures on basics of MEG, fMRI, TMS, and MEG/MCG, EEG/ECG modeling issues, respectively. We are happy that the list of the invited speakers includes also very prominent researchers, C. Aine C., J..-H. Gao, E. Halgren, A. Papanicolaou, and J. Vieth, to give review presentations on most important basic and clinical results using the noninvasive functional imaging techniques of interest. In addition, two workshops are included, the Modeling workshop organized by M. Scherg and the Clinical application workshop organized by A. Papanicolaou. The focus of the workshops is on dynamic functional source imaging to cover both modeling strategies aspects and current clinical advances. The Roundtable Discussion, chaired by G.-L. Romani, was introduced as an informal forum to present current status, most important initiatives, graduate programs, and future prospective of the noninvasive functional imaging in the participating countries.

Even though the number of submitted contributions is smaller compared to the NFSI-97 due to the fact that the Kosovo crisis escalated close to the time of the abstract submission deadline, we are happy that it is likely that we will exceed the number of participants who participated at the NFSI-97. We did our best to attract Croatian researchers and especially clinicians to the NFSI-99 in a hope that the NFSI-99 will make a difference and increase an interest into more advanced functional brain and heart imaging techniques. It is extremely important to nurture the interdisciplinary nature of the functional imaging field and improve collaboration between researchers and clinicians in order to benefit most from the emerging and rapidly developing functional imaging modalities. Our hope and expectations are that the recently opened Croatian Institute for Brain Research will be successful in starting functional brain imaging program and be instrumental in bringing together researchers and clinicians in an interdisciplinary effort toward understanding the working brain. Also, international collaborations are very important and I hope that the NFSI-99 will help in that regard as well.

I would like to express my gratitude to the members of the Organizing Committee, the NFSI-99 secretary Mrs. Marina Kavur, the members of the Scientific Program Committee, and especially to my undergraduate students (D. Kovacic, J. Bozikov, A. Radenovic, S. Kovacevic, A. Susac, A. Cvitkovic, S. Tomaskovic, M. Loncaric) for all their help and support. We are very happy that so many Croatian professional societies were supportive of the NFSI-99. Without sponsors the NFSI-99 would not have been possible, especially not in this form. Their support is highly appreciated. I would like to acknowledge with gratitude the Organization for Human Brain Mapping (OHBM) for allowing access to their electronic mailing list. My deepest appreciation goes to the OHBM Chair Leslie Ungerleider for her personal support that was very important and encouraging for me.

The organization of the NFSI-99 went through a major change. Due to the Kosovo crisis and concerns expressed by many participants, the NFSI-99 venue was changed from Dubrovnik to Zagreb. My deepest gratitude goes to the stuff of the two L-category hotels, Sheraton Zagreb Hotel that is the NFSI-99 venue and the Excelsior Hotel in Dubrovnik that was supposed to be the venue of our meeting. Their understanding and highly professional support is very much appreciated. It was a real pleasure to make the arrangements for the NFSI-99 at both places. While I am sure that you will enjoy Zagreb and the Plitvice Lakes, I would like to hope that you will have a chance to visit Dubrovnik soon and admire its beauty, history, art, and culture that makes Dubrovnik so unique.

Zagreb, July 1999

Selma Supek
Symposium Chair

NFSI-99

PROCEEDINGS

2nd International Symposium on

NONINVASIVE FUNCTIONAL SOURCE IMAGING

Within the Human Brain and Heart

September 3-7, 1999
Zagreb, Croatia

Editor: **Selma Supek**

Organizer

Department of Physics, Faculty of Science, University of Zagreb
Croatian Institute for Brain Research, Faculty of Medicine, University of Zagreb

Organizing Committee

Selma Supek, Department of Physics, Faculty of Science, Symposium Chair

Bešenski Nada, Clinical Hospital Rebro, Radiology
Brnjas-Kraljević Jasminka, Department of Biophysics, Faculty of Medicine
Demarin Vida, Clinical Hospital "Sestre Milosrdnice", Neurology
Folnegović-Šmalc Vera, Psychiatric Hospital Vrapče, Faculty of Medicine
Goldner Vladimir, Clinical Hospital Rebro, Cardiology
Išgum Velimir, Clinical Hospital Rebro, Neurophysiology
Jernej Branimir, Rudjer Bošković Institute
Judaš Miloš, Faculty of Medicine, Anatomy
Kurjak Asim, General Hospital Sveti Duh, Obstetrics and Gynecology
Lončarić Sven, Faculty of Electrical Engineering and Computing
Magjarević Ratko, Faculty of Electrical Engineering and Computing
Miklić Pavle, Clinical Hospital Rebro, Neurosurgery
Radoš Marko, Clinical Hospital Rebro, Radiology
Šantić Ante, Faculty of Electrical Engineering and Computing
Spaventi Radan, Pliva - Research Institute

Supported by

Ministry of Health, Croatia
University of Zagreb
Croatian Biophysical Society
Croatian Physical Society
Croatian Medical and Biological Engineering Society
Croatian Society of Radiology
Croatian Society of Neurology
Croatian Society of Psychiatry
Croatian Psychological Association
Croatian Society of Cardiology

Scientific Program Committee

Aine Cheryl, USA
Doessel Olaf, Germany
Halgren Eric, USA
Johnston Peter, Australia
Kostović Ivica, Croatia
Nenonen Jukka, Finland
Nowak Hannes, Germany
Peters Maria, The Netherlands
Pfurtscheller Gert, Austria
Posse Stefan, Germany
Romani GianLuca, Italy
Salanius Stephan, Finland
Sekihara Kensuke, Japan
Sippens Arne, The Netherlands, USA
Supek Selma, Croatia
Tesche Claudia, Finland
Tilg Bernhard, Austria, USA
Van Leeuwen Peter, Germany
Van Oosterom Adriaan, The Netherlands
Vieth Juergen, Germany
Wach Paul, Austria

The Organizers of NFSI-99 gratefully acknowledge support from the following organizations:

Biomagnetic Technologies Inc.
Neuromag Ltd.
General Electric Medical Systems
Pliva d.d.
Nycomed
Croatia Airlines
Andrija Štampar School of Public Health
Croatian Institute for Brain Research
Department of Physics, Faculty of Science, University of Zagreb
Tourist Office Croatia
Tourist Office Zagreb
Zagrebački električni tramvaj - ZET
Đakovačka vina d.d.
Sloboda d.d., Osijek

Exhibitors

Biomagnetic Technologies Inc.	www.biomagtech.com
Neuromag Ltd.	www.neuromag.com
MEGIS Software GmbH	www.BESA.com
Pharmakon – AG	
Silicon Biomedical Instruments BV	
Tamaris d.o.o.	

CONTENTS

Invited Tutorials and Rewiew Lectures

P - 1 **MEG: Principles, methods, and applications ---------- 11**
Del Gratta C., and Romani G.L.

P - 2 **Modeling aspects of bioelectric source imaging ---------- 24**
van Oosterom A.

P - 3 **Introduction to Designing *f*MRI-Based Experiments ---------- 35**
Robert L. Savoy

Introduction to Analyzing Data from *f*MRI-Based Experiments ---------- 41
Robert Savoy

P - 4 **Transcranial Magnetic Stimulation—New Modality In Brain Mapping ---------- 48**
Ilmoniemi R.J.

P - 5 **Combining Electromagnetic and Hemodynamic Signals to Derive Spatiotemporal Brain Activation Patterns: Theory and Results ---------- 53**
Halgren, E., and Dale, A.M.

P - 6 **The Clinical Use of MEG Activity Associated with Brain Lesions ---------- 61**
Vieth J.B., Kober H., Ganslandt O., Möller M., Kamada K.

P - 7 **Applications of MEG to the Mapping of the Language Cortex ---------- 70**
Papanicolaou, A.C., Simos, P., Breier, J.I., Zouridakis, G., Constantinou, J., Wheless, J.W., Maggio, W.W.

MEG Empirical Studies

P - 8 **MEG Study of Hippocampal Theta During a Working Memory Task ---------- 74**
Tesche, C.D, Karhu, J.

P - 9 **Estimating Neural Source of High-Frequency Magnetic Oscillation Evoked by Posterior Tibial Nerve Stimulation Using Time Frequency MEG-MUSIC Algorithm ---------- 79**
Sakuma K., Sekihara K., Hashimoto I.

Bioelectromagnetic Forward and inverse Problems

P - 10 **On the effective passive Conductivity of human Tissues at low Frequencies -------- 83**
Peters M.J., van Burik M.J., and Stinstra J.G.

P - 11 **Informed spatial basis functions in minimum norm solutions for the electromagnetic source localisation problem. ---------- 87**
Phillips C., Rugg M.D., Friston K.J.

P - 12 Secondary Sources in the Skull ---------- 91
M.J. van Burik, M.J. Peters

P - 13 The Electrically Silent Cardiac Magnetic Field ---------- 95
Fischer G., Tilg B., Modre R., Fetzer J., Rucker W., Huiskamp G., and Wach P.

P - 14 A Linearized Iterative Algorithm for Myocardial Activation Time Imaging -------- 99
Modre R., Tilg B., Fischer G, and Wach P.

P - 15 Influence of randomly displaced BSPM leads on theidentification of ventricular preexcitation sites ---------- 104
Jazbinšek V., and Hren R.

FMRI Empirical Studies

P - 16 Selective BOLD Activation of the Receptive Speech Area Using aNovel Passive Listening Paradigm ---------- 108
Lowe M.J., Lurito J.T., Mathews V.P., Phillips M.D., and M. Dzemidzic

P - 17 On the organisation of the SII human somatosensory cortices: preliminary results with fMRI and electrical peripheral nerve stimulation---------- 112
Della Penna S., Del Gratta C., Ferretti A. , Franciotti R., Tartaro A, Torquati K., Bonomo L., Rossini P.M. and Romani G.L.

P - 18 The use of single event fMRI and fuzzy clustering analysis to examine haemodynamic response timecourses in supplementary motor and primary motor cortical areas. ---------- 116
Cunnington R., Windischberger C., Deecke L., and Moser E.

P - 19 Quantification of Supplementary Motor Area activation with movements of different practice levels using Functional Magnetic Resonance Imaging at 3T --- 120
Erdler M., Windischberger C., Cunnington R., Edward V., Streibl B., Gartus A., Moser E., Deecke L. and Beisteiner R.

P - 20 Functional Discrimination of Thalamic Nuclei Using BOLD Contrast fMRI at 1.5 T---------- 123
Dzemidzic M., Lowe M.J., Mathews V.P., Lurito J.T., and Phillips M.D.

Modeling Workshop

P - 21 Application of Eigenspace Beamformer to Virtual Depth-Electrode Measurement Using MEG ---------- 127
Sekihara K., Peoppel D., Miyashita Y.

P - 22 Cortical oscillatory activity assessed by combined EEG and MEG recordings and High-Resolution ERD methods---------- 131
Edlinger G., Bastiaansen M., Brunia C., Neuper C., Pfurtscheller G.

MCG Clinical Studies

P - 23 Cardiomagnetic Source Imaging Studies with Focal and Distributed Source Models ---------- 135
Nenonen J., Pesola K., Lötjönen J., Lauerma K., Hänninen, H., Korhonen, P., Mäkijärvi, M., Fenici, R. , and Katila, T.

P - 24 Spatial and Temporal Changes during the QT-Interval in the Magnetic Field of Patients with Coronary Artery Disease ---------- 139
Van Leeuwen P., Hailer B., Lange S., Donker D., Grönemeyer D.

P - 25 Current density estimation on the left ventricular epicardium: A potential method for ischemia localization ---------- 143
Pesola K., Hänninen H., Lauerma K., Lötjönen J., Mäkijärvi M.,Nenonen J., Takala P. , Voipio-Pulkki L.-M[5], Toivonen L. , and Katila T.

P - 26 Validation of Noninvasive Functional Cardiac Electrical Source in a 43-year old Male Patient ---------- 147
Tilg B., Modre R., Fischer G., SippensGroenewegen A., Mlynash M., Roithinger F.X., Reddy G., Roberts T., Wach P., Lesh M.D., and Steiner P.R.

P - 27 Magnetocardiography under Clinical Conditions ---------- 152
Erné, S.N., Kammrath, H.G., Ziolkowski, M., Tenner, U., Müller, H.-P.

P - 28 Topographic Presentation of the Dipolar Content of Cardiac Electric Field ------ 156
Bacharova L. , Chorvat D. , Mateasik A. , Titomir L.I.

MEG/EEG Basic and Clinical Studies

P - 29 Functional Mapping of Speech Evoked Brain Activity by Magnetoencephalography and its Clinical Application ---------- 159
Möller M., Kober H., Ganslandt, O., Nimsky, Ch., Vieth J.B., and Fahlbusch, R.

P - 30 Scalp current density (SCD) mapping of cerebral activity during object and space selection in humans---------- 162
Alberto Zani, Carmela Avella, Stefania Lilli, Alice Mado Proverbio

P - 31 Spatio-temporal mapping of electrocortical activity during selective processing of colour and shape in humans ---------- 165
Alice Mado Proverbio, Fabiana Burco, Alberto Zani

P - 32 Clinical DC applications using MEG: Moving the curtains aside ---------- 170
Bowyer, S.M.

P - 33 Diagnosis of Myocardial Viability Based on Magnetocardiographic Recordings - 174
Nowak H., Leder U. , Pohl P., Brauer H., Tenner U., Haueisen J.

P - 34 ERP mapping of brain activation during phonological processing---------- 178
Alice Mado Proverbio, Stefania Lilli, Alberto Zani

P - 35 Signal to Noise Improvement in fMRI Analysis---------- 181
Erné S.N., Müller H.-P., Kammrath H.G., Tomczak R., Wunderlich A.

P - 36 Physical Phantoms for Biomagnetic and Bioelectric Measurements ---------- 184
Tenner U., Erné S.N., Haueisen J, Nowak H., Brauer H.

P - 37 Localization of somatosensory activity evoked by tactile and painful and non-painful electrical stimulation – A comparison using whole head magnetencephalography ---------- 188
Sterr, A., Kreyer, I., Elbert, T.

MEG: Principles, methods, and applications

Del Gratta C., and Romani G.L.

Institute of Advanced Biomedical Technologies, and Department of Clinical Sciences and Biomedical Imaging, University "G. D'Annunzio", Chieti, Italy

Introduction

This contribution reviews some of the theoretical and experimental aspects of magnetoencephalography (MEG), including the basics of field calculation and source estimation, an overview of the principles of MEG instrumentation, and some of the most recent applications in neurophysiological and clinical research. A complete review of neuromagnetism, that covers theoretical and experimental fields, may be found in [1].

Generation of biomagnetic fields and the current dipole model

The time variability of bioelectric phenomena corresponds to a frequency range extending from dc to a few hundred hertz - typically below 1 kHz. Inductive, and displacement effects at these relatively low frequencies are negligible [2]. Therefore, there is no direct coupling between electric and magnetic field. The only link between electric and magnetic field is established by the electric current.

Typical nerve cells consist of a soma surrounding the nucleus, several terminations called dendrites, and an additional longer termination called the axon. The dendrites receive connections from other neurons, whereas the axons connect the cell to other neurons, or to muscles and organs. The axon terminates in a *synapse* that allows signal transmission by electrical or chemical means. When the intracellular potential in the soma, at the base of the axon, falls below a certain threshold value, a depolarisation wave is triggered that can travel along the axon, followed by a repolarisation wave. The close succession of these two waves is called an *action potential*. The duration of an action potential is of a few milliseconds.

The electric potential in the soma is, in turn, determined by the impulses coming from the dendrites of the cell. These impulses are triggered at the synapse from other neurons, and are therefore called *postsynaptic potentials*. They consist of a slow depolarisation wave followed by a much slower repolarisation. In comparison with the action potential, the postsynaptic potential may last several tens of milliseconds.

Currents in the brain may be divided into intracellular currents, transmembrane currents and extracellular currents. Intracellular currents flow from a depolarising region to a region in the resting state, or from a region in the resting state to a repolarising region. Transmembrane currents flow radially out of the cell in repolarising regions or into the cell in depolarising regions. They contribute negligibly to the magnetic field because they are directed radially and because they are very short, due to the thinness of the membrane. Finally, extracellular currents close the current loop from a depolarising region to a repolarising region, spreading in the extracellular medium. The contribution of extracellular currents is also negligible due to their symmetric pattern and to their small dimensions compared to the conducting medium [3].

The intracellular current may be represented by a straight and short current element along the axis of the dendrite or axon, characterised by its length and its intensity. Such a current element is called a current dipole because the current pattern it determines in the extracellular medium is equal to that of two pointlike, closely spaced, positive and negative current sources - source and sink, or equivalently that of a time varying electric dipole. The moment **Q** of a current dipole is a vector and is equal to the product of current intensity and length:

$$\mathbf{Q} = I\mathbf{L} \qquad (1)$$

The electric potential and magnetic field for a current dipole immersed in an infinite homogeneously-conducting medium are [4,5]:

$$\Phi_\infty(\mathbf{x}) = \frac{1}{4\pi\sigma}\,\mathbf{Q}\bullet\frac{(\mathbf{x}-\mathbf{x}_0)}{|\mathbf{x}-\mathbf{x}_0|^3} \qquad (2)$$

$$\mathbf{B}_\infty(\mathbf{x}) = \frac{\mu}{4\pi}\,\mathbf{Q}\times\frac{(\mathbf{x}-\mathbf{x}_0)}{|\mathbf{x}-\mathbf{x}_0|^3} \qquad (3)$$

The current dipole can be used as a model of elementary cellular events. For example, a postsynaptic potential may be represented by a current dipole, whereas an action potential may be represented by two closely spaced and oppositely-directed current dipoles. The latter source configuration has a vanishing current dipole moment and is called a current quadrupole. The field of a quadrupole falls off as the inverse cubic distance. Therefore, quadrupole fields are much weaker than dipole fields. For this reason magnetic signals from the brain are believed to originate mainly from postsynaptic potentials rather than from action potentials.

When large assemblies of cells are involved in a cooperative process, as in brain function, it is not possible to take into account every cell, and the current distribution must be integrated over the active area. Thus, a macroscopic description of the sources is adopted, in accordance with the experimental fact that macroscopic fields are measured. When the integral of the microscopic current distribution over the active area is non-vanishing, the current distribution has a leading first-order term called the *equivalent current dipole*.

In the case of brain activity, the size of an active cell group may be estimated by comparing the magnetic signal of a single neuron to those actually measured. The field due to a postsynaptic potential may be evaluated using a simple model [3]. Let us consider the dendrite as a cylinder with diameter d, length L, and conductivity σ; let V be the potential difference along the dendrite. The current in the dendrite is given by V / R, where R is the dendrite resistance, equal to $4\,L / (\sigma\,\pi\,d^2)$. Therefore, the magnitude of the corresponding current dipole moment is, according to (1):

$$Q = V\,\sigma\,\pi\,d^2 / 4 \qquad (4)$$

Substituting for typical values of $\sigma \approx 0.25\ \Omega^{-1}m^{-1}$, $d \approx 4$ μm, $V \approx 10$ mV, we obtain $Q \approx 3\times10^{-14}$ Am. The corresponding field intensity at a 4-cm distance is, according to (3), about 2×10^{-18} T. This value is well below the sensitivity limits of biomagnetic instrumentation and also below the thermal noise of tissues. For comparison, typical field values measured over the scalp in response to somatosensory or auditory stimulation are on the order of 10^{-13} T. Therefore, about 50,000 synapses are needed to build typical fields. Fields over the scalp mainly originate from these postsynaptic potentials, rather than from action potentials. The latter are, indeed, much faster and their field is much weaker.

In conclusion, the equivalent current dipole can be used as a model of active sources. It must be considered as a macroscopic current dipole, in the sense that it results from the summation over a large number of microscopic dipoles, even though it is small compared to the size of body organs.

Solution of the direct problem

The direct, or forward, problem consists of the calculation of the magnetic field distribution, given the current distribution inside the body. This calculation requires a model for the currents as well as for the surrounding conductor. Note that there are two types of current: a current representing the activity of the cells and which is driven by variatons in the transmembrane potential, and an ohmic current due to the potential distribution generated by the former currents. The former currents are termed *active* or *impressed currents*, while the latter currents are termed *passive* or *volume currents*. The volume currents depend on the conductivity distribution and hence on the shape of the volume conductor. We shall consider here only the equivalent current-dipole model as a source model. In principle, any current distribution may be viewed upon as made of a large number of current dipoles.

We shall indicate the solution of the biomagnetic direct problem for a case that is general enough to be useful in most applications. We will assume that tissue conductivity is isotropic and piecewise homogeneous, i.e., tissue inhomogeneities are concentrated at the interfaces between different tissues. Moreover, we shall assume that any region of uniform conductivity is surrounded by another region of uniform conductivity, while currents are confined to the innermost region [4,5]. The field is to be calculated outside the outermost region. Let $V_1, V_2, \ldots, V_n$ be n regions such that $V_1 \subset V_2 \subset \ldots \subset V_n$, and let $S_1, S_2, \ldots, S_n$ be their respective boundary surfaces, so that S_1 is the innermost interface and S_n is the outermost interface. For each surface S_j, with j = 1,..., n, let σ_{j+}, and σ_{j-} be the outer and inner conductivity, respectively, and let **n** be the unit vector normal to the surface and directed outwards. It can be shown that the magnetic field of a current dipole, at point **x** outside the volume conductor, is given by [6]:

$$\mathbf{B}(\mathbf{x}) = \mathbf{B}_\infty(\mathbf{x}) + \frac{\mu_0}{4\pi}\Sigma_j(\sigma_{j+}-\sigma_{j-})\int_{S_j}\Phi\mathbf{n}' \times \frac{(\mathbf{x}-\mathbf{x}')}{|\mathbf{x}-\mathbf{x}'|^3}\,da' \qquad (5)$$

where $\mathbf{B}_\infty(\mathbf{x})$ is the field of the dipole at point x if the conductor were infinite and homogeneous and is given by (3). Φ is the electric potential at point **x'** on surface S_j. The second term represents the contribution of the volume currents to the total magnetic field.

We thus see that, in a bounded piecewise homogeneous medium, the contribution of volume currents may be described as due to a fictitious current distribution restricted to the interfaces between regions with different conductivities. These fictitious currents also are called *secondary currents*, whereas the impressed currents are called *primary currents*. Note that the secondary currents do not flow on the surfaces, but are orthogonal to them. Rather than a surface current density, the secondary sources constitute a current dipole distribution with dipole moment per unit area equal to $(\sigma_{j+} - \sigma_{j-})\Phi$. Therefore, to calculate the volume current contribution to the magnetic field, the electric potential over the surfaces S_j must be known.

An integral equation can be derived for the potential at any point of surfaces S_k [6, 7]:

$$\frac{(\sigma_{k+}+\sigma_{k-})}{2}\Phi(\mathbf{x}) = \Phi_\infty(\mathbf{x}) + \frac{1}{4\pi}\Sigma_j(\sigma_{j+}-\sigma_{j-})\int_{S_j}\Phi(\mathbf{x}')\mathbf{n}'\bullet\frac{(\mathbf{x}-\mathbf{x}')}{|\mathbf{x}-\mathbf{x}'|^3}\,da' \qquad (6)$$

where $\Phi_\infty(\mathbf{x})$ is the electric potential at point **x** for an infinite homogeneous medium with unit conductivity

and is given by (2). This integral equation must be solved for the electric potential over all the surfaces S_j. Then the magnetic field may be calculated using (5).
If the conductivity distribution is spherically symmetric, the volume-current contribution can be shown to be tangential to the conductor surface, and the total field to be independent from the conductivity distribution itself. The following formula gives the expression for the total field of a current dipole of moment **Q** in a spherically symmetric conductor, including the volume current contribution [3, 8, 9]:

$$\mathbf{B}(\mathbf{x}) = \frac{\mu_0}{4\pi F^2} \quad (F\mathbf{Q} \times \mathbf{x}_0 - \mathbf{Q} \times \mathbf{x}_0 \bullet \mathbf{x} \text{ grad } F) \qquad (7)$$

where: $F = a(a\,x + \mathbf{a} \bullet \mathbf{x})$, $\mathbf{a} = \mathbf{x} - \mathbf{x}_0$,

and: $\text{grad } F = (x^{-1} a^2 + a^{-1}\, \mathbf{a} \bullet \mathbf{x} + 2a + 2x)\mathbf{x} - (a + 2x + a^{-1}\, \mathbf{a} \bullet \mathbf{x})\mathbf{x}_0$

We can see from the above formula that the field of a radial dipole in a sphere is identically vanishing.
The spherical model has proven useful for the qualitative analysis of neuromagnetic fields as well as for the interpretation of real neuromagnetic data. Although the brain shape is not spherical, some qualitative conclusions may be drawn from the above results: (i) when a field component is measured that is almost perpendicular to the head surface, its dependence on volume currents is very weak; (ii) if a source is almost radial, its field is very weak, therefore, assuming that the dendrites are mostly directed perpendicularly to the cortex - as occurs for the apical dendrites of pyramidal neurons, magnetic measurements are most sensitive to the activity of neurons located in the fissures of the cortex; (iii) the radial field pattern of a current dipole in a sphere gives good insight to the field that is measured outside the head when the source has a leading dipolar moment. The radial field of a dipole in a sphere may be obtained by taking the radial component of (3).
In order to take into account the precise shape of the organ boundaries, (6) and the surface integrals in (5) must be solved using a numerical representation of real surfaces. Such a representation is a list of a large number of points lying on the surface.
In the Boundary Element Method, the integrals are calculated by triangulating the surfaces: the latter are approximated by a large number of adjacent triangles, the vertices of which are the surface points. The integrals then are calculated over the triangulated surfaces. Each integral over a surface can therefore be approximated by a sum of integrals over triangles. In turn, each integral may be approximated by the integrand mean value over the triangle [10, 11, 12, 13]. In this way, the integral equation (6) can be discretised in the form:

$$\Phi_j = 2\,\Phi_{j\infty} + (1/2\pi)\,\Sigma_{jk}\,\omega_{jk}\,\Phi_k \qquad (8)$$

where the indices j and k run over all triangles, Φ_j is the potential value at the centroid of triangle j, $\Phi_{j\infty}$ is the potential value at the centroid of triangle j calculated as though the medium were infinite, homogeneous and with unit conductivity, and ω_{jk} is the solid angle subtended by triangle k at the centroid of triangle j if $j \neq k$, and is equal to unity if $j = k$. Therefore, the potential Φ_j is the solution of a linear system:

$$\Sigma_k\, A_{jk}\, \Phi_k = \Phi_{j\infty} \qquad (9)$$

the coefficients of which depend only on conductor geometry and not on the current distribution. The matrix A_{jk} is singular, corresponding to the fact that the potential is determined only to within an additive constant. The singularity may be removed by deflation [14], which in practice means that A_{jk} is replaced by $A_{jk} + 1/N$, where N is the total number of triangles. Solving this new linear system yields the potential at each triangle:

$$\Phi_j = \Sigma_k\, M_{jk}\, \Phi_{k\infty} \qquad (10)$$

where $\Phi_{k\infty}$ can be calculated by means of (2).
Finally, we can calculate the field according to (5). After substituting for the potential at each triangle according to (12), we have an equation of the type:

$$\mathbf{B}(\mathbf{x}) = \mathbf{B}_\infty(\mathbf{x}) + \Sigma_j\, \mathbf{P}_j\, \Sigma_k\, M_{jk}\, \Phi_{k\infty} \qquad (11)$$

where $\mathbf{P}_j = (\sigma_{j+} - \sigma_{j-})\, a_j\, \mathbf{n}_j$, a_j is the area of the j-th triangle and $\mathbf{n}_j$ is a unit vector orthogonal to the j-th triangle.
This method has been applied to the direct problem solution in magnetoencephalography . Tipically, the homogeneous conductivity compartments are: the brain, the cerebro-spinal fluid, the skull, and the scalp. A simplified version is the homogeneous head model that neglects the skull and the scalp volume current contribution, thereby reducing the calculation burden. It has been shown [15] that the latter model gives satisfactory results. This is due to the poor conductivity of the skull, which has the effect of confining the most intense currents into the brain volume.

Solution of the inverse problem

The retrieval of current sources inside a conductor from measurements of the external magnetic field is an ill-posed problem. Indeed, there are sources that produce zero magnetic field outside the conductor (e.g., a radially-oriented current dipole inside a homogeneous sphere) and, due to the superposition principle, adding such a source to a solution for a specific field distribution gives another solution for the same field. Although a solution of this problem is not possible in a mathematical sense, a meaningful estimate of the currents

may still be undertaken. To this end it is necessary to constrain the problem in order that it have a unique solution. This is done by means of a model, describing the source and the conductor, which does not contain silent sources. Due to the availability of only a finite and noisy data set, such a model must be characterised by a limited number of parameters. It must be stressed that any information on electrophysiological sources obtained by this method, does not come from a direct measurement, but instead comes from a parameter estimation. Therefore, any conclusion about the sources is valid only to the extent that the model assumptions are valid. This aspect is very important in clinical applications.

The first step in the interpretation of biomagnetic data is the choice of a model for the equivalent source, as well as for the volume conductor. The simplest model of a bioelectric source is the equivalent current dipole. However, it is a suitable model only when the currents are confined to a single small region. In the presence of several simultaneously active regions, multiple dipole models may be used. Higher order multipolar terms may be used in addition to a current dipole.

The second step is the choice of the conductor model, which is primarily dictated by the measurement conditions. Generally, the smaller the area of field measurement and the shallower the source, the better is the approximation obtained by means of analytical models. While the source-model parameters are the object of the biomagnetic investigation, the volume-conductor-model parameters are obtained by means of an anatomical investigation, typically by means of MRI, that allows reconstruction of brain, skull and scalp boundaries.

The choice of a volume-conductor model also is a compromise between accuracy and computational costs. The sphere and half-space models have been the most widely used models during the early years of biomagnetism due to the simplicity of the calculations. It may be noted that in some neuromagnetic investigations, important results were obtained using the half-space model [16]. The development in recent times of realistic models has been prompted by larger available computing power, but also responds to an increased need for accuracy. Magnetoencephalography has evolved towards the use of large multichannel instruments allowing simultaneous whole- head mapping of the magnetic field. Under these conditions, volume current contributions are detected coming from several parts of the brain, which are modelled as a secondary source distribution over the brain surface. The latter shows different curvature radii in different regions and therefore cannot be represented by a sphere.

A practical method for the estimation of the model parameters is the use of the least-squares estimator. This is a maximum likelihood estimator, i.e., it yields parameter estimates for which the measured data values have the largest probability. In addition, the least-squares estimator gives a statistical criterion for the acceptance or the rejection of the model and confidence intervals for the parameters [17]. The parameter values obtained by this method are those that minimise the quantity:

$$\chi^2 = \Sigma_j \frac{(B'_j - B(\mathbf{x}_j; \mathbf{a}))^2}{\sigma_j^2} \qquad (12)$$

where B'_j is the measured field component at point $\mathbf{x}_j$, $B(\mathbf{x}_j; \mathbf{a})$ is the value predicted by the model, which depends on the parameter vector $\mathbf{a}$, and σ_j^2 is the expected variance of B'_j. When B is a linear function of $\mathbf{a}$, the parameter values $\mathbf{a}_m$ that minimise (12) may be found by solving a linear system. This is the case for a fixed dipole, i.e., a dipole the location of which is assumed *a priori*. This method may be useful in reducing the number of parameters when the active region is expected to have one or more precise anatomical locations. Generally, however, the dipole location cannot be assumed *a priori*, and its three space coordinates must be considered as free parameters. In this latter case, the field dependence is nonlinear and the minimisation of (12) must be performed by an iterative method. The most widely used one is the Levenberg-Marquardt algorithm [18], which combines a steepest descent, far from the minimum, with a Hessian matrix inversion near the minimum. Note that this algorithm requires that the forward solution corresponding to the current parameter values be calculated many times. Therefore, it is important that the forward calculation be as time efficient as possible. Once the best estimate parameters are found, confidence regions and confidence limits may be obtained by using a linear approximation of the function $\chi^2(\mathbf{a})$ near the minimum. The usual percentage levels corresponding to $\Delta\chi^2$ values are valid when the errors σ_j are normally distributed [17]. This does not seem to be the case in biomagnetic measurements. Therefore, Monte Carlo techniques for the estimate of parameter uncertainty are to be preferred. In the latter case, appropriate noise simulation must be provided, taking into account various noise sources. The uncertainty in a biomagnetic measurement arises mainly from instrument noise, sensor positioning errors and subject noise. The first contribution is small in state-of-the-art instruments that feature a field-noise density below 5 fT/√Hz, compared to a signal level of several tens of fT. The second contribution is, in large multichannel systems, a systematic error, and hence shows coherence among different channels. This means that these errors may be taken into account using a model with a small number of parameters. Finally, subject noise shows correlation among channels as well [19]. Subject noise comes from thermal noise in the body, as well as from physiological activity which the experimenter is not interested in. A typical example of this situation is background brain activity when measuring specific evoked or spontaneous signals.

Other, more complex, source models consist of a large number of dipoles fixed in location, and which may have either variable orientation and intensity, or fixed

orientation and variable intensity. In both cases, the magnetic field is linearly dependent on the free model parameters. These models are often referred to as distributed source models. They are based on a priori assumptions on the location of the sources (e.g. the whole cortex or a specific cortical area). Their advantage lies in making the source estimation a linear estimation problem. However, the resulting linear system is generally underdetermined and requires regularisation, which may be based on some assumed regularity property of the source, or on additional physiological and anatomical information.

The above models result from a more general approach to the resolution of the inverse biomagnetic problem, in which the current density distribution in the brain is considered as a vector function, belonging to an appropriate class of functions, and defined in the brain volume, or a subset of the brain volume. Given a number of magnetic field measurements, the current density function is the solution of a set of integral equations, one for each measurement - where the kernel of each integral is the so-called *lead field function* of the particular sensor considered. In practice this problem is treated numerically, and therefore discretised, so that the current density function is represented by an array of current dipoles, appropriately distributed in the brain volume. The transfer function from the source to the mesurements is represented by a matrix that is also called *lead field matrix*. The number of rows of the lead field matrix is equal to the number of sensors, while the number of columns is equal to the number of dipoles in the source. The j-th column of the lead field matrix contains the measured magnetic field values when the j-th dipole is unity and all the other dipoles in the source vanish. The resulting linear system is highly underdetermined: typically the number of dipoles used for the coverage of the whole cortex is 5,000, while the number of sensors is in the order of 100.

Several methods have been developed for the resolution and the regularisation of this problem. However, their description is beyond the scope of this tutorial. Some of them are reviewed in [1]. An instructive methodological work on this topic, with a good reference list may be found in [20].

Instrumentation for neuromagnetism

The challenge for biomagnetic instrumentation is the detection of extremely weak magnetic signals (1 fT to 100 pT) in the presence of a very noisy background (~ 10 μT and above). Properly designed instrumentation must, therefore, combine high sensitivity with the ability to reject unwanted signals (or noise).

Modern biomagnetic instrumentation is based on SQUIDs that provide the sensitivity to detect magnetic fields as weak as 1 fT. For our purposes, the SQUID, and its related electronics, may be considered as a black box with a low-noise magnetic-flux-to-voltage converter in it. Reviews of biomagnetic instrumentation may be found in [1, 21, 22, 23]

The main components of a single sensing unit of a neuromagnetic system are: the detection coil with the flux transformer, and the SQUID with its related electronics. These components are always present in a biomagnetic system, although their characteristics may vary according to specific needs.

The detection coil is actually the sensor of the magnetic field. It is convenient to use a separate detection coil apart from that of the SQUID loop, because it is possible to change the field spatial sensitivity of the device without affecting the SQUID performance. The magnetic flux sensed by the detection coil is transferred to the SQUID through an input coil which is often built directly onto the SQUID chip. It is worth noting that the entire flux transformer - detection coil and input coil - is a superconducting loop. Thus, the external magnetic field induces a current in this loop which is proportional to the field itself, rather than to the field derivative. This extends the range of SQUID sensitivity down to very low frequencies. In practice, DC signals may be detected by moving the sensor.

The simplest detection coil is made by a single turn - or few turns - of superconducting wire, and is called a magnetometer. If the magnetic field is constant over the coil area, the current flowing in the loop is simply proportional to the field intensity. The important advantage of this simple type of detection coil is that it is easy to integrate within the SQUID chip, thus simplifying the construction of complex biomagnetic systems.

The multiturn coil is the best type of detection coil from the sensitivity point of view. Specific geometries for the detection coil may reduce conveniently the sensitivity to noise sources, with little loss of sensitivity for the biomagnetic sources of interest. The most used detection coil of this type is the first-order gradiometer. latter is made by connecting in series two magnetometer coils wound in opposite senses. These coils may be displaced along their common axis - thus forming an axial gradiometer - or in their common plane - thus forming a planar gradiometer. This type of coil is insensitive to uniform fields, and it is used to attenuate the field from distant sources. These gradiometer-type detection coils are the most widely used in the currently-available multichannel biomagnetic systems.

The dewar used in biomagnetic systems is a critical part of the instrument and must satisfy severe requirements: (i) the distance of the detection coils from the head of the subject must be as small as possible - usually less than 20 mm, typically 15 mm - since the field intensity decreases as $1/r^2$; (ii) the magnetic noise must be less than the noise of the sensors. Usually fiberglass is used as a material to build the dewar. Fiberglass has optimal magnetic properties. However, its use poses some problems in the mechanical stability of the dewar, especially in the tail section. To guarantee the safety of the subject, thick fiberglass layers are used, especially in flat-bottomed systems, but this causes the detection coils to be far from the subject. Moreover fiberglass does not provide any shield against thermal radiation, and therefore, many (50 - 100) layers of mylar must be wrapped around the inner portion of the

dewar for radiation shielding. However, these shields increase the magnetic noise of the dewar, since eddy currents are allowed to flow on the aluminated side of the mylar and generate magnetic field noise [24]. A compromise must be made to obtain the best overall performance. Typical biomagnetic dewars exhibit noise below 5 fT/Hz$^{1/2}$. Last, when designing clinical systems, it is important to consider practical issues for system operation and maintainance. For instance, the helium reservoir should be large enough to ensure several days between helium refills, yet without increasing by too much the external dimensions and weight of the dewar. Typical whole-head neuromagnetic dewars have a helium capacity of ≈30 liters with a helium refill interval of 2-4 days, whereas for smaller dewars, helium may last for 7-8 days.

Nowadays, biomagnetic multichannel systems always operate in magnetically-shielded rooms. These rooms are relatively large - typical inner dimensions are 3×4×2.5 meters - and comfortable. The shielded rooms are built in accordance with two physical phenomena: eddy-current shielding (provided by layers of highly-conducting materials, copper or aluminum), and magnetic shielding (provided by layers of high-magnetic-permeability materials, Fe-Ni alloys, typically with small percentages of Mo, Cu, Cr and Al). A description of the different techniques used to build these rooms may be found in [25].

Eddy-current shielding works as follows: time-varying magnetic fields induce electrical currents circulating in the conducting layer in such a way that their magnetic field tends to cancel the changes of the applied magnetic field by virtue of Lenz's law. The efficiency of the shield depends on the layer thickness, on the conductivity of the materials and on the frequency of the external magnetic field. While it is relatively simple to shield against radiofrequency interference (f > 500 kHz) using conducting layers with less than 1-mm thickness, the efficiency of eddy-current shielding drops dramatically at low frequencies, i.e. in the range of the power-line frequency and below. Usually aluminum layers, 20 mm or more thick, are used. At very low frequencies, where the eddy-current shielding is no longer effective, the only effective shielding method is to use low hysteresis ferromagnetic materials with high magnetic permeability μ, the so-called soft magnetic materials. Pure iron ("soft" iron with a carbon content less then 100 ppm) and several alloys based on iron and nickel show μ values larger than 10^3 and are suitable for shielding applications. However, for practical reasons, and especially to obtain a reasonable price-to-performance ratio, a value of $\mu > 10^4$ is required. Today, typical medium-quality shielded rooms are built using two layers of high-μ materials, with a thick layer of high-conductivity material (usually aluminum) in between.

Several multichannel systems (most of which are commercial units) now are operating in laboratories and hospitals in several countries. Two different kinds of systems are in use: flat-bottomed systems, mainly devoted to magnetocardiographic measurements, but also used for the study of the peripheral nervous system, and spherical, or "head-shaped", systems for neuromagnetic measurements. Most of these systems operate in a medium-quality shielded room, although some of them are designed to operate in an unshielded environement. In the head-shaped systems, particular attention is given to the design of the array of sensors. On one side it is important to thoroughly cover the scalp, including the temporal and the lower occipital areas in order to better investigate temporal lobe epilepsy and the functions of the cerebellum. On the other side, it is also advisable to have a good spatial sampling in order to detect patterns with high spatial frequencies such as, for example, those generated by shallow sources. Tipically, the number of sensing positions ranges, in the currently operating instruments, from about 100 to about 160. The number of sensors actually used is normally larger, in that some SQUIDs are used to perform software compensation of the residual noise from distant sources, measured by the sensors. For example, the neuromagnetic system [26] operating at the Institute of Advanced Biomedical Technologies, University of Chieti, features 153 measuring magnetometers, integrated on the SQUID chip, and 12 additional magnetometers, assembled in four orthogonal triplets, for noise compensation.

All biomagnetic measurements are performed using computerised data acquisition systems, therefore signal conditioning is required to best match signal characteristics in terms of amplitude and bandwidth with the dynamic range, the resolution and the sampling rate of the analog-to- digital converter (A/DC) in use. Indeed, thanks to digital signal processors (DSPs), the implementation of digital filters, featuring much better performance than their analog counterparts, is now possible at very reasonable prices. Therefore, the use of analog filters is limited to DC filtering to avoid offset problems and anti-aliasing low-pass filters prior to A/D conversion.

Currently the use of dedicated analog filters for rejection of the magnetic signal due to power lines is limited to special applications with small systems operating in unshielded environments. As a matter of fact, the use of a shielded room, and often electronic noise suppression, greatly reduces this noise, and residual noise is either negligible or comfortably treatable with digital filtering after the A/D conversion.

If measurements are carried out in an unshielded environment without special electronic noise cancellation, it is mandatory to filter out this noise prior to the A/D conversion to properly use the A/DC resolution. Notch filters are not used for this purpose because of their poor performance. Two other types of filters, namely the comb filter and the hybrid filter, although complex and expensive, are used to fulfill this task [27].

After analog conditioning, the signal is A/D converted. Usually a 12-bit A/DC provides enough dynamic range. Only if no analog high-pass filter is used, or power-line noise is large, 14- or 16-bit converters are required. Since modern A/DCs are much faster and less expensive than in the past, it is now favorable to per-

form the A/D conversion by "oversampling" at a much higher frequency (32 to 64 times) than the signal bandwidth. In this way, to avoid aliasing, a simple first-order 6 dB/octave analog filter may be used, with low-pass frequency set at $f_s/32$ or $f_s/64$.

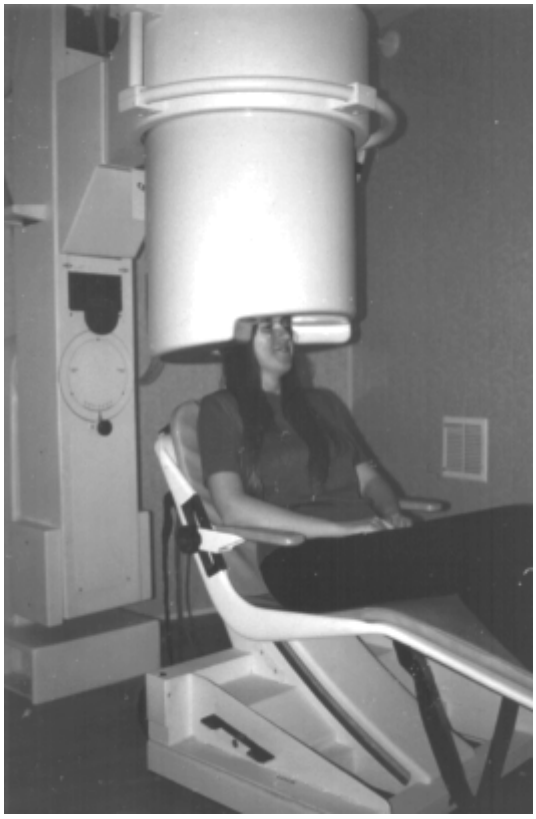

Figure 1: The 153 channel neuromagnetic system (ATB S.r.l.) at the University of Chieti.

In multichannel systems it is very important that all channels are sampled simultaneously: for this reason every channel must be connected to its own sample-and-hold circuit, followed by an analog multiplexer and an A/D converter. If oversampling is used, an A/D converter is dedicated to each channel, thus avoiding multiplexing.
In modern systems most of the on-line data treatment, e.g., done by bandpass filters and line-frequency filters, is done after A/D conversion. For instance, for the case of oversampling, data should be low-pass filtered and downsampled to the desired sampling rate before being written to disk. There are many available DSPs that can be used to accomplish this task. The main advantages in using digital filters for the low-pass and high-pass filters are the identical behaviour of these filters across different channels, and the absence of thermal drifts, ageing and noise pick-up. Additionally, it is possible to filter out environmental noise from data using suitable data processing algorithms. The use of DSPs allows also to simulate different types of detection coils from actual measurements.
Usually the system hardware, including data acquisition, is controlled through a high-end PC or, preferably, a workstation. Highly graphic performance is needed in order to monitor all measuring channels during data acquisition. From different windows it is possible to set the SQUID operating parameters and the data acquisition parameters such as sampling frequency and bandpass filters, as well as to monitor incoming data

Applications and examples

A complete review of the studies carried on in the last years by means of magnetoencephalography (MEG) is beyond the scope of this tutorial. The number of scientific papers published in peer reviewed journals has impressively increased in the last few years, thus demonstrating that MEG has now evolved from a pioneering technique into a well established experimental methodology. The main reason for this evolution lies in the good quality of the scientific results obtained, not only in basic research, but also, and particularly, in the clinical field. In order to illustrate this progress, we will briefly describe a few examples of basic and clinical applications in the areas where this technique has provided the most significant findings, and raised the interest of clinicians.

Functional imaging of sensory areas and of cognitive functions
In the last few years much attention has been paid to the investigation of the sensory areas in order to reproduce and confirm what was already known from the pioneering work by Penfield [28]. For example, in addition to what already known about the properties of the auditory cortex, i.e. its tonotopic organisation, [29, 30], some other interesting properties have been discovered by means of neuromagnetic measurements, such as the characterisation of an amplitopic map in the auditory cortex [31], or the localisation of the missing fundamental [32].
A new thrust in the area of evoked activities, more concerned with recognition and attention, has been given by Näätänen and his co-workers, who first described the so-called mismatch negativity (MMN), an electrically negative component that could be detected when a rare different stimulus was randomly inserted in a series of equal stimuli [33]. The same group has devoted particular attention over the past years to the magnetic counterpart of MMN - see [34] for a review of their work. These experiments now are performed in many research and clinical centers, including MEG laboratories, and their importance for cognitive functions, learning, memory and language development is generally accepted.
Kristeva and co-workers [35] have recently performed recordings of the motor evoked field (MEF) due to finger movement as compared to stimulation of the same finger, with the aim at investigating whether it is possible to non-invasively discriminate in humans the different projections of proprioceptive and cutaneous fibers in the primary somatosensory area. The results showed that the equivalent dipolar source for the first component of the motor evoked field (MEF I) was

significantly deeper than that associated with the first component of the somatosensory evoked field (SEF), consistently with a position on the floor of the central sulcus and with a generator located in the posterior bank of the central sulcus (area 3b), respectively. This study together with the studies by Hari and co-workers [36, 37] well demonstrates the MEG capability of sub-area discriminating inside the primary cortices in man.

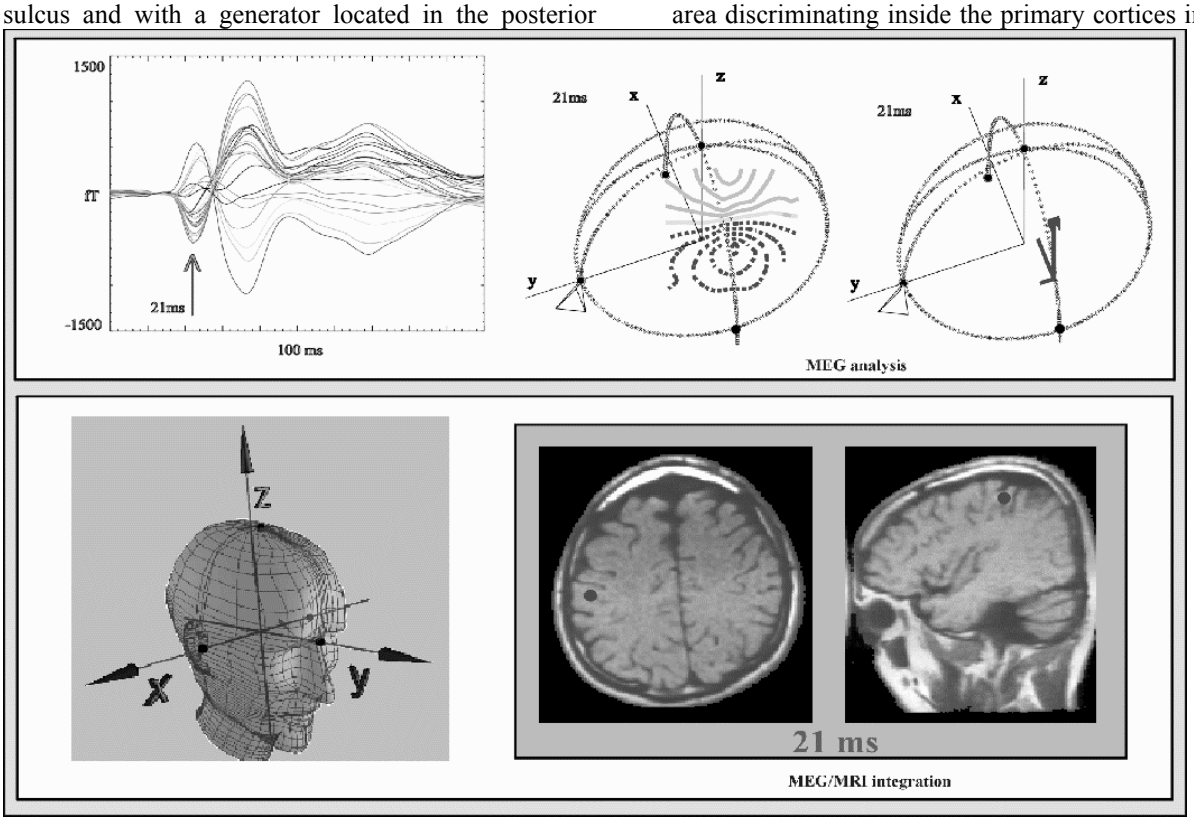

Figure 2: An example of magnetic fields evoked by median nerve stimulation. The steps of MEG data analysis are highlighted. Upper left: averaged time curves all channels in the system. Upper right: isofield contour map, at the latency indicated on the time curves superimposed on a spherical head model, and coordinates of the coresponding ECD. Lower left: the refeernce system defined by three current carrying coils for system positioning and integration with anatomical MRI. Lower right: ECD location superimposed on MRI images. Data were collected with the 28-channel MEG system in Rome, IESS-CNR and AFaR-CRCCS "Isola Tiberina".

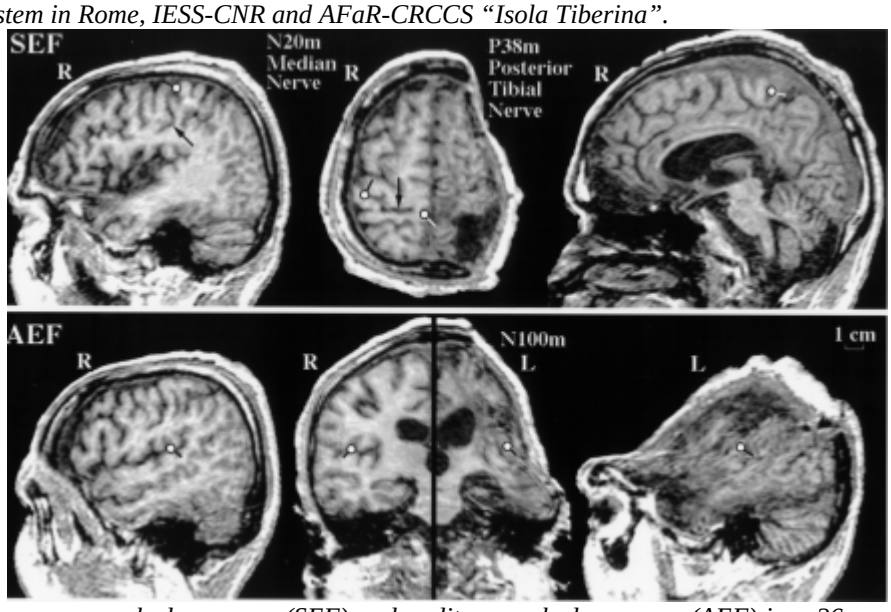

Figure 3: Somatosensory evoked response (SEF) and auditory evoked response (AEF) in a 26-year-old male with a cerebral contusion on left frontal and temporal lobes. Upper: SEF dipoles of N20m of median nerve and P38m of posterior tibial nerve. Lower: N100 dipoles on the upper surface of the bilateral temporal lobes (Courtesy of Dr. N. Nakasato [42]).

Pre-surgical investigation in epilepsy

The neuromagnetic approach was applied to the study of focal epilepsy almost two decades ago [38]. After a

first series of findings [39,40], all focused on the possibility of identifying the location of foci of interictal activity, efforts were diminished due to the lack of instrumentation adequate to a routine clinical trial. More recently, the development of large multichannel systems, has given new impulse to the field and the presurgical investigation of epilepic patients is being carried on in various laboratories in many countries. There has been an impressive development in this area, and the current trend relies strongly on the combination of MEG with other techniques, both invasive and non-invasive. As an example, we cite the work by Nakasato and co-workers [41], where the non-invasive source analysis obtained with MEG and EEG was compared with ECoG localizations, surgical outcome and the presence of lesions suggested by MRI. The authors show that whenever a good dipole fit could be obtained with satisfactory reproducibility, there was "excellent agreement between MEG dipole sources and ECoG sources, as well as surgical outcome and presence of MRI lesions" while EEG source analysis, though satisfactory, was not as consistent. It should be stressed, however, that the main contribution of the neuromagnetic approach is provided in cases where no lesion is revealed by CT and MRI, and therefore no suggestions for the surgeon are available. These are the most crucial cases, where only a combination of MEG with EcoG or Stereo-EEG, plus clinical evidence from video-EEG will decide whether or not proceed to the surgical excision.

Pre-surgical mapping

The possibility of accurately identifying the location of the equivalent generators elicited during sensory stimulation and/or simple motor tasks inside primary areas (somatomotor, visual, auditory) is another interesting feature of the neuromagnetic method. Whenever the standard anatomic topography is modified by an enlarging neo-plastic mass or by a trauma [42] the *a priori* knowledge of functional landmarks to be "respected" during surgical excision is of fundamental aid to the surgeon. With the modern technology such an information can be directly integrated with the best neuro-navigator apparatuses to obtain maximum benefit for the patient.

Cerebral plasticity

In 1994 Rossini and co-workers performed a study [43] aimed at verifying the existence of a short-term functional rearrangement of single-finger representation in the primary somato-sensory cortex of man during temporary sensory deprivation, similarly to what had been previously observed in animals [44]. By producing a relatively brief (20 min) anesthetic block of the sensory information from adjacent fingers, Rossini and co-workers demonstrated that the location and strength of the equivalent generators responsible for the cortical responses N20m and P30m from the non-anesthetised finger were significantly modified.

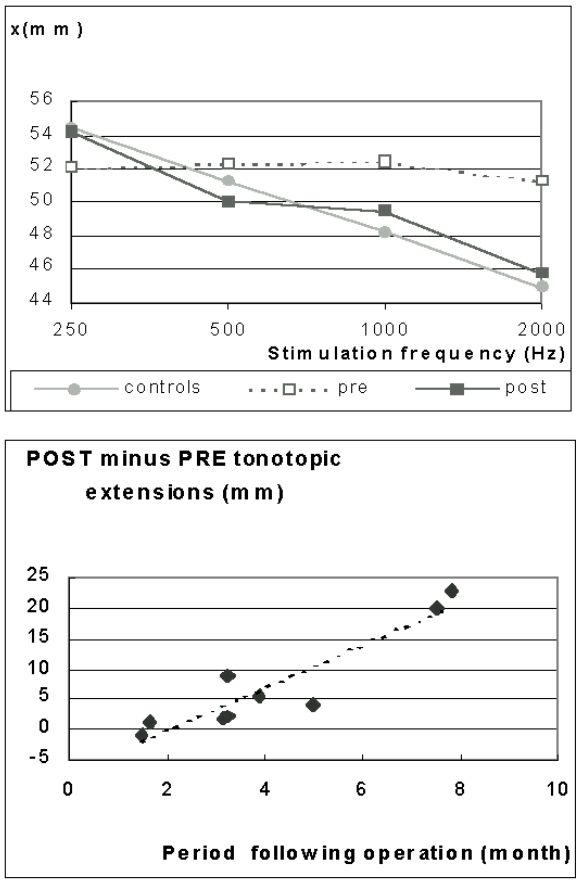

Figure 4: MEG recording of auditory evoked fields by tone burst stimulation at octave frequencies between 250 and 2000 Hz in 10 othosclerotic patients. Upper: mean distance from the centre of the head of ECDs as a function of frequency in controls, and in patients before and after surgery. Lower: extension of representation area as a function of time after surgery [48].

These first results induced the same group to start a systematic investigation of hemispheric asymmetries in a population of patients with focal hemispheric vascular lesions [45]. The aim of the study was at establishing whether or not the neuromagnetic method was suitable for identifying some parameters to be associated with cerebral *plasticity*, during recovery of sensory motor functions after a stroke. The authors studied the location and strength of the equivalent sources activated in the primary somatosensory cortex after stimulation of the left and right median nerve, and of the first and fifth digit of each hand. After identifying in a population of normals as relevant parameters i) the *location asymmetry* of the digits and of the median nerve with respect to their projection in the two hemispheres, and ii) the *hand extension* in the right and left hemisphere, the authors demonstrated that either one or both parameters were altered in stroke patients whenever the lost somatic function was being recovered during rehabilitation. Additionally these authors observed that cortical reorganization following a subcortical lesion was larger than that occurring after a cortical damage, and that ECD strength from the dam-

aged side was more intense than normal. Last, the selective reorganization of N20m and P30m observed in some patients suggested at least a partial independence of the sources active during these two components.
Another demonstration of the capabilities featured by the neuromagnetic method in the investigation of cerebral plasticity was recently provided by the work of Flor and co-workers [46]. These authors studied the modification of cortical representation in the somatosensory cortex of subjects suffering of the phantom-limb syndrome. In this pathology, an amputated limb may produce pain or other feelings that can, in turn, result in severe impairment. The results of the neuromagnetic investigation demonstrated that a strong correlation existed between cortical reorganisation and phantom-limb pain, in the sense that the stronger the reorganisation, the greater the pain. The authors concluded by suggesting "that phantom-limb pain is related to, and may be a consequence of, plastic changes in the primary somatosensory cortex."
More recently, Pantev and co-workers [47] measured the tonotopic organization of the auditory cortex of a population of musicians as compared with a similar population of controls: they found a significantly increased strength (~25%) of the ECDs elicited in musicians only by stimulation with piano tones with respect of that with pure tones. They also observed that the enlargement of the cortical representation correlated with the age at which musicians had begun to practice.
As a last example, we want to mention a result recently obtained by Rossini and co-workers [48] by studying a population of patients suffering for an othosclerosis process of the staples, before and after staples substitution. The authors observed that in all the 10 patients studied the tonotopic organization of the auditory cortex was missing, in contrast with what was commonly seen in normals, and that after surgery, and recovery of the auditory perception, in a subset of patients the tonotopic structure was recovered too. Interestingly, the recovery of cortical organization was significant in those patients who were younger and characterized by a shorter period of hearing impairment.

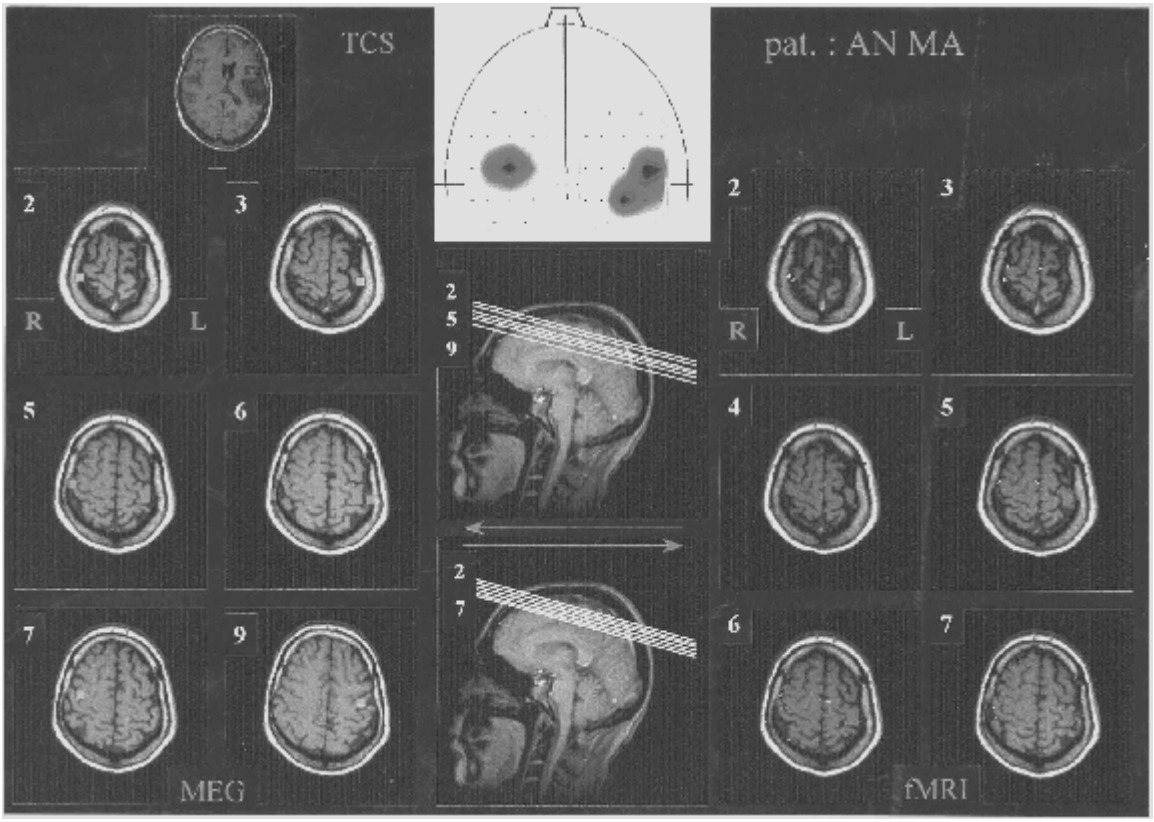

Figure 5: MEG, fMRI, and TCS data from a post stroke patient. The insert upper left shows the lesion in the fronto-parieto-temporal region. On the left, selected slices (see insert in the middle) of an MRI with superimposed the dipole localisations elicited by electrical stimulation of little finger (upper), median nerve (middle), and thumb (lower). On the right, fMRI activations due to sequential finger oppostition. In the top middle insert a TCS mapping of opponens pollicis muscle. Left hemisphere is on the right and vice versa. The three techniques show an identical asymmetry in the representations due to reorganisation after stroke, the left side representation being more posterior and more lateral [51].

Multimodal imaging

One of the most promising fields of research is the so-called multimodal approach, i.e. the use of different imaging techniques to study a specific problem, in order to possibly get a synergic effect for the comprehension of the problem itself. Several studies of this kind appeared recently in the literature [49,50]. As an example we mention a study, recently performed by Rossini and co-workers [51], that utilised MEG, functional magnetic resonance imaging (fMRI) and transcranial magnetic stimulation (TMS) to investigate a stroke patient with a malacic lesion in the left fronto-parieto-temporal cortex that had produced hemiplegia and motor aphasia. At the time of the study, 12 months after the event, the patient had satisfactorily recovered the hand motor control, with only a minimal residual paresis in the right forearm, whereas no recovery from aphasia was observable. The investigation of the somatosensory functions was performed by means of MEG under single digit and median nerve stimulation; the efferent pathway was studied by means of TMS and, additionally, the extension and location of the hand motor area were studied by means of fMRI during execution of a simple motor task. All the three techniques evidenced an asymmetrical enlargement and posterior shift of the sensorimotor areas localized in the affected hemisphere. This supports the idea that fMRI, TMS and MEG rely on similar functional substrates and therefore may be safely combined in studying patients with the aim of testing presence and amount of plasticity phenomena underlying partial or total clinical recovery of the lost function

Conclusions

The availability of large systems now provides a variety of results both for fundamental studies and in clinical applications. This will strengthen the interest of researchers and clinicians, and lead to widespread use of MEG. Particular attention should be paid to the integration of the results of neuromagnetic investigation with those of PET and functional MRI, since multimodal images will provide the most powerful diagnostic tool for the near future.

References

[1] Hämäläinen, M., Hari, R., Ilmoniemi, R., Knuutila, J., and Lounasmaa, O. Magnetoencephalography - theory, instrumentation, and applications to noninvasive studies of the working human brain, Rev. Mod. Phys., 1993, 65:413-497.

[2] Wikswo, J.P. Biomagnetic sources and their models, In Williamson, S.J., Hoke, M., Stroink, G., and Kotani, M., Advances in Biomagnetism, New York, Plenum Press, 1989, pp. 1-18.

[3] Williamson S.J., and Kaufman L. Theory of neuroelectric and neuromagnetic fields, In Grandori, F., Hoke, M., and Romani, G.L., Auditory Evoked Magnetic Fields and Electric Potentials, Basel, Adv. Audiol., Karger, 1990, pp. 1-39.

[4] Tripp, J.H. Physical concepts and mathematical models, In Williamson, S.J., Romani, G.L., Kaufman, L., and Modena, I. Biomagnetism: An Interdisciplinary Approach, New York, Plenum Press, 1983, pp. 101-139.

[5] Sarvas, J. Basic mathematical and electromagnetic concepts of the biomagnetic inverse problem, Phys. Med. Biol., 1987, 32:11-22.

[6] Geselowitz, D.B. On the magnetic field generated outside an inhomogeneous volume conductor by internal current sources, IEEE Trans. Magn., 1970, 6:346-347.

[7] Geselowitz, D.B. On bioelectric potentials in an inhomogeneous volume conductor, Biophys. J., 1967, **7**:1-11.

[8] Ilmoniemi, R., Hämäläinen, M., and Knuutila, J. The forward and the inverse problems in the spherical model, In Weinberg, H., Stroink, G., and Katila, T., Biomagnetism: Applications and Theory, Oxford, Pergamon, 1985, pp. 278-282.

[9] Grynszpan, F., and Geselowitz, D.B. Model studies of the magneto-cardiogram, Biophys. J., 1973, 13:911-925.

[10] Meijs, J.W.H., Peters, M. and Oosterom, A. Computation of EEGs and MEGs using a realistically shaped multi-compartment model of the head, Med. Biol. Eng. Comput., 1985, 23 suppl. part 1:36-37.

[11] Hämäläinen, M., and Sarvas, J. Realistic conductivity geometry model of the human head for the interpretation of neuromagnetic data, IEEE Trans. Biomed. Eng., 1989, 36:165-172.

[12] Oostendrop, T.F., and Oosterom, A. Source parameter estimation in inhomogeneous volume conductors of arbitrary shape, IEEE Trans. Biomed. Eng., 1989, 36:382-391.

[13] Barnard, A.C.L., Duck, I.M., Lynn, M.S., and Timlake, W.P. The application of electromagnetic theory to electrocardiology II, Biophys. J., 1967, **7:**463-491.

[14] Lynn, M.S., and Timlake, W. P. The use of multiple deflations in the numerical solution of singular systems of equations to potential theory, SIAM J. Numer. Anal., 1968, 5:303-322.

[15] Hämäläinen, M., and Sarvas, J. Feasibility of the homogeneous head model in the interpretation of neuromagnetic data, Phys. Med. Biol., 1987, 32:91-92.

[16] Romani, G.L., Williamson, S.J., and Kaufman, L. Tonotopic organization of the human auditory cortex, Science, 1982, 216:1339-1340.

[17] Press, W.H., Flannery, B.P., Teukolski, S.A., and Vetterling, W.T. Numerical Recipes - The Art of Scientific Computing, Cambridge University Press, 1986.

[18] Marquardt, D.W. An algorithm for least-squares estimation of nonlinear parameters, J. Soc. Ind. Appl. Math., 1963, 11:431-441.

[19] Knuutila, J., and Hämäläinen, M. Characterization of brain noise using a high sensitivity 7-channel magnetometer, In Atsumi, K., Kotani, M., Ueno, S., Katila, T., and Williamson, S.J. Biomagnetism '87, Tokyo Denki University Press, 1988, pp. 186-189.

[20] Grave de Peralta Menendez, R., Hauk, O., Gonzalez Andino, S., Vogt, H., and Michel, C. Linear inverse solutions with optimal resolution kernels applied to electromagnetic tomography, Human Brain Mapping, 1997, 5:454-467.

[21] Romani, G.L., Williamson. S.J., Kaufman. L. Biomagnetic Instrumentation, Rev. Sci. Instrum., 1982, 53:1815-1845.

[22] Ryhänen, T., Seppä, H., Ilmoniemi, R., Knuutila J. SQUID magnetometers for low-frequency applications, J. Low Temp. Phys., 1989, 76:287-386.

[23] Weinstock, H., SQUID Sensors, Fundamentals, Fabrication, and Applications, Dordrecht, Kluwer, 1996.

[24] Nenonen, J., Katila, T., and Montonen J. Thermal noise of a biomagnetic measurement dewar, In Williamson, S.J., Hoke, M., Stroink, G., Kotani M., Advances in Biomagnetism, New York, Plenum Press, 1989, pp.729-732.

[25] Erné, S.N. Shielded rooms, In Williamson, S.J., Romani, G.L., Kaufman, L., Modena, I., Biomagnetism: An Interdisciplinary Approach, New York, Plenum Press, 1983, pp. 569-578.

[26] ATB S.r.l., Chieti, Italy.

[27] Erné, S.N. Analog filtering techniques, In Williamson, S.J., Romani, G.L., Kaufman, L., Modena, I., Biomagnetism: An Interdisciplinary Approach, New York, Plenum Press, 1983, pp. 579-589.

[28] Penfield, W. and Rasmussen T. The cerebral cortex of man, Macmillan, New York, 1950.

[29] Romani, G. L., Williamson, S. J., and Kaufman, L. Tonotopic organization of the human auditory cortex, Science, 1982, 216:1339-1340.

[30] Pantev, C., Hoke, M., Lehnertz, K., Lütkenhöner, B., Anogianakis, G., and Wittkowski, W. Tonotopic organization of the human auditory cortex revealed by transient auditory evoked magnetic fields, Electroencephalography and clinical Neurophysiology, 1988, 69:160-170.

[31] Pantev, C., Hoke, M., Lehnertz, K., and Lütkenhöner, B. Neuromagnetic evidence of an amplitopic organization of the human auditory cortex, Electroencephalography and clinical Neurophysiology, 1989, 72:225-231.

[32] Pantev, C., Hoke, M., Lütkenhöner, B., and Lehnertz, K. Tonotopic organization of the auditory cortex: pitch versus frequency representation, Science, 1989, 246:486-488.

[33] Näätänen, R., Simpson, M., and Loveless, N. E. Stimulus deviance and evoked potentials, Biological Psychology, 1982, 14:53-98.

[34] Näätänen, R., Paavilainen, P., Tiitinen, H., Jiang, D., and Alho, K. Attention and mismatch negativity, Psychophysiology, 1993, 30(5):436-450.

[35] Kristeva-Feige, R., Rossi, S., Pizzella, V., Tecchio, F., Romani, G. L., Erné, S., Edrich, J., Orlacchio, A., and Rossini, P. M. Neuromagnetic fields of the brain evoked by voluntary movement and electrical stimulation of the index finger, Brain Research, 1995, 682:22-28.

[36] Hari, R., Karhu, J., Hämäläinen, M., Knuttila, J., Salonen, O., Sams, M., and Vilkman V. Functional organisation of the human first and second somatosensory cortices: a neuromagnetic study, European Journal of Neuroscience, 1994, 5:724-734.

[37] Kaukoranta, E., Hämäläinen, M., Sarvas, J., and Hari R. Mixed and sensory nerve stimulations activate different cytoarchitectonic areas in human primary somatosensory cortex SI, Experimental Brain Research, 1986, 63:60-66.

[38] Barth, D.S., Sutherling, W., Engel Jr., J., and Beatty, J. Neuromagnetic localization of epileptiform spike activity in the human brain, Science, 1982, 218:891-894.

[39] Barth, D.S., Sutherling, W., Engel Jr., J., and Beatty, J. Neuromagnetic evidence of spatially distributed sources underlying epileptiform spikes in the human brain, Science, 1984, 223:293-296.

[40] Ricci, G.B., Romani, G.L., Salustri, C., Pizzella, V., Torrioli, G., Buonomo, S., Peresson, M., and Modena, I. Study of focal epilepsy by multichannel neuromagnetic measurements, Electroencephalogr. clin. Neurophysiol., 1987, 66:358-368.

[41] Nakasato, N., Levesque, M. F., Barth, D., Baumgartner, C., Rogers, R. L., and Sutherling, W. W. Comparisons of MEG, EEG, and ECoG source localization in neocortical partial epilepsy in humans, Electroencephalogr. Clin. Neurophysiol., 1994, 91:171-178.

[42] Nakasato, N., Karou, S., Tsuyoshi, K., Satoshi, F., Akitake, K., Satoru, F., and Takashi, Y. Functional brain mapping using an MRI-linked whole head magnetoencephalography (MEG) system, in: Barber, C., Celesia, G., Comi, G.C., and Mauguiere, F. Functional Neuroscience, Amsterdam, Elsevier, 1996, pp. 119-126.

[43] Rossini, P. M., Martino, G., Narici, L., Pasquarelli, A., Peresson, M., Pizzella, V., Tecchio, F., Torrioli, G., and Romani, G. L. Short-term brain 'plasticity' in humans: transient finger representation changes in sensory cortex somatotopy following ischemic anaesthesia, Brain Research, 1994, 642:169-177.

[44] Merzenich, M.M., Kaas, J:H., Wall, J., Nelson, R.J., Sur, M., and Felleman, D. Topographic reorganization of somatosensory cortiacl areas 3b and 1 in adult monkeys following restricted deafferentiation, Neuroscience, 1983, 8:33-55.

[45] Rossini, P.M., Tecchio, F., Pizzella, V., Lupoi, D., Cassetta, E., Pasqualetti, P., Romani, G.L., and Orlacchio, A. On the reorganization of sensory hand areas after mono-hemispheric lesion: a functional (MEG) / anatomical (MRI) integrative study, Brain Research, 1998, 782:153-166.

[46] Flor, H., Elbert, T., Knecht, S., Wienbruch, C., Pantev, C., Birbaumer, N., Larbig, W., and Taub, E. Phantom-limb pain as a perceptual correlate of cortical reorganization following arm amputation, Nature, 1995, 375:482-484.

[47] Pantev, C., Oostenveld, R., Engelien, A., Ross, B., Roberts, L.E., and Hoke, M. Increased auditory cortical representation in musicians, Nature, 1998, 392:811-814.

[48] Rossini, P.M., Tecchio, F., Pizzella, V., Romani, G.L., Cassetta, E., Indovina, I., Bicciolo, B., and De Campora, E. Auditory cortical changes induced by otosclerosis and their variations after stapes substitution, In: Comi, G.C., Lucking, C.H., Kimura, J., and Rossini, P.M. Clinical Neurophysiology: From Receptors to Perception, Amsterdam, Elsevier Science BV, 1999.

[49] Grimm, C., Schreiber, A., Kristeva-Feige, R., Mergner, T., Hennig, J., Lucking, C.H. comparison between electric source localisation and fMRI during somatosensory stimulation, Electroencephalogr. Clin. Neurophysiol., 1998, 106(1):22-29.

[50] Babiloni, F., Carducci, F., Del Gratta, C., Babiloni, C., Roberti, G.M., Cincotti, F., Bagni, O., Romani, G.L., and Rossini, P.M. Multimodal integration of high resolution EEG, MEG and functional magnetic resonance data, Intern. Jour. Bioelectromagnetism, 1999, 1:1-19.

[51] Rossini, P.M., Caltagirone, C., Castriota-Scanderbeg, A., Cicinelli, P., Del Gratta, C., Demartin, M., Pizzella, V., Traversa, R., Romani, G.L. Hand motor cortical area reorganization in stroke: a study with fMRI, MEG and TCS maps. NeuroReport, 1998, 9:2141-2146.

Acknowledgements

The authors wish to acknowledge the contribution of several people from the groups in Chieti and Rome to the work presented in this tutorial: Della Penna S., Pizzella V., Rossini P.M., Tecchio F., Torquati K.

Modeling aspects of bioelectric source imaging

van Oosterom A.

Laboratory of Medical Physics & Biophysics, University of Nijmegen, Nijmegen, the Netherlands

Scope

This paper introduces various concepts that relate to the modeling that is required for the functional imaging of bioelectric sources, be it in the world of electro-encephalography (EEG), magneto-encephalography (MEG), electro-cardiography (ECG), magneto-cardiography (MCG) or otherwise. These notions are relevant for the methods applied to the processing of recorded electric signals as well as magnetic signals.

The formulations used in this text are in terms of electric potentials, but they are expressed in as general terms as is possible; they relate to the field of ECG as well as to EEG. Several of these formulations are drawn from similar introductory papers as presented by the author. They have been 'polished' and tuned to the scope of the NFSI-99 meeting.

In addition to this paper and the references included, which reflect a personal view on the field, the interested newcomer to this field is advised to consult the relevant chapters in the following recently published textbooks:

Bioelectromagnetism: J. Malmivuo and R. Plonsey [1] and
Bioelectricity and Biomagnetism: R.M. Gulrajani [2].

Introduction

The necessity for using models to support the interpretation of observed bioelectric (magnetic) signals, as is the objective of bioelectric functional imaging, stems from the fundamental impossibility (as realized by Helmholtz as early as 1853 [3]) of deriving a unique specification of internal (bio-)electric sources on the basis of observations on the body surface (ECG,EEG) or just outside the body (MCG,MEG). A multitude of different sources may give rise to identical data as observed outside the actual source region. To circumvent this problem a description of the bio-electric generator needs to be postulated *a priori*, the source model. In addition, a model needs to be involved describing the passive effects on the observed data of the body tissues that surround the active electric sources.

A brief summary of the main topics discussed in this paper is as follows.

Source models
Source models of different natures have been developed. They can be classed as having either a purely physical nature or as having a nature that is closely linked to the source properties that one may want to 'image'. It is the second type that is the most interesting one for an ultimate clinical application, but also the most challenging one.

Volume conduction models
The tissues around the primary electric sources play an essential role in the wave forms that can be observed. The full documentation of the conductive properties of the tissues is impossible because of their complex nature, involving the inhomogeneity and anisotropy implied in their morphology. Simplifying models have been developed over the years that seem to be able to do sufficient justice to this complexity.

Forward Problem
Both models having been formulated, this leads to the Forward Problem, *i.e.*, the computation of the potential or the magnetic field distributions in the points of observation. Within the limitations of both models involved the computation of the transfer between sources and observed data does not pose a major problem: fast numerical algorithms have been developed that can solve the forward problem accurately.

Inverse Problem
The restrictions implied in the source models make it possible to compute (estimate) their parameters on the basis of observed data outside the source region. The latter procedure is known as the Inverse Problem. Several of the methods being studied at the moment involve a specification of the solution, the sources, in a format that allows the solution to be presented as an image, hence the term 'bioelectric source imaging'.

Constraints
The fundamental impossibility mentioned above, caused by the physics involved, demands that the physiological basis of the source configurations used needs to be secured *a priori*. Moreover, the more interesting the sources are allowed to be, the heavier are the demands on the quality of the volume conductor model.

Source Models

The electric potential distribution on the body surface and the magnetic field just outside the body are generated by internal biological sources. In the description of these phenomena two source types are distinguished: *primary* sources and *secondary* sources. The primary sources are those that result from the nature of the biochemical processes at the membranes of individual cells. It is the primary sources that will be discussed here. The term 'secondary source' is used in some descriptions of the effect of the conductive properties of the medium surrounding the

primary sources. Such sources are implied in the discussion on the volume conductor models.

If the source model is to give a physiological interpretation of the observed signals, *a priori* knowledge about the source character is essential. If, on the other hand, the model is merely used for data representation or for data reduction the requirements are less stringent.

When describing primary source models three different levels can be distinguished. The required level depends on the objective of any specific application. The first level is the microscopic, cellular level, directly linked to cellular electrophysiology. The second level is the macroscopic level of the impressed currents expressed in terms of the physics of electric volume conduction. This is the level of electric potentials observed by means of electrodes placed within, or in direct contact with, the tissue carrying the primary sources. The third level is that of the equivalent generators used to describe the fields at more remote observation points, such as the positions of the electrodes placed on the thorax or the scalp, or by magnetometers placed just outside the body.

All of these source descriptions, even the ones at the cellular level, are so-called *equivalent* sources in the sense that they (only) serve to describe observed phenomena. They are derived from observed potentials and measured, or assumed conductivity values. When assessing macroscopic source strength from observed local macroscopic fields, the local conductivity has to be taken into account. When the derived source strength is used to compute, or interpret, distal fields, the entire spatial distribution of electric conductivity needs to be considered.

The theory of electric volume conduction allows one to characterize bioelectric sources in two steps. First, the potential distribution is expressed as generated by the primary sources when situated in a hypothetical, infinite space having homogeneous conductive properties. This expression will be referred to as the 'infinite medium' potential. Next, the effect of the actual inhomogeneities in the volume conductor, in particular of its bounds, on the potentials is determined. This effect can be expressed as a linear operator acting on the infinite medium representation. The linearity arises from the fact that the strengths of the secondary sources describing the volume conductor influence depend linearly on those of the primary sources. Further on, some major source models are commented on that have a direct application in the field of functional source characterization. While considering these models, one should realize that all source models of bio-electric phenomena are theoretical constructs: equivalent sources that serve the purpose of describing the fields at some distance from the active membranes. For the point sources as discussed below, this is obvious: if one approaches such a source the expression for the potential becomes infinite.

Point Sources; Dipoles

Outside the actual source region the potential can be characterized by means of an equivalent source description arising from the multipole expansion of the source distribution [4]. The nature of this description is such that a single point in space suffices to specify its location.

At the cellular level the electric current is 'pumped around' by the local biochemical processes. As a consequence, the first term in the multipole expansion, the monopole, is zero. The next term in the expansion is the *dipole*. Its potential varies as R^{-2}, where R is the distance between source and observation point. Because of its dominance in the far-field potentials, it is a much used equivalent source, both in the fields of ECG and EEG. It forms the basis of vectorcardiography (VCG) and is used as an elementary building block for more complex models. In VCG the position of the dipole is not considered explicitly: merely the three components of the dipole (vector) are used. In other applications the position is allowed to vary as a function of time. Single or multiple dipoles have been postulated, fixed in position, orientation or both.

The dipole potential depends linearly on the (three) dipole components and non-linearly on its three coordinates in 3-D space: six parameters in all. If the dipole components are expressed in Polar coordinates rather than in Cartesian coordinates, the potential depends linearly on one parameter: strength and non-linearly on the two angles defining the dipole orientation in 3-D space as well as on its three positional coordinates, again a total of six. If both position and orientation are fixed *a priori* just a single, linear parameter remains. In some applications multiple dipoles are postulated for describing observed potentials. The total number of parameters involved in that case is that of the individual dipoles, multiplied by N, the number of dipoles considered. Generally, if this total number is large, a stable estimation of all parameters involved is impossible and additional constraints have to be incorporated [5].

The next term in the multipole expansion is the *quadrupole*. Its potential varies as R^{-3}. Its strength can be specified by five independent parameters.

In a similar fashion moments of the distribution of higher order still may be introduced. The corresponding equivalent sources are referred to as the *octopole*, the *hexadecapole*, etc, each time doubling the number of elementary poles involved. In general, the potential generated by the m-th order moments of the multipole expansion varies as $R^{-(m+1)}$. This dependency of the various expansion terms on the different powers of the distance to the source explains why the apparent nature of observed potentials is so often dipolar. A more elaborate source description is required for observations made close to the actual source (heart, nerve fiber,..). The values of the expansion coefficients for multipoles of order greater than zero (dipole, quadrupole, octopole,...) depend on the origin chosen in the expansion. These various terms in the expansion have a different physical dimension (A.m, A.m^2, *etc*).

The multipole expansion provides an efficient method for data reduction. In this respect its use is similar to the expansion of observed potentials in terms of spherical harmonics [6, 7]. However, a major difficulty in the use the multipole expansion for describing bioelectric sources is the fact that the individual expansion terms cannot usually be interpreted physiologically. Only in some instances,

e.g., when determining the position of a source: the topic of source *localization*, can the solution benefit from the inclusion of a quadrupolar source term next to the dipole that is usually involved.

Distributed Sources

Because of the difficulty in interpreting the multipolar terms in terms of the underlying electrophysiology, several attempts can be witnessed in the recent literature of having used source descriptions in which multiple — usually dipolar — sources are distributed throughout a particular region of 3-D space. In some cases they have been restricted to surfaces. As such these can be classed as 2-D source models. A major advantage of using distributed sources is the fact that, the source position being fixed, the subsequent source characterization is a linear problem.

A brief characterization of the major 2-D models is as follows.

Monolayer

The first of the basic 2-D models considered here is the monopole sheet. Each element $dS = dS(\vec{r})$ of the surface considered is assumed to carry a monopole of strength $J_S dS$, with J_S the local current surface density (unit A.m^{-2}).

This source configuration has experienced a limited use so far as a model of primary sources of macroscopic bioelectric fields (however, see [8, 9, 10]). As a secondary source description it is utilized in the work of Gelernter and Swihart (see [11]). It is also involved in the handling of boundary conditions expressed in terms of prescribed potentials over a surface [12, 13, 9].

Double layer/Dipole layer

The most commonly used 2-D source model is the dipole layer, or double layer [14, 15]. Here each element $dS = dS(\vec{r})$ of the surface considered is assumed to carry an elementary current dipole $p(\vec{r})d\vec{S}$, with $p(\vec{r})$ the local current dipole surface density (unit: A.m.m^{-2}=A.m^{-1}). Note that in this case the elementary dipoles are directed along the local surface normal. This source configuration has a considerable importance, both as a model of primary sources of macroscopic bioelectric fields, and as a secondary source as used in treating the effect of differences in conductivities at boundaries in the medium. This source configuration is known as either *double layer*, *current dipole layer* or *dipole layer*. The local strength of the layer may be specified by either $p(\vec{r})$ or by the local potential jump $V_D(\vec{r}) = p(\vec{r})/\sigma(\vec{r})$ that is seen when crossing the layer, with $\sigma(\vec{r})$ the local electric conductivity.

If the strength of the double layer is constant (p) over the surface S carrying the source this configuration is known as the *uniform dipole layer*. In this case, the infinite medium potential can be shown to be proportional to the solid angle at which the surface S is seen from the observation point. An important property of the uniform double layer is that, when situated in a homogeneous medium, any *closed* surface carrying such a layer generates zero potential (differences) in the exterior medium, whereas the potential in its interior is lower than in its exterior by $V_D = p/\sigma$.

For a uniform double layer with S having an arbitrary shape, numerical methods have to be used for computing the resulting infinite medium potentials or fields (see [16, 17, 18]).

The uniform double layer model has a special place in electrocardiography. It can be called the classical source model of the depolarization wave front: surfaces S_D carrying equivalent sources are considered, which represent depolarization wave fronts as they progress through the myocardium. It was introduced in 1933 by Wilson *et al.* [19] and has served very well since for explaining ECG wave forms *qualitatively* [20]. It has a much more direct link with electrophysiology than the different terms in the multipole expansion. Conceptual notions derived from the uniform double layer can be found in most basic text books on practical electrocardiography. In addition, several *quantitative*, computer model, studies have been successfully based on the uniform double layer, be it implicitly [21] or explicitly [22, 23, 24]. A theoretical support to using this model in spite of the acknowledged anisotropic nature of the myocardium is implied in [25]; a recent demonstration of its usefulness in an inverse procedure, validated by means of tank measurements, can be found in [26].

General Dipole Layer

In EEG neither the uniformity of the elementary dipoles nor their alignment parallel to the local surface normal can be always assumed to be in agreement with the underlying electrophysiology. Here the surface postulated as carrying the sources usually correspond to (folded) parts of the cortical surface. In an application to describing the magnetic signals outside a volume conductor of spherical symmetry a model has been postulated in which the dipoles are directed along the surface [27]. However, beyond the restriction of this spherical configuration, this source model loses most of its attractiveness.

Voltage Sources

Voltage sources are based on the unique theoretical one-to-one relationship between the potentials at the surface bounding a volume conductor and those at some interior closed surface, on condition that no primary sources are present in between [28]. All active sources are assumed to lie within the inner surface. Inverse methods based on this relationship aim at obtaining a 'closer look' at the sources without assuming any *a priori* knowledge about the character of these sources. In this method the interpretation of the computed potentials in terms of the underlying electrophysiology is deferred.

In electrocardiography the interior surface considered is the pericardium, usually referred to as the epicardium. The associated inverse problem has received considerable attention (see [29, 30, 31, 32, 33, 34, 35, 36, 37, 38, 39, 40]).

In the world of EEG the interior surface considered is the surface bounding the cortex. Early references to this approach include [41],[42],[43] and [44].

The voltage model is directly linked to that of the monolayer: if the voltages on the inner surface are known, feeding current into the outer region, these currents can be computed and *vice versa* (see [9]).

Source Models and Anisotropy

Most tissues in which the primary sources are situated have an anisotropic electric conductivity ([45, 46, 47]). In the modern handling of anisotropy by means of the *bi-domain* model [48, 49] the anisotropy in the electric conductivity of both the extra-cellular and the intra-cellular space, treated as a macroscopic continuum, is included. In the expression of the macroscopic electric field the true source strength and the local conductivity of the medium interact [50, 51]. These factors taken together, they can in fair approximation in some situations be represented by a single equivalent source. In most situations this is even a necessity, based on the fact that insufficient data are available to take these factors separately into account. The much quoted figure for the transverse intracellular/extracellular conductivity ratio [52] of myocardial tissue is incorrect, based as it is on an incorrect interpretation of experimental data (see [53]).

Volume Conductor Models

Several methods have been developed for treating the influence of volume conduction on observed the potentials. To this end a model of the volume conductor is postulated, describing the distribution throughout 3-D space of the electric conductivity of the medium.

One of the earlier models is the semi-infinite space, in which the influence of the surface bounding the currents can be found by 'image' methods [7], as used in electrostatics. Other models used in those days are the homogeneous sphere, cylinder and spheroid [34]. These models evolved in an increasing realism; their introduction closely followed the development of the analytical solutions to the implied forward problems as these became available. Early attempts in using truly 'realistic' models were based on torso-shaped tanks containing a conductive fluid. This approach was perfected by allowing the conductivity to be inhomogeneous and/or anisotropic (see, *e.g.* ,[54]). Such models have a very high 'persuasive' value. However the flexibility of these tanks representing the volume conduction model is very limited.

Shortly after the first introduction by Gelernter and Swihart [11] of computer methods for the numerical handling of the volume conductor models, the tank methods disappeared. Since that time different numerical methods have been introduced. The most commonly used are the boundary element method (BEM), the finite difference method (FDM) and the finite element method (FEM). These methods have now been refined to such an extent that the 'problematic' element in the forward problem mainly lies much more in the selection of an appropriate volume conductor model, rather than in the computation of their effect.

Models that can be solved by analytical methods are relevant for developing insight into the basics of electric volume conduction problems [55]. Moreover, they are extremely useful in testing the accuracy of numerical methods that are in use for treating the practical configurations that cannot themselves be solved by analytical methods [56, 57, 58]. An analytical solution for handling anisotropy in the case of the concentric spheres models was described by de Munck ([59]). Some of the numerical problems involved in this analytical computation have been solved by Zhou *et al.* [60].

The numerical method which has been used most extensively so far is the boundary element method [34, 11, 56, 57, 58]. Based on Green's laws from potential theory, this method expresses volume conduction in 3-D space within the body by means of a system of integral equations, the integrals being taken over any multi-contained, (2-D) surfaces (interfaces) bounding regions of different electric conductivity. This reduction of dimensionality greatly facilitates the numerical handling of this problem.

The major interface is the boundary of the body, at the skin, where the conductivity drops to zero. For the genesis of the ECG inhomogeneities, which have been shown to have a pronounced effect [61, 23] are the lungs (approximately five fold lower conductivity relative to that of the 'overall' thorax), and the heart's cavities (approximately three fold higher conductivity). In EEG it is the skull, having a much lower conductivity than the other tissues, that is the most prominent influence. In the concentric spheres models, the analytical expressions can cope with high values of the conductivity ratio $cr \triangleq$ (conductivity scalp)/(conductivity skull), provided a sufficiently large number of terms is included in the series expansion (see [60]). In the numerical methods a high value of cr severely limits the accurate of the results. The accuracy can only be safe-guarded by increasing the discretization level of the surfaces involved [56, 57]. There seems to be an uncertainty in the literature on the value of cr. Most studies report using the value of $cr = 80$. Recently it has been argued that a more realistic value is of the order of 20 [62]. If the isolation of the skull would be complete, the MEG could be computed by considering just the inner boundary of the skull [63]. For the EEG, the potential at this boundary can be used to replace the infinite medium potential when computing the effect of the poorly conducting skull. This idea has given rise to the concept of the Isolated Problem Approach (IPA); see [63, 56]. This approach will be less valid the more cr tends to one. A pragmatic approach to handling this complexity can be found in [57].

In early studies using numerical methods the relevant geometry (of the interface) was 'realistic', derived from anatomy textbooks. More recently the actual geometry of the individual subjects involved is incorporated. In ECG studies Magnetic Resonance Imaging (MRI) is being used for this purpose. The accurate imaging of the skull by means of this technique is problematic. Here, computer tomography remains the best method, its application being

restricted by radiation hazards.

The Forward Problem

The Forward Problem deals with the potentials on the boundary (or magnetic fields outside the body) computed from assumed sources and from a transfer function derived from the volume conductor model used. Expressed in terms of potentials, a general formulation of the Forward Problem reads: compute the potentials $\Phi(\mathbf{y}, t; \mathbf{p}(\mathbf{x}, t))$ from

$$\Phi(\mathbf{y}, t; \mathbf{p}(\mathbf{x}, t)) = \int_V M_s(\mathbf{y}, \mathbf{x}; \mathbf{p}(\mathbf{x}, t)) s(\mathbf{x}; \mathbf{p}(\mathbf{x}, t)) dv(\mathbf{x}), \quad (1)$$

with

$\Phi(\mathbf{y}, t; \mathbf{p}(\mathbf{x}, t))$	: the potential at $\mathbf{y}$ and time t,
$s(\mathbf{x}; \mathbf{p}(\mathbf{x}, t))$	: the source strength in position $\mathbf{x}$ at time t,
$\mathbf{p}(\mathbf{x}, t)$	: the parameter (vector) specifying the source at position $\mathbf{x}$ and time t,
$M_s(\mathbf{y}, \mathbf{x}; \mathbf{p}(\mathbf{x}, t))$	: the medium transfer function as related to the source s and its character,
V	the volume containing all primary sources.

This is a formulation that is quite general, paving the way for treating the Inverse Problem as a parameter estimation problem.

The Inverse Problem

As stated, the inverse problem deals with the determination of bioelectric sources from measured potentials $V(\mathbf{y}, t)$ and a computed medium transfer function $M_s(\mathbf{y}, \mathbf{x})$ as computed from on the volume conductor model used. The uniqueness of sources as determined from external observations (potentials, fields) is, in general, not guaranteed: it falls within the class of the so-called 'ill-posed' problems. However, if *a priori* information on the source is available the problem may be circumvented.

The Inverse Problem treated as a Parameter Estimation Procedure

The inverse problem can be formulated as a parameter estimation problem. In the formulation used here, the values of the elements of parameter vector $\mathbf{p}$ may be required to be different at each subsequent time instances. In that situation the parameter vector is replaced by a matrix $\mathbf{P}$.

In the least squares approach, the source parameters $\mathbf{P}$ are found by minimizing, with respect to the elements of $\mathbf{P}$, the object function

$$R = \|V - \Phi(\mathbf{P})\|^2 \quad (= \|V - M_s(\mathbf{P}_2, \mathbf{q}) s(\mathbf{P}_1)\|^2), \quad (2)$$

thus yielding the least squares residual difference between observed potentials V and model 'predictions' Φ ($\|\ \|$ denotes the Euclidean norm). Note that the parameter matrix $\mathbf{P}$ is divided into the part $\mathbf{P}_1$, related to the source *strength* and the part $\mathbf{P}_2$ related to other source aspects, such as position. The particular version of M involved may further depend on the conductivity or the geometry the volume conductor. In (2) any parameters involved in specifying the volume conductor are denoted by $\mathbf{q}$. Note that this formulation allows one to incorporate all temporal aspects involved. If just a single time instant needs to be considered, all parameter matrixes reduce to parameter vectors.

A major subdivision in the handling of this problem relates to whether the potentials depend *linearly* or *non-linearly* on the source parameters.

The nature of the Forward Problem is such that in practical applications the potentials can be treated in matrix form: data 'predicted' by the model at T time instants (*temporal* sampling) and L lead (electrode) positions (*spatial* sampling) are represented by a matrix $\mathbf{\Phi}$, of which row vector $\mathbf{\Phi}_{\ell.}$ (dimension T) represents the signal of lead ℓ and column vector $\mathbf{\Phi}_{.t}$ (dimension L) represents the potential distribution (map) at time t, hence its dimension is L×T.

Similarly, discretized versions of the observed potentials V can be represented by a matrix $\mathbf{V}$. The corresponding transfer function $M(\mathbf{y}, \mathbf{x})$, can be represented as a L×M dimensional transfer matrix $\mathbf{M}$, and the source S by a M×T dimensional matrix $\mathbf{S}$ involving the source strength parameters at all T time instants considered. In some publications the rows of the transfer matrix $\mathbf{M}$ are referred to as the 'lead vectors'. In this notation, a sparse version of (1) reads

$$\mathbf{\Phi}(\mathbf{P}) = \mathbf{M}(\mathbf{P}_2)\mathbf{S}(\mathbf{P}_1). \quad (3)$$

The Linear Case

If the parameter matrix $\mathbf{P}$ includes source strengths only, $\mathbf{\Phi}$ depends linearly on the matrix of dimension M×T, in other words: the parameters are identical to the source strengths. In this situation the position of the sources is assumed to be known *a priori*.

Examples are: point sources (dipoles, multipoles) for which their position in space is fixed, and in particular for the the various distributed sources (see section: Sources).

This situation leads to the Linear Least Squares (LLS) problem. The formulation of the Inverse Problem then reads: solve $\mathbf{S}$ from

$$\mathbf{V} \approx \mathbf{M}\ \mathbf{S},$$

the notation $\approx$ indicating that a least squares solution is to be found. This system of linear equations has at least one solution (see [64, 65]). The solution is unique if the matrix $\mathbf{M}$ is full rank, which means that its rank k (see, *e.g.*, [64]) satisfies k=min(L,M). If the matrix is rank deficient the solution can be made unique by choosing the norm of the solution to be minimal by forcing the projection of the solution onto the null space of the matrix to be zero. This solution is the Moore-Penrose Pseudo Inverse [64]. However, adding other selections from the null space of $\mathbf{M}$ will

lead to the same residual, and may make the total solution to comply better with *a priori* knowledge on its character.

The least squares minimal norm solution for the general case can be found from
1) Application of the algorithm HFTI ([66])
2) Use of the Singular Value Decomposition (SVD) [67, 68]
The latter is a more elaborate method for treating the general case, but one that allows one to study separately the nature of the transfer matrix $\mathbf{M}$: its rank, range, domain, null space and unreachable space. The latter is the null space of $\mathbf{M}^t$. It is orthogonal to the range of $\mathbf{M}$. All column vectors of the matrix of least squares residuals lie entirely within this space (see [64]). These column vectors represent the components of the observed signal that are incompatible with the models involved.

The *Non*-Linear Case

In some cases Φ depends *non*-linearly on at least some of the parameters. Examples are: stationary dipole(s) and/or moving dipoles. A stationary dipole is a dipole for which the determination of its (stationary) position is a part of the inverse procedure. The term 'fixed' dipole denotes the situation where this position is known *a priori*.

Here a minimization problem can be formulated as: find $\mathbf{P}$ which minimizes the object function

$$R = \|\mathbf{V} - \mathbf{\Phi}(\mathbf{P})\|^2 \ \ (= \|\mathbf{V} - \mathbf{M}(\mathbf{P}_2)s(\mathbf{P}_1)\|^2), \quad (4)$$

with $\mathbf{P}_1$ now referring to linear parameters only, and $\mathbf{P}_2$ referring to the non-linear parameters involved, such as source positions.

The problem is classed as a Non Linear Least Squares (NLLS) problem. The solution can be found from one of the several iterative minimization procedures, like Quasi Newton, Marquardt [69], Box-Kanemasu (see:[70]) or simulated annealing, described in the literature. These methods require 'sensible' initial estimates of the solution (the parameters estimated).

The Handling of Volume Conductor Effects

When formulated as a parameter estimation problem, the Inverse Problem entails a specific difficulty arising from the computational burden related to the handling of volume conductor effects. This difficulty has been resolved as follows [71]. The numerical solution to the forward problem — for a single time instant — in a bounded, inhomogeneous volume conductor can be formulated by means of the system of linear equations

$$\phi = \mathbf{B}\mathbf{g}(\mathbf{p}). \quad (5)$$

Here, ϕ is the solution vector of the potentials, matrix $\mathbf{B}$ expresses the properties of the volume conductor, and $\mathbf{g} = \mathbf{g}(\mathbf{p})$ is a vector representing the potentials generated by the sources, as specified by the parameter vector $\mathbf{p}$, in the infinite medium. The formulation stems directly from the solution of Poisson's equation by means of the Boundary Element Method BEM (see *e.g.*, [72]), but other solution methods, like the FEM [73], or analytical ones [57] may also be cast in this form. The formulation in (5) replaced the earlier method for solving ϕ by means of an iterative matrix inversion, see[71]. Note that the vector $\mathbf{g}$ depends on the source parameters, but matrix $\mathbf{B}$ does not.

Since $\mathbf{B}$ depends exclusively on the properties of the volume conductor, the potential distribution generated by any source inside that volume conductor can be found at little computational cost from (5) once $\mathbf{B}$ has been obtained. As a consequence, matrix $\mathbf{B}$ may be pre-computed and does not change during the course of the iteration process outlined below.

A non-linear parameter estimation procedure iteratively minimizes the object function R (residual difference), as defined in (4) or (6). The more efficient parameter estimation techniques make use of the partial derivatives of the residual difference function with respect to all parameters [74]. This works out as having to compute all partial derivatives of the (model) potential ϕ. So, when using an efficient parameter estimation procedure, the (model) potential at the observation points, as well as the partial derivatives of the (model) potential to all parameters involved, need to be computed at each iteration step. Once matrix $\mathbf{B}$ has been computed, the potential for any source $\mathbf{g}(\mathbf{p})$, which may be a non-linear function of the parameter vector $\mathbf{p}$, can be found from (5). By taking the partial derivatives to parameter elements p_j at both sides of (5) one finds

$$\frac{\partial \phi_i}{\partial p_j} = \mathbf{B}\frac{\partial g_i(\mathbf{p})}{\partial p_j}.$$

The elements of the vector $\frac{\partial \phi_i}{\partial p_j}$ can be interpreted as the potentials generated by a source which generates a field $\frac{\partial g_i}{\partial p_j}$ at point i in an infinite medium. As a result, the effect of volume conduction on the potential as well as on the partial derivatives of the potential to all parameters involved at each iteration step of the parameter optimization procedure can be obtained by means of a multiplication by the same matrix $\mathbf{B}$.

Following its description in 1989 ([71]) this same idea was described in 1991 (application to MCG, [75]) and again in 1995 (application to EEG, [76]) and once again in 1996 by the same author ([77]) each time without including a reference to the 1989 paper. This probably means that it is a beautiful wheel that was worth to be re-invented *ad infinitum* (SIC!).

The Decoupling Algorithm

In some cases the potentials as computed from the forward models (source- and volume conductor) depend linearly on some of the source parameters as well as non-linearly on others. An obvious example in the domain of the Inverse Problem is the case of stationary, or of moving dipoles, which depend linearly on dipole strength and non-linearly on dipole position as discussed above. Various strategies for handling this situation have been described in the literature of bioelectric source identification. Since the linear parameter estimation problem has solution methods which are much faster than those related to non-linear ones, one

is tempted to treat these problems separately. This has in fact been practiced by some [78]. In this approach in each iteration step the linear parameters and the non-linear ones are adjusted subsequently, each by their own optimal solution method. A far more powerful method is the decoupling algorithm, described in the general literature of the numerical treatment of parameter estimation [79, 80]. The method is particularly effective in the situation where the parameters related to source strength, are linear ones, and those related to position, non-linear ones, are separated in the forward formulation (3). In this situation the latter can be reformulated as

$$\phi = \mathbf{M}_{\mathbf{p}_2}\mathbf{s}(\mathbf{p}_1),$$

with $(\mathbf{p}_1, \mathbf{p}_2)$ being the full parameter vector as before. The method minimizes, first of all, the residual difference in the space orthogonal to the image space of $\mathbf{M}_{\mathbf{p}_2}$, relating to the non-linear parameters $\mathbf{p}_2$ only. This can be carried out by means of one of the general non-linear minimization algorithms that are available in most computer libraries devoted to numerical analysis (*e.g.*,[81]). Upon completion, a single estimation step related to the linear part of the parameter vector is required. The method was found to save a lot of computing time, in particular for cases where the number of linear parameters is large relative to the number of non-linear ones [82].

The Precision of the Estimated Parameters

Most studies on inverse procedures end by stating the final solution reached. What is usually lacking is an analysis of the precision of the solution obtained. If this analysis is carried out at all, it is usually based on a Monte Carlo type of approach: numerous runs of noise added to the potential data are considered and their effect on the inversely determined source characteristics is documented. In dipole localization problems, scattergrams of the computed source positions are usually presented. Alternatively, the variances of the computed estimates are listed.

In the parameter estimation literature, methods can be found for directly computing the variance-covariance matrix of the computed estimates, both for the linear and the non-linear case. For the linear case, if the elements of the residual difference can be assumed to be independent stochastic variables, following a Gaussian distribution with known variance σ^2, the variance-covariance matrix $cov(\mathbf{p})$ of the solution to $\mathbf{Mp} \approx \mathbf{V}$, *i.e.* $\mathbf{p} = (\mathbf{M}^t\mathbf{M})^{-1}\mathbf{M}^t\mathbf{V}$, reads

$$cov(\mathbf{p}) = (\mathbf{M}^t\mathbf{M})^{-1}\sigma^2.$$

If σ^2 is unknown it can be estimated from the norm of the residual differences [70]. If more detailed information is available on the nature of the residual, *e.g.*, its variance-covariance matrix, the quality of the computed $cov(\mathbf{p})$ can be improved [70].

For the non-linear case, the iteration process produces an estimate $\mathbf{p}$ of the actual, unknown, optimal parameter $\mathbf{p}_o$. Since the object function is a minimum around this point, one has

$$\mathbf{G}(\mathbf{p} - \mathbf{p}_o) \simeq 0,$$

with $\mathbf{G}$ a matrix with elements $g_{i,j} = \frac{\partial \phi_i}{\partial p_j}$, the sensitivity matrix of the problem [70]. Since the unknown optimal parameter vector $\mathbf{p}_o$ is a non-stochastic variable, one has for this case:

$$cov(\mathbf{p}) = (\mathbf{G}^t\mathbf{G})^{-1}\sigma^2.$$

Note that here the gradient matrix $\mathbf{G}$ plays the role of $\mathbf{M}$ in the linear case. This comes as no surprise since the sensitivity matrix of the linear problem is in fact the transfer matrix $\mathbf{M}$ itself. This procedure for finding the covariance matrix of the estimates was included in the original Marquardt paper [69].

Constraints

Implicit Constraints

Any source formulation used in the Forward Problem effectively constrains the solution space of the sources. Some of these formulations indeed imply a powerful constraint (see [83, 84]). However, in particular if the number of source terms involved is large, as is generally the case if distributed sources are used, additional explicit constraints are required.

Explicit Constraints

Even if the nature of the sources is restricted *a priori* to be within a certain class (implicit constraint), the physics involved, *i.e.*, the spreading out of the currents in the volume conductor, makes that any errors involved in the expression of the volume conduction effects, *i.e.*, in the nature of M, (the condition number of matrix $\mathbf{M}$) will amplify any inaccuracy involved in the inverse determination of the source characteristics. This is the reason why additional explicit constraints are sought.

Explicit constraints may be incorporated in the LS procedure by including an appropriate penalty function. This amounts to minimizing the object function

$$O = \|\mathbf{V} - \mathbf{\Phi}(\mathbf{p})\|^2 + \lambda\|\mathbf{C}(\mathbf{p}) - \mathbf{c}\|^2 \qquad (6)$$

with respect to $\mathbf{p}$, with $\mathbf{C}$ and $\mathbf{c}$ representing the additional constraint, and λ a parameter that is varied until the constraint is met.

Explicit constraints may be of a statistical nature, may be related to the source model used, and may be based on the physics or on the electrophysiology involved. Examples are: minimum norm [30, 85, 86, 87], spatial smoothness [30, 88], temporal smoothness [89], minimum norm and smoothness [90], spatio-temporal smoothness [39], prescribed covariance [42, 40] and the closely related MUSIC-algorithm [91].

For the linear case $\mathbf{\Phi}(\mathbf{p}) = \mathbf{Mp}$. Here the explicit constraint in (6) can be effected by choosing $\mathbf{C}(\mathbf{p}) = \mathbf{p}$ and $\mathbf{c} = 0$. This amounts to restricting the norm of the solution vector, which can be effected by means of the truncated singular value decomposition (TSVD) [92]. Alternatively, the Damped Least Squares method (DLS) [92] can be used.

Like the TSVD based method, it is based on the SVD of $\mathbf{M}$, but it reduces the influence of small singular values of the matrix, rather than discarding these altogether.

Similar solutions result by treating the problem from the view point of 'regularization' (see [84]). Here the parameter λ is called the regularization parameter, the value of which setting the weight that is allowed to the bias introduced by the regularization procedure. The various methods to find the value for λ include: CRESO (see [30]), the L-curve method as introduced in [66] and popularized by Hanssen ([93]), or covariance estimates (see [31, 33, 40]).

Conclusion

The formulation of the imaging problem in terms of a parameter estimation procedure facilitates the link between this problem and the vast literature that is available on the general problem of parameter estimation (*e.g.*, [70]) or optimization (*e.g.*, [74]) and general image processing (see [94]).

When the number of sources implied in the forward formulation is large, as is generally attempted in bioelectric source imaging, the incorporation of prior information is essential. This information has to come from dedicated invasive electrophysiological measurements. It is particular in the field of EEG that this information is insufficient, but some gaps in the knowledge on this point in the field of ECG need to be filled as well. The current literature seems to be struggling to come to terms with this fact, which stems from the basic indeterminacy of source characterization as derived from observations at a distance [3]. Added computer power alone just won't solve this problem.

References

[1] Malmivuo J. and Plonsey R., Bioelectromagnetism, New York, Oxford University Press, 1996.

[2] Gulrajani R.M., Bioelectricity and Biomagnetism, New York, John Wiley & Sons, 1998.

[3] Helmholtz H., Ueber einige Gezetze der Verteilung elektrischer Ströme in körperliche Leitern mit Anwendung auf die thierisch-elektrischen Versuche, Pogg. Ann. Physik und Chemie, 1853, 89:211–233; 353–377.

[4] van Oosterom A., Mathematical Aspects of Source Modeling, Acta Otolaryngol., 1991, Suppl.491:70–79.

[5] Scherg M. and von Cramon D., A new interpretation of the generators of BAEP waves I-V: Results of a spatio-temporal dipole model, J. Cogn. Neurosc., 1989, 1:336–355.

[6] Plonsey R., Bioelectrical Phenomena, New York, McGraw-Hill, 1967.

[7] Panofski W.K.H. and Phillips M., Classical Electricity and Magnetism, London, Addison-Wesley, 1962.

[8] Zablow L., An Equivalent Cardiac Generator which Preserves Topology, Biophysical J., 1966, 6:535–536.

[9] van Oosterom A. and Oostendorp T.F., On Computing Pericardial Potentials and Current Densities, J. Electrocardiol, 1992, 25 Sup:102–106.

[10] Dössel O. and Schneider F., The Nullspace of Electrocardiography, Biomedizinisch Technik, 1997, 42-E1:37–40.

[11] Swihart J.J., Numerical methods for solving the forward problem in electrocardiography, In: Nelson C.V. and Geselowitz D.B., The theoretical basis of electrocardiology. Clarendon Press, Oxford, 1976, Chapter 11.

[12] Barr R.C., Ramsey M., and Spach M.S., Relating Epicardial to Body Surface Potentials by means of Transfer Coefficients based on Geometry Measurements, IEEE Trans. Biomed. Eng., 1977, BME-24:1–11.

[13] Oostendorp T.F. and van Oosterom A., The potential distribution generated by surface electrodes in inhomogeneous volume conductors of arbitrary shape, IEEE Trans. Biomed. Eng., 1991, BME-38:409–417.

[14] van Oosterom A., Cell Models - Macroscopic Source Descriptions, In: Macfarlane P.W. and Lawrie T.T.V., Comprehensive Electrocardiology. Pergamon Press, Oxford, 1989, volume I.

[15] de Munck J.C., The potential distribution in a layered anisotropic spheroidal volume conductor, J. Appl. Phys., 1988, 64(2):464–470.

[16] van Oosterom A. and Strackee J., The Solid Angle of a Plane Triangle, IEEE Trans. Biomed. Eng., 1983, BME-30:125–126.

[17] de Munck J.C., A Linear Discretization of the Volume Conductor Boundary Integral Equation using Analytically Integrated Elements, IEEE Trans. Biomed. Eng., 1992, 39:986–990.

[18] Ferguson A., Zhang X., and Stroink G., A complete linear discretization for calculating the magnetic field using the boundary element method, IEEE-Trans. Biomed. Eng., 1994, 41:455–460.

[19] Wilson F.N., Macleod A.G., and Barker P.S., The Distribution of Action Currents produced by the Heart Muscle and Other Excitable Tissues immersed in Conducting Media, J. Gen. Physiol., 1933, 16:423–456.

[20] Holland R.P. and Arnsdorf M.F., Solid angle theory and the electrocardiogram. physiologic and quantitative interpretations, Progr. Cardiovasc. Dis., 1977, 19:431–457.

[21] Ritsema van Eck H.J., Digital Simulation of Cardiac Excitation and Depolarization, PhD thesis, Dalhousie University, Halifax, NS, Canada, 1972.

[22] Huiskamp G.J.M. and van Oosterom A., The depolarization sequence of the human heart surface computed from measured body surface potentials, IEEE Trans. Biomed. Eng., 1988, BME-35:1047–1058.

[23] van Oosterom A. and Huiskamp G.J.M., The effect of torso inhomogeneities on body surface potentials quantified by using tailored geometry, J Electrocardiol, 1989, 22:53–72.

[24] Greensite F. and Huiskamp G., An Improved Method for Estimating Epicardial Potentials from the Body Surface, IEEE Trans. Biomed. Eng., 1998, BME-45/1:98–104.

[25] Simms H. and Geselowitz D., Computation of Heart Surface Potentials Using the Surface Source Model, J Cardiovasc Electrophysiol, 1995, 6:522–531.

[26] Oostendorp T., MacLeod R., and van Oosterom A., Non-invasive determination of the activation sequence of the heart: validation with invasive data, Proc IEEE-EMBS Conf, 1997, pages 335–338, CD-ROM.

[27] Ilmoniemi R.J., Estimates of current distributions, Acta Otolaryngol., 1991, Supl.491:80–86.

[28] Kellogg O.D., Foundations of Potential Theory, New York, Dover Publications, 1954, first published in 1929 by J, Springer.

[29] Martin R.O. and Pilkington T.C., Unconstrained Inverse Electrocardiography, IEEE Trans. Biomed. Eng., 1972, BME-19/4:276–285.

[30] Colli-Franzone P., Guerri L., Tentonia S., Viganotti C., Baruffi S., Spaggiari S., and Taccardi B., A mathematical procedure for solving the inverse potential problem of electrocardiography. Analysis of the time-space accuracy from in vitro experimental data, Math. Biosc., 1985, 77:353–396.

[31] Barr R.C. and Spach M.S., Inverse calculation of QRS-T epicardial potentials from body surface potential distributions for normal and ectopic beats in the intact dog, Circulation Res., 1978, 42:661–675.

[32] Rudy Y. and Messinger-Rapport B.J., The inverse problem in electrocardiology: Solutions in terms of epicardial potentials, CRC Critical Reviews in Biomed. Eng., 1988, 16:215–268.

[33] Gulrajani R.M., Savard P., and Roberge F.A., The inverse problem in electrocardiography: solution in terms of equivalent sources, CRC Crit. Rev. in Biomed. Eng., 1988, 16:171–214.

[34] Gulrajani R.M., Roberge F.A., and Mailloux G.E., The forward problem of electrocardiography, In: Macfarlane P.W. and Lawrie T.T.V., Comprehensive Electrocardiology. Pergamon Press, Oxford, 1989, vol I.

[35] Johnston P.R., Walker S.J., Hyttinen A.K., and Kilpatrick D., Inverse electrocardiographic transformations: dependency on the number of epicardial regions and body surface data points, Mathematical Biosciences, 1994, 120:165–187.

[36] Shahidi A.V., Savard P., and Nadeau R., Forward and inverse problems of electrocardiography: modeling and recovery of epicardial potentials in humans, IEEE Trans. Biomed. Eng., 1994, BME-41/3:249–256.

[37] Throne R.D., Olson L.G., Hrabik T., and Windle J., Generalized Eigensystem Techniques for the Inverse Problem of Electrocardiography Applied to a Realistic Heart-Torso Geometry, IEEE Trans. Biomed. Eng., 1997, 44:447–454.

[38] Oster H.S., Taccardi B., Lux R.L., Ershler P., and Rudy Y., Noninvasive Electrocardiographic Imaging: Reconstruction of Epicardial Potentials, Electorograms, and Isochrones and Localization of Single and Multiple Electrocardiographic Events, Circulation, 1997, 96/1:1012–1024.

[39] Brooks D.H., Ahmad G., MacLeod R.S., and Maratos G.M., Inverse Electrocardiography by Simultaneous Imposition of Multiple Constraints, IEEE Trans. Biomed. Eng., 1999, BME-46/1:3–18.

[40] van Oosterom A., The use of the spatial covariance in computing pericardial potentials, IEEE-Trans Biomed Eng., 1999, BME-46/7:xx–yy.

[41] Gevins A., Le J., Brickett P., Desmond J., and Reutter B., Seeing through the skull: advanced EEGs use MRIs to accurately measure cortical activity from the scalp, Brain Topography, 1991, 3:53–64.

[42] Dale A.M. and Sereno M., Improved Localization of Cortical Activity by Combining EEG and MEG with MRI Cortical Surface Reconstruction: a Linear Approach, J. Cogn. Neurosci., 1993, 5:162–176.

[43] Nunes P.L., Silberstein R., Cadush P., Wijensinghe R., Westdorp A., and Srinivasan R., A theoretical and experimental study on high resolution EEG based on surface Laplacians and Cortical Imaging, J. Clin. Neurophysiol., 1994, 93:40–57.

[44] Gevins A., Le J., Martin N., Brickett P., Desmond J., and Reutter B., High resolution EEG: 124-channel recordings, spatial deblurring and MRI integration methods, Electroenc. Clin. Neurophysiol., 1994, 90:337–358.

[45] Colli-Franzone P., Guerri L., Viganotti C., Macchi E., Baruffi S., Spaggiari S., and Taccardi B., Potential fields generated by oblique dipole layers modeling excitation wavefronts in the anisotropic myocardium: Comparison with potential fields elicited by paced dog hearts in a volume conductor, Circulation Res., 1982, 51:330–346.

[46] Nicholson P.W., Specific impedance of cerebral white matter, Exp. Neurol., 1965, 13:386–401.

[47] Nicholson C., Theoretical Analysis of Field Potentials in Anisotropic Ensembles of Neurons, IEEE Trans. Biomed. Eng., 1973, BME-20:278–288.

[48] Geselowitz D.B. and Miller W.T.I., A bi-domain model for anisotropic cardiac muscle, Ann. Biomed. Eng., 1983, 11:191–206.

[49] Henriquez C.S., Simulating the electrical behavior of cardiac tissue using the bidomain model, Critical reviews in Biomedical Engineering, 1993, 21:1–77.

[50] Nicholson C. and Freeman J.A., Theory of Current Source Density Analysis and Determination of Conductivity Tensor for Anuran Cerebellum, J. Neurophysiol., 1975, 38:356–368.

[51] van Oosterom A., Anisotropy and the double layer concept, In: Macfarlane P., Progress in Electrocardiology. Pitman Med. Pub., Tunbridge Wells, 1979.

[52] Clerc L., Directional differences of impulse spread in trabecular muscle from mammalian heart, J. Physiol., 1976, 255:335–346.

[53] Plonsey R. and van Oosterom A., Implications of macroscopic source strength on cardiac cellular activation models, J. Electrocardiology., 1991, 24/2:99–112.

[54] Rush S., An inhomogeneous anisotropic model of the human torso for electrocardiographic studies, Med. and Biol. Eng. and Comput., 1971, 9:201–211.

[55] Edlinger G., Wach P., and Pfurtscheller G., On the Realization of an Analytic High-Resolution EEG, IEEE Trans. Biomed. Eng., 1998, BME-45/6:736–745.

[56] Meijs J.W.H., Weier O.W., Peters M.J., and van Oosterom A., On the numerical accuracy of the boundary element method, IEEE Trans. Biomed. Eng., 1989, BME-36:1038–1049.

[57] Fuchs M., Dreckhahn R., Wischmann H., and Wagner M., An Improved Boundary Element Method for Realistic Volume-Conductor Modeling, IEEE-Trans. Biomed. Eng., 1998, BME-45/8:980–997.

[58] Mosher J., Leahy R., and Lewis P., EEG and MEG: Forward Solutions for Inverse Methods, IEEE Trans Biomed Eng, 1999, BME-46:245–259.

[59] de Munck J.C., The potential distribution in a layered anisotropic spherical volume conductor, J. Appl., Phys., 1988, 64:464–470.

[60] Zhou H. and van Oosterom A., Computation of the potential distribution in a four-layer anisotropic concentric spherical volume conductor, IEEE Trans. Biomed. Eng., 1992, 39:154–158.

[61] Gulrajani R.M. and Mailloux G.E., A simulation study of the effects of torso inhomogeneities on electrocardiographic potentials, using realistic heart and torso models, Circulation Res., 1983, 52:45–56.

[62] Oostendorp T. and Delbeke J., The conductivity of the human skull in vivo and in vitro, In: Trans IEEE-EMBS Conf'99, Piscataway, 1999. IEEE Computer Society Press, in press.

[63] Hämäläinen M.S. and Sarvas J., Realistic Conductivity Geometry Model of the Human Head for the Interpretation of Neuromagnetic Data, IEEE Trans. Biomed. Eng., 1989, BME-36:165–171.

[64] Steward G.W., Introduction to Matrix Computations, New York, Academic Press, 1973.

[65] Golub G.H. and Van Loan C.F., Matrix Computations, Baltimore, The John Hopkins Univ Press, 1996, 3rd edition.

[66] Lawson C.L. and Hanson R.J., Solving Least Squares Problems, Englewood Cliffs, N.J., Prentice-Hall, 1974.

[67] Golub G.H. and Reinsch C., Singular value decomposition and least squares solutions, Numer. Math., 1970, 14:403–420.

[68] Forsythe G.E., Malcolm M.A., and Moler C.B., Computer methods for mathematical computations, Englewood Cliffs, N.J., Prentice-Hall, 1977.

[69] Marquardt D.W., An algorithm for least-squares estimation of non-linear parameters, J. Soc. Indust. Appl. Math., 1963, 2:431–441.

[70] Beck J.V. and Arnold K.J., Parameter Estimation in Engineering and Science, New York, Wiley, 1977.

[71] Oostendorp T.F. and van Oosterom A., Source parameter estimation in inhomogeneous volume conductors of arbitrary shape, IEEE Trans. Biomed. Eng., 1989, BME-36:382–391.

[72] van Oosterom A., Electrocardiography, In: Strackee J. and Westerhof N., The Biophysics of Heart and Circulation. Inst of Physics Publ, Bristol, 1993.

[73] Zhou H. and van Oosterom A., The Handling of Point Singularities in the Finite Element Computation, Proc IEEE-EMBS'91 conf, 1991, 13/2:519–520.

[74] Gill P.E., Murray W., and Wright M.H., Practical Optimization, New York, Academic Press, 1981.

[75] Nenonen J., Katila T., Leiniö M., Montonen J., Mäkijärvi M., and Siltanen P., Magnetocardiographic functional localization using current multipole models, IEEE Trans. Biomed. Eng., 1991, BME-38:648–657.

[76] Cuffin B.N., A Method for Localizing EEG Sources in Realistic Head Models, IEEE Trans. Biomed. Eng., 1995, BME-42/1:68–71.

[77] Cuffin B.N., EEG Localization Accuracy Improvements Using Realistically Shaped Head Models, IEEE Trans. Biomed. Eng., 1996, BME-43/3:299–303.

[78] de Munck J.C., The estimation of time varying dipoles on the basis of evoked potentials, Electroencephalogr and Clin Neurophysiol, 1990, 77:146–160.

[79] Cadzow J., Signal Processing via Least Squares Error Modeling, IEEE ASSP Magazine, 1990, –:12–31.

[80] Golub G.H. and Pereyra V., The differentiation of pseudo-inverses and nonlinear least squares problems whose variables separate, SIAM J Numer Analysis, 1973, 10:413–432.

[81] Press W.H., Flannery B., Teukolski S.A., and Vetterling W., Numerical Recipes in C, The Art of Scientifiv Computing, Cambridge, Cambridge University Press, 1988.

[82] Oostendorp T.F. and van Oosterom A., Decoupling linear and non-linear parameters in biolectric source estimation, In: Szeto A. and Rangayyan R., Engineering solutions to current health problems. IEEE publishing services, New York, 1993.

[83] van Oosterom A. and Huiskamp G.J.M., Implicit and Explicit Constraints in Inverse Electrocardiography, J. Electrocardiol, 1992, 25 Sup:87–92.

[84] van Oosterom A. and Huiskamp G., Spatio-Temporal Constraints in Inverse Electrocardiography, In: Ghista D., Biomedical and Life Physics, pages 203–314, Wiesbaden, 1996. Vieweg.

[85] Wang J., Minimum-norm least squares estimation: Magnetic source images for a spherical model head, IEEE Trans. Biomed. Eng., 1993, BME-40:387–396.

[86] Wang J., Kaufman L., and Williamson S., Imaging regional changes in the spontaneous activity of the brain: An extension of the minimum-norm least-squares estimate, Electroencephalogr and Clin Neurophysiol, 1993, 86:36–50.

[87] Hämäläinen M.S. and Ilmoniemi R.J., Interpreting magnetic fields in the brain: Minimium norm estimates, Med. Biol. Eng. Comp., 1994, 32:35–42.

[88] Pascual-Marqui R. and Michel C., Low resolution electromagnetic tomography: A new method for localizing electrical activity in the brain, Int. J. Psychphysiol, 1994, 18:49–65.

[89] Oster H.S. and Rudy Y., The use of temporal information in the regularization of the inverse problem of electrocardiography, IEEE Trans. Biomed. Eng., 1992, 39:65–75.

[90] Brooks D.H., Maratos G.M., Ahmad G., and MacLeod R.S., The augmented inverse problem of electrocardiography: Combined time and space regularization, In: Szeto A.Y.J. and Ranggayyan R.M., Engineering solutions to current health care problems. Proceedings of the Annual International Conference of the IEEE Engineering in Medicine and Biology Society, pages 773–774, Piscataway, 1993. IEEE publishing services.

[91] Mosher J., Lewis P., and Leahy R., Multiple Dipole Modeling and Localization from Spatio-Temporal MEG Data, IEEE Trans Biomed Eng, 1992, BME-39:541–557.

[92] Varah J.M., A practical examination of some numerical methods for linear discrete ill-posed problems, SIAM Review, 1979, 21:100–111.

[93] Hansen P.C., Numerical tools for the analysis and solution of Fredholm integral equations of the first kind, Inverse Problems, 1992, 8:849–872.

[94] Pratt W.K., Digital Image Processing, New York, John Wiley & Sons, 1991.

Introduction to Designing *f*MRI-Based Experiments

Robert L. Savoy

fMRI Education, MGH-NMR Center, Charlestown, MA 02129

Contents

Designing experiments in functional neuroimaging is a special challenge. This challenge has been addressed for the last 15 years by the cognitive neuroscientists using positron emission tomography (PET) as their investigative tool. Functional MRI requires the use of many of the same lessons for experimental design that were learned by the PET community. However, *f*MRI also presents a unique set of challenges and strengths. The first part of this essay will discuss some of the general design issues that are shared by PET and fMRI. The remainder of the essay will discuss the issues specific to *f*MRI.

Outline

Introduction
Tight and Loose Task Comparisons
Behavioral Measures
Spatial and Temporal Resolution Limits
Slice Selection and Susceptibility Artifact
MR Scanner Limits
Motion
Closing

Introduction

Designing experiments for *f*MRI-based studies presents unique opportunities and challenges. First, there are the subtleties associated with any experiment in cognitive, perceptual, and sensory/motor psychology. The present essay does not address those issues at all. Rather, it highlights some of the tradeoffs that are specific to volumetric functional neuroimaging in general, and magnetic resonance imaging in particular. The art of experimental design is driven by the continual interplay between details of brain anatomy and physiology, MR imaging technology, and the stimulus/response demands required by a specific neuroscience question. This essay touches on a few of these issues. More systematic treatments are mentioned in the closing.

Tight and Loose Task Comparisons

It seems obvious that the right way to design an experiment in functional neuroimaging is to create two tasks that are identical except for one small difference. This is the basis of the classic "subtraction" method originally delineated by Donders and widely used in cognitive research (see, e.g. [1] for a general discussion). Such experimental designs are sometimes called "tight" task comparisons. This is the way that most experiments are designed. Furthermore, the difference between experimental conditions should be *either* in the stimulus (while keeping the response task of the subject fixed), *or* in the response task (while keeping the stimulus fixed); they should not both be changed at once.

However, there are practical and theoretical reasons for including experimental conditions that are more broadly different from the main conditions of interest. Frequently this is in the form of a "low-level control task"[2] such as simple visual fixation or rest. This has sometimes been called a "loose" task comparison.*

Consider a situation in which one is interested in the difference between two tightly coupled tasks "A" and "B". Assume also that there is a loosely coupled, low-level control task "C". In the context of a simple block design (i.e., data is collected for a block of time such as 60 seconds for each condition), there are many ways in which this experiment can be conducted. Figure 1 presents 4 variations on the theme of the simple AB design indicated in part (i) of the figure. (NOTE: In all parts of Figure 1, the vertical axis has no particular meaning, except to indicate that different heights represent different experimental conditions.

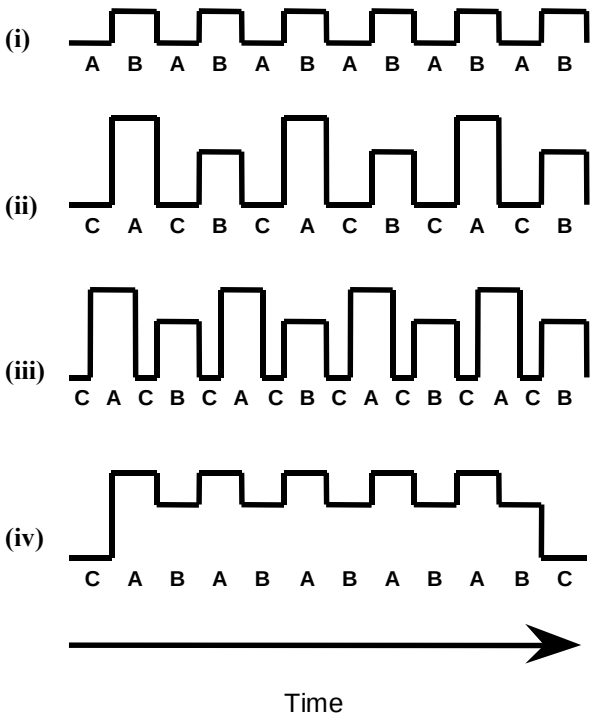

Figure 1.

* I have taken the "tight" versus "loose" task comparison terminology from lectures given by Dr. Randy Buckner.

Data from an experiment of type (i) permits comparison of the relative activation due to the differences between condition "A" and "B". However, from this data alone it is not possible to know whether any difference is due to an increase caused by "A" or a decrease caused by "B". Furthermore, the only differences that will appear in functional neuroimaging data are those that represent the tight task comparison. In many situations, it is useful to have some idea of the broader range of brain activity (i.e., the putative network) that underlies the task. (See, e.g., Figure 4 of [2].) In addition, while the AB comparison may be very subtle or weak, an AC or BC comparison to the low-level task can be designed to be robust. This has the practical advantage that, if *no* difference is detected between A and B, at least you can know that your subject and your equipment are functioning properly because of the clear AC and BC comparisons. How might these additional comparisons be organized, and what are the tradeoffs involved?

Part (ii) of Figure 1 indicates one approach (dubbed the "Castle Paradigm" by O'Craven [3] because it resembles the outline of a castle wall) that is often helpful, especially during initial pilot studies. In this paradigm the conditions of interest (A and B) are separated by the low-level comparison task (C). This obviously increases the number of conditions to 3, thereby permitting comparisons that can reveal whether differences between A and B are the result of increases for one of these conditions, rather than decreases for the other (at least as compared to C as the baseline.) In terms of exploratory data analysis in *f*MRI, this paradigm also makes it easy to see changes in the timecourse of activation, as there should be many large fluctuations in various areas between the low-level control task "C" and the tightly coupled higher-level tasks "A" and "B".

What are the penalties of using this task design? * The primary penalty is one of time. In (i), all the imaging time is being used to collect data on the conditions of ultimate interest (A and B). In (ii) fully half of the imaging time is being used to collect the low-level task data, which may be of marginal interest. Two ways to improve the situation are shown in parts (iii) and (iv) of Figure 1. In (iii), the same basic temporal layout as (ii) is used, but the time allotted in each epoch for the C task is halved. Thus, more imaging time is devoted to A and B, but otherwise, all the advantages (e.g., in terms of the timecourse data and multiple comparisons) are retained. In (iv), the C condition is used only at the beginning and end of the experiment. Of the three "Castle" paradigms shown (ii-iv), this last one is the most efficient in terms of the amount of A and B data collected.

When conducting pilot studies, some variation of the castle paradigm almost always makes sense. Once the basics of the experimental situation and data are better understood, the simple AB design (i), or the most efficient castle paradigm (iv) may be more routinely used to increase the amount of relevant data collected.

Some of the preceding discussion applies to PET and *f*MRI data equally. In PET studies each epoch shown would correspond to a single injection and would represent about 60 seconds of data collection. Decreasing collection time (as in part (iii), for example) would not make sense in a PET study, but the necessity for more than 2 conditions, and the time tradeoffs indicated in (i), (ii), and (iv) are similar in PET and *f*MRI.

With rare exception, the block design entails the presentation of many repetitions of the same or similar stimuli during the period of time represented by a single epoch. In PET, this is a necessary situation. In *f*MRI it is possible to detect the hemodynamic changes due to single events such as the presentation of a brief visual stimulus in a passive viewing task [4,5,6] or a single word in a word generation task [7]. This permits the design of experiments in which each "block" is only a single "event", rather than the repetition of similar events. Some of the issues and published work relevant to the design of such studies are presented in [6] and in the lecture notes on *f*MRI Data Analysis, prepared by Randy Buckner for this workshop.

Behavioral Measures

It might seem obvious that obtaining observable behavioral responses could only be a good thing in functional neuroimaging research. For example, Cohen and Bookheimer suggest that:

"Ideally, a concurrent, observable and measurable behavioral response, such as a yes or no bar-press response, measuring accuracy or reaction time, should verify task performance."[8]

Certainly most investigators try to have an observable behavioral measure for their tasks, when possible. (In "imagination" studies, such as imagining visual images or imagining performance of a motor task, it is more difficult to have an observable *behavioral* response measure, though certain studies of mental rotation have associated reaction time and accuracy measures.) At least one psychologist (Steve Pinker) has argued against the necessity of behavioral response measures:

"I wonder whether PET [or fMRI] research so far has taken the methods of experimental psychology too seriously. In standard psychology we need to have the subject do some task with an externalizable yes-or-no answer so that we have some reaction times and error rates to analyze -- those are our only data. But with neuroimaging you're looking at the brain directly so you literally don't need the button-press or the overt blurting. I wonder whether we can be more clever in figuring out how to get subjects to think certain kinds

* Sometimes, of course, the particular experiment may not permit the intervening low level task—that is, the logic of the tasks might require that conditions A and B follow each other without interruption. This, however, is relatively rare.

of thoughts silently, without forcing them to do some arbitrary classification task as well. I suspect that when you have people do some artificial task and look at their brains, the strongest activity you'll see is in the parts of the brain that are responsible for doing the artificial tasks."[9]

Another position voiced by an anonymous *f*MRI researcher is:

"I make my subjects do something when they're in the scanner so they don't fall asleep."

Each of these passages is correct! There is no absolute requirement nor prohibition for behavioral responses. Nonetheless, it is much more likely that reviewers will be concerned if there is no observable behavioral measure to accompany the neuroimaging data. While Pinker's comment is logically true, in most experiments it is sensible to have a reason to believe that the subject is doing what you are asking them to do, and an behavioral response can be evidence. On the other hand, in an experiment where "imagined finger movements" are being studied, this may not be possible.
One additional consideration in experimental design is the use of a behavioral task that can be parametrically varied. It is essential that the field progress beyond the statements of the form "cortical area X is more active than cortical area Y during task A". More powerful imagers, novel approaches to data analysis, and more explicit brain models will all contribute to that effort; but experimental design may have the most to contribute. Examples of a designs that uses such parametric variation in stimulus or task attributes can be found (e.g., [10,11]).

Spatial and Temporal Resolution

Like positron emission tomography (PET), functional MRI measures something having to do with blood flow or blood oxygenation; it does not measure neural activity directly. The ultimate limits of the spatial and temporal resolution of *f*MRI will be determined by this fact of biology, rather than by the limitations of the scanner per se. It is important to have a clear idea of what the present limits, and ultimate limits, of spatial and temporal resolution are for *f*MRI when designing experiments. For example, if you know that your scanner's spatial resolution is about 45 cubic mm for a particular *f*MRI pulse sequence, it is probably a bad idea to try to detect a structure that is 25 cubic mm in size. Not only may there be little signal, but if the structure happens to land across a voxel boundary, there will be even less relevant signal in each voxel. (These effects are sometimes called "partial voluming" because the relevant hemodynamic signal fills only part of a voxel and/or is splits across more than one voxel.)
Significant improvements in the spatial and temporal resolution are being made, though not always by techniques that are likely to be available to everyone. In particular, higher field MR (3 and 4 Tesla now, and 7 and 8 Tesla in the near future) will improve spatial resolution and yield the added signal that helps the "single-event" *f*MRI designs [6] and possible use of the "initial dip" in oxygenation [12] to improve temporal resolution. However, these high field machines will not be as widely available as 1.5 Tesla machines for the foreseeable future.
For a detailed discussion of pulse sequences and related issues, especially as they affect spatial and temporal resolution, see [13].

Spatial Resolution
The meaning of spatial resolution is fairly clear: What is the smallest activated area that can be reliably detected?
There are other plausible definitions of spatial resolution. For example, what is the smallest ***hole*** in a field of otherwise active cortical surface that can be detected. (This question has been recently investigated with surprising results...the size of the hole needed was much larger than anticipated!) This question has some important theoretical implications, but it is not routinely relevant in experimental design.

Current Spatial Resolution Limits
Functional MRI is routinely conducted at 1.5 Tesla using voxels whose dimensions are 3 mm x 3 mm x 7 mm. Studies using isotropic voxels of 3x3x3 have also been reported. This resolution is also available at higher fields strength. There have been a few studies (at high field strength) that report successful fMRI-based activity at 1mm x 1mm x 3 mm resolution. However, the vast majority of studies at 1.5 Tesla use voxels of 3x3x5 mm or larger.

Ultimate Spatial Resolution Limits
Although there are some safety issues as field strength increases, there is no known reason why MRI cannot be done with living humans at much higher field strength than the conventional 1.5 Tesla. There are 3 and 4 Tesla machines in operation now, and an 8 Tesla machine is in operation at Ohio State University. These machines will be able to image smaller voxels. Even without the higher field strengths it would be possible to increase spatial resolution by using longer imaging times. However, the ultimate spatial resolution limits will not be determined by the MR camera. Rather, they will be determined by physiological limits (in terms of imaging time) and by the hemodynamic limits, i.e., by the spatial resolution of the smallest vessels that show local changes with neural activity. Based on the available evidence, this limit should be approximately the size of a cortical column—somewhere between 1 mm and 0.1 mm in linear dimension.

Temporal Resolution
While there is little controversy or confusion about the meaning of spatial resolution, the plausible definitions of "temporal resolution" are more seriously varied. For

instance, the temporal analogy to spatial resolution (defined as the smallest point that can be detected) is to ask how brief a stimulus can be in time and still elicit an fMRI-based response. The answer almost certainly: with high brightness and contrast, the stimulus could be arbitrarily brief. The closest actual experiment used a high contrast visual pattern flashed on for a mere 34 millisecond duration, and a clear MR response was detectable[4]. If the flash had only been 1 micro second, but it had been comparably bright (in terms of integrated energy), there is little doubt that a similar MR response would have been seen, because the retinal processing is closely approximated by a simple integrator on such time scales. These brief stimuli elicited a response that took the usual 2 or more seconds to develop and faded away after about 5 seconds. So, is the temporal resolution 1 microsecond?

Suppose we ask a related question. How quickly can an "ON" and "OFF" type of stimulus manipulation be alternated and still elicit a detectable MR signal modulation. The answer is something like 2-3 seconds. As the duration of each "ON" and "OFF" epoch decreases below about 6 seconds, the magnitude of the MR signal contrast between the epochs starts to drop sharply. So, this temporal resolution might be said to be 6 seconds.

Finally, suppose we ask how precisely can we specify the ***onset*** of a detectable MR signal change. This is an important definition of temporal resolution because it tells us how large a temporal gap we might be able to see in the response of different parts of the brain to a particular experimental challenge. That is, it addresses the question of whether, using *f*MRI alone, we can detect a time delay between the response in two different portions of the brain.

This turns out to be a complicated question. At any one location, using stimuli that come on at different times, we can easily detect differences of 500 milliseconds, and could probably reach 100 milliseconds without too much difficulty [5]. However, in order to reach such numbers across different brain areas, we really need a task that excites those areas but is not used in the particular experiment. That would give us a baseline response time against which to compare the critical task activations [6, 14].

Current Temporal Resolution Limits

In the context of experimental design, a good rule is that stimulus presentation should be no briefer than 1 second. For a "single trial" design the longest duration should be no more than about 3 seconds. For standard "block" design experiments, the duration should be at least 6 seconds, and a more usual minimum is 20 seconds.

Ultimate Temporal Resolution Limits

In the best situations, it may be possible to detect onset differences in different parts of the brain with a resolution of 100 milliseconds, but this has not yet been achieved.

The biggest gains in true temporal resolution may come about by combining the fast technologies (like MEG and EEG) with the three dimensional imaging technologies, like fMRI.

Slice Selection in general, and Susceptibility Artifact in particular

In PET the data is collected in an orientation and with volumetric coverage and spatial resolution that are all essentially fixed; and the data varies little in quality as a function of the subject's head orientation relative to the imager. The situation is very different in MR imaging. All of the imaging parameters (spatial resolution, orientation of slices imaged, etc.) can be varied by the machine operator after the subject is in place, and these parameters can have a very significant effect on the quality of the data.

One of the most salient parameters is the orientation of the imaging slices. This is due to the fact that materials (such as air) with different magnetic susceptibility than the tissue we are trying to see can cause significant signal loss, and the amount of loss can be influenced by the slice orientation. In many instances the "in-plane resolution", that is the dimensions of the voxels within a given imaging slice, is smaller than the "through-plane resolution", that is the thickness of the slice. (For example, many *f*MRI studies at 1.5 Tesla use 3x3 mm resolution in-plane and as much as 8 mm slice thickness.) The orientation of the slices relative to air pockets near the brain (e.g., the sagittal sinus and sphenoid sinus) can cause significant loss of signal, especially in the frontal and temporal lobes. In most cases, coronal slices show less loss than axial slices in this portion of the brain. Decreasing slice thickness results in less signal loss due to susceptibility artifact, but also yields less signal everywhere, because smaller voxels have fewer hydrogen nuclei to generate the signal.

Susceptibility artifact is always bad, and slice orientation is often chosen to minimize it. However, there are times when susceptibility artifact is not an issue, and the ability to vary imaging orientation can be an advantage. One example was in an early study by Tootell, et al. [15] in which the occipital lobe was imaged using orientations parallel or perpendicular to the calcarine fissure. The first studies used the parallel orientation, which had the effect of getting large sections of specific visual areas (e.g., V1) in a single slice. In later studies, when the boundaries across visual areas were the most critical piece of information, the orthogonal imaging orientation yielded many boundaries in a single slice.

MR Scanner Limits

There are a number of ways in which the physical or computational limits of your particular imaging system will influence experimental design. Recall that in whole-brain fMRI data is being collected at a very rapid rate. This data has to be stored somewhere dur-

ing a given experimental run. While there is no technological reason that all this data could not be shipped off to a disk or other processor, the actual means for doing so may not exist on your machine. The result is that there will be a practical limit to the number of images that can be stored on any given run.
This kind of "memory" limitation will change as more scanners are equipped with more memory, but it is a genuine problem for most people at this time. MR scanners were not designed with the kind of massive data collection in mind that *f*MRI studies typically can use.
A second kind of scanner limit is the rate at which images can be collected. On the echo planar imaging system with which I am familiar, the maximum rate of image collection was 20 per second. However, long before image memory would be used up, the gradient coils would overheat from such intense use. So images could be collected very quickly for only a brief period of time—much less than a minute. (This capability had uses in cardiac imaging, but not in neural activation studies). At a rate of 10 images per second, data could be collected for something over a minute, but then the subject had to be idle in the scanner while everyone waited for the system to cool down. More typically 7 images per second are collected on this particular system and at that scanning rate can continue until memory is used up.
Other kinds of scanner limitations can be the slice orientation permitted for imaging. Some systems cause peripheral nerve stimulation if echo planar imaging is conducted with sagittal slices. This limitation is not universal, but most scanners have some such limits and they impinge upon the design of fMRI studies.

Motion

There are three different types of motion that can cause problems with *f*MRI data, and which limit some kinds of experimental design. The first (and most obvious) is any task that causes the head to move. A task design that causes laughter or sudden tension is very likely to also cause head movement.
The second kind of movement that is problematic is overt speech. Asking someone to talk may not cause movement of the head (other than the jaw and tongue, of course), but it does change the size of the air volume in the mouth. This can cause susceptibility artifacts, especially in the portions of the brain near the mouth cavity.
Finally, there are potential problems caused by gross movements even when the skull is still and the air in the head is unchanged. It is possible for some movements (for example twisting of the arm at the shoulder) to change the coupling of the body to the head coil. Since such changes are very likely to be correlated in time with the task manipulation, the resulting artifacts can severely affect the *f*MRI data.
All three of these motions are generally to be avoided in experimental design. Of the three, overt speech is the one that is most often desired, and it is an empirical question (for a particular area of brain, for a particular task, for a particular scanner) as to whether the distortions caused by overt speech will be bad enough to prevent the collection of useful *f*MRI data. (In other words, some laboratories have said they can do such experiments successfully, and some have said the opposite. Try it yourself and find out.)
Subject movement is generally regarded as *the* biggest problem for getting consistent data in *f*MRI-based experiments. Experienced, well-motivated subjects who use bite bars in the scanner can routinely be expected to yield data free of serious motion artifact. In contrast, in studies with patients or other difficult subjects, it is wise to expect that 20-30% of your experiments may need to be discarded because of subject motion, especially initially. There are methods for helping to minimize physical motion during data acquisition and to detect and possibly compensate for it after data acquistion, but none of these is, as yet, fully satisfactory.

Closing

Experimental design will always be one of the most challenging aspects of functional neuroimaging. Summaries of classic work (e.g.,[1]), and summaries of the latest advances (e.g.,[6]) are the best place to start.

Acknowledgments

Since October of 1994 a number of people have helped teach the "Experimental Design" and related portions of the MGH Visiting Fellowship in Functional MRI. Discussion with each has contributed significantly to the ideas presented in this essay. These people include Randy Buckner, Nancy Kanwisher, Kathleen O'Craven, and Chantal Stern. More general discussions of experimental design are part of the evening workshops, in which participants design their own experiments. In addition to the people mentioned above, others have regularly contributed to that hands-on experience in experimental design, including Peter Bandettini, Ken Kwong, Aina Puce, and Tom Zeffiro. Finally, I want to acknowledge the participants from those workshops, who keep us thinking about how to push the limits of design.

[1] Posner, M.I. & Raichle, M.E. *Images of Mind* (Scientific American Library, New York, 1994).

[2] Buckner, R.L. *Psychonomic Bulletin & Review* **3**, 149-158 (1996).

[3] O'Craven, K.M., Rosen, B.R., Kwong, K.K., Treisman, A. & Savoy, R.L. *Neuron* **18**, (1997).

[4] Savoy, R.L., *et al. Exploring the temporal resolution boundaries of fMRI: Measuring Responses to very brief visual stimuli* (Miami Beach, FL, 1994).

[5] Savoy, R.L., *et al*. *Proceedings of the International Society of Magnetic Resonsance in Medicine, Third Scientific Meeting* **2**, 450 (1995).
[6] Rosen, B.R., Buckner, R.L. & Dale, A.M. *Proceedings of the National Academy of Sciences* **95**, 773-780 (1998).

[7] Buckner, R.L., *et al*. *Proceedings of the National Academy of Science* **93**, 14878-14883 (1996).

8] Cohen, J.D. & al., e. *Behavior Research Methods, Instruments & Computers* **25**, 101-113 (1993).

[9] Pinker, S. *Journal of Cognitive Neuroscience* **Winter**, (1994).

[10] Beauchamp, M.S., Cox, R.W. & DeYoe, E.A. *Journal of Neurophysiology* **77**, 516-520 (1997).

[11] Boynton, G.M., Engel, S.A., Glover, G.H. & Heeger, D.J. *Journal of Neuroscience* **16**, 4207-4221 (1996).

[12] Menon, R.S., Ogawa, S. & Ugurbil, K. *International Journal of Imaging Systems and Technology* **6**, 209-215 (1995).

[13] Bandettini, P.A. & Wong, E.C. *Neurosurgery Clinics of North America* **8**, 345-371 (1997).

[14] Lee, A.T., Glover, G.H. & Meyer, C.H. *Magnetic Resonance in Medicine* **33**, 745-754 (1995).

[15] Tootell, R.B.H., *et al*. *Journal of Neuroscience* **15**, 3215-3230 (1995).

Introduction to Analyzing Data from *f*MRI-Based Experiments

Robert Savoy

fMRI Education, MGH-NMR Center, Room 2301, Building 149, 13-th Street, Charlestown, MA 02129
Senior Scientist, The Rowland Institute for Science, 100 Edwin H. Land Boulevard, Cambridge, MA 02142-1297

Outline

Introduction
Fundamental Question
Statistical Tests
Some Important Details
Motion
Comparing Brains
Combining Data Across Runs, Sessions, and Subjects
Software Tools
Closing Comments

Introduction

Data analysis is a critical and controversial part of the enterprise of *f*MRI-based experimentation. There is wide agreement upon the nature of the important issues. There is general agreement on how to handle some of these issues (e.g., motion detection and motion correction algorithms) but there are no universally agreed upon approaches to many of the other issues (e.g., the appropriate statistical tests, the best way to compare data across different subjects, and the best way to visualize and report the results of data analysis). Consequently, there are a host of software tools (many available for free and some that can be purchased from companies), each having its strengths and weaknesses. Because of the rapid development in all aspects of *f*MRI-based research, no standard approach to data analysis that will suit the medical community has been developed yet, but several groups are working toward that goal.

Fundamental Question

The first goal of any analysis of *f*MRI-based data is to determine if the experimental manipulation has resulted in a measurable change in the MR signal, and to specify where in the brain, and when (in time) that change has occurred. The usual form in which this question is posed is very specific. Namely, the collection of images that have been collected during an experimental session are grouped together according to the experimental manipulation that was active during each image, and then the MR signal strength during in one group of images is compared, on a voxel-by-voxel basis, with the MR signal strength during another group of images. If the difference between these two groups of images is sufficiently great (as determined by some statistical test applied at a particular voxel) then we conclude that the experimental manipulation has caused a measurable effect (at that particular voxel).

As a specific example, consider the following "Demonstration Experiment". This experiment uses a simple motor task called "sequential finger opposition" (SFO) in which a subject touches his thumb to each finger on his hand in sequence. A visual cue is used to indicate when the SFO task should be performed and when the subject should rest. The SFO (or "ON") task will be performed for 25 seconds. Then the rest (or "OFF") task is performed for 25 seconds. One image per slice of brain is collected every 2.5 seconds. This results in 10 images per slice for each "ON" and each "OFF" epoch. This repeats 3 times each, for a total of 60 images per slice (i.e., a total of 60 volumetric brain images in a multi-slice experiment).

Given one experimental run of the above task, select a single voxel in the brain. This yields 60 numbers divided into two groups: 30 in the "ON" group and 30 in the "OFF" group. How do we compare these two groups of numbers? How do we make statistical statements about the meaning of any differences between these two groups of numbers? What happens when we apply whatever "comparison" criterion we choose to the entire volume of MR data?

Statistical Tests

A very brief summary of a few of the simplest statistical tests is given below. With the exception of Principle Component Analysis (PCA), each of these tests is applied at a voxel level, i.e., to a single volume element in the brain image data. When these statistics are computed for each voxel in the brain, and the resulting collection of statistics is presented in the form of an image in which color or intensity is used to represent the value of that statistic, the result is called a "statistical map" of brain activation.

Subtraction

In positron emission tomography (PET) studies of the neurally activated changes in blood flow, the initial comparison tool was simple subtraction. And historically, this was the first approach taken with *f*MRI data. That is, the data from one group were averaged together on a voxel-by-voxel basis, and the two averages were subtracted. This was done for each voxel in an image. (Today this would be done for each voxel in a volume, but in the original study only one slice of data

was being collected.) The resulting "difference image" showed clear areas that were brighter, indicating greater MR signal during the "ON" epochs than during the "OFF" epochs.
This sort of comparison is the only one that should be called "subtraction", although many writers and speakers use the term "subtraction" informally whenever they talk about contrasts between epochs, even if those contrasts are based on some other statistic. The proper term is "contrast" or "comparison" when one is describing more generic statistical computations on these grouped images.

Parametric Statistics
The most obvious and simple statistical test that can be used in this analysis is student's t-test. This test assumes that each number in each group is independent, and that the underlying distribution of numbers is Gaussian. In fact, unless TR is greater than 4 seconds, these numbers are not independent. Furthermore, there is data that indicates the distribution of numbers is not strictly Gaussian.
However, the differences from Gaussian are not great, and parametric statistics like the t-test are the most widely used measures of the difference between the groups of numbers.
On problem with applying such a test across a whole brain image is the number of such comparisons that are made. In a volumetric brain scan using typical fMRI resolution of about 3 mm x 3 mm x 7 mm resolution, there are more than 40,000 voxels in the brain. If the threshold for statistical significance is set at the 5% level (i.e., the usual level for most t-tests), one would expect to find 200 activated voxels *just by chance*. A correction of some sort must be applied to take into account these multiple comparisons.
The most stringent correction is the "Bonferroni" correction, in which case the required significance level would be 5% divided by the number of voxels. In this case, that leads to a significance threshold of approximately 10^{-6}. Many sensory and motor *f*MRI activations meet such a threshold, but it is harsher than necessary. In particular, there is some spatial non-independence in the data, as well as temporal non-independence. This means that the effective size of a "real" activation will be bigger than a single voxel, and therefore the total number of voxels for the Bonferroni correction will be much smaller than 40,000.
This concern about multiple comparisons applies to both parametric and non-parametric tests, and is handled in the same way.

Non-Parametric Statistics
Because the underlying distribution is probably not Gaussian, some laboratories use non-parametric statistical tests, such as the Kolmogorov-Smirnov (KS) statistic. Instead of basing the comparison just on the mean and standard deviation of the distribution of numbers in each comparison group (such as the t-test does), the KS statistic is based on the entire distribution of numbers in each group. A cumulative distribution is generated for each group (i.e., a graph that plots the fraction of values in each group that are above a specific value, versus those specific values). The maximum vertical distance between these distributions is the KS statistic.
There is nothing special about the KS statistic other than its being non-parametric and its depending upon data from the entire collection (not just mean and standard deviation). Its use by one or two prominent research groups, however, has led to its frequent mention in the literature.
There are many other parametric and non-parametric statistics that can be used in these analyses. However, they all have one thing in common. They depend upon prior knowledge of the experimental design so that the images can be grouped into putative "ON" and "OFF" conditions. This means that the only temporal functions that these tests can detect are those that are built in by the experimenter. Suppose that the response of the brain is not so simple? Suppose, for instance, that there is a brief burst of activity at the beginning of each epoch, but that the brain is dormant during the remaining portion of the epoch. Neither of the preceding tests could detect such a change, but other tests can.

Principal Component Analysis
Principal Component Analysis (PCA) is not really a statistical test. Rather, it is a re-representation of the data that condenses as much of the variability in that data as possible into a small number of "eigenimages", each of which is associated with an "eigenvector" that specifies a temporal fluctuation for the entire image. Thus, instead of one temporal variation for each voxel in a brain volume, there are a small number of volumetric images, each of which varies as a single relative image according to some time course.
The key virtue of PCA is that it has the power to pick out particular areas in the brain that exhibit a time course similar to that in the experimental design without the experimenter ever having specified that design to the analysis procedure. Similarly, it can detect temporal changes that are different from the ones built into the experiment. On the other hand, there is no obvious way to *know* which eigenimages and eigenvectors actually correspond to an important variation.
PCA and related techniques have great theoretical appeal, but they have been rarely used in practical *f*MRI data analysis.

Some Important Details

Temporal Offset Due to Hemodynamic Lag Time
In the description of the original "Demonstration Experiment", images collected during sequential finger opposition (SFO) were put in one group, and images collected while fingers were at rest were collected in another group. However, this grouping ignores the fact that the changes in blood flow and blood oxygenation that fMRI can detect do not occur at the instant that the SFO starts or stops. There is a significant lag time between the start of motor activity and the change in

blood flow. In the case of SFO, the lag time from the initiation of finger movement until any MR signal change can be detected is about 2 seconds; and the lag time from initiation of movement until the MR signal change has reached its maximum is 4-8 seconds, depending upon the duration and strength of the finger movement.

In many data analysis packages there is a facility for allowing the experimenter to group the data in a manner that takes these time lags into account. Images collected during the time that the MR signal change is expected to be rising or falling can be ignored, and images collected during the time that the MR signal change is expected to be greatest can be grouped appropriately. These groupings typically do not match the original experimental design, especially in situations where TR (the time between images of a specific slice of brain) is short (i.e., less than about 6 seconds). In the case of the "Demonstration Experiment", the TR was 2.5 seconds, so one grouping would be shifted by one or two images and the images collected during the rising or falling periods (i.e., immediately after the onset or cessation of SFO) might be ignored.

In analysis packages that used correlational techniques, the rising and falling portions of the data yield valuable information, and would not be ignored. In the more usual analysis packages that just compute a statistic to measure the difference between an "ON" and an "OFF" epoch, the rising and falling periods tend to weaken the strength of the test and are therefore ignored.

More Than One Grouping

There are often more than two different experimental manipulations in a block design. The usual way in which this complication is handled is to compute many statistical maps, each of which is based on a comparison of two groups. Consider an experiment in which there are three types of epochs, labeled "A", "B", and "C". The two groups to be used in one statistical comparison can be defined in such a way that some of the images are ignored (e.g., comparing just the images associated with the "B" versus "C" epochs while ignoring the images associated with the "A" epoch). Alternatively, the groups can be constructed so that all the images are used by combining across different types of epochs (e.g., all the images associated with epochs "B" and "C" are combined into a single group and these are compared with the images associated with epoch "A").

There are more elaborate ways to model the data that take multiple groupings into account. Most of these are based on some kind of linear regression model, with basis functions that represent various combinations of the different experimental manipulations.

Single Trial Analysis

Demonstrations of the ability of *f*MRI to detect the effects of single, brief stimuli (sensory, motor, or cognitive) has led to much excitement about experimental designs in which single trials are each treated as independent epochs. Because these stimuli are so brief (typically 1 or 2 seconds in duration), the data analysis procedures ***must*** take hemodynamic lags into account. Furthermore, the techniques for grouping and comparing the data become more complicated. At present, only the institutions using these experimental designs have developed software tools for routine analysis of such data. However, the *f*MRI community understands that there will be more experiments designed along these lines and the various software developers are rapidly moving to incorporate the appropriate new analysis tools that these designs demand.

In general, the time between development of a new experimental design and the availability of software for analyzing the data generated by such designs is getting shorter. There appears to be strong motivation to keep up with the latest developments by the software developers. Given the basic package, it is often easy for the developer to add new features relatively rapidly.

Motion

The problem of subject motion is a pervasive one in *f*MRI. It is relevant in the context of experimental design. It places practical limitations on the behavior of subjects in the magnet and on the selection of some subject populations. There are many reasons for this, most of which are explicable in the context of the underlying physics of nuclear magnetic resonance (NMR) and magnetic resonance imaging (MRI). In the present context, however, we will only be concerned with the analysis of data that includes images of a brain that may have moved.

Recall that we are typically using high speed imaging techniques to minimize the effects of movement in any one image. The problem is that, in the context of *f*MRI, we are collecting many images in each run, and many runs in a 2-hour session. These runs are typically 2-8 minutes long, and can be much longer. With a TR of 3 seconds, this represents 40-160 images per slice. Because the fMRI-based signal modulation is intrinsically small (typically 0.5-5%), data from all the images collected in these long runs are needed to gain statistical power. Thus, it is important that the images within a run are aligned.

For similar reasons, it is often important to average data across runs in a given experimental session. So, for instance, it is not unusual to have 8 runs, each 5 minutes long (with a brief rest in between runs), that are all collected in a single imaging session, while repeating the same stimulus. Again, statistical power is gained by averaging the data collected across these 8 runs (or concatenating them into one long "virtual" run), and this requires alignment between all the images of the various runs. Head motion makes this process a challenge.

And finally, even if the skull were perfectly immobile, the brain still moves. The pulsatile flow of arterial blood causes movement virtually everywhere in the brain, and particularly so in subcortical structures.

For all of these reasons, the data analytic approach to motion detection and motion correction has been based on the brain images themselves, rather than on moni-

toring head movement externally. Efforts are made to *minimize* subject head movement, and it is not presently possible to correct for severe or rapid (relative to TR) movement. However, if the movement is not too great in amplitude and not too rapid, there are algorithms available in most *f*MRI data analysis packages that are adequate to detect the motion and to transform the data in an attempt to compensate for the effects of that motion.

Virtually all these algorithms are based on the basic idea of Roger Wood who developed a software program called "AIR" (for Automatic Image Registration). The key idea is to use the entire volumetric image data and look at the variance across voxels while comparing one standard volume (typically the first functional image collected) with each subsequent volume. The subsequent volume is then rigidly rotated in an attempt to find the orientation of minimum variance from the first image. This procedure yields a measure of motion of the brain. Other algorithms (which have subtle complications) can be used to transform the data based on this movement information. A key point, however, is that this procedure automatically reveals many kinds of movement. By comparing plots of movement with the experimental time course built into a specific experiment one can immediately detect the worst kind of movement: stimulus-correlated movement. That is, if the subject moves every time they are supposed to start a task, the MR signal artifacts thus generated will appear to be an "activation" signal. There is no good way to correct for such data and it must be detected and discarded. If one does not ascertain the amount of movement in one's *f*MRI studies, journal reviewers would be likely to dismiss the data immediately.

There is one last point that might be confusing. Recall that we are doing functional neuroimaging experiments, and that, therefore, there will be differences in the brain images based upon that neural activity. How can the AIR programs work? Why don't these functional activity changes appear to be movement changes and cause the AIR algorithm to fail? The answer is that the *f*MRI-based signal changes are a small percentage of the raw MR signal which is driven by anatomical structures. The variations created by these anatomical structures (such as the border between brain matter and the skull, or the border of ventricles) are very large compared to the changes induced by the functional studies.

Comparing Brains

In the previous section we described the difficulties encountered in data analysis when an individual subject's brain moves, and we described the generally accepted software approach to dealing with this problem. While no approach was perfect, the fact that the underlying anatomy was fixed (because it was a single individual's brain) enabled the software tools to either handle the problem adequately, or to provide information that would enable us to decide whether the motion was too large to permit accurate data analysis.

The situation is much more complicated when we try to compare brains across different subjects. If the only problem were differences in size or orientation of the brains, then simple rigid transformations and simple linear scaling of the brains of different people would suffice to generate alignment between their brains. This is what transforming to Talairach Coordinates accomplishes. Other approaches to "Spatial Normalization" (i.e., the attempt to transform different brains to each other or to a standard brain) try to deal with the differences in individual sulcal and gyral anatomy.

Talairach Transformations

In the full Talairach transformation, a rigid rotation and translation to a standardized orientation is followed by a piecewise linear scaling of the anterior, middle, and posterior portions of each hemisphere, independently. The orientation is determined by a line and a plane. The plane is determined by the inter-hemispheric fissure (i.e., the space between the two hemispheres). The line is called the "AC-PC Line" and is determined by the two small fiber bundles called the "anterior commisure" and "posterior commisure" that cross the between the left and right hemispheres below the corpus callosum. The "anterior", "middle", and "posterior" portions of each hemisphere are defined in terms of the AC-PC line: the portion of each hemisphere in front of the anterior commisure is the "anterior", the portion of each hemisphere between the AC and PC points is the middle, and the portion behind the posterior commisure is the "posterior".

In some software packages an abbreviated form of the Talairach transformation is performed, in which the brain is scaled as a whole, without piecewise linear portions for each hemisphere. This has the advantage of being much faster and simpler to implement. Indeed, some packages compute this transformation automatically, by comparing the given brain to a standard "average" brain that was generated by transforming the anatomical MR images of 305 brains to Talairach coordinates and averaging. This process eliminates the tedious and often tricky steps of finding the AC-PC line and other landmarks for each individual brain. Despite the fact that the indivdiual anatomy is ignored and the transformation has fewer degrees of freedom than the full Talairach transformation, this automatic process yields data that is adequate for most purposes. The more serious problems with either the simplified Talairach transformation or the full Talairach transformation are caused by the fact that brains are not rigid transformations of one another. The simplified Talairach transformation, being strictly linear, cannot hope to account for these differences. Even the full Talairach transformation, which is only piecewise linear with a small number of pieces, is clearly inadequate for dealing with these individual differences in brain anatomy. More powerful non-linear approaches have therefore been developed.

Other Approaches to Spatial Normalization

There are a wide range of approaches to more general transformations of brains to facilitate data display and inter-subject comparison. One approach is to permit complicated non-linear warping procedures based on sulcal and gyral landmarks to guide computer generated distortions of one brain into another (or two a standard). Another approach, which is also based on non-linear transformations, is to try to match the outline of given brain slices (i.e., their perimeters) between two different brains. Perhaps the most widely used alternative to Talairach and these other non-linear transformations is to "inflate" the brain as a means of removing all sulci and gyri. This "inflation" is typically followed by cutting the inflated brain in a small number of places to permit "flattening".

The goal of inflating is to obtain a three-dimensional smooth, non-convoluted surface representation of cortex. The goal of flattening is to lay that surface representation on a flat plane. Given that a brain hemisphere (when inflated) looks something like an ellipsoid, it is necessary to cut the ellipsoid in one or more places to allow it to be flattened. Qualitatively, this is similar to the need to cut a globe to get a flattened representation of the world, or to cut a cylinder to get a flattened representation of the wrapper on a tube. Quantitatively, however, the analogy to the tube is closer. When a globe is cut flattened, it is necessary to create many cuts or else to have some very large distortions. When a cylinder is cut, the resulting surface can be flattened with virtually no distortions. In these terms, the inflated cortex is more like a cylinder than a sphere, and the distortions are not terribly large.

Flattened representations are visually and logically very appealing. Unlike Talairach coordinates, however, they are not three dimensional and only apply to the cortical surface. Subcortical structures cannot be represented. (Talairach originally invented his system for subcortical structures, although it does not include the cerebellum.)

Combining Data Across Runs, Sessions, and Subjects

In order to increase the signal to noise in *f*MRI data, a given experimental paradigm is typically run many times on a given subject. Sometimes this is done in a single experimental MR imaging session (typically lasting between 1 and 3 hours, with 1.5 -2 hours being the usual design duration). Occasionally the same task is repeated on the same subject across sessions for further statistical power. More commonly, multiple sessions for the same subject occur when many different functional studies are being conducted. Finally, it is often the case that the same experimental paradigm is conducted on many subjects. How do we take advantage of these multiple experimental runs to increase the power of our analysis?

Single Subject

Consider, first, the case of multiple runs of a given experiment on one subject in a single session. The motion detection and correction algorithms work well within a session (if the subject has remained relatively still). The machine typically does not have large fluctuations in its performance across a single 2 hour session. Hence, it is often possible to concatenate the data, as if they all came from one very long run. That is, if there are 70 images across a single run, and there is data for 6 runs, a new concatenated data set can be created with 420 images and the statistic computed for this longer "run". This approach yields the most statistical power in data analysis, especially for some of the non-parametric statistics such as the K-S. However, it is subject to major inaccuracies if the baseline MR signal drifts.

Recall that the MR signal change due to functional activation is very small—often only 1%. It is not uncommon in a two hour study to see baseline drift in the MR signal that is of comparable size: 1%. This drift may well be due to general physiological changes rather than instabilities in the MR scanner itself. But whatever the source of the change in baseline level, its presence makes concatenation of the data across multiple runs problematic. For instance, if the drift is a 1% increase in MR signal, and the faster experimentally induced MR signal change is also a 1% increase, then the "OFF" epoch of a later run may have the same raw MR signal value as the "ON" epoch of an earlier run. Obviously, concatenating such data into one long run would severely weaken the statistical power of a test.

There are two ways to deal with this. One is to normalize each run in some way. For example, the mean level of MR signal could be scaled to the same value. It is hard to justify such a transformation in theory, but it is sometimes used. Another approach, which is both simpler to implement and easy to justify, is to average the data across runs. That is, if there are 70 images across a single run, and there is data for 6 runs, average the data at each time point across the 6 runs, and then compute the statistic on the averaged data. This does not yield as much power as concatenation of the images, but it is easier to implement, easier to justify, and does give a significant improvement in power.

Single Subject in Multiple Sessions

In the context of *f*MRI, this is not very different from the problem of averaging within a session. The reason is that the motion detection / motion correction algorithms work very well with a specific brain. Thus, even though the subject will usually be in a different position within the scanner, and the head will be at a different angle with respect to the scanner, the data from a second imaging session can be transformed spatially to coincide with data collected during an earlier session.

Multiple Subjects

Combining functional neuroimaging data across subjects has its basis in earlier PET studies. In the early days of PET research, the imaging device did not have

enough power to detect functional activations in single subjects. This problem could not be remedied by increased number of runs because of the limitations imposed by radiation dosages to patients and volunteers. Therefore, data was collected on many subjects and this data had to be combined. The question was, how? Two significant developments came out of this dilemma. The first was the establishment of Talairach space as the standard coordinate system for representing the three dimensional neuroimaging data. The second was the need for spatial smoothing in order to get significant spatial overlap of the excitations from individual subjects. If the data were not spatially smoothed, activations in nearby, but not exactly identical areas in other subjects (as often happens because of subject variability and/or because of inadequacies of the Talairach system) would be averaged with unactivated areas from those other subjects. By incorporating a step of spatial smoothing, the activations from individual subjects added.
Modern PET scanners are more sensitive, and some of these procedures are not as critical as they once were. Nonetheless, the basic procedure of transforming individual subject data to Talairach space and then averaging (with or without a spatial smoothing step in between) is the standard way to average across subjects in both PET and *f*MRI research.

Alternatives to Averaging
Given the good spatial resolution of *f*MRI and the ability to detect activations in individual subjects, some researchers eschew averaging across subjects. Their position seems to be that the right way to compare across subjects is to look at ***each individual's functional map*** (preferably in a flattened brain format to facilitate inter-subject comparison). Elaborations on this approach can include warping within the flattened space, and could therefore eventually include averaging in that space.

Software Tools

There is a substantial collection of software packages for analyzing data from *f*MRI-based experiments. Some (like MEDx and iMIPS) are commercial. Some (like AFNI and Stimulate) are specific to *f*MRI and are free. This software is changing and improving rapidly. Most of these systems incorporate tools for transformation to Talairach space. None (as yet) include tools for flattening and warping in a routine way. Some depend upon purchasing licenses for other software.
In the context of the medical community, it will probably be another year or two before there is a package designed to be used by a non-expert. The attempt to make *f*MRI a standard clinical tool is still in its early stages.

Names
The list shown below is *not* complete. It is included primarily as a way to get started in searching for such software on the World Wide Web. A few e-mail addresses to specific people are included.

Specific to fMRI Data Analysis
AFNI (Specific to fMRI, From Robert Cox and the Medical College of Wisconsin rwcox@mcw.edu)
AVS (An imaging platform, used by iMIPS, for example, in the context of fMRI and PET)
FIASCO (From William Eddy at Carnegie Mellon University in Pennsylvania bill@stat.cmu.edu)
MEDx (From Tom Zeffiro and Sensor Systems in Virginia zeffiro@sensor.com)
SPM (From the Welcome Department of Cognitive Neurology in the United Kingdom)
Stimulate (From John Strupp and the University of Minnesota in Minneapolis)

Other
AIR (Automatic Image Registration)
ANALYZE (From the Mayo Clinic in Minnesota, not specific to fMRI)
BrainMap (Database of reviewed journal reports of brain activation)
IDL (Platform)
MATLAB (Platform)
MNI (Montreal Neurological Institute supplies some free software)

Closing Comments

In a laboratory setting, the amount of time spent analyzing data is a large fraction of all working time. It seems to constitute about half of everything that the experimenter does. In such a context it is critically important that the experimenter be fluent in the use of whatever software package they use.

Exploratory versus Confirmatory Data Analysis
The emphasis in this essay has been on what is usually called "Confirmatory" data analysis. That is, data analysis which is designed to test specific hypotheses. Often, the hypothesis may be something as simple as "There is activation in the primary motor cortex as a result of performing a sequential finger opposition task." The data analysis procedures outlined here are appropriate for addressing a collection of such hypotheses by applying statistical tests of some kind at every voxel in the imaged brain, usually after applying a motion detection / motion correction algorithm, and often based on multiple different groupings of the data. Such data analysis is often slow; some motion detection / motion correction software runs overnight.
In day-to-day work, however, there is another type of data analysis that is of practical importance. It often goes by the name of "Exploratory" data analysis. This refers to the ability of the investigator to look quickly and interactively at the results of a given fMRI experimental session. Some software packages offer a host of tools that allow one to assess the presence of motion artifact in a few seconds by showing a suitably scaled animation of the data. For instance, if the first image

in a functional run is subtracted from every other image, and the resulting data set is windowed (i.e., its gray level scaling is reset to account for the much smaller dynamic range in the subtracted data), then an animation of the resulting images (i.e., rapidly presenting the images in succession) can reveal the presence of motion.

Similarly, there are very fast ways to compute correlational analyses and to look interactively at the time course of MR signal across a given run for individual voxels or for selected averages across voxels. These exploratory procedures help to keep the investigator in good contact with the data and permit rapid detection of problems when something went wrong in an imaging session.

The Practical Importance of Statistical Tests?

In the context of clinical studies, where the subject pool is often limited, the power of a given statistical test can be critical, and hence the choice of the particular statistic is important. In the context of experiments with normal subjects, the choice of statistical test is probably irrelevant. If an effect can be demonstrated in a given experimental situation, it is usually very clear, and the strength of the effect is highly significant no matter which test is used. If the effect is so weak or marginal that the choice of statistical test makes a difference between significance or non-significance, then more data should be collected (via more runs or more subjects), or, even better, the experiment should be improved to generate a stronger effect.

Transcranial Magnetic Stimulation—New Modality In Brain Mapping

Ilmoniemi R.J.

BioMag Laboratory, Medical Engineering Centre, Helsinki University Central Hospital, Helsinki, Finland

Introduction

One of the newcomers in the field of brain mapping is transcranial magnetic stimulation (TMS) [1–3]. In TMS, the cortex is stimulated non-invasively by strong magnetic field pulses that induce a flow of current in the tissue leading to the excitation of neurons. TMS can be used in three quite different ways: 1) by studying the electrophysiological response either locally or as mediated by neuronal pathways from the stimulated spot (electrophysiology), 2) by disturbing ongoing neuronal signal processing in the brain in order to study cortical areas that are important for specific tasks (temporary lesions), or 3) by treating patients with targeted repetitive stimulation (therapy). Many variations and combinations of these paradigms exist.

In this tutorial, after a brief history of the field and some fundamentals of the technique, two points will be emphasized. First, frameless stereotaxy, computer-assisted operation, and the integration of TMS with MRI and other brain-imaging modalities will transform TMS into a true brain-mapping tool. Second, the integration of TMS with EEG, PET and other functional imaging methods will open an exciting new area of research as the reactivity and connectivity of the cortex can be studied noninvasively for the first time.

History of TMS

Magnetic stimulation is based on electromagnetic induction, which was discovered by Faraday in 1831. In 1896, d'Arsonval reported that when his head was placed in a changing magnetic field, he observed flickering lights, so-called phosphenes. Later it has been concluded that instead of having stimulated the visual cortex, d'Arsonval had stimulated the retina, which is more sensitive to induced fields than the brain.

The first successful TMS experiment was done in Sheffield, England in 1985, when Barker *et al.* [4] stimulated the motor cortex, observing muscle responses. The early use of the technique was limited mainly to studies of neural conduction from the brain to the periphery: *e.g.*, when the hand representation area of the motor cortex is stimulated, a twitch of the contralateral thumb may be observed provided that the neural pathway is intact. TMS thus became used as a noninvasive method for the study of neural conduction.

A new TMS paradigm was introduced by Amassian *et al*. [5]. They showed that a subject's performance in a character identification task was impaired when single magnetic pulses were administered between 60 and 140 ms after the onset of the visual stimulus; a temporary functional lesion had been created. This lesion paradigm has been subsequently used in a variety of experiments. A few further examples may suffice here. Pascual-Leone *et al*. [6] showed that by applying repetitive TMS (rTMS) to language areas in the dominant hemisphere, speech production can be arrested. Miller *et al*. [7] showed that the optimal latency for TMS suppression of visual detection depends on target luminance, thereby showing the power of magnetic stimulation in timing sequential processes in the brain. Seyal *et al*. [8] found that parietal-lobe stimulation elevates contralateral sensory thresholds for detecting tactile stimuli. Cohen *et al*. [9], on the other hand, disrupted Braille reading in blind subjects with visual-cortex stimulation, whereas in control subjects tactile processing remained intact during visual-cortex stimulation. Direct evidence was therefore obtained for the assertion [10–11] that the brain of the blind is modified so that the visual cortex performs some non-visual functions it would not do in the sighted.

The third application of TMS is therapy. George *et al.* [12] treated medication-resistant depressed patients by applying rTMS to the left dorsolateral prefrontal cortex, where neuronal activity appears to be lowered in depression. After daily sessions of treatment for at least 5 days, two out of 6 subjects showed robust mood improvement. Several other authors (see, *e.g.*, [13]) have subsequently reported positive results on depressed patients as well as on other patient groups, but it is still too early to draw final conclusions on the efficacy of TMS therapy [14]. In any case, there is hope that rTMS may replace the inconvenient electroconvulsive therapy (ECT) at least in some cases of drug-resistant depression.

Ziemann *et al*. [15] studied effects of epileptic drugs on motor cortex excitability using TMS, opening the way to a promising new paradigm. With pharmaceutical studies, new kinds of information of cellular-level mechanisms in vivo can be obtained and the efficacy of drugs in individual patients can be assessed.

Electrophysiological mechanisms

TMS is the converse of magnetoencephalography (MEG) [16]. Instead of measuring the magnetic field produced by neural activation, in TMS a magnetic field is generated that induces an electric current in the desired brain area, producing neural activation. The

mathematical basis of TMS and MEG is largely the same.1

An important point to understand is the following. The head is transparent to magnetic fields at the frequencies used in TMS, *i.e.*, the magnetic field pattern from a coil is not altered by the presence of the head in the vicinity. However, the electric field generated by the changing magnetic field does depend on the conductivity structure of the head in a significant way. The most conspicuous consequence of the volume conductor geometry is that the macroscopic electric current produced by TMS is always tangential. Although the induced field can be computed directly for a coil with its axis oriented in the head's radial direction, the sphere has to be taken explicitly into account if the coil is tilted [17].

The magnetic field itself has practically no effect on the tissue; it is the electric field **E** induced by the changing magnetic field **B** (from Maxwell's equation, $\nabla\times\mathbf{E} = -\partial\mathbf{B}/\partial t$) that causes ion flow in the brain. In the cellular scale, the current tends to follow low-resistance pathways within the cellular matrix. When the electric current induced by a TMS pulse meets a cell membrane, the membrane potential is altered and the probability of firing of the cell is changed. It is not known which cortical cell types or which of their parts are most easily activated by TMS. It has been shown that in a homogeneous medium, a straight axon is activated at places where the $\partial E_x/\partial x$ is maximum, E_x being the component of the electric field along the axon. However, there are no straight axons in the cortex. Instead of the electric field gradient, for cortical excitation the important quantity is the amplitude of the field. Excitation probably takes place best at bends of cell processes, at constrictions in the extracellular space or at synaptic terminals. The role of glial cells in TMS remains unknown.

The technology

The field strength of up to several tesla required in magnetic brain stimulation is achieved by discharging a capacitor, charged at several kilovolts, through a coil placed over the scalp; the resulting current pulse of several kiloamperes lasts less than a millisecond, the rise to maximum field strength being less than 100 ms; the rate of change of the magnetic field is thus on the order of 30 kT/s. The rate of energy transfer from the capacitor to the coil can be tens of megawatts; at this power level, the thyristors used as switches and the diodes directing current flow in the circuit have to be quite massive. This is of great significance when one attempts to build multichannel stimulators, since each stimulator channel will require its own power electronics.

The focality of stimulation depends on the type of coil and on its distance from the head, small coils pressed against the scalp generally producing the most focal stimulation. In early magnetic stimulators, only circular coils were used; better focus can be obtained with the figure-of-eight coil [18]. It has been shown that further improvement is possible by using arrays of small coils [19–20]. While focusing is possible tangentially, it is not possible to focus in depth even with combined magnetic and electric fields [21]. In other words, the maximum induced field is always at the most superficial part of the brain.

With proper design of the coils, we can improve the focality of stimulation, minimize energy usage, eliminate problems from heating, and minimize the high electromagnetic forces giving rise to the disturbing click sound. For focality and minimal energy usage, the coil should be brought as close to the head as possible. The use of small coils to achieve the best possible focality is limited by the very high currents required.

Stereotactic TMS

In most TMS studies, the coil is placed over the head by using external landmarks on the head or by trial and error until the desired response (*e.g.*, thumb twitch) is generated. In contrast, in stereotactic TMS, the stimulator coil is positioned over the target location on the basis of individual MRI [22–25].

Because of the strong dependence of the magnetic field on the distance from the coil, even millimeter-level changes in the position or small changes in its orientation may change the induced field considerably. Therefore, stimulation amplitudes are typically selected on the basis of muscle response thresholds, but this is not possible when other than motor areas are studied. An alternative is to use the EEG response to adjust the field. Stereotactic TMS, when made sufficiently precise, will allow one to select the level of the induced field instead of selecting stimulus amplitude as a percentage of the maximum stimulator output or on the basis of the individual motor threshold or cortical response.

TMS combined with PET

Paus *et al.* [25] combined TMS and positron-emission tomography (PET), introducing a new technique permitting the mapping of neural connections in the living human brain. While stimulating a selected cortical area, they simultaneously measured changes in cerebral blood flow. The exact location of the stimulation site was achieved by frameless stereotaxy. They found significant correlations between cerebral blood flow and the number of TMS pulse trains, demonstrating functional connectivity from the left frontal eye field (FEF)

1 While an MEG signal detected by a coil is the integral of the dot product of lead field and the primary current density, the electric field generated by TMS is proportional to the lead field of the stimulating coil. The relevant electromagnetic frequencies in TMS are several kHz; thus, the quasistatic approximation is valid in the sense that the time derivative of the electric field as a source term for magnetic field can be neglected.

to visual areas in the superior parietal and medial parieto-occipital cortex.
Fox *et al.* [26] stimulated the hand area of the left primary motor cortex (M1) with TMS while blood flow was recorded with PET. At the stimulated site, TMS increased blood flow by 12–20%. Remote increases in blood flow were observed in ipsilateral primary and secondary somatosensory areas, in ipsilateral ventral, lateral premotor cortex and in contralateral supplementary motor area. Reduced blood flow was observed in contralateral M1.

TMS combined with EEG

Electrophysiological cortical responses elicited by TMS were first measured with EEG by Cracco *et al.* [27] and by Amassian *et al. [*28]. The early measurements were difficult because of the huge artefacts produced by the strong TMS pulses. To overcome the difficulties, we have developed methods to eliminate the artefacts; our current EEG system, comprising a 60-electrode cap and electronics, can function without problem in the presence of the TMS pulses [29–30].
The electrodes in our cap are 0.5-mm-thick Ag/AgCl rings, each interrupted with a 3-mm-wide slit to reduce the eddy currents that might otherwise cause excessive heating. In addition to heating, the TMS pulse produces a force on metallic objects; this force appears to cause an artefact in the EEG signal but fortunately the force and the artefact are also dramatically reduced when a slit is introduced.
A key feature in avoiding the stimulus artefact is a sample-and-hold circuit that keeps the amplifier output at a constant level during the pulse. Although the stimulus artefact can be dealt with by a hold period of just 1 ms, one often observes artefacts from muscles activated by the TMS pulse, in particular when the lateral aspect of the head is stimulated. These can often be handled with by a longer hold period, although at the expense of losing data.
Although the TMS-evoked responses are quite strong, averaging is required to obtain a good signal-to-noise ratio. High-quality curves can be obtained by averaging 50–100 individual responses. One should keep in mind that we do not yet know how many stimuli can be delivered in the same cortical location without risk; therefore, one should limit the number of pulses to the minimum required in a given experiment.
We are developing the use of EEG mapping and source localization in conjunction with stereotactic computer-assisted TMS. By recording the cortical response just milliseconds after a TMS pulse, we can obtain an index of the local reactivity of the cortex; subsequent activity reflects also corticocortical and transcallosal connectivity.
In one set of experiments, we stimulated motor and visual cortices of volunteers [29]. The stimulation of the left sensorimotor hand area elicited an immediate strong response at the stimulated site. The activation spread to adjacent ipsilateral motor areas within 5–10 ms and to homologous regions in the opposite hemisphere within 20 ms. Similar activation patterns were generated by magnetic stimulation of the visual cortex: after the immediate ipsilateral response, the contralateral response was observed at about 20 ms. To locate the activity underlying the observed signals, various source modelling techniques can be used. When only one area of the cortex is active, which may be a reasonable approximation in many cases, dipole modeling is appropriate. In more complicated cases, continuous current estimates are more reliable in indicating the active areas. We have used minimum-norm estimation [31] when observing the evolution of TMS-evoked brain activity, although original data and potential maps must always be carefully studied, at least in order to evaluate the quality of the data and to detect possible artefacts.
One advantage of EEG is that it provides direct information about the timing of signals transmitted from the stimulated site to other areas. It is also possible to combine sensory evoked potential and TMS studies. A potentially useful application of EEG might be the early detection of approaching seizures during rapid-rate TMS treatment.
The combination of stereotactic TMS with EEG and PET gives rise to a completely new brain imaging modality. We can, for the first time, measure local reactivity of the cortex as well as functional connectivity between different brain areas.

Safety

Safety of TMS is of key importance to the patients, volunteer subjects and to the success of the field in general. So far, no significant risks from TMS have been reported except for the risk of an epileptic seizure when repetitive TMS (rTMS; stimulus rate 5/second or more) is used or when low-rate stimulation is applied to stroke patients.
The following guidelines are suggested. This is only a brief, partial list; consult the literature to obtain more thorough recommendations (*e.g.*, [32–33]) 1) Avoid unnecessarily large numbers of stimuli per subject and cortical area, 2) avoid unnecessarily high stimulation rates or amplitudes, 3) make sure that competent personnel is available in the case of a seizure or other hazards, 4) do not perform TMS to people with intracranial metallic or magnetic materials, 5) protect the ears of the patient and yourself from the click produced by the stimulator, 6) in EEG studies, use slitted electrodes to avoid their excessive heating, 7) document and report to the TMS community any ill effects from TMS with the experimental paradigm used. Note also that magnetic stimulation may disturb nearby electronic devices such as cardiac pacemakers, hearing aids, or any other implanted electrical devices.

Future developments and challenges

In the future, the brain can be stimulated by means of superposed fields from an array of dozens of small coils in a helmet-like arrangement [19–20]. The current

amplitude in the coils will be individually controlled, which makes it possible to move the stimulated spot electronically to any desired location without moving the coils themselves. Electronic targeting can give a dramatically improved accuracy and specificity of stimulation. The activating field can be focused on a smaller volume of critical tissue with an array of coils than with the traditional single-coil equipment.
TMS offers a new modality in brain mapping. While CT and MRI give us information on anatomy, MEG and EEG about electrical events, fMRI and PET about hemodynamics, PET and SPECT about metabolism and transmitter distribution, TMS can provide maps of reactivity and connectivity. In addition, TMS can be used to map areas that are important for the performance of a given task or areas that influence the activation of a muscle. With many new paradigms to come, the future of TMS as a brain mapping tool seems very bright.

References

[1] Nilsson, J., Panizza, M., and Grandori, F., editors, Advances in Magnetic Stimulation: Mathematical Modeling and Clinical Applications, Advances in Occupational Medicine & Rehabilitation 2, Pavia, Maugeri Foundation, 1996.

[2] Walsh, V., and Cowey, A. Magnetic stimulation studies of visual cognition, Trends Cogn. Sci. 1998, 2: 103–110.

[3] Jalinous, R. Guide to Magnetic Stimulation, The Magstim Company Ltd., UK, 1998.

[4] Barker, A.T., Jalinous, R., and Freeston, I.L. Noninvasive magnetic stimulation of human motor cortex, Lancet, 1985, 1**:** 1106–1107.

[5] Amassian, V.E., Cracco, R.Q., Maccabee, P.J., Cracco, J.B., Rudell, A., and Eberle, L. Suppression of visual perception by magnetic coil stimulation of human occipital cortex, Electroenceph. Clin. Neurophysiol., 1989, 74: 458–462.

[6] Pascual-Leone, A., Gates, J.R., and Dhuna, A. Induction of speech arrest and counting errors with rapid-rate transcranial magnetic stimulation, Neurology, 1991, 41: 697–702.

[7] Miller, M.B., Fendrich, R.J., Eliassen, C., Demirel, S., and Gazzaniga, M.S. Transcranial magnetic stimulation: delays in visual suppression due to luminance changes, NeuroReport, 1996, 7: 1740–1744.

[8] Seyal, M., Ro, T., and Rafal, R. Increased sensitivity to ipsilateral cutaneous stimuli following transcranial magnetic stimulation of the parietal lobe, Ann. Neurol., 1995, 38: 264–267.

[9] Cohen, L.G., Celnik, P., Pascual-Leone, A., Corwell, B., Falz, L., Dambrosia, J., Honda, M., Sadato, N., Gerloff, C., Catala, M.D., and Hallett, M. Functional relevance of cross-modal plasticity in blind humans, Nature, 1997, 389: 180–183.

[10] Kujala, T., Huotilainen, M., Sinkkonen, J., Ahonen, A.I., Alho, K., Hämäläinen, M.S., Ilmoniemi, R.J., Kajola, M., Knuutila, J.E.T, Lavikainen, J., Salonen, O., Simola, J., Standertskjöld-Nordenstam, C-G., Tiitinen, H., Tissari, S.O., and Näätänen, R. Visual cortex activation in blind humans during sound discrimination, Neurosci. Lett., 1995, 183: 143 – 146.

[11] Sadato, N., Pascual-Leone, A., Grafman, J., Ibanez, V., Deiber, M.P., Dold, G., and Hallett, M. Activation of primary visual cortex by Braille reading in blind subjects, Nature, 1996, 380: 526–528.

[12] George, M.S., Wassermann, E.M., Williams, W.A., Callahan, A., Ketter, T.A., Basser, P., Hallett, M., and Post, R.M. Daily repetitive transcranial magnetic stimulation (rTMS) improves mood in depression, NeuroReport, 1995, 6: 1853–1856.

[13] Pascual-Leone, A., Rubio, B., Pallardó, F., and Catalá, M.D. Rapid-rate transcranial magnetic stimulation of the left dorsolateral prefrontal cortex in drug-resistant depression, Lancet, 1996, 348**:** 233–237.

[14] Markwort, S., Cordes, P., and Aldenhoff, J. Die transkranielle Magnet-stimulation als Behandlungsalternative zur Elektrokrampf-therapie bei therapieresistenten, Fortschritte der Neurologie-Psychiatrie, 1997, 65: 540–549.

[15] Ziemann, U., Lönnecker, S., Steinhoff B.J., and Paulus, W. The effect of lorazepam on the motor cortical excitability in man, Exp. Brain Res., 1996, 109: 127–135.

[16] Hämäläinen, M., Hari, R., Ilmoniemi, R.J., Knuutila, J., and Lounasmaa, O.V. Magnetoencephalography —theory, instrumentation, and applications to noninvasive studies of the working human brain, Rev. Mod. Phys., 1993, 65: 413 – 497.

[17] Ilmoniemi, R.J., Ruohonen, J., and Virtanen, J. Relationships between magnetic stimulation and MEG/EEG, In: Nilsson, J., Panizza, M., and Grandori, F. Advances in Magnetic stimulation: Mathematical Modeling and Clinical Applications. Advances in Occupational Medicine & Rehabilitation 2, Pavia, Maugeri Foundation, 1996, 65 – 72.

[18] Ueno, S., Tashiro, T., and Harada, K. Localized stimulation of neural tissue in the brain by means of a paired configuration of time-varying magnetic fields. J. Appl. Phys., 1988, 64: 5862–5864.

[19] Ilmoniemi, R.I., and Grandori, F. Device for applying a programmable excitation electric field to a target, European Patent Application No. EP 0 709 115 A1, 27 October, 1994.

[20] Ruohonen, J., and Ilmoniemi, R.J. Focusing and targeting of magnetic brain stimulation using multiple coils, Med. & Biol. Eng. & Comput., 1998, 36: 297–301.

[21] Heller, L., and van Hulsteyn, D.B. Brain stimulation using electromagnetic sources: Theoretical aspects, Biophys. J., 1992, 63: 129–138.

[22] Ruohonen, J., and Ilmoniemi, R.J. Multichannel magnetic stimulation: improved stimulus targeting, In: Nilsson, J., Panizza, M., and Grandori, F. Advances in Magnetic stimulation: Mathematical Modeling and Clinical Applications. Advances in Occupational Medicine & Rehabilitation 2, Pavia, Maugeri Foundation, 1996, 55 – 64.

[23] Krings, T., Buchbinder, B.R., Butler, W.E., Chiappa, K.H., Jiang, H.J., Cosgrove, G.R., and Rosen, B.R. Functional magnetic resonance imaging and transcranial magnetic stimulation: complementary approaches in the evaluation of cortical motor function, Neurology, 1997, 48: 1406–1416.

[24] Krings, T., Buchbinder, B.R., Butler, W.E., Chiappa, K.H., Jiang, H.J., Rosen, B.R., and Cosgrove, G.R. Stereotactic transcranial magnetic stimulation: correlation with direct electrical cortical stimulation, Neurosurgery, 1997, 41: 1319–1325.

[25] Paus, T., Jech, R., Thompson, C.J., Comeau, R. Peters, T., and Evans, A.C. Transcranial magnetic stimulation during positron emission tomography: a new method for studying connectivity of the human cerebral cortex, J. Neurosci., 1997, 17: 3178–3184.

[26] Fox, P., Ingham, R., George, M.S., Mayberg, H., Ingham, J., Roby, J., Martin, C., and Jerabek, P. Imaging human intra-cerebral connectivity by PET during TMS, NeuroReport, 1997, 8: 2787–2791.

[27] Cracco, R.Q., Amassian, V.E., Maccabee, P.J., and Cracco, J.B. Comparison of human transcallosal responses evoked by magnetic coil and electrical stimulation, Electroenceph. Clin. Neurophysiol., 1989, 74: 417–424.

[1]
[28] Amassian, V.E., Cracco, R.Q., Maccabee, P.J., and Cracco, J.B. Cerebello-frontal cortical projections in humans studied with the magnetic coil, Electroenceph. Clin. Neurophysiol., 1992, 85: 265–272.

[29] Ilmoniemi, R.J., Virtanen, J., Ruohonen, J., Karhu, J., Aronen, H.J., Näätänen, R., and Katila, T. Neuronal responses to magnetic stimulation reveal cortical reactivity and connectivity, NeuroReport, 1997 8: 3537–3540.

[30] Virtanen, J., Ruohonen, J., Näätänen, R., and Ilmoniemi, R.J. Instrumentation for measuring electric brain responses to transcranial magnetic stimulation, in preparation, 1998.

[31] Hämäläinen M.S., and Ilmoniemi, R.J. Interpreting magnetic fields of the brain: minimum-norm estimates, Med. & Biol. Eng. & Comput. 1994, 32: 35–42.

[32] Pascual-Leone, A., Houser, C.M., Reese, K., Shotland, L.I., Grafman, J., Sato, S., Valls-Solé, J., Brasil-Neto, J.P., Wassermann, E.M., Cohen, L.G., and Hallett, M. Safety of rapid-rate transcranial magnetic stimulation in normal volunteers, Electroenceph. Clin. Neurophysiol., 1993, 89: 120–130.

[33] Wassermann, E.M., Grafman, J., Berry, C., Hollnagel, C., Wild, K., Clark, K., and Hallett, M. Use and safety of a new repetitive transcranial magnetic stimulator, Electroenceph. Clin. Neurophysiol., 1996, 101: 412–417.

[34] Ilmoniemi, R.J. Transcranial magnetic stimulation–New modality in brain mapping, In Paus, T., and Evans, A. Brain Mapping Course, Monteal, 4th International Conference on Functional Mapping of the Human Brain, 1998, pp. 103–112.

Acknowledgements

Grants from TEKES, the Foundation for Finnish Inventions, Runar Bäckström Foundation, Instrumentarium Foundation, the Academy of Finland, and the Helsinki University Central Hospital Research Grants are acknowledged. This material has been used previously in a brain mapping course [34].

Combining Electromagnetic and Hemodynamic Signals to Derive Spatiotemporal Brain Activation Patterns: Theory and Results

Halgren, E.[1-3], and Dale, A.M.[2]

[1]Radiology, University of Utah, Salt Lake City, USA
[2]MGH-NMR, Harvard Medical School, USA
[3]INSERM E 9926, Marseilles, France

EEG/MEG for when, fMRI for where

The construction of accurate spatio-temporal maps of human brain activity during higher cognitive tasks poses substantial technical and theoretical difficulties. Since no single technique has the ability to provide accurate and certain resolution in both the temporal and spatial domains, it is necessary to combine techniques with complementary sensitivities. Functional magnetic resonance imaging (fMRI) has emerged as the best technique for *localizing* neural activation due to cognition. It provides high, certain, and fairly uniform spatial accuracy (to about 3 mm), but low temporal resolution (>1 s), due to its indirect relationship to neural activity. In contrast, electromagnetic measures, the electroencephalogram and magnetoencephalgram (EEG and MEG) have temporal accuracy that is limited only by the sampling rate (typically a few ms), but have limited, uncertain and biased spatial accuracy [1]. In this paper, we discuss the physiological justification for combining these measures, and some initial results of their combination in studying the neural basis of cognition.

The limited temporal resolution of fMRI is due to its origin in the Blood Oxygenation Level Dependent (BOLD) response [2]. Although it is not well-established, it is thought that the BOLD response is produced by an increase in blood flow that in turn is caused by byproducts of increased energy utilization during neural activity [3]. Each of these linkages, from neural activity to metabolic demand to changes in microcirculation, may act as low-pass filter, with the relatively sluggish dynamic response of the capillaries and arterioles forming a biophysical limit on the ability of the BOLD response to follow rapid fluctuations of neural activity [4].

In contrast to the fMRI, the EEG and MEG result directly from current flow across post-synaptic membranes. Aligned intracellular currents generate the MEG, whereas aligned extracellular currents are measured as EEG [5, 6]. Consequently, the EEG and MEG have identical generators but propagate differently. Thus, they provide complementary localizing information [7], and are considered as a unit in the current chapter.

The uncertain spatial resolution of EEG/MEG was articulated in the 19th century by Helmholtz [8]: for any given extracranial distribution of electromagnetic activity, there are an infinite number of possible generator configurations in the brain. Even given a simple dipolar pattern as measured outside the head, it is easy to imagine complex arrangements of dipoles that cancel each other except for a residual that can appear as a small dipole at a distance [9]. Furthermore, a focal source may produce an external pattern that is indistinguishable from a more superficial field of activation distributed over a broad area [10]. For these reasons, uncertainty in the location of generating sources is worse for their depth than their other dimensions, i.e. there is a nonuniformity in the spatial localizing ability of EEG/MEG [7]. Despite these uncertainties, it must be emphasized that there is still a great deal of spatial information in the EEG/MEG.

One approach to a combined solution

The problem of inferring synaptic generators from extracranial EEG/MEG (i.e., the Inverse Problem) is considered by many chapters in this collection. In the most common approach, the EEG/MEG signal is assumed to result from activation of only one or a few highly localized areas, each of which is represented by an equivalent current dipole. While this approach has yielded much valuable data, it has had limited success in identifying the generators of the later cognitive components. Intracranial EEG (iEEG) recordings have clearly shown that during cognitive tasks, many areas become rapidly engaged, and remain engaged in an overlapping and distributed fashion [11-13].

One approach to the Inverse Problem that produces a distributed solution was described by Dale and Sereno in 1993 [14]. This approach finds the minimum norm solution [15] for each point on the cortical surface, normalized by estimated noise at that point. In addition, the solution is regularized according to a reasonable estimate of the signal to noise ratio of the recording. We term these inverse solutions 'Anatomically-constrained MEG' (aMEG).

The aMEG procedure assumes that MEG is generated in the cortex. This assumption of is reasonable given that the spatial summation of synaptic currents necessary for producing externally measurable signals requires a parallel alignment of dendrites and a laminar distribution of synapses. This alignment is not known to exist on a significant scale outside of the cortex. Simulations show that additional accuracy is obtained by further assuming that the generating dipoles are perpendicular to the cortical surface [7]. This again is

reasonable given that the main orientation of aligned dendrites in the cortex is radial, and synaptic terminations tend to intersect these dendrites in different laminae. Although activation of particular cortical columns would produce current flows parallel to the cortical surface, these flows would have radial symmetry and thus their fields would cancel at a distance.

The aMEG methodology requires that the cortical surface be accurately reconstructed on each individual. Such reconstructions are now routine, using modern structural MRI and well-tested algorithms [16, 17]. In addition to providing constraints for the aMEG procedure, the folded surface tessellation can be "inflated" to reveal cortex within the sulci, thereby providing a convenient format for visualizing cortical activation patterns. Finally, the surface reconstruction methodology can be directly extended to derive the conductivity boundaries necessary to implement a realistic forward solution using the boundary element method [18].

For purposes of inter-subject averaging, the reconstructed surface for each subject can be morphed into an average spherical representation, optimally alligning sulcal and gyral features across subjects while minimizing metric distortion [19]. This non-rigid surface-based deformation procedure results in a substantially better alignment of corresponding anatomical features and functional activations across subjects than does the more commonly used normalization approach of Talairach. Its use thus increases the statistical significance and anatomical precision of the inter-subject aMEG averages. A freeware program that can perform these tasks is available at www.nmr.mgh.harvard.edu/freesurfer.

In our experience, the aMEG maps in cognitive studies seem reasonable (see below), but are less focussed than the fMRI maps obtained in the same subjects and tasks. The aMEG maps are greatly sharpened when fMRI is used to bias the aMEG solution (termed 'fMEG'), as described in Dale and Sereno [14]. For fMEG analysis, the fMRI weighting was set to 90%, a value suggested by simulation studies [7]. This partial fMRI weighting tends to bias the EEG/MEG solution towards regions that are activated based on fMRI, without completely ruling out areas in which the fMRI activation does not reach the specified threshold.

The addition of fMRI as a functional prior assumes that the EEG/MEG generators in a given subject and task are also activated in fMRI. This assumption is consistent with a variety of physiological evidence for a tight coupling between electromagnetic and hemodynamic cortical changes [20, 21]. However, there are also many ways that, in theory at least, EEG/MEG sources may not be seen with fMRI, and *vice versa*.

In this chapter, we will consider how the generators of EEG/MEG and fMRI may be dissociated, and how the fMEG procedure can be made robust to such dissociations. Then we consider the empirical evidence that fMRI and EEG/MEG generators are similar in cognitive tasks involving lexical access of visually-presented words. Finally, we review our recent results with the aMEG and fMEG procedures in cognitive studies, especially with regard to their accuracy given what we know about the generators of neural activity in these paradigms from other techniques.

fMRI-silent EEG/MEG activations

There are several reasons why fMRI may fail to detect an EEG/MEG source. EEG/MEG records the instantaneous current flows, whereas fMRI integrates hemodynamic changes over seconds. Thus, a brief highly synchronous activation may result in a large EEG/MEG signal, but no significant fMRI signal. However, iEEG recordings find that once a structure is activated, it tends to remain activated for an extended period, even in sensory cortex [13, 22, 23]. This is consistent with the robust fMRI activation that is observed in visual cortex to short simple stimuli at long intervals [24].

A related issue arises when comparing signals recorded in different task conditions, where the EEG/MEG signal is highly sensitive to the latency of activation across conditions but the fMRI is not. For example, suppose that some area were equally activated to conditions A and B, but at different latencies. The A-minus-B signal would then be large in the EEG/MEG (where the subtraction is made latency-by-latency), but would not be present in the fMRI (where the subtraction is made after integrating across all latencies). Consequently, one may miss generators of signals present in the EEG/MEG subtraction if one uses the fMRI subtraction as an anatomical prior. This error can be avoided if one includes all areas showing an fMRI difference in *any* task comparison as priors.

An EEG/MEG generator may also fail to be detected with fMRI if it lies in an area where susceptibility artifacts reduce the signal. Of particular concern is the anteroventral temporal lobe, which may have reduced fMRI-sensitivity due to magnetic susceptibility artifacts near the ear canals [25], but is found to be responsive during semantic tasks according to PET and iEEG studies [11, 12, 26, 27].

One may use several strategies to try to detect fMRI differences that may be weak for this, or any other reason. First, one can use a relatively low significance threshold for the fMRI. Note that the use of a low threshold is actually the most conservative approach in this context, because it helps to avoid the possibility of missing fMRI sources. Second, one can use both increases and decreases of the fMRI signals to bias the fMEG solution. EEG/MEG signals can be produced by both excitatory and inhibitory synaptic current flows, as can fMRI signals. Although increases in local glucose metabolism have been reported after strong recurrent inhibition of hippocampal neurons [28], it is not clear if weak synchronous inhibition as may produce some EEG/MEG signals is associated with an increase or a decrease in metabolism. Until the transfer function from synaptic activity to the BOLD signal is better understood, it is more conservative to allow the possibility that a decreased BOLD signal may be associated with an increased EEG/MEG response. Finally, it is especially important in studies attempting to combine

hemodynamic with electromagnetic responses that each has high signal-to-noise, so that the errors in each do not interact unpredictably.
Despite these measures, it is always possible that EEG/MEG generators will be missed by the fMRI constraint. Consequently, in calculating the fMEG, one should not force the active dipoles to lie in the areas activated according to fMRI, but only bias them toward those areas. Simulations indicate that this strategy maintains most of the focusing effect of fMEG while avoiding the major errors induced by missing sources [7].

EEG/MEG-silent fMRI activations

There are several circumstances in which fMRI activation could occur in an area that does not produce a recorded EEG/MEG signal. For example, metabolic energy may be utilized in a manner that does not lead to synaptic currents, for example in synaptic remodeling. Even when the metabolic activation *does* result from restoring ionic and/or transmitter balance after excitatory or inhibitory post-synaptic currents (EPSCs or IPSCs), the production of a measurable EEG/MEG response requires temporal synchrony and spatial organization.
The generation of EEG/MEG requires synaptic activation that overlaps in time, whereas fMRI does not. That is, synaptic activation that is temporally-asynchronous is likely to produce an fMRI signal but no EEG/MEG response. Temporal overlap is especially hard to achieve for short-duration electrophysiological events. Consequently, except in some very exceptional circumstances where the reactions to thousands of brief sensory stimuli are averaged [1], action-potentials are thought to contribute nothing to EEG/MEG signals [29]. Similarly, the fast cortical EPSCs that carry out most specific information-processing last about 10 ms, and thus their summation would require tight synchronization. Fast IPSCs are only slightly longer. Thus, extracranial EEG/MEG is probably biased towards the slower EPSCs and especially IPSCs because their requirements for synchronization are less stringent.
It is not known what proportion of the EPSCs and IPSCs on cortical neurons summate to produce local field potentials, and what proportion cancel. However, there do exist powerful interacting intrinsic and intrinsic mechanisms for synchronizing cortical synaptic activity [29]. The power spectrum of EEG tends to be pink (i.e., weighted toward the lower frequencies), confirming the importance of these synchronizing influences in production of the EEG. One synchronizing mechanism arises from the reciprocal local fast excitatory-inhibitory circuits that appear to 'reverberate' within the cerebral cortex, and between the cortex and thalamus, in the gamma range (30-80 Hz) [30, 31]. These high-frequency oscillations may form envelopes for the synchronized communication of information within cortical ensembles [32].
The influence of synchrony is so powerful that it could result in an *increase* in EEG/MEG is associated with a *decrease* in fMRI. For example, the largest EEG waves are the 0.5-4 Hz activity during slow wave sleep produced by thalamocortical mechanisms that have been well-studied in animals [33]. These large waves are associated with greatly reduced synaptic activity and decreased metabolism [34].
Two spontaneous 'resting' rhythms deserve individual discussion, because they often dominate waking EEG/MEG [35]. One is the alpha rhythm, generated at about 10 Hz in visual cortices when the eyes are closed and the subject is relaxed but alert [36]. Trsansient alpha suppression can also occur in response to cognitive activation or other arousal, even in the absence of visual input. The mu rhythm is similar to the alpha, except that it includes a broader range of frequencies (from about 10 to 20 Hz), is generated in peri-Rolandic cortices, and occurs mainly when movement is absent and the subject is relaxed mentally [37].
The alpha rhythm has been extensively studied in animals [38], but its physiological basis in humans is not well understood. It is generally assumed that the alpha rhythm is associated with decreased synaptic activity compared to the actual engagement of the generating cortex in visual processing. However, it may be that certain areas that have been noted to have increased metabolism during the 'rest' periods of visual tasks [39] may actually be expending energy on alpha generation. One such area, at the medial occipito-parietal junction, has also been suggested as the likely focus of alpha generation in MEG studies [35]. It should be noted that although these rhythms are termed 'resting'; the relatively activated areas may actually be performing internal monitoring, rehearsal, or some other function that is not under experimental control [40].
There are two general views of the relation of background EEG/MEG rhythms to event-related neural activation. In one view, 'background' EEG/MEG waves are considered to be idling noise to be eliminated by time-locked averaging with respect to a cognitive event [1]. The resulting averages are termed Event Related Potentials and Fields (ERPFs). In this view, a *decrease* in background rhythms indicates an *increase* in functional activation. The decrease in spectral power can be monitored on a trial-by-trial basis, and is termed Event-Related Desynchronization (ERD) [41]. In the other view, EEG/MEG waves *are* the signal, and ERPFs are simply background EEG/MEG waves that have become phase-locked to the stimulus [42]. Since such phase-locking is imperfect, this view suggests that EEG/MEG should be analyzed according to their power at different frequencies, at different latencies after the cognitive event [43]. The resulting measure is termed Event-Related Spectral Power (ERSP).
There are data to support both views. As noted above, some prominent rhythms clearly are associated with functional *in*activation: they *decrease* when an area becomes engaged in information processing. However, if these special 'idling rhythms' are not present in the baseline, then it appears that functional processing is associated with a wideband increase in spectral EEG power. For example, locally-recorded EEG in the right

fusiform face area shows an increase in power from 4 to 45 Hz in response to faces but not other stimuli [43]. This increase occurs from about 180 to 230ms after stimulus presentation, i.e., precisely at the time that this area is thought to make an essential contribution to face-encoding. These data suggest that, provided the effects of the 'idling rhythms' can be excluded, EEG/MEG *does* reflect functional activation, and can be used for timing that activation. The effects of the idling rhythms can be eliminated from EEG/MEG by measuring them specifically and then projecting them out with a spatial filter, or by extensive averaging.

Following the transient, face-selective, localized increase in fusiform EEG power, there is a wideband decrease centered at about 400ms, when the center of processing is presumed to have passed to more anterior areas. At the same time as this late fusiform decrease, there is an increase in EEG spectral power in ventrolateral prefontal areas that are involved in cognitive/emotional processing of faces. At around 400ms, when the fusiform and prefrontal areas show opposite responses in spectral power, they display similar ERPs. Furthermore, much of the event-related EEG change seen in the ERSP response is not phase-locked to the stimulus, and thus would not contribute to the ERP.

These dissociations between averaged ERPs and spectral measures suggest that ERPs may sometimes be an imperfect measure of underlying cortical activation. When using spectral measures as a supplement to averages, the broadband nature of the EEG response implies that analysis of a narrow frequency range (e.g., around 40Hz) is too restrictive. The common use of averaging to extract the event-related EEG/MEG signal imposes an additional bias on what synaptic activity is analyzed; the underlying PSCs must not only be sufficiently synchronous so as to summate to produce instantaneous EEG/MEG, they must also be phase-locked to the stimulus to average across trials.

Fortunately, the non phase-locked EEG activity seems to occur in the same locations and at the same times as the phase-locked activity [43]. In large part, this is because the cognitive EEG/MEG signals include components that are sufficiently long duration to permit summation even if they are not strictly synchronous. Thus, in practice, the averaged ERPF are adequate to provide time-courses in the currently used techniques for integration with fMRI. As described above, these techniques do not attempt to incorporate a quantitative relationship between different BOLD signal levels and the averaged EEG/MEG. Rather, these techniques simply use a probability threshold applied to the BOLD signal to identify areas that might generate ERPFs.

Potentially, a model that described in quantitative terms how the underlying current flows lead to both the hemodynamic and the electromagnetic signals would allow more powerful mutual constraints. The above data clearly indicate that the application of this model will require the use of single-trial spectral measures as well as more traditional ERPFs. In any case, it is important to realize that none of the non-invasive measures allow excitation to be distinguished from inhibition, nor the level of unit activity to be inferred (all are lumped together under the ambiguous term 'activation'). Analysis at a sufficient level of neuronal detail to permit the construction of neuro-computational models of cognitive studies requires coordinated studies using invasive techniques.

The second general reason why fMRI may record activation in an area that does not produce a recordable EEG/MEG signal is that identical EEG/MEG signals in different areas may either summate or cancel depending upon the spatial arrangement of the generating elements, whereas fMRI signals will not. At the micro-level, the production of EEG/MEG signals requires that the generating synapses and dendritic elements be spatially aligned. At a larger spatial scale, EEG/MEG signals of similar amplitude may cancel if they lie on opposite sides of a sulcus. Again, it is not known what proportion of PSCs cancel, and what proportion actually propagate extracranially.

Temporal synchrony and spatial alignment work together in determining what synaptic activity ultimately results in a recordable EEG/MEG signal. Optimal propagation will be achieved by relatively slow synaptic activations synchronized over large areas of the cortex by the thalamus, brainstem or cortico-cortical fibers. The degree of synchrony between cortical sites has been examined using coherence measures applied to iEEG. These studies show a fairly high level of coherence both at relatively short distances [44], as well as at longer ranges, with average coherence measures of about .35 [45]. These coherences can transiently increase dramatically across the cortex during information processing. For example, at the same time that fusiform spectral activity increases in response to faces, there is a phasic increase in its coherence with many temporal, parietal and even frontal sites [45]. It is interesting to note that many methods used for the inverse problem assume independent or at least uncorrelated sources in order to reduce the dimensionality of the dataset. This assumption does not appear to be justified.

In summary, there are many reasons, especially spatio-temporal cancellation of synaptic currents, why areas producing an increased BOLD signal may not generate an extracranial EEG/MEG signal. Fortunately, such occurrences should not seriously compromise the accuracy of the fMEG solutions. Simulations show that the inclusion of fMRI bias from sources that do *not* generate a recorded EEG/MEG signal would not result in a mis-estimation of the time-course of the true sources [7]. Estimates of the time-courses of these 'silent' areas may be inaccurate, if they lie close to an actual EEG/MEG generator. However, it is likely that in most cases the anatomical localizing information inherent in EEG/MEG is sufficient to prevent spurious time-courses from being inferred. Simulations of the aMEG procedure indicate that the cross-talk between sites greater than about 1 to 2 cm apart is minimal [7]. That is, since fMEG localization arises from the synergistic application of the localizing information present in the

fMRI *and* EEG/MEG signals, it is robust to EEG/MEG-silent fMRI activations.

Correspondence of hemodynamic *versus* electromagnetic activations to words

In the previous two sections, we have reviewed the reasons why the BOLD and EEG/MEG signals may, or may not, be generated by the same cortical locations. Existing data support a general correspondence, but theoretical considerations suggest that significant deviations could occur. In our view, it is important that absolute correspondence not be assumed, but be tested empirically whenever possible, and that measures be taken to make the method as robust as possible to breakdowns in correspondence. Some of these measures were referred to above. In this section, we consider the empirical evidence for a correspondence between patterns of hemodynamic and EEG/MEG activation during the cognitive processing of words.

In the classical lesion-based neuropsychological model, visual processing in reading tasks is followed by lexical access in the left angular gyrus, and then semantic evaluation in Wernicke's area [46]. While these structures are sometimes found to be activated using fMRI and Positron Emission Tomography (PET) during semantic word-reading, activation is more prominent in the ventral visual processing stream and the left ventrolateral prefrontal cortex [47, 48]. The ventral visual stream begins at the occipitotemporal junction, and extends anteriorly through the posterior parahippocampal and fusiform gyri, to the anteromedial temporal lobe [49, 50]. Beyond the multimodal integration of complex stimuli, the anteromedial temporal lobe serves as the principle relay of neocortical information in and out of the hippocampal formation and amygdala, concerned with recent declarative memory and emotion [49].

The most prominent locus of fMRI/PET activation in word-reading tasks is the left ventrolateral prefrontal cortex. While this area *is* activated during overt word reading (as suggested by neuropsychological evidence [46]), it is also activated by words in the absence of speech [47, 48]. Activation of this area requires that the words be semantically processed, and may support a "domain-specific working memory" for verbal material [51]. In addition to these areas, fMRI/PET activation during word-reading can be found in the intraparietal, supplementary motor and cingular cortices [47].

Activation in several of the areas noted above is found to decrease if the same item is processed repeatedly. Again, repetition effects in both explicit and implicit memory tasks are most prominent in the ventrolateral prefrontal cortex, and these are specific to semantic tasks [47, 51]. Hemodynamic changes in medial frontal and occipitotemporal cortices have also been noted [47].

Following potentials in the first 200ms related to visual processing and attention, EEG is also strongly modulated by semantic processing and memory. The most prominent late EEG responses to words are termed the N400 (or N4) and LPC (Late Positive Component or P3b) [1]. The N4 is evoked by the semantic processing of words, objects, faces, and other potentially meaningful items, and is modulated by the difficulty of integrating the item with the current cognitive context. For example, the N4 to the final word in a sentence is smaller if it can be inferred from the sentence context. The N4/P3b to words are also strongly modulated by repetition. In short, the cognitive correlates of the ventrolateral prefrontal fMRI activation and the N4 EEG component have several similarities: they are both evoked by words, objects, or other potentially meaningful stimuli; they both require semantic processing of these stimuli; and they both are decreased by a broad range of manipulations, such as repetition, that ease integration of the stimulus in the current cognitive context.

The generators of these EEG signals have been localized using intracranial recordings, as those regions with large amplitudes and gradients relative to surrounding areas [1]. Since depth electrodes are only implanted in humans for clinical purposes, iEEG recordings are limited by idiosyncratic sampling, and confounded by individual epileptiform pathology. In addition, iEEG recordings from the same tasks and subjects as fMRI studies are not available. However, extensive iEEG recordings *have* been made in a similar visual verbal-semantic tasks in other subjects. The generators of the N4 EEG component found in these studies bear a remarkable resemblance to the areas found with fMRI to be activated in similar tasks: the strongest N4-like signals were located in the perirhinal, occipitotemporal, and ventrolateral prefrontal cortical areas, with secondary generators in the anterior cingulate and intraparietal cortices [11, 12, 26]. These similarities in the cognitive correlates and cortical generators of hemodynamic versus electromagnetic activations during verbal-semantic processing provide empirical evidence that the neural substrates of these signals are similar enough to allow their integration.

General pattern and apparent validity of results using aMEG and fMEG

We have recently studied the spatiotemporal patterns of brain activation evoked by words in a variety of paradigms, using aMEG and/or fMEG. These patterns have been compared with those evoked in face-processing and tactile recognition. The results are generally consistent with what would be expected based on previous neuroscientific studies.

In one task, words were presented briefly, and the subjects judged whether they referred to an object or animal more than one foot in length (Dale et al., submitted). According to fMEG, activation began at about 80ms in visual cortex and spread within 100ms to occipito-temporal, medial-temporal, superior temporal, supramarginal, anterior-cingulate, and ventrolateral-prefrontal sites. These areas remained active for about 400ms, with the dominant activation shifting from temporal to frontal. Half of the words were repeated

several times each. Repetition effects started at about 250ms, after all areas were activated, and then were widespread in ventral temporo-frontal cortex from 300 to 600ms. Similar patterns were observed in other tasks that presented single words but required rhyming or verb conjugation, with delayed repetition of some words. In all three studies, the areas sensitive to repetition priming are consistent with the findings of previous PET and fMRI studies [47]. Similarly, the timing of the MEG signals and their changes with repetition resemble the N4/LPC components recorded in many previous EEG studies [1].

It should be emphasized that the assignment of activation to different sites for each latency and task condition is a result of localizing information from both fMRI and MEG. Since all fMEG calculations used the same fMRI bias across latencies and task conditions, differences between latencies and conditions are due entirely to the localizing information contained in the MEG signal. Examination of these differential effects indicate that the anatomical selection by MEG among different fMRI sites is reasonable. For example, early activation is in visual areas, late in cognitive. Similarly, fMEG repetition effects are limited to certain areas (e.g., to ventral occipitotemporal, medial temporal and prefrontal; not to the occipital pole or rolandic). The fact that fMRI found similar areas as displaying repetition effects provides an independent confirmation of the validity of the fMEG procedure.

The fMEG technique allows activation waveforms to be estimated for each cortical location. These fMEG waveforms can be compared to the waveforms directly recorded from the same structures using iEEG in similar visual-verbal tasks [11, 12, 26]. This comparison reveals a remarkable correspondence between the fMEG and iEEG waveforms. The fMEG analysis of the response to novel vs. repeated stimuli showed two maxima, at about 385 and 540ms after stimulus onset, consistent with what would be expected in the same task for the N4 and LPC, respectively. Like the fMEG response, the repetition effect associated with the N4/LPC extends from about 250 to 650ms. The first fMEG peak was due to greater activity evoked by novel words, and the second was due to greater activity evoked by repeated words. Similarly, N4 amplitude declines and the LPC increases when a word is repeated. Finally, the fMEG locations of the repetition effects at 385 and 455ms are remarkably similar to each other, as has been previously noted for the generators of the N4 and LPC in iEEG recordings. The similarity in the location, timing and task-correlates of the major fMEG responses to those that had previously been described for iEEG provides strong support for the general validity of the fMEG technique.

In other studies, aMEG was used to locate the N4/LPC evoked by incongruous (compared to congruous) words at the ends of sentences, or to novel (compared to repeated) 3-letter word-stems that require completion. Although differences in the aMEG patterns between these tasks are seen, their spatiotemporal patterns are globally similar. All are centered in the anterior temporal and ventrolateral prefrontal cortices, in the 250-650ms period. Furthermore, all show initial activation in the temporal lobe, and all show a long period during which both areas are co-activated. Thus, the aMEG patterns that seem to correspond to previously described PET/fMRI activations in ventral temporo-frontal cortices, and to the N4/LPC in ERPs, are consistently observed across several visual-verbal tasks.

However, quite different aMEG patterns are evoked by other stimuli and tasks. For example, faces evoke a strong activation in the right fusiform gyrus at 180ms (Marinkovic et al., unpublished), corresponding closely in location to that found with PET/fMRI [50], and in timing with that found with iEEG [12]. At longer latencies, the aMEG patterns evoked by faces come to more closely resemble those described above for words, but lateralized to the right, unlike the words which evoked strongly left-lateralized activation. Similar ventral temporo-frontal activation to faces has been described with iEEG [11]. Yet another aMEG pattern is evoked by tactile stimuli, with initial activation in the pre- and post-central gyri, spreading into parietal association cortices when a perceptual judgement is demanded (Reed et al., unpublished).

In short, the spatiotemporal patterns produced by the aMEG and fMEG techniques are reasonable, given what we know already regarding the timing and location of brain processing of different verbal, facial and tactile stimuli. Furthermore, the aMEG/fMEG patterns have been confirmed in specific instances with intracranial recordings.

Conclusions

Spatiotemporal estimates of human brain activity during cognition can be constructed by combining fMRI (which has high spatial resolution) with EEG/MEG (which has high temporal resolution). This combination is justified because fMRI and EEG/MEG are thought to arise from the same ultimate cause: transsynaptic currents. However, for a variety of technical and physiological reasons, the signals recorded by these techniques may not always be generated by the same brain areas. Analytic strategies have been developed to make the hemodynamic/electromagnetic integration procedure robust to such dissociations. The results of these procedures have good face validity.

References

[1] Halgren, E., Evoked potentials. In A. A. Boulton, G. Baker and C. Vanderwolf, Neuromethods, Vol.15: Neurophysiological Techniques - Applications to Neural Systems, Clifton,N.J., Humana, 1990, pp. 147-275.

[2] Kwong, K.K., Belliveau, J.W., Chesler, D.A., Goldberg, I.E., Weisskoff, R.M., Poncelet, B.P., Kennedy, D.N., Hoppel, B.E., Cohen, M.S., Turner, R., Cheng, H.M., Brady, T.J. and Rosen, B.R., Dynamic magnetic resonance imaging of human brain activity during primary sensory stimulation, Proceedings of the

National Academy of Science, USA, 1992, 89: 5675-5679.
[3] Davis, T.L., Kwong, K.K., Weisskoff, R.M. and Rosen, B.R., Calibrated functional MRI: mapping the dynamics of oxidative metabolism, Proceedings of the National Academy of Sciences of the United States of America, 1998, 95: 1834-9.
[4] Buxton, R.B., Wong, E.C. and Frank, L.R., Dynamics of blood flow and oxygenation changes during brain activation: the balloon model, Magnetic Resonance in Medicine, 1998, 39: 855-64.
[5] Nicholson, C. and Freeman, J.A., Theory of current source density analysis and determination of the conductivity tensor for anuran cerebellum, Journal of Neurophysiology, 1975, 38: 356-368.
[6] Hämäläinen, M.S., Hari, R., Ilmoniemi, R.J., Knuutila, J. and Lounasmaa, O.V., Magnetoencephalography - theory, instrumentation, and applications to noninvasive studies of the working human brain, Reviews of Modern Physics, 1993, 65: 413-497.
[7] Liu, A.K., Belliveau, J.W. and Dale, A.M., Spatiotemporal imaging of human brain activity using fMRI constrained MEG data: Monte Carlo simulations, Proceedings of the National Academy of Sciences of the United States of America, 1998, 95: 8945-8950.
[8] Helmholtz, H., Ueber einige Gesetze der Vertheilung elektrischer Strome in korperlichen Leitern, mit Anwendung auf die thierisch-elektrischen Versuche, Ann. Phys. Chem., 1853, 89: 211-233, 353-377.
[9] Nunez, P.L., The brain's magnetic field: some effects of multiple sources on localization methods, Electroencephalography and Clinical Neurophysiology, 1986, 63: 75-82.
[10] Ary, J.P., Darcey, T.M. and Fender, D.H., Locating electrical sources in the human brain, IEEE Transactions on Biomedical Engineering, 1981, 28: 1-5.
[11] Halgren, E., Baudena, P., Heit, G., Clarke, J.M., Marinkovic, K. and Chauvel, P., Spatio-temporal stages in face and word processing. 2. Depth-recorded potentials in the human frontal and Rolandic cortices, Journal of Physiology (Paris), 1994, 88: 51-80.
[12] Halgren, E., Baudena, P., Heit, G., Clarke, J.M. and Marinkovic, K., Spatio-temporal stages in face and word processing. 1. Depth-recorded potentials in the human occipital, temporal and parietal lobes, Journal of Physiology (Paris), 1994, 88: 1-50.
[13] Halgren, E., Marinkovic, K. and Chauvel, P., Generators of the late cognitive potentials in auditory and visual oddball tasks, Electroencephalography and Clinical Neurophysiology, 1998, 106: 156-164.
[14] Dale, A.M. and Sereno, M.I., Improved localization of cortical activity by combining EEG and MEG with MRI cortical surface reconstruction: A linear approach, Journal of Cognitive Neuroscience, 1993, 5: 162-176.
[15] Hamalainen, M.S. and Ilmoniemi, R.J., Interpreting measured magnetic fields of the brain: Estimates of current distribution, Helsinki, University of Technology, Dept. of Technical Physics Report TKK-F-A559, 1984.
[16] Dale, A.M., Fischl, B. and Sereno, M.I., Cortical surface-based analysis I: Segmentation and surface reconstruction, NeuroImage, 1999, 9: 179-94.
[17] Fischl, B., Sereno, M.I. and Dale, A.M., Cortical surface-based analysis II: Inflation, flattening, a surface-based coordinate system, NeuroImage, 1999, 9: 195-207.
[18] Oostendorp, T.F. and Van Oosterom, A., Source parameter estimation using realistic geometry in bioelectricity and biomagnetism. In J. Nenonen, H. M. Rajala and T. Katila, Biomagnetic Localization and 3D Modeling, Helsinki, Helsinky Univ. of Technology, Rport TKK-F-A689, 1992.
[19] Fischl, B., Sereno, M.I., Tootell, R.B.H. and Dale, A.M., High-resolution inter-subject averaging and a coordinate system for the cortical surface, Human Brain Mapping, 1999, in press.
[20] Woolsey, T.A., Rovainen, C.M., Cox, S.B., Henegar, M.H., Liang, G.E., Liu, D., Moskalenko, Y., Sui, J. and Wei, L., Neuronal units linked to microvascular modules in cerebral cortex: Response elements for imaging the brain, Cerebral Cortex, 1996, 6: 647-660.
[21] Raichle, M.E., Circulatory and Metabolic Correlates of Brain Function in Normal Humans. In F. Plum, Handbook of Physiology. The Nervous System V, Higher Functions of the Brain, Bethesda, MD, Amer Physiol Soc, 1987, pp. 643-674.
[22] Halgren, E., Baudena, P., Clarke, J.M., Heit, G., Liégeois-Chauvel, C., Chauvel, P. and Musolino, A., Intracerebral potentials to rare target and distractor auditory and visual stimuli: 1. Superior temporal plane and parietal lobe, Electroencephalography and Clinical Neurophysiology, 1995, 94: 191-220.
[23] Halgren, E., Baudena, P., Clarke, J.M., Heit, G., Marinkovic, K., Devaux, B., Vignal, J.P. and Biraben, A., Intracerebral potentials to rare target and distractor auditory and visual stimuli: 2. Medial, lateral and posterior temporal lobe, Electroencephalography and Clinical Neurophysiology, 1995, 94: 229-250.
[24] Burock, M.A., Buckner, R.L., Woldorff, M.G., Rosen, B.R. and Dale, A.M., Randomized event-related experimental designs allow for extremely rapid presentation rates using functional MRI, Neuroreport, 1998, 9: 3735-9.
[25] Ojemann, J.G., Akbudak, E., Snyder, A.Z., McKinstry, R.C., Raichle, M.E. and Conturo, T.E., Anatomic localization and quantitative analysis of gradient refocused echo-planar fMRI susceptibility artifacts, NeuroImage, 1997, 6: 156-167.
[26] McCarthy, G., Nobre, A.C., Bentin, S. and Spencer, D.D., Language-related field potentials in the anterior-medial temporal lobe: I. Intracranial distribution and neural generators, Journal of Neuroscience, 1995, 15: 1080-9.
[27] Damasio, H., Grabowski, T.J., Tranel, D., Hichwa, R.D. and Damasio, A.R., A neural basis for lexical retrieval, Nature, 1996, 380: 499-505.
[28] Ackermann, R.F., Finch, D.M., Babb, T.L. and Engel, J., Jr., Increased glucose metabolism during long-duration recurrent inhibition of hippocampal py-

ramidal cells, Journal of Neuroscience, 1984, 4: 251-264.
[29] Nunez, P.L., Electric Fields of the Brain, New York, Oxford University , 1981.
[30] Steriade, M., Synchronized activities of coupled oscillators in the cerebral cortex and thalamus at different levels of vigilance, Cerebral Cortex, 1997, 7: 583-604.
[31] Sukov, W. and Barth, D.S., Three-dimensional analysis of spontaneous and thalamically evoked gamma oscillations in auditory cortex, Journal of Neurophysiology, 1998, 79: 2875-84.
[32] Chrobak, J.J. and Buzsaki, G., Gamma oscillations in the entorhinal cortex of the freely behaving rat, Journal of Neuroscience, 1998, 18: 388-98.
[33] Steriade, M. and Amzica, F., Slow sleep oscillation, rhythmic K-complexes, and their paroxysmal developments, Journal of Sleep Research, 1998, 7: 30-5.
[34] Maquet, P. and Phillips, C., Functional brain imaging of human sleep, Journal of Sleep Research, 1998, 7: 42-7.
[35] Hari, R., Salmelin, R., Makela, J., Salenius, S. and Helle, M., Magnetoencephalographic cortical rhythms., International Journal of Psychophysiology, 1997, 26: 51-62.
[36] Niedermeyer, E., Alpha rhythms as physiological and abnormal phenomena, International Journal of Psychophysiology, 1997, 26: 31-49.
[37] Gastaut, Étude électrocorticographique de la réactivité des rhythmes rolandiques., Revue Neurologique, 1952, 87: 176-182.
[38] Andersen, P. and Andersson, S.A., Physiological basis of the alpha rhythm, New York, Meredith Corp., 1968.
[39] Shulman, G.L., Buckner, R.L., Corbetta, M., Fiez, J.A., Miezin, F.M., Raichle, M.E. and Petersen, S.E., Common bloodflow changes across visual tasks. II. Decreases in cerebral cortex, Journal of Cognitive Neuroscience, 1997, in press.
[40] Klimesch, W., EEG-alpha rhythms and memory processes., International Journal of Psychophysiology, 1997, 26: 319-40.
[41] Pfurtscheller, G. and Aranibar, A., Evaluation of event-related desynchronization (ERD) preceding and following voluntary self-paced movement, Electroencephalography and Clinical Neurophysiology, 1979, 46: 138-46.
[42] Basar, B.a.L., Demiralp, T., Schurmann, M., Basar-Eroglu, C. and Ademoglu, A., Oscillatory brain dynamics, wavelet analysis, and cognition., Brain and Language, 1999, 66: 146-83.
[43] Klopp, J.C., Halgren, E., Marinkovic, K. and Nenov, V.I., Face-selective event-related spectral changes in the human fusiform gyrus, Clinical Neurophysiology, 1999, 110: 677-683.
[44] Bullock, T., McClune, M., Achimowicz, J., Iragui-Madoz, V., Duckrow, R. and Spencer, S., EEG coherence has structure in the millimeter domain: subdural and hippocampal recordings from epileptic patients., Electroencephalography and Clinical Neurophysiology, 1995, 95: 161-177.
[45] Klopp, J.C., Halgren, E., Marinkovic, K. and Nenov, V.I., Face specific wide-spread wide-band intracranial EEG coherence in humans, Society for Neuroscience Abstracts, 1998, 24: 1762.
[46] Benson, D.F., Aphasia, Alexia, and Agraphia, New York, Churchill Livingstone, 1979.
[47] Buckner, R.L. and Koutstaal, W., Functional neuroimaging studies of encoding, priming, and explicit memory retrieval, Proceedings of the National Academy of Sciences of the United States of America, 1998, 95: 891-8.
[48] Fiez, J.A. and Petersen, S.E., Neuroimaging studies of word reading, Proceedings of the National Academy of Sciences of the United States of America, 1998, 95: 914-921.
[49] Murray, E.A. and Bussey, T.J., Perceptual-mnemonic functions of the perirhinal cortex, Trends in Cognitive Sciences, 1999, 3: 142-151.
[50] Halgren, E., Dale, A.M., Sereno, M.I., Tootell, R.B.H., Marinkovic, K. and Rosen, B.R., Location of human face-selective cortex with respect to retinotopic areas, Human Brain Mapping, 1999, 7: 29-37.
[51] Gabrieli, J.D., Poldrack, R.A. and Desmond, J.E., The role of left prefrontal cortex in language and memory, Proceedings of the National Academy of Sciences of the United States of America, 1998, 95: 906-913.

Acknowledgements

Supported by USPHS NS18741 and HFSPO RG 25/96. Thanks to K. Marinkovic, C. Rabbel, P. Dhond, B. Fischl, C. Reed, R. Buckner and J.D. Lewine.

The Clinical Use of MEG Activity Associated with Brain Lesions

Vieth J.B., Kober H., Ganslandt O.[1)], Möller M.[1)], Kamada K.

Department of Experimental Neuropsychiatry and [1)]Clinic of Neurosurgery,
University of Erlangen-Nürnberg, Erlangen, Germany

Abstract

Brain lesions may influence their border zones by moving, compressing, infiltration, edema or by a mixture of all. Sources of evoked and spontaneous activity in border zones can be localized by magnetoencephalography (MEG) giving information on the function of these areas.
The inherent multisource problem of the MEG can be handled by using spatial average techniques (Dipole-Density-Plot (DDP) and Current-Density-Plot (CDP)). The reliability was tested with structural lesions (tumors and infarctions).
The localizing of the somatosensory, the motor, and the auditory cortex and the speech related areas in relation to adjacent tumors is established in our clinical routine. The MEG results will be fused into the neuronavigator for image guided neurosurgery. In two studies with subjcets and patients our MEG results have been compared to the results of the functional MRI (fMRI). In the presurgical evaluation of epileptic patients the localization of the epileptogenic lesion is an additional valuable tool, especially when the lesion is not visible in the MRI. In patients with multiple sclerosis we could demonstrate that the white matter lesions produce abnormal activity only in the adjacent neuronal areas. In the field of cerebrovascular accidents the penumbra can be localized in infarctions and TIAs. The feasibility to localize the penumbra by the MEG was demonstrated by our two comparisons of MEG results and those of the proton magnetic resonance spectroscopic imaging (^{1}H MRSI) of *N*-acetyl and lactate in patients with brain infarction and tumors.

Introduction

Brain lesions may alter the surrounding brain tissue structurally by either moving or compressing it, or by infiltration or edema or by a mixture of these. The function of these border zones might be impaired. Neurophysiological signs of this deficit might be lesional activity (focal slow and fast waves) and epileptic activity (focal spike or seizure activity). Therefore in clinical diagnostics it is of great interest to know the localization and the extent of focal sources of abnormal spontaneous activity in or around lesions.
But it is clinically also very important to know the location and the extent of the evoked and event related activity of functionally important areas around brain lesions, especially when the lesions should be removed surgically. Additionally it is of clinical interest to know whether the electrophysiological part of the function is still normal or not, and if a displacement of the area took place.
But electric or magnetic fields of brain activity not only originate from the sources of interest but also from those of the rest of the brain (background activity). Therefore in order to get reliable results the so called ”multisource problem” must be handled. So this paper gives also a short description how this problem can be solved, and in the main part shows clinical applications in neurosurgery and neurology with their present progress towards clinical relevance, partly compared to results of fMRI and ^{1}H MRSI of *N*-acetyl and lactate.

Methods

Biomagnetic recording and source localization:
From 1990 to 1994 we used the 37 channel system (Krenikon^R) of Siemens, Erlangen (planar recording surface of 20 cm in diameter), and since 1995 the 2x37 channel system (MAGNES II^R) of Biomagnetic Technologies Inc., San Diego, CA, USA, (curved recording surface with a 14 cm open diameter). The transfer of the coordinates from the head to the recording device and to the magnetic resonance imaging (MRI) data set was done with our surface fit (edge detection algorithm) of the electrically measured head surface (Isotrack^{TM} 3D-digitizer, Polhemus Navigation Sciences, Colchester, Vermont, USA) and the head surface which was reconstructed from the MR images. The error of the coordinate transfer is less than 2 mm. The advantages are: the electrical scanning is much easier to perform than using fiducial points and no MRI fiducial points are necessary at all. So any 3D-MRI (or CT, or PET or fMRI) scan can be used [22].
We used the sphere as the MEG volume conductor model, since it is sufficient in most cases [24,48]. Depending on the task we used either the single current dipole model or a current distribution solution. In order to apply the single current dipole in a more adequate way, the localization procedure will be done only on signal section with one component predominantly describing the signal. The principle component analysis (PCA) selects these sections out of the whole recording time of 10 minutes (typically only 1-2 %) [21].
The second approach will be used when extended or multiple sources must be assumed. We adjusted for our needs an approach which Robinson and Rose [35] first described. In our approach, the CLSF (Current Localization by Spatial Filtering), the analyzing space (a sphere) consists of 7000 voxels which is adjusted in size and location to the area of interest. The individual

current flow of each voxel will be obtained by applying a (spatial) filter on the signals measured at the surface of the skull showing the current intensity for individual time instants [11].

The multisource problem:
To reduce the background activity we use the alpha blocking effect during the recording (eyes open) and a kind of spatial averaging of the already localized sources, in order to show the spatial distribution of the activity over the recording time. This is possible, when the signal of interest is differing from the background by its focal nature, by its frequency band (slow or fast waves or epileptic activity) and by its time locked appearance (evoked responses or epileptic activity). For the dipole analysis we developed the Dipole-Density-Plot (DDP), a three dimensionally working convolution using a three dimensional Gaussian envelope, which takes into account the localization uncertainty [21,42,45]. For the current solution (CLSF) a similar technique was developed, the Current-Density-Plot (CDP) showing the current intensity over the analyzing time [14].
For details of comparing methods see for functional MRI in Stippich et al. [40], and Nimsky et al. [30], and for magnetic resonance spectroscopic imaging (^{1}H MRSI) in Kamada et al. [17].

Results and Discussion

In the last 10 years we were able to develop clinical applications with different progress towards clinical usefulness and relevance. The applications were validated by using structural lesions when applicable.

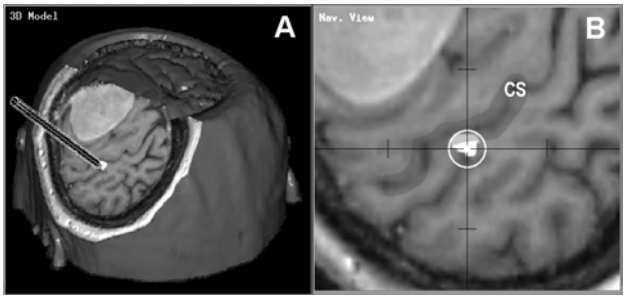

Figure 1: Single dipole MEG source localization of the postcentral gyrus using the somatosensory evoked field (SEF) at 50 ms after the tactile stimulus at the right index finger (200 samples averaged) of a 65 years old female patient (wwa) with a meningeoma. A: display of the neuronavigator showing in a tangential plane the tumor and the MEG SEF source and the intraoperatively used pointer instrument. B: enlarged section view of A, the central sulcus is marked by "CS" and the SEF source by a white encircled spot.

Evaluation with structural lesions:
We tested the reliability of the DDP and the CDP of spontaneous focal activity of structural brain lesions (tumors, infarctions) and their border zones, up to now in 91 cases with focal slow wave activity (2-6 Hz) and in 32 cases with fast wave activity (12.5-30 Hz) with the tendency of less cases of infarctions than of tumors. 19 cases of each group were additionally investigated using the magnetresonance-spectroscopy (see below). On the basis of our results we found the accuracy to localize the associated sources of the abnormal brain activity considerably high when the focal activity is present [16,17,21,42, 45], and we can be sure to localize at least the main portion of the area of the functionally impaired neuronal activity - with or without visible structural lesions in the MRI.
It should be stressed here, that our approaches (DDP, CLSF, and CDP) also can be used with the EEG provided that the EEG source localization is accurate enough.

Clinical applications:
Normal activity:
The clinical application to determine the relation of tumors to the cortical somato-sensory, motory, auditory and cortical speech areas was developed and established in Erlangen by the Department of Experimental Neuropsychiatry with the goal of acceptance in clinical environment. Now these approaches are routinely used by the Erlangen Clinic of Neurosurgery for operation planning and intraoperative functional neuronavigation [8]**.** This image guided neurosurgery is performed in a "twin operation room" with a Siemens Open-MRI (Magnetom Open) in one room and the movable operation table (into the Open-MRI) and the Zeiss microscope neuronavigation system (MKM) and the additional Stealth pointer neuronavigation system in the other room [38]**.** So an optimum of carefulness is possible during the operation with special reference to important eloquent brain areas in order to have less postoperational neurological deficits.

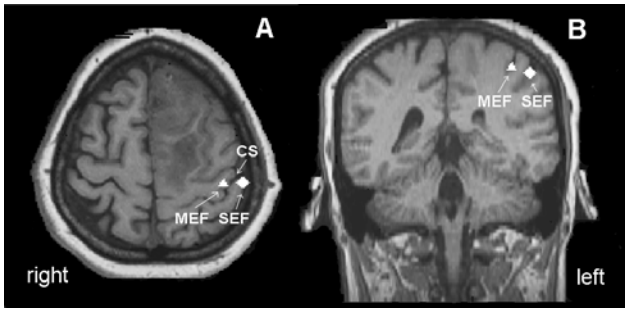

Figure 2: Single dipole MEG source localizations of the motor related source (MEF) in the precentral and of the somatosensory evoked field (SEF) in the postcentral gyrus of a 39 years old female patient with a left astrocytoma. SEF and MEF are marked respectively. The central sulcus is marked by CS in A. The SEF source was localized 50 ms after the tactile stimulus at the index finger (200 samples averaged). The MEF source was localized 100 ms after the movement onset (trigger by rectified surface electromyogram) of selfpaced brisk movements of the right index finger (100 samples averaged).

Evoked Responses: Gallen et al. [6,7] demonstrated first the clinical usefulness of this approach using somato-sensory evoked responses (SEF = somatosensory evoked field). Subsequently this technique was used by others [8,9,10,18,28,29,33]. A coupling of MEG results to the neuronavigator was first described by Watanabe et al. [47]. The interactive use of MEG in image guided neurosurgery was reported first by Rezai et al. [34].

Event related motor responses: Deecke et al. [5] reported first on a motor related MEG activity, the so called "Bereitschaftsfeld". Later also the localization of the motor induced activity was possible. More generally Lewine und Orrison [23] reported about this procedure. Our group developed for clinical usage in neurosurgery the clinical application to localize the cortical motor activity, which was induced by selfpaced finger movements (MEF = motor evoked field). The trigger signal was obtained from the rectified electromyogram of the corresponding muscles of the lower arm [8,20].

Event related speech responses: It also is possible to localize the cortical areas which are activated by speech recognition [37]. In our approach - similar to the WADA-Test [46] - we activate visually by written words and pictograms of monosyllabic concrete objects. The presentation was conducted via a glass fiber bundle from a television screen from outside the shielded room. If the term is also spoken internally the area of the speech induction (Broca's area) can be activated and localized too [12]. Also meaningless pictograms were presented in order to enhance the signals of the meaningful presentation by subtracting the signals of the meaningless presentation from that from the signals of the speech related presentation [14].

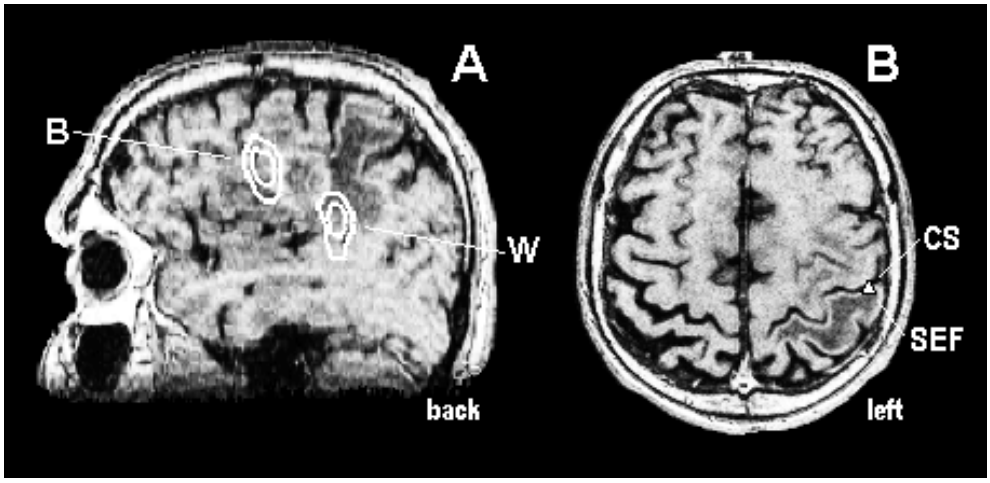

Figure 3: Speech related MEG source localizations in A and somatosensory evoked field (SEF) in B of a 69 years old male (jza) with a left temporo-parietal glioma. The speech responses were elicited by presenting pictograms of monosyllabic concrete objects for 800 ms on a television screen (conducted via a glass fiber bundle to the inside of the shielded room). 250 samples have been averaged and the CLSF (current density) of the of the response determined. Isocontour lines show the intensity of the CLSF results. The task was to recognize the object and internally speak the word of the object. The first response was at 340 ms after the onset of the presentation in the posterior part of the left superior temporal gyrus (Wernicke area) marked by W, and the second response was at 745 ms after the onset of the presentation in the left inferior frontal gyrus (Broca area) marked by B. The SEF source (marked by SEF) was localized 50 ms after the tactile stimulus at the index finger (200 samples averaged). The central sulcus is marked by CS

In right handed people the activity density was highest in the posterior part of the left superior temporal gyrus (Wernicke area) at around 350 ms and at around 500-600 ms (internal speaking) in the left inferior frontal gyrus (Broca area) but also some at the same time in the superior temporal gyrus [14]**.** This procedure even can be used to show differences of two differently written languages: a phonetic oriented language (German) and a language consisting of morphograms (*Kanji* characters of Japanese) [14].

Experiences in Erlangen: In our studies (up to Mai/1999) in the first group of 81 patients with temporal or frontal tumors we localized clinically successfully the somatosensory and the motor associated cortical responses.

In all patients the somatosensory activity has been localized and out of these in 33 cases the motor response. In all patients the projection of the magnetic single dipole localization on the brain surface of the postcentral gyrus was coinciding with intraoperatively evoked phase reversal of the potentials measured at the surface of the cortex, which was elicited by electric finger stimulation (only possible in 90% !) [c.f. 8,9,10,40]. 67 patients out of the 81 patients were operated by using the functional neuronavigation. 14 patients have not been operated on the basis of the MEG findings. An example of the localization of the somato-sensory evoked response in the postcentral gyrus in a patient with a meningeoma is shown in figure 1 with coupling of the result to the Stealth neuronavigator. Figure 2

shows an example of the localization of the motor related responses and the somato-sensory evoked responses in a patient with a left astrocytoma in the pre- and post-central gyrus respectively.
In the second group of 16 patients (14 right and 2 left handed) with brain tumors in the speech related cortical areas were localized by using the average version of the CLSF, the CDP.
Our approach was tested with 11 healthy subjects. The handedness was determined by the Edinburgh Handedness Inventory [31]. Our approach allowed to differ between the sensory and the motor speech areas (methods c.f. [14]). 12 out of 16 patients suffered from transient or permanent speech disturbances. In 15 patients the sensory area and in 12 patients also the motor area could be localized.
In order to determine the hemisphere with the larger activity MEG recordings were done simultaneously on both sides. Our current density approach showed a two to four times larger activity on one side, sometimes up to eight times larger. All patients (right and left handed) had their higher activity on the left side [26,27]. The WADA-test [46] confirmed in three cases the hemisphere with the higher intensity on the left side also in one left handed patient.
Because of its invasiveness the WADA-test was applied restrictively. Up to now 3 patients out of the 16 patients were operated by using the functional neuronavigation. 3 patients have not been operated on the basis of the MEG findings [25,27]. Figure 3 shows an example of the localization of the speech areas and the somato-sensory evoked responses in a patient with a left temporo-parietal glioma.

MEG and functional MRI (fMRI):
Since 1991 [2] the functional magnetic resonance imaging (fMRI) is used to localize three dimensionally the local oxygen tissue deficit elicited by evoked or event related brain activity. The effect is called the "blood oxygenation level dependent contrast (BOLD)". There are some fundamental differences between both approaches, which can be the reason of misinterpretation:

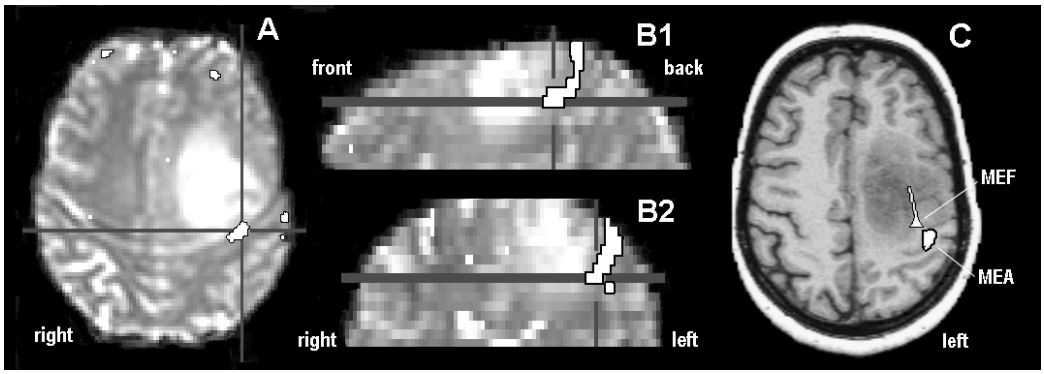

Figure 4: Localization of motor related responses in functional MRI (fMRI) in A, B (T2), and C (T1) and of the somatosensory magnetic evoked field (SEF) in B in a 32 years old female (gdb) with a left astrocytoma suffering from a light motor deficit of the right hand. fMRI was measured using a T2-weighted EPI sequence. The recording consisted of three activation (iterative right fist clenching) and three baseline (rest) periods with 10 EPI volumes data sets for each period. Functional activation maps were obtained using a cross correlation coefficient of the measured and the expected activation higher than 0.7. A: axial view, B1: sagittal view, B2 coronal view of the fMRI motor activity (MEA) BOLD (blood oxygenation level dependent contrast) effect. C: axial view showing MEA and the MEG single dipole source localization (MEF). The MEF was localized 100 ms after the movement onset (trigger by rectified surface electromyogram) of selfpaced brisk movements of the right index finger (100 samples averaged). The MEF was localized on the edge of the tumor (light motor deficit of the right hand) in the precentral gyrus. The MEA was found in the central sulcus (venous drainage), especially visible in B1 and B2.*

(1) The signal to noise ratio is in MEG source imaging (MSI) much higher than in fMRI. (2) In fMRI always a base line recording is necessary. (3) On the basis of this fact movements in fMRI can produce a lot of new (artifact) sources. In MSI only the sources will loose sharpness. (4) In MSI the neuronal areas will be localized. In fMRI the drainage section of the venous branch shows oxygen deficits as already demonstrated by Segebarth et al. [36]. So the interpretation of the fMRI findings should be done with general caution [36]. Up to now no procedure was published to get around this situation. (5) In fMRI the time resolution depends on the diffusion time of desoxyhemoglobin, which is in the order of seconds. In MSI the time resolution depends on the electric properties of the tissue and the recording equipment, so it is in the order of one millisecond or less.
In two comparing studies with 6 subjects [40] and 15 patients [30] we found the localization of evoked cortical responses obtained by MEG and fMRI typically dislocated by around 1 cm, showing the consequence of the two different aspects of the techniques: the measuring of the electric neuronal activity (MSI) and the measuring of venous drainage induced by neuronal

activity (fMRI) (c.f [36]). Figure 4 shows an example of the comparison of the localization of the motor related MEG response and the motor related fMRI response.

Clinical applications:
Abnormal activity:
Epileptogenic lesion: One valuable application of localizing abnormal activity is in the field of the presurgical evaluation of epileptic patients: Normally the epileptogenic zone is removed to cure the epilepsy. But results with structural lesions show that the removal of the epileptogenic lesion (assumed to be the original cause of a seizure disorder) is also important for the clinical outcome [1,4]. Thus the localization of the epileptogenic lesion is of great interest. In addition it is very easy to record the spontaneous interictal activity associated with epileptogenic lesions. Neither a spike nor a seizure must be catched.
Up to now only two other groups and our group demonstrated, that the spontaneous slow wave activity can be used to localize the epileptogenic lesion of focal epilepsies, which are associated either with or without structural lesions [7,23,43,44].
In our study we had one group of epileptic patients withstructural lesions as the reason of the epilepsy, and the second group without any visible structural lesion. In the first group in the border zone of the tumors we got a strong coincidence of the MSI localizations of the three different spontaneous signal components: (1) interictal epileptic spikes, (2) slow wave activity, (3) fast wave activity. For source enhancement both the DDP and the CDP have been used. Occasionally occurring spike/wave complexes have been discarded, when slow and fast wave activity was analyzed. An example is shown in figure 5**,** which also very nicely shows the shell like distribution of the slow and fast wave sources around the tumor. The same coincidence of the results in all six approaches also was found in epileptic patients without any visible structural lesion [41,43,44].

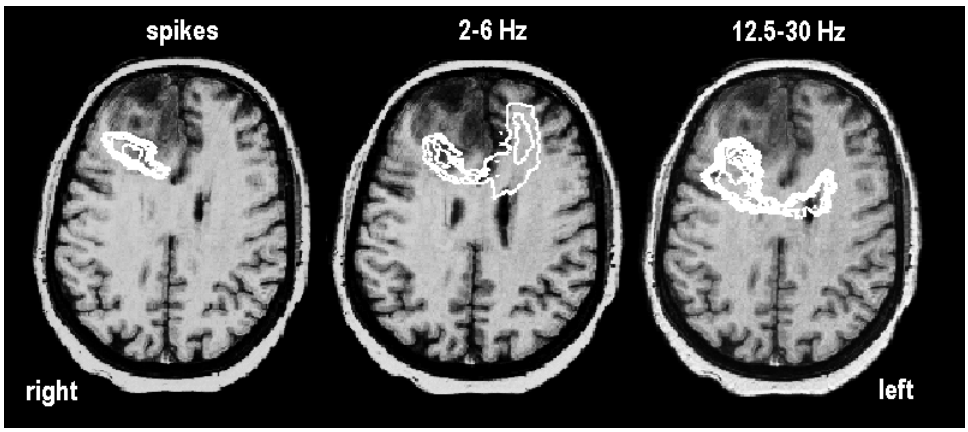

Figure 5: MEG source localization of focal abnormal spontaneous interictal activity in the border zone of a right frontal astrocytoma of a 67 years old female patient (ida) with grand mal epileptic seizures. The averaging version of the CLSF, the Current-Density-Plot (CDP) was used to localize the current density during the whole recording time of 10 minutes. A: spikes, B: slow (2-6 Hz) and C: fast (12.5-30 Hz) wave activities. B and C without spike and wave activity. Especially in B and C the shell like abnormal activity can be seen.

Focal abnormal lesional activity even could be found associated with the (focal) Rolandic epilepsy of children [17]. Thus we demonstrated that even in these cases an epileptogenic lesion may be present, in spite of, that "per definitionem" no structural lesion is associated with this disease. So our approach to localize the epileptogenic lesion seems to be a valuable additional tool or maybe in some cases an alternative in the presurgical evaluation of epileptogenic patients, when no structural lesion is visible in the MRI. It is worthwhile to test in multicenter studies the value of this approach compared to the localization of interictal spikes and of the epileptogenic zone.
White matter lesions: The sources of the MEG are mainly the longitudinal flowing currents inside the neurons, which are generated at the synapses, the postsynaptic potentials [32]. Therefore lesions in the fiber section of the neurons (white matter) should have no significant contribution to the normal and abnormal electric activity of the brain. Since the multiple sclerosis (MS) is a disease, which mainly destroys the myelin sheath of the neuronal fibers, and gives a contrast in the MRI in the white matter, we wanted to know if these fiber lesions produce abnormal activity at all, and if it is present where the activity comes from.
In our study we included 8 patients suffering from MS and a baseline group of 8 healthy subjects. The two groups got the same recording protocol. The spatial dipole distribution was quantified and compared between the groups statistically. In all MS patients the maximum of focal abnormal slow and fast wave activity was found in cortical (neuronal) areas adjacent to the fiber lesions, whereas in the healthy subjects no focal abnormal brain activity could be found [19]. These results let assume that if subcortical fiber lesions may occur together with abnormal cortical neuronal activity, it might be difficult to differ the location of the lesion, which is responsible for the abnormal cortical activity, unless other informations are available.

Cerebrovascular accidents: Cerebrovascular accidents account for around a quarter of the total mortality and the bulk rate of the disabled people. Therefore it would be of great value to have diagnostic measures for an early detection of prestages.
In our studies we found that the MEG is able to localize not only the disturbed function around a structural brain lesion (infarction) but also that of an area with only functional - maybe reversible - impairment. These can be transient ischemic attacks (TIA) or lesions too small to be detected by the standard MRI resolution. Up to now we localized not only the pathological activity associated with brain infarctions in 23 patients, but also the activity associated with the penumbra of transient ischemic attacks (TIA) [17,42,45] in 21 cases.

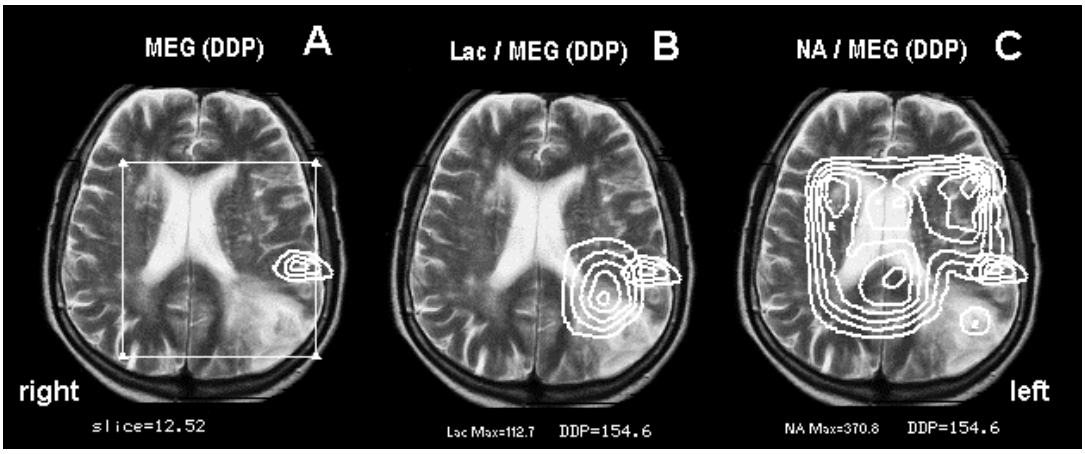

Figure 6: Dipole-Density-Plot (DDP) MEG source localization of focal abnormal spontaneous slow wave (2-6 Hz) activity during the recording time of 10 minutes in the border zone of a left brain infarction of a 60 years old male patient (kfa) in A, B and C. Additional overlay of a separately recorded proton magnetic resonance spectroscopic imaging (^{1}H MRSI) signals of lactate (Lac) in B and of N-acetyl (NA) in C. Field of view (FOV) 200x200 mm, marked in A by a white line and seen in C by the outer limit of the NA activity; 16x16 phase encoding; nominal in-plane resolution: 12.5 mm, point resolved spectroscopy (PRESS); TR: 1500 ms; TE 135 and 270 ms. For details see [17].

Thus we are also able to localize clinically silent reversible ischemic brain deficits in accordance to silent brain infarcts [3]. This finding is clinically important for the decision, whether an extracranial stenosis of the internal carotid artery is to be assumed symptomatic or not, and in the case of a symptomatic stenosis for an indication of an endarterectomy [47]. The feasibility to localize the penumbra of infarctions is also very important, when new therapeutic approaches are available that prevent neurons to be damaged irreversibly.
Brain functions and metabolism: Another support, that our approaches are able to localize the penumbra comes from the two following studies:
In order to show the feasibility of the MEG to localize brain areas of impaired activity as the penumbra or edema zones we studied the relationship between electric brain functions and metabolic brain functions in patients with brain infarcts and brain tumors, using the MEG and the proton magnetic resonance spectroscopic imaging (^{1}H MRSI).
In the first study we investigated 12 patients with brain infarction in comparison to 12 normal cases, showing the MEG slow wave dipole density (DDP) in the border zone of the infarction and the signal intensity of *N*-acetyl (NA) and the lactate (Lac) inside the infarction, in the border zone, and in normal tissue, where NA is a measure for normal function of the brain. The signal intensity of NA was significantly reduced in the regions with the highest slow wave activity but was well correlated interindividually with the dipole density (DDP) of the quantified maximum of slow waves. Though Lac was mildly accumulated in the lesions, the Lac level had no correlation with slow wave magnetic activity. We could assume, that preserved and metabolically active tissue with NA signal produced the abnormal slow wave activity under lactic acidosis (mild accumulation of Lac).

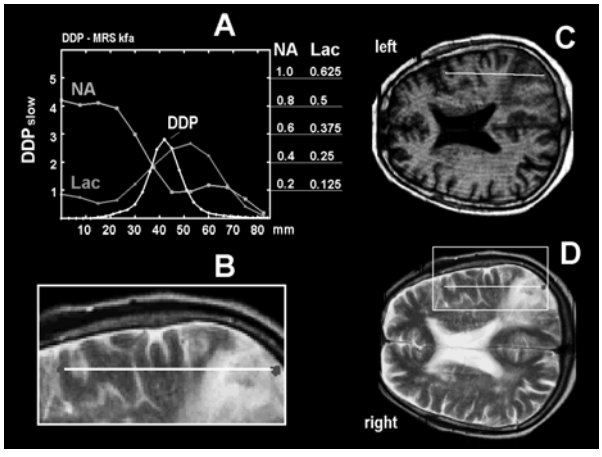

Figure 7: Intensity of abnormal spontaneous slow wave (2-6 Hz) activity, lactate (Lac) ^{1}H MRSI activity, and N-acetyl (NA) ^{1}H MRSI activity of the same patient (kfa) as in figure 6 with a left brain infarct along a line drawn from normal tissue through the bulk of the brain infarct. Same recording protocol as in figure 6. C: line seen in a T1 image; D: line seen in a T2 image en-

closed by a white rectangular line showing the enlarged area in B, where the line is in direct spatial relation to the four different activities (in A) for comparison. A relative far away start of the decrease of NA and the increase of Lac appears in the border zone of the infarct (3.5 to 4 cm apart from the visible limit of the infarct). Abnormal slow wave activity also starts that far, coming to a peak 2 cm apart from the infarct limit. Then steadily the slow wave activity decreases to zero until the limit of the infarct. The neurons beyond this limit are not able even to produce slow waves. They have no measurable electric activity.

Figure 6 shows the spatial distribution of the intensities of the abnormal slow waves, the Lac and the NA activities in a patient with a brain infarct. Figure 7 shows an example of the same patient with the topographic development of the three activities along a line from normal to pathological tissue. It appears that all three distributions start with abnormal values relatively far away from the infarct, typically 3 cm or more. From the results of the study we could assume, that the MEG quantified slow wave sources give an indication whether a penumbra is present at all, and where it is localized [17]. The clinical importance is also in the field to prevent neurons to be damaged irreversibly.

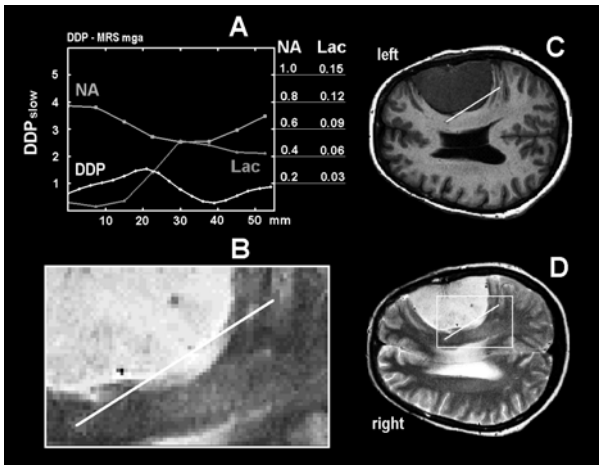

Figure 8: Intensity of abnormal spontaneous slow wave (2-6 Hz) activity, lactate (Lac) ^{1}H MRSI activity, and of N-acetyl (NA) ^{1}H MRSI activity of a 53 years old female with a left meningeoma along a line drawn from normal tissue through one pole of the tumor to normal tissue again. Same recording protocol as in figure 6 and 7. C: line seen in a T1 image; D: line seen in a T2 image enclosed by a white rectangular line showing the enlarged area in B, where the line is in direct spatial relation to the four different activities for comparison. Na is decreasing from normal tissue to the tumor tissue and increasing to normal tissue again. Lac is increasing mildly (compared to infarcts) from normal tissue to the tumor tissue and does not reach the baseline in tissue outside the visible tumor on the other side. The slow wave activity has two peaks in both border zones of the tumor corresponding to the assumption that inside the tumor are no neurons to produce electric activity.

The second study was performed on 7 patients with common brain tumors (i.e. astrocytic tumor and menigeoma) compared to a group of 10 healthy subjects. The recording protocol of MEG and ^{1}H MRSI was in both groups the same as in the previous study. Increased slow, fast waves activities and spikes were observed in the neuronal area adjacent to the bulk of the tumor with a mild reduction of NA and a slight accumulation of Lac. Lac intensity was less pronounced than in the study with the infarcts.
The bulk of the tumors was magnetically silent. The extension of the tumor border zone seems to depend on the invasiveness of the tumor, but it seems to be smaller than that of the infarcts, typically about 2 cm. Figure 8 shows an example of the intensity of the three activities along a line from normal tissue through the tumor and back to normal tissue. The clinical importance may be the early detection of prestages of a tumor by MEG. Details in Kamada et al. [16].

Conclusions

In our work we could demonstrate: the localization of the function of eloquent cortical areas is well established in neurosurgery. The localization of the epileptogenic lesion is a very promising tool in the presurgical investigation of epileptic patients. The penumbra of transient ischemic attacks (TIA), of infarcts and of tumors can be localized. A possible screening for asymptomatic "TIA" (reversible neuronal deficit) might also be a promising tool in the prevention of strokes.

References

[1] Awad, I.A., Rosenfeld, J., Ahl, J., Hahn, J.F., and Lüders, H. Intractable epilepsy and structural lesions of the brain: Mapping, resection, strategies, and seizure outcome, Epilepsia, 1991, 32: 179-186.

[2] Belliveau, J.W., Kennedy, D.N. Jr., McKinstry, R.C., Buchbinder, B.R., Weisskoff, R.M., Cohen, M.S., Vevea, J.M., Brady, T.J., and Rosen,B.R. Functional mapping of the human visual cortex by magnetic resonance imaging, Science, 1991, 254: 716-719.

[3] Caplan, L.R. Silent brain infarcts, Cerebrovasc Dis 1994, 4 (Suppl 1): 32-40.

[4] Cascino, G.D., Kelly, P.J., Sharbrough, F.W., Hulihan, J.F., Hirschorn, K.A., Trenerry, M.R. Longterm followup of stereotactic lesionectomy in partial epilepsy: Predictive factors and electroencephalographic results, Epilepsia, 1992, 33: 639-644.

[5] Deecke, L., Weinberg, P. and Brickett,P. Magnetic fields of the human brain accompanying voluntary movement: Bereitschaftsmagnetfeld, Exp. Brain Research, 1982, 48: 144-148.

[6] Gallen, C.C., Sobel, D.F., Waltz, T., Aung, M., Copeland, B., Schwartz, B.J., Hirschkoff, E.C. and Bloom, F.E. Noninvasive presurgical neuromagnetic mapping of somatosensory cortex, Neurosurgery, 1993, 33: 260-268.

[7] Gallen, C.C., Tecoma,E., Iragui, V., Sobel, D.F., Schwartz, BJ and Bloom, F.E. Magnetic source imaging of abnormal low-frequency magnetic activity in presurgical evaluations of epilepsy, Epilepsia, 1997, 38: 452-460.

[8] Ganslandt, O., Fahlbusch, R., Nimsky, C., Kober, H., Möller,M., Steinmeier, R., Romstöck, J. and Vieth, J. Functional neuronavigation with magnetoencephalography: outcome in 50 patients with lesions around the motor cortex. Neurosurgical Focus 6(3): Article 3, 1999; and Neurosurgery (in press).

[9] Ganslandt, O., Steinmeier, R., Kober, H., Vieth, J., Kassubek, J., Romstöck, J., Strauss, C., and Fahlbusch, R. Magnetic source imaging combined with image guided, frameless stereotaxy: a new method in surgery around the motor strip, Neurosurgery, 1997, 41: 621-627.

[10]Ganslandt,O., Ulbricht,D., Kober,H., Vieth,J., Strauss,C. und Fahlbusch,R. SEF-MEG localization of somatosensory cortex as a method for presurgical assessment of functional brain area. Electroenceph Clin Neurophysiol, 1996, 46(Suppl.): 209-213.

[11]Grummich, P., Kober, H., and Vieth J. Localization of the underlying currents of magnetic brain activity using spatial filtering. Biomed Engineer (Berlin), 1992, 37 (Suppl 2): 158-159.

[12]Grummich, P., Kober, H., Vieth, J., Matschke, J. and Ganslandt, O. Sensory speech area investigated by magnetoencephalography, Biomed. Engineer. (Berlin), 1994, 39(Suppl): 129-130.

[13]Grummich P, Vieth J, Kober H, Pongratz H, Ulbricht D, Ganslandt O. Localization of focal spontaneous beta wave activity associated with structural lesions in the brain. In: Baumgartner, C., Deecke, L., Stroink,G., Williamson, S.J. Biomagnetism: Fundamental Research and Clinical Applications, Elsevier Science IOS Press, 1995, pp 75-79.

[14]Kamada, K., Kober, H., Saguer, M., Möller, M., Kaltenhäuer, M. and Vieth,J. Responses to silent *kanji* reading of the native japanese and german in task subtraction magnetoencephalography. Cognitive Brain Res, 1998, 7: 89-98.

[15]Kamada, K., Möller, M., Saguer, M., Kassubek, J., Kaltenhäuser, M., Kober, H., Überall, M., Lauffer, H., Wenzel, D. and Vieth, J. Localization analysis of neuronal activities in benign rolandic epilepsy using magnetoencephalography, J. Neurological Sciences, 1998, 154: 164-172.

[16]Kamada, K., Möller, M., Saguer, M., Ganslandt, O. Kaltenhäuser, M., Kober, H., and Vieth, J. A combined study of tumor-related brain lesions using magnetoencephalography and proton MR spectroscopic imaging. Neurosurgery (submitted for publication).

[17]Kamada, K., Saguer, M., Möller, M., Wicklow, K., Kaltenhäuser, M., Kober, H. and Vieth,J. Functional and metabolic analysis of cerebral ischemia using magnetoencephalography and proton magnetic resonance spectroscopy. Annals of Neurology, 1997, 42: 554-563.

[18]Kamada, K., Takeuchi, F., Kuriki, S., Oshiro, O., Houkin, K., and Abe, H. Functional Neurosurgical Stimulation with Brain Surface Magnetic Resonance Images and Magnetoencephalography, Neurosurgery, 1993, 33: 269-273.

[19]Kassubek, J., Sörös, P., Kober, H., Stippich, C., and Vieth, J. Focal slow and beta wave activity in patients with multiple sclerosis revealed by magnetoencephalography, Brain Topography, 1999 11: 193-200.

[20]Kassubek, J., Stippich, P., Sörös, P., Ganslandt, O., Kamada, K., Hopfengärtner, R., Kober, H., Steinmeier, R and, Vieth, J.B. A motor field source localization protocol using magnetoencephalography, Biomed. Engineer. (Berlin), 1996, 41(Suppl. 1): 334-335.

[21]Kober, H., Vieth, J., Grummich, P., Daun, A., Weise, E., and Pongratz, H. The factor analysis used to improve the dipole-density-plot (DDP) to localize focal concentrations of spontaneous magnetic brain activity. Biomed Engineer (Berlin), 1992, 37 (Suppl 2): 164-165.

[22]Kober, H., Grummich, P., and Vieth, J. Fit of the digitized headsurface with the surface reconstructed from MRI-Tomography. In: Baumgartner, C., Deecke, L., Stroink,G., Williamson, S.J. Biomagnetism: Fundamental Research and Clinical Applications, Elsevier Science IOS Press, 1995, pp 309-312.

[23]Lewine, J.D. and Orrison, W.W. Magnetoencephalography and magnetic source imaging. Functional Brain Imaging, Mosby Year Book Inc., 1995, pp 369-417.

[24]Meijs, J.W.H., Bosch, F.G.C., Peters, M.J., and Lopes Da Silva, F.H. On the magnetic field distribution generated by a dipolar current source situated in a realistically shaped compartment model of the head. Electroenceph clin Neurophysiol, 1987, 66: 268-298.

[25]Möller, M., Kober, H., Ganslandt, O., Nimsky, C., and Fahlbusch, R. Presurgical localization of the motor and sensory speech area in brain tumor patients by magnetoencephalography, Zentralbl Neurochir, 1999(Suppl), 20.

[26]Möller, M., Kober, H., Ganslandt, O., Nimsky, Ch., and Fahlbusch, R. Magnetoencephalographic investigation of speech evoked magnetic fields and their

hemispheric dominance, Zentralbl Neurochir, 1999(Suppl), 21.

[27]Möller, M., Kober, H., Ganslandt, O., Nimsky, Ch., and Fahlbusch, R. Functional mapping of speech evoked brain activity by magnetoencephalography and its clinical application, Proceedings of this symposium, Biomed. Engineer, 1999, this symposium.

[28]Morioka, T., Yamamoto, T., Katsuta, T., Fujii, K., and Fukui, M. Presurgical Three-Dimensional Magnetic Source Imaging of the Somatosensory Cortex in a Patient with a peri-Rolandic Lesion: Technical Note, Neurosurgery, 1994, 34: 930-934.

[29]Nakasato, N., Seki, K., Kawamura, T., Ohtomo, S., Kanno, A., Fujita, S., Hatanaka, K., Fujiwara, S., Kayama, T., Takahashi, A., Jokura, H., Kumabe ,T., Ikeda, H., Mizoi, K. and Yoshimoto,T. Cortical mapping using an MRI-linked whole head MEG system and presurgical decision making, Electroencephalogr Clin Neurophysiol, 1996, 47(Suppl): 333-341.

[30]Nimsky, C., Ganslandt, O., Kober, K., Möller, M. Ulmer, S., Tomandl, B., Fahlbusch, R. Integration of Functional Magnetic Resonance Imaging Supported by Magnetoencephalography in Functional Neuronavigation, Neurosurgery, 1999, 44: 1249-1256.

[31]Oldfield, E.C. The assessment and analysis of handedness: the Edinburgh inventory, Neuropsychologia, 1971, 9: 97-113.

[32]Okada, Y.C., and Kyuhou,S. Genesis of MEG signals in mammalian CNS structure, Electroenceph Clin Neurophysiol, 1997, 103: 474-485.

[33]Orrison, W.W.Jr., Douglas, F.R., Blaine, L.H., Edward, L.M., Sanders, J.A., Willis, B.K., Marchand, E.P., Wood, C.C., and Davis ,L.E. Noninvasive Preoperative Cortical Localization by Magnetic Source Imaging, A J N R, 1992, 13: 1124-1128.

[34]Rezai, A.R., Hund, M., Kronberg, E., Zonenshayn, M., Cappell, J., Ribary, U., Kall, B., Llinas, R., and Kelly, P,J. The Interactive Use of Magnetoencephalography in Stereotactic Image-guided Neurosurgery, Neurosurgery, 1996, 39: 92-102.

[35]Robinson, S.E., and Rose, D.F. Current source image estimation by spatially filterered MEG. In: Hoke, M., Erné, S.N., Okada, Y.C., Romani, G.L. Biomagnetism. Clinical Aspects, 1992, pp 761-765.

[36]Segebarth, C., Belle, V., Delon, C., Masarelli, R., Decety, J., Le Bas, J.-F., Décorps, M., and Benabid, A.L. Functional MRI of the human brain: predominance of signals from extracerebral veins, Neuroreport, 1994, 5: 813-816.

[37]Simos, P.G., Breier, J.I., Zouridakis, G. und Papanicolaou, A.C. Identification of language-specific brain activity using magnetoencephalography, J Clin Exp Neuropsychol, 1998, 20: 706-722.

[38]Steinmeier, R., Fahlbusch, R., Ganslandt, O., Nimsky, C., Buchfelder, M., Kaus, M., Heigl, T., Lenz, G., Kuth, R., and Huk, W. Intraoperative magnetic resonance imaging with magnetom open scanner: concepts neurosurgical indications, and procedures: a preliminary report, Neurosurgery, 1998, 43: 739-748.

[39]Stippich, C., Freitag, P., Kassubek, J., Sörös, P., Kober, H., Scheffler, K., Hopfengärtner, R., Kamada, K., Bilecen, D., Radü, E.W., and Vieth, J.B. Motor, somatosensory and auditory cortex localization by fMRI and MEG, Neuroreport, 1998, 9: 1953-1957.

[40]Stippich, C., Kassubek, P., Sörös, P., Ganslandt, O., Kamada, K., Kober, H., Hopfengärtner, R., Steinmeier, R. and Vieth, J.B. Precise pre- and intraoperative assessment of functional cortex by-magnetoencephalography (MEG), Biomed. Engineer., 1996, (Berlin) 41(Suppl. 1): 306-307.

[41]Vieth, J., Grummich, P., Kober, H., Ulbricht, D., Fenwick, P.B.C., and Claus, D. Localization of slow and beta wave MEG waves associated with epileptogenic lesions. Epilepsia, 1993, 34:123.

[42]Vieth, J.B., Kober, H., and Grummich, P. Sources of spontaneous slow waves associated with brain lesions, localized by using the MEG. Brain Topography, 1996, 8: 215-221.

[43]Vieth, J., Kober, H., Grummich, P., Ulbricht, D., Brigel, C., Claus, D., and Fenwick, P.B.C. Localization of the epileptogenic lesion by focal slow and beta wave MEG activity, Biomed. Engineer. (Berlin), 1994, 39(Suppl): 133-134.

[44]Vieth, J.B., Kober, H., Kamada, K. and Ganslandt, O. Normal and abnormal MEG activity in border zones of brain lesions, In: Koga, Y., Nagata K., and Hirata, K. Brain Topography Today, Excerpta Medica, International Congress Series 1147, Elsevier, Amsterdam, Lausanne, New York, Oxford, Shannon, Singapore, Tokyo, 1998, pp 39-46.

[45]Vieth, J., Kober, H., Weise, E., Daun, H., Moeger, A., Friedrich, S., and Pongratz, H. Functional 3D localization of cerebrovascular accidents by magnetoencephalography (MEG). Neurol Res, 1992, 14: 132-134.

[46]Wada, J., and Rasmussen, T. Intracarotis injection of sodium amytal for the lateralization of cerebral speech dominance: Experimental and clinical observations, J. Neurosurg., 1960, 17: 266-282.

[47]Watanabe, E., Mayanagi, Y. and Kaneko, Y. Identification of the central sulcus using magnetoencephalography and neuronavigator, No To Shinkei, 1993, 45: 1027-1032.

Zanow, F. Realistically shaped models of the head and their applications to the EEG and MEG. PhD Thesis, University of Twente, The Netherlands, 1997, pp 144.

Applications of MEG to the Mapping of the Language Cortex

Papanicolaou, A.C.,[1] Simos, P.,[1] Breier, J.I.,[1] Zouridakis, G.,[1] Constantinou, J.,[2] Wheless, J.W.,[2] Maggio, W.W.[1]

The University of Texas Health Science Center
Departments of Neurosurgery[1] and Neurology[2], Houston, Texas U.S.A.

Introduction

In the past two years we have developed Magnetoencephalographic (MEG) procedures for mapping the receptive language cortex in normal subjects, epileptic patients who are also undergoing the WADA procedure, other neurosurgical patients who are also undergoing intraoperative electrocortical stimulation mapping, as well as dyslexic children. The purpose of this presentation is to describe briefly, (a) the normative studies that lead to the development of these procedures (b) their application in determining hemispheric dominance for speech in epileptic patients (c) their application in presurgical mapping and precise localization of receptive language areas within the dominant hemisphere and (d) their use in disclosing brain activation profiles unique to dyslexic children.

The normative studies were conducted in order to accomplish the following specific goals: (1) To obtain clear brain activation profiles or maps from individual subjects and circumvent the usual practice of using average maps of activity projected onto averaged brain scans. (2) To establish the stability of the language-specific brain maps over time for each individual subject or patient. (3) To ascertain that the maps are specific to language and not to some other cognitive function. (4) To establish the validity of the maps in terms of their agreement with expectations based on prior and independent knowledge about the location of the language areas in the brain and (5) To refine the procedures such that the maps can be derived easily and quickly, so that they would not present difficulties to and compromise the cooperation of prospective subjects, especially cognitively impaired patients and children with behavioral disorders.

Following successful completion at these studies, the procedures were used with epileptic patients for determining their hemispheric dominance for language. The purpose of that project was (and remains) to test the validity of the MEG mapping procedures by comparing their results with those of the WADA procedure and thus establish the equivalence of the two methods.

In parallel, the procedures were (and are) used for presurgical mapping of the precise language regions within the dominant hemisphere for the purpose of establishing once more, the validity of their results by comparing them with those of intraoperative stimulation mapping, for determining the accuracy and spatial resolution of the maps and for exploring the possibility of their routine clinical use. Preliminary results of both the normative studies and the above-mentioned clinical applications were summarized in a recent paper. [1]

Finally, and equally successfully, the procedures were used with dyslexic children for the purpose of exploring the possibility that there is a brain activation profile associated with the function of reading which is specific to such children and may shed some light on the cerebral correlates of dyslexia.

Methods

In all studies to be described below the methods were essentially identical. All MEG recordings were made with a 148 channel BTI system. During the recording sessions the subject or patient was exposed to a series of stimuli (whether verbal or non-verbal) delivered either visually or auditorily, and their task was to attend to each stimulus in the series and indicate, by slightly moving their index finger, if the stimulus (a word, a tone or a picture of a face, depending on the particular experiment) had been presented before, within the same series. Visual presentation of stimuli was accomplished by a projection system situated outside the chamber and a system of mirrors, and auditory presentation was done by Macintosh Powerbook, and a pair or plastic tubes terminating in ear-inserts. Each individual simulus in a particular series (whether visual, auditory, verbal or non-verbal) produced an Evoked Field (EF). These were averaged together after the end of the recording session. The resulting average EFs, in all cases, consisted of early (30-150 ms post-stimulus) and late (150-700 ms post-stimulus) components.

To identify the intracranial sources of both components, the magnetic field distribution recorded during the evolution of each, was analyzed at successive points (4ms apart) using the single-dipole-in-a sphere model. In all cases, the sources of the early components were located in the auditory and visual cortex, as expected. Those of the late components were localized in what turned out to be the language-specific areas. The degree of activation of each of these areas (or the

total duration of their activation), was estimated by the total number of successive dipoles localized in it.

Results and Discussion

(a) Normative Studies

The first two experiments were conducted to demonstrate that valid maps can be obtained using the methods described above. Namely, maps that show a much greater degree of activation of the left posterior temporal-parietal region than the right in nearly all normal right handed subjects, and that such maps are unique to the linguistic task, by showing that comparable non-linguistic tasks result in quite different maps in the same subjects.

The first experiment [2] involved fifteen subjects who were given a series of aurally presented words (language condition) and a series of tones of comparable loudness and duration (auditory control condition). In both conditions the subject's tasks were to identify target words (or tones). The results of this experiment showed that brain activation maps based on number of sources of the late EF components to words do conform to expectation based on prior knowledge in that they reveal, in the majority of the subjects, more than twice as much activation of Wernicke's area over its homotopic one in the right hemisphere. Moreover, the experiment showed that the maps are unique to language since the comparable tone task resulted in a distinctly different map featuring bilaterally symmetrical perisylvian activation in the same subjects.

To the same conclusion lead the results of the second experiment involving eleven subjects who either had to process the same words, but now presented visually, (language task) or a series of pictures of faces (non-linguistic control task). Again, the experimental results showed that the language-specific map involves more than twice as much left than right hemisphere activation whereas the face-specific map was quite different and involved, on average, bilaterally symmetrical, basal and middle temporal lobe activation. [3]

The third experiment [4], involving seven subjects, was conducted to demonstrate that the language-specific maps were independent of the modality of the stimulus used to evoke the language function; that were, in fact, identical in each subject no matter whether the linguistic task involved words presented visually or aurally. So, each of the seven subjects was given, in turn, the auditory and the visual word tasks (the same ones used in the first two experiments). All subjects, in thia case, showed greater degree of left hemisphere activation involving nearly identical brain regions in each subject.

A fourth experiment [5] involving eleven dextral adults was conducted in order to replicate, once more, the results of visual language task, and to determine whether MEG-derived language maps are indeed spatio-temporal. That is, that they involve activation of the different regions that comprise the left hemisphere language maps in the same oreder, reliably. The results of this experiment revealed a typical succession of activation beginning with the basal posterior temporal, the hippocampal and finally involving superior and lateral temporal and parietal areas.

Finally, a fifth experiment [6] was conducted to examine whether the language maps meet the requirement of reliability in the sense of stability, over time. Sixteen subjects participated in the experiment. They were tested in two separate occasions, at least one hour apart. On both occasions they performed the visual language task. On average, the number of late EF sources was nearly identical for the two replications, as shown in Fig. 1. Of the 16 subjects, 14 showed a clear asymmetry in the degree of activation favoring the left hemisphere, one subject showed bilaterally symmetric activation, whereas in one subject, favoring the right than in the left hemisphere.

This set of normative studies demonstrated the reliability of the procedure and its validity (defined as degree of concordance between the MEG-derived maps and expectations based on prior knowledge of the functional brain organization for language).

(b) Determination of hemispheric dominance: MEG/WADA comparison

To ascertain the degree of concordance between the

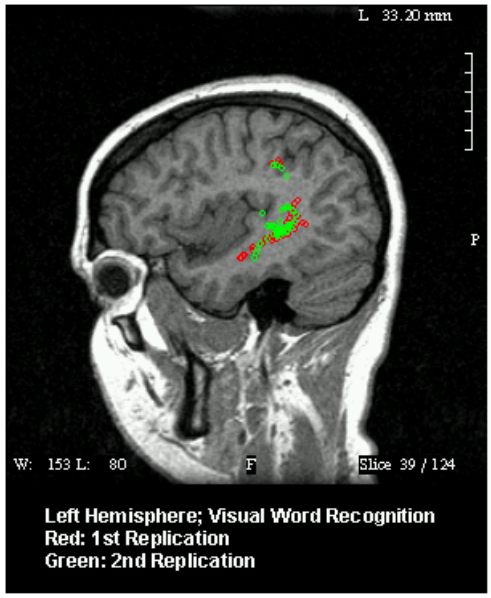

Figure 1: Overlapping language maps obtained during two repetitions of the same task.

MEG and the WADA test we have thus far evaluated 30 consecutive candidates for epilepsy surgery who had undergone WADA testing. Two of these patients were identified by the MEG procedures as right hemisphere dominant for language. Twenty-three patients were identified as left hemisphere dominant and five as having bilateral language representation. The same patients were classified on the basis of the WADA results in exactly the same way. Therefore, as we have

recently reported [7] concordance between MEG and WADA has been, up to now extremely satisfactory.

(c) Presurgical mapping

This on-going study is conducted in order to correlate MEG maps and maps derived through direct brain stimulation. A series of 14 patients, who were all surgical candidates have participated thus far. Ten of the patients underwent electrical stimulation of the cortex intraoperatively and four extraoperatively through implanted electrode grids. Language mapping was performed by applying cortical stimulation during the presentation of a short phrase or question. Interruption of receptive language was inferred when the patient had difficulty with repeating phrases or correctly responding to questions. Disruption of language occurred only at those cortical regions identified by MEG as language specific, and nowhere else in each and every one of the 14 patients examined thus far [8]. An example of verified cortical map from one patient is shown in Figure 2.

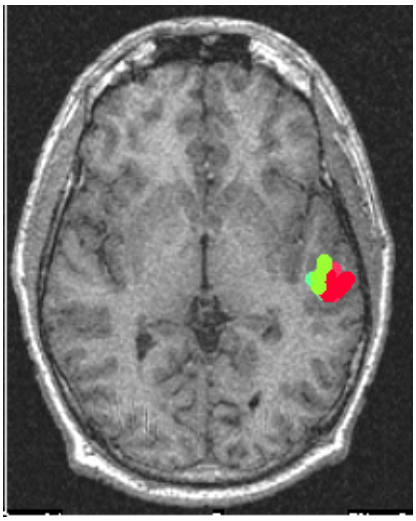

Figure 2: The language map of a patient established during two repetitions of the same task, represented in green and red. Intraoperative stimulation over the colored area produced arrest of language processing verifying the MEG-derived map.

In view of the results of the two on-going clinical studies just described, as well as the normative studies described previously, it seems reasonable to argue that functional maps fulfilling all the requirements of reliability and validity, can be, and are, in fact, derived through MEG, using simple efficient and eminently replicable procedures.

(d) Reading-specific maps unique to dyslexia

The auditory and visual language tasks used in all studies are identical in all respects except, of course, in that the second involves reading of the words. Consequently, in normal subjects (whether adults or children) the sources of the late EF components are localized in the same cortical regions, thus forming language-specific maps. The language maps of normally reading and of dyslexic children have been found to be indistinguishable. However, the maps of all twenty-one dyslexic children tested thus far, obtained during the word reading task are distinctly different from those obtained during the auditory task (and those obtained in normals during both tasks) as shown in Figure 3.

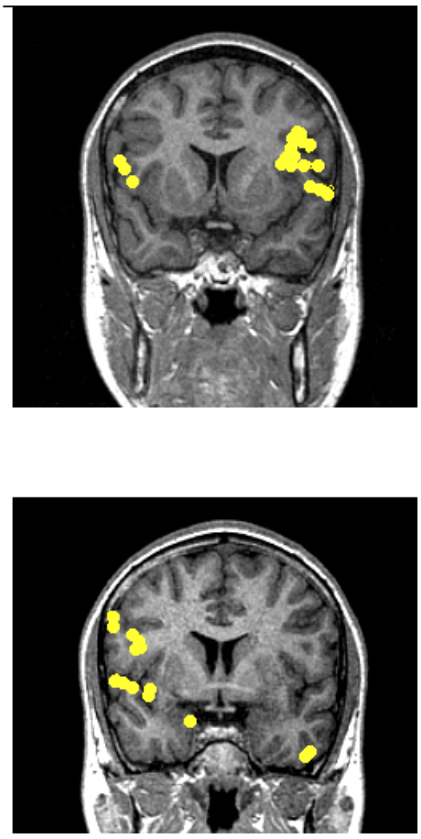

Figure 3: Examples of brain maps specific to reading from a normal reader (top) and a dyslexic child (bottom) showing the clear difference in the direction of hemispheric asymmetries between the two.

The most salient feature of those maps that are unique to dyslexics is reduced activation of the left perisylvian region and increased activation in the homotopic region of the right hemisphere. The results of this on-going MEG-study may contribute to our understanding of the neurophysiological basis of reading disorders.

References

[1] Papanicolaou, A.C., Simos, P.G., Breier, J.I., Zouridakis, G., Willmore, L.J., Wheless, J.W., Constantinou, J.E.C., Maggio, W.W., and Gormley, W.W.: Magnetoencephalographic mapping of the language-specific cortex. Journal of Neurosurgery, 90: 85-93, 1999

[2] Breier, J.I., Simos, P.G., Zouridakis, G., and Papanicolaou, A.C.: Lateralization of cerebral activation in auditory verbal and non-verbal memory task using magnetoencephalography. Brain Topogr (In Press).

[3] Zouridakis, G., Simos, P.G., Breier, J.I., and Papanicolaou, A.C.: Cerebral dominance assessment using magnetoencephalography. Brain Topogr. 11(1):57-65, 1998

[4] Simos, P.G., Breier, J.I., Zouridakis, G., and Papanicolaou, A.C.: Idendtification of language-related brain activity using magnetoencephalography. J. Clin. Exp. Neurophsychol 20:706-722, 1998

[5] Breier, J.I., Simos, P.G., Zouridakis, G., and Papanicolaou, A.C.: Relative timing of neuronal activity in distinct temporal lobe areas during a recognition memory task for words. J clin Exp Neuropsychol (In Press).

[6] Breier, J.I., Simos, P.g., Zouridakis, G., and Papanicolaou, A.C.: Lateralization of activity associated with language function using magnetoencephalography: a reliability study. J Clin Neurophys (In Press).

[7] Breier, J.I., Simos, P.G., Zouridakis, G., Wheless, J.W., Willmore, L.J., Maggio, W.W., and Papanicolaou, A.C.: Language dominance determined by magnetic source imaging: A comparison with Wada test. Neurology (In Press).

8] Simos, P.G., Papanicolaou, A.C., Breier, J.I., Wilmore, L.J., Wheless, J.W., Constantinou, J.C., Gormley, W., & Maggio, W.W.: Localization of language-specific cortex using MEG and intraoperative stimulation mapping, Journal of Neurosurgery, (In Press).

MEG Study of Hippocampal Theta During a Working Memory Task

Tesche, C.D.[1], Karhu, J.[1, 2]

[1]Helsinki University of Technology, Espoo, Finland;
[2]Kuopio University Hospital, Kuopio, Finland

Introduction

Hippocampal dysfunction is well known in neurological disorders such as epilepsy and Alzheimer's. Hippocampus is also implicated in various developmental disorders, including child-onset schizophrenia and autism. The ability to characterize the dynamics of neuronal population responses in normal and diseased hippocampus may facilitate understanding of these disorders and provide a valuable tool for the evaluation of the efficacy of various treatment strategies.

Current flow generated by neuronal activity within the brain produces electromagnetic signals which can be detected at the scalp either as potential differences between electrodes in encephalographic (EEG) arrays or as magnetic flux signals which are detected by an array of magnetoencephalographic (MEG) sensors. Both EEG and MEG have excellent temporal resolution. Many EEG and MEG studies have focused on elucidating the dynamics of neuronal populations located in relatively superficial cortical fissures. However, modern whole-scalp MEG arrays with hundreds of sensors are also appropriate for detection of activity originating deep within the brain.

Current flow generated by post-synaptic activity in pyramidal cells is a primary generator of scalp magnetic fields. However, a neuronal population which spans adjacent walls of a cortical fissure may generate current flow of equal magnitude but opposite direction on each fissural surface. The resultant signals will tend to cancel out in scalp MEG/EEG data. The cancellation of signal is believed to be particularly severe for hippocampus, a structure in which the pyramidal cells are oriented, to first approximation, on a roughly cylindrical surface. Although depth electrode recordings reveal large potential gradients within hippocampus, signals recorded with electrodes located external to the hippocampus are very substantially reduced. Certainly, identification of hippocampal activity in EEG scalp recordings has been very difficult [1].

The conventional wisdom has been that hippocampus is a "closed field", and thus not amenable neither to EEG nor to MEG investigation. However it is possible to determine from *in vivo* measurements if the firing of neuronal assemblies in hippocampus generate detectable external magnetic fields. MEG signals have been recorded both from transverse [2, 3] and longitudinal [4, 5] guinea pig hippocampal slice preparations. Interestingly, the MEG responses following electrical stimulation were large, ~300 fT, even for transverse slice preparations [2, 3]. The origin of this MEG signal is believed to be post-synaptic current flow in pyramidal cells, with amplitude ~0.2 pAm/neuron [3]. This figure suggests production of a dipolar source of several to tens of nAm may correspond to a hippocampal volume of ~3 mm^3. Since the coherence of in vivo neural networks is probably not as high as in electrically stimulated slice preparations, and substantial cancellation of magnetic responses may occur, active volumes corresponding to possible MEG responses detectable in human subjects may be considerably larger. However, the hippocampus is certainly not a magnetically closed field.

Following an initial report of hippocampal activity by Okada, et al. [6], there is now a growing body of literature which describes the use of whole scalp MEG arrays to detect neuronal population activity identified with hippocampal structures [7, 8, 9, 10, 11, 12, 13, 14]. We utilized a 122-channel MEG array [15] to investigate the dynamics of hippocampal activation during the performance of a working memory task.

Method

We used a modified "Sternberg" working memory task [16]. Subjects viewed a visually-presented set of stimuli. Trials began with a prompt to blink, followed 1.2 s later by a prompt "start". A memory set selected from single digits (0, 1, ... , 9) was presented sequentially to the center of the visual field at interstimulus intervals of 1.2 s. The last memory-set digit was followed 3 s later by a "probe" digit. The size (either 1, 3, 5 or 7 elements) of each memory set was randomized between trials. Probes were either a member of the most recently presented memory set ("in-set") or not in that memory set ("out-of-set"). Subjects were instructed to lift the right (left) index finger following in-set (out-of-set) probes.

A multi-component signal-space (SSP) analysis [17, 18] was used to derive waveforms characterizing stimulus-related responses recorded over visual and parietal cortex, movement-related responses recorded over sensorimotor cortex, and responses corresponding to activation of left and of right anterior hippocampus. Sensorimotor responses were characterized by ECDs. Activity recorded over occipital and parietal cortex were characterized as MEG sig-

nals topographies. Hippocampal SSP waveforms corresponded to generators located in left and right anterior hippocampus close to main input-output routes (for a discussion of the method as applied to hippocampal structures, see ref. [8]).
Activity phase-locked to stimulus presentation was characterized by averaged evoked response waveforms. Event-related synchronization and desynchronization (ERD/S) of ongoing activity was investigated by filtering single-trial responses, squaring and then averaging across all trials [19]. Phase-locked activity was characterized by averaging subject-specific evoked responses across all trials first, and then filtering and squaring the hippocampal waveforms. Grand averaging across subjects and memory-set sizes was performed following normalization of responses for to the mean value obtained during a 100-ms epoch immediately prior to the "blink" prompt.
The corresponding system noise for each analysis was calculated by applying the algorithm to data recorded by the sensor array with no subject present in the room. System noise is uncorrelated with brain activity, and thus additive with respect to the brain signals for ongoing activity, averaged evoked responses, and also for power spectral density and ERD/S measures of the signal characteristics.

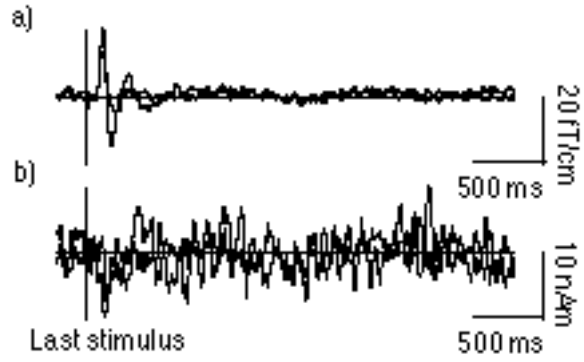

Fig. 1: Examples of grand averaged evoked responses across all subjects for a) responses recorded over occipital cortex and b) responses for SSP component for left anterior hippocampus. Responses for memory-set (solid lines) and control (dashed lines) trials were averaged over all set sizes.

Results

Neurophysiological data are often characterized as a sequence of evoked response peaks. In the present study, waveforms for responses recorded over occipital and parietal cortex and also for left and right anterior hippocampus showed a series of evoked response peaks following stimulus presentation. The early (< 600 ms) evoked responses were followed by substantial activity in SSP waveforms for hippocampus, but not for activity in visual or parietal cortex. The hippocampal responses were not reproducible between trials and were of sufficient magnitude to survive grand averaging over 1726 memory-set and 1202 control trials, respectively. The presence of large on-going background activity may confound possible hemodynamic fingerprints of hippocampal responses in PET and fMRI data. In contrast, it may be possible to utilize the temporal resolution of MEG to identify rather subtle changes in the dynamics of the underlying activity.

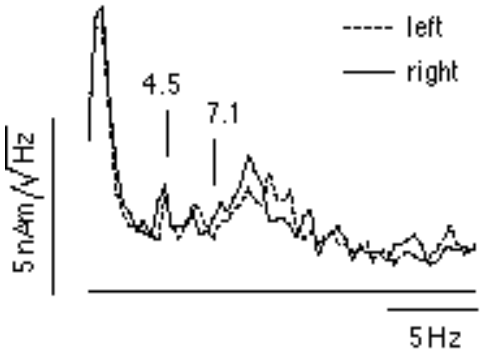

Fig. 2: Power spectra of grand average over subjects and memory set sizes of evoked responses following the probe stimulus for in-set memory trials.

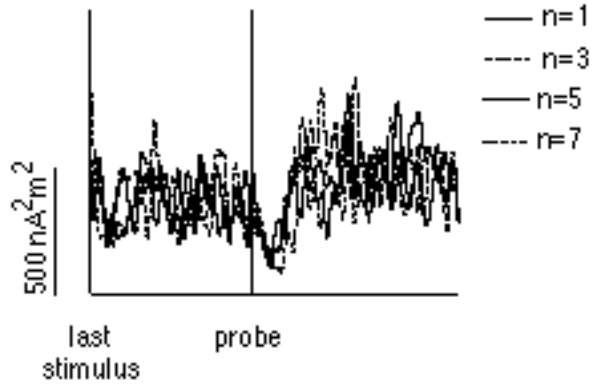

Fig. 3: ERD/S of left hippocampal responses in a 4–8-Hz bandwidth: out-of-set memory trials for a single subject.

We investigated the spectral-temporal properties of the hippocampal activity. Fig. 2 shows the power spectra of the average evoked responses. The spectra for 2.5-s epochs following the probe stimuli contain both 4–8-Hz (theta) and 8–12-Hz (alpha) activity. Fig. 3 shows that the ongoing (non-stimulus-locked) theta activity is reduced immediately following presentation of probe stimuli. This response is sufficiently robust to be visible in single-subject data.
Fig. 4 shows that phase-locked activity is strongly enhanced immediately following both memory-set and probe stimuli.
The reduction of non-phase-locked activity coincident with synchronization of responses in the same bandwidth provides a window of opportunity for the characterization of stimulus-locked theta in these normal human subjects.

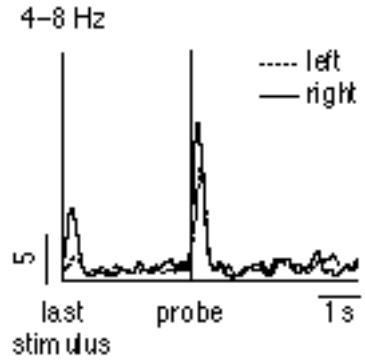

Fig. 4: Grand average of phase-locked hippocampal responses in a 4–8-Hz bandwidth for in-set memory trials.

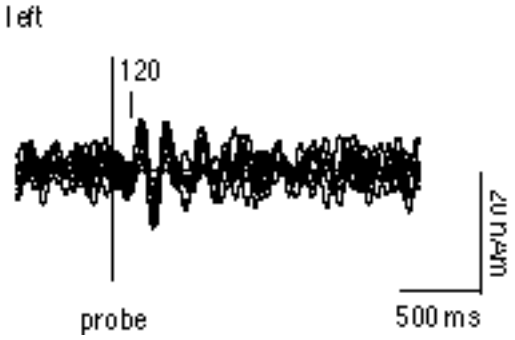

Fig. 5: Superposition of grand averaged left hippocampal responses to probe stimuli for all memory-set sizes (filter 4–8 Hz).

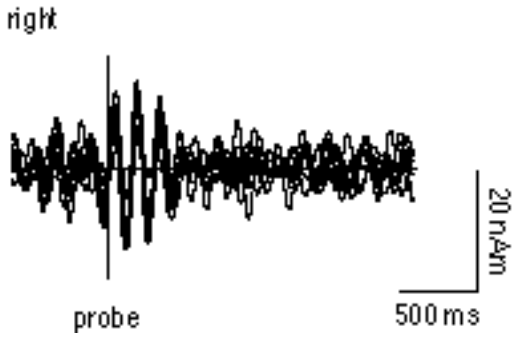

Fig. 6: Superposition of grand averaged right hippocampal responses to probe stimuli for all memory-set sizes (filter 4–8 Hz).

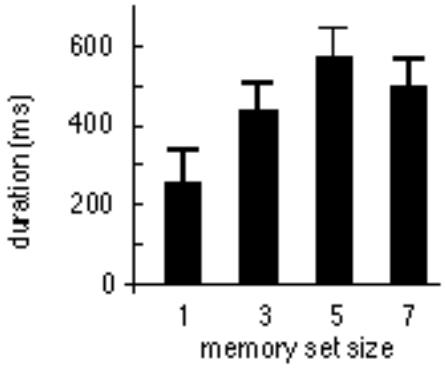

Fig. 7: Duration of stimulus-locked theta as a function of memory set size for in-set trials.

Figs. 5 and 6 show filtering of evoked response waveforms revealed resetting of the phase of 4–8 Hz theta for both left and right hippocampal components. Activity in left hippocampal waveforms was at ~5 Hz, and on the right at ~7 Hz. Resetting of the phase was observed on the left at 120 ms following presentation of the probe stimuli. In contrast, phase-resetting commenced in right hippocampal waveforms even before presentation of the probe stimulus.

The duration of right hippocampal theta increased with memory set size for n=1 to n=5, to a limit ~ 600 ms. Interestingly, phase-locking was also observe following stimulus presentation, with duration for right hippocampal activity ~550–650 ms.

Discussion

Clinical and pathological analysis of human amnesic cases [20] and experimental studies in monkey [21] have confirmed that the hippocampal region, including hippocampus proper, dentate gyrus, subicular complex and entorhinal and parahippocampal cortex, is an important component of the medial temporal lobe memory system. Hippocampus is viewed as essential for declarative memory function [22, 23, 24, 25]. Hippocampal structures also participate to the selection of pertinent information which needs to be held “in line" during the temporal interval required for a decision or for the performance of an operation, i.e. to working memory [26, 27]. One of the characteristic features of working memory is a limit on the capacity of retained items to 7±2 elements [28]. The origin of the capacity limit is unknown.

A wealth of single cell and intracranial field potential recordings within rodent hippocampus indicate that oscillatory 4–12-Hz field potentials (theta) are implicated in the synchronization of input-output functions of hippocampus (for a review, see [29]). During attentive behavior, oscillatory cortical activity, which may characterize an “idling state”, desynchronizes to a fast pattern, whereas simultaneous hippocampal recordings show a synchronized 4–7-

Hz cognitive component and/or a 8–12-Hz motor-related component [30].
A direct role for theta in the sculpting of hippocampal networks is suggested by the association of long-term potentiation (LTP) and depression (LTD) with phase-locking of oscillatory activity to presented stimuli [31]. Afferentation seems to be crucially involved in the generation of theta, which is abolished by removal of entorhinal input [32]. Interestingly, resetting of the phase of dentate theta with stimulus presentation has been observed in rats during working, but not reference, memory tasks [33].
We found that both memory-set and probe stimuli in a Sternberg working memory task elicited a resetting of the phase of ongoing theta in normal human subjects. Our results suggest that the increased duration of 4–8 Hz theta with memory-set size may index involvement of hippocampus and associated structures in the scanning of the memory set. Responses to the stimuli which comprise the memory-set suggest that a limited time of ~550–600 ms may be available for theta-mediated processing of salient input. If this is the case, then a duration of ~600 ms for memory-set sizes of 5-7 items may evidence a mechanism which limits the capacity of working memory.

References

[1] Polich, J. and Squire, L. P300 from amnesic patients with bilateral hippocampal lesions. Electroenceph. clin. Neurophysiol., 1993, 86: 408–417.

[2] Tesche, C.D., Krusin-Elbaum, L. and Knowles, W.D. Simultaneous measurement of magnetic and electrical response of in vitro hippocampal slices. Brain Res, 1988, 462: 190–193.

[3] Kyuhou, S. and Okada, Y. Detection of Magnetic Evoked Fields Associated with Synchronous Population Activities in the Transverse CA1 Slice of the Guinea Pig. J. Neurophysiol., 1993, 70: 2665–2668.

[4] Okada, Y.C. and Kyuhou, S. Characteristics of the magnetic evoked fields associated with neuronal activites in longitudinal slices of the guinea pig. 9th Intl. conf. on Biomangetism, 1993, 404–405.

[5] Wu, J. and Okada, Y.C. Physiological bases of the synchronized population spikes and slow wave of the magnetic field generated by a guinea-pig longitudinal CA3 slice preparation. Electroenceph clin Neurophysiol, 1998, 107: 361–373.

[6] Okada, Y.C., Kaufman, L. and Williamson, S.J. The hippocampal formation as a source of the slow endogenous potentials. Electroenceph. clin. Neurophysiol., 1983, 55: 417–426.

[7] Ioannides, A.A., Liu, M.J., Liu, L.C., Bamidis, P.D., Hellstrand, E. and Stephan, K.M. Magnetic field tomography of cortical and deep processes: examples of "real-time mapping" of averaged and single trial MEG signals. Int J Psychophysiol, 1995, 20: 161–175.

[8] Tesche, C., Karhu, J. and Tissari, S. Non-invasive detection of neuronal population activity in human hippocampus. Cogn. Brain Res., 1996, 4: 39-47.

[9] Kikuchi, Y., Endo, H., Yoshizawa, S., Kait, M., Nishimura, C., Tanaka, M., Kumagai, T. and Takeda, T. Human cortico-hippocampal activity related to auditory discrimination revealed by neuromagnetic field. Neuroreport, 1997, 8: 1657–1661.

[10] Simos, P.G., Basile, L.F. and Papanicolaou, A.C. Source localization of the N400 response in a sentence-reading paradigm using evoked magnetic fields and magnetic resonance imaging. Brain Res, 1997, 762: 29–39.

[11] Tesche, C. Non-invasive detection of ongoing neuronal population activity in normal human hippocampus. Brain Res., 1997, 749: 53–60.

[12] Nishitani, N., Nagamine, T., Fujiwara, N., Yazawa, S. and Shibasaki, H. Cortical-hippocampal auditory processing identified by magnetoencephalography. J Cogn Neurosci, 1998, 10: 231–247.

[13] Tesche, C.D. and Karhu, J. Interactive processing of sensory input and motor output in human hippocampus. J Cogn Neurosci, 1999, 11: 424–436.

[14] Nishitani, N., Ikeda, A., Nagamine, T., Honda, M., Mikuni, N., Taki, W., Kimura, J. and Shibasaki, H. The role of the hippocampus in auditory processing studied by event-related electric potentials and magnetic fields in epilepsy patients before and after temporal lobectomy. Brain, 1999, 122: 687–707.

[15] Ahonen, A.I., Hämäläinen, M., Kajola, M., Knuutila, J., Laine, P., Lounasmaa, O., Parkkonen, L., Simola, J. and Tesche, C. 122-channel SQUID instrument for investigating the magnetic signals from human brain. Physica Scripta, 1993, T49: 198-205.

[16] Sternberg, S. High-speed scanning in human memory. Science, 1966, 153: 652–654.

[17] Ilmoniemi, R.J. and Williamson, S.J. Analysis for the magnetic alpha rhythm in signal space. Soc. Neurosci. Abstr., 1987, 13 (2): 46.

[18] Tesche, C., Uusitalo, M., Ilmoniemi, R., Huotilainen, M., Kajola, M. and Salonen, O. Signal-space projections of MEG data characterize both distributed and well-localized neuronal sources. Electroenceph. Clin. Neurophysiol., 1995, 95: 189-200.

[19] Pfurtscheller, G. and Aranibar, A. Evaluation of event-related desynchrinization (ERD) preceding and following voluntary self-paced movement. Electroenceph. Clin. Neurophysiol., 1979, 46: 138-146.

[20] Zola-Morgan, S. and Squire, L.R. Human amnesia and the medial temporal region: enduring memory impairment following a bilateral lesion limited to field CA1 of the hippocampus. J Neurosci, 1986, 6: 2950–2967.

[21] Zola-Morgan, S. and Squire, L.R. Memory impairment in monkeys following lesions limited to the hippocampus. Behav Neurosci, 1986, 100: 155–160.

[22] Scoville, W.B. and Milner, B. Loss of recent memory after bilateral hippocampal lesions. J. Neurol. Neurosurg. Psychiatry, 1957, 20: 11-21.

[23] Mishkin, M. Memory in monkies severely impaired by combined but not by separate removal of amygdala and hippocampus. Nature, 1978, 297-298.

[24] Zola-Morgan, S., Squire, L.R., Amaral, D.G. and Suzuki, W.A. Lesions of the parahippocampal cortex that spare the amygdala and hippocampal formation produce severe memory impairment. J. Neurosci., 1989, 9: 4355-4370.

[25] Squire, L.R. Memory and the hippocampus: synthesis from findings with rats, monkeys and humans. Psychol. Rev., 1992, 99: 195-231.

[26] Goldman-Rakic, P.S. Cortical localization of working memory. In: J.L. McGaugh, N.M. Weinberger, G. Lynch (Eds.), Brain organization and memory: cells, systems and circuits. Oxford University Press, New York, 1989: 1-29.

[27] Baddeley, A. Working memory: The interface between memory and cognition. J. Cogn. Neurosci., 1992, 4: 281-288.

[28] Miller, G.A. The magical number seven, plus or minus two: some limits on our capacity for processing information. Psychol Rev, 1956, 63: 81–97.

[29] Buzsáki, G. The hippocampo-neocortical dialogue. Cerebr. Cortex, 1996, 6: 81-92.

[30] Vanderwolf, C.H. Hippocampal electrical activity and voluntary movement in the rat. Electroenceph. Clin. Neurophysiol., 1969, 26: 407–418.

[31] Stanton, P.K. and Sejnowski, T.J. Associative long-term depression in the hippocampus induced by hebbian covariance. Nature, 1989, 339: 215–218.

[32] Ylinen, A., Soltesz, I., Bragin, A., Penttonen, M., Sik, A. and Buzsáki, G. Intracellular correlates of theta rhythm in hippocampal pyramidal cells, granule cells and basket cells. Hippocampus, 1995, 5: 78-90.

[33] Givens Stimulus-evoked resetting of the dentate theta rhythm: relation to working memory. NeuroReport, 1996, 8: 159–163.

Acknowledgments

This study was supported by NIH grant NS34533.

Estimating Neural Source of High-Frequency Magnetic Oscillation Evoked by Posterior Tibial Nerve Stimulation Using Time Frequency MEG-MUSIC Algorithm

Sakuma K.[1], Sekihara K[2]., Hashimoto I.[1,3]

[1]National institute for Physiological Sciences, Okazaki, Japan
[2]JST Mind Articulation Project, Tokyo, Japan
[3]Department of Psychophysiology, Tokyo Institute of Psychistry, Tokyo, Japan

Introduction

High-frequency primary cortical oscillations characterized by a frequency range of 500-800 Hz superimposed on the ascending slope of the N20 primary response following stimulation of the median nerve have been reported previously [1][2][3]. We recorded high frequency oscillations (HFOs) evoked by posterior tibial nerve stimulation using magnetoencephalography (MEG), and demonstrated the intracranial locations of the HFOs sources with respect to brain anatomy [4]. Since the HFOs are of extremely low amplitude with low signal-to-noise ratio (S/N) compared with the underlying P37m, it was difficult to estimate the location of HFOs source precisely. We applied the time-frequency multiple signal classification (TF-MUSIC) algorithm to HFOs, and could demonstrate the superiority of this method compared with a single moving dipole fit method (SMD).

Methods and Materials

Measurements of HFOs Ten normal subjects (5 females and 5 males; mean age 26.6 years, range from 21 to 35 years) were studied. They gave their consent to the experimental procedures. Electrical stimuli with a 0.2 ms duration were delivered to the right posterior tibial nerve at the ankle (cathode proximal). The stimulus intensity was about three times sensory threshold and elicited a mild twitch of toe. The stimuli were delivered at regular intervals with a repetition rate of 4 Hz. Magnetic recordings (bandpass 0.1-1200 Hz) were taken from the vertex centering around the Cz of the international 10-20 system with a 37-channel biomagnetometer (Magnes, Biomagnetic Technologies Inc., San Diego,) in a magnetically shielded room. An epoch of 60 ms duration (10 ms pre and 50 ms post stimulus) was digitized at a 4167 Hz/channel sampling rate and 9,999 responses were averaged offline. For separation of the HFOs from the underlying P37m, the wide-band (0.1-1200 Hz) recorded responses were digitally filtered with a 500-800 Hz band-pass filter. The DC offset was compensated using the data in the pre-stimulus period.

Single moving dipole fit (SMD) method A local spherical model was fitted to the digitized head shape over the recording area for each subject. The location, orientation, and amplitude parameters of a dipole source in the spherical head model were iteratively adjusted by minimizing the least-squares error between an observed field and a theoretical field. The correlation between the theoretical field generated by the model and the observed field was calculated and only equivalent current dipoles (ECDs) with this correlation value above 0.86 were analyzed.

Time-frequency MUSIC algorithm The TF-MUSIC algorithm allows us to estimate the locations of neural sources from any time-frequency region of interest [5]. Let us define the magnetic field measured by the mth detector coil at time t as $b_m(t)$, and a vector $\boldsymbol{b}(t) = (b_1(t), b_2(t), \ldots, b_M(t))^T$ as a set of measured data where M is the total number of detector coils. A total of P current sources are assumed to generate the biomagnetic field, and the locations of these sources are denoted as $(\boldsymbol{x}_1, \boldsymbol{x}_2, \ldots, \boldsymbol{x}_P)$. The magnitude of the pth source is defined as $s_p(t)$, the source magnitude vector is defined as $\boldsymbol{s}(t) = (s_1(t), s_2(t), \ldots, s_P(t))^T$, and the source orientation is defined as its normal vector $\boldsymbol{\eta}_p = (\eta_p^x, \eta_p^y, \eta_p^z)^T$, where $||\boldsymbol{\eta}_p|| = 1$. Here, $\boldsymbol{\eta}_p$ is assumed to be time independent. We define a $3P \times P$ matrix that expresses the orientations of all P sources as $\boldsymbol{\Psi}$ such that the pth diagonal entry of this matrix is equal to the matrix $\boldsymbol{\eta}_p$ where $p = 1, \ldots, P$, and all other terms are equal to zero. The lead field vector for the θ (=x, y or z) component of the source at $\boldsymbol{x}$ is defined as

$$\boldsymbol{l}^\theta(\boldsymbol{x}) = (l_1^\theta(\boldsymbol{x}), l_2^\theta(\boldsymbol{x}), \ldots, l_M^\theta(\boldsymbol{x}))^T.$$

Here $l_m^\theta(\boldsymbol{x})$ expresses the mth sensor output induced by the unit-magnitude source directed in the θ direction. We define the lead field matrix for the source at $\boldsymbol{x}$ as $\boldsymbol{L}(\boldsymbol{x}) = [\boldsymbol{l}^x(\boldsymbol{x}), \boldsymbol{l}^y(\boldsymbol{x}), \boldsymbol{l}^z(\boldsymbol{x})]$. The composite lead field matrix for the entire set of P sources is defined as

$$\boldsymbol{L}_c = [\boldsymbol{L}(\boldsymbol{x}_1), \boldsymbol{L}(\boldsymbol{x}_2), \cdots, \boldsymbol{L}(\boldsymbol{x}_P)]. \qquad (1)$$

Then the relationship between $\boldsymbol{b}(t)$ and $\boldsymbol{s}(t)$ is expressed as

$$\boldsymbol{b}(t) = (\boldsymbol{L}_c\boldsymbol{\Psi})\boldsymbol{s}(t) + \boldsymbol{n}(t), \quad (2)$$

where $\boldsymbol{n}(t)$ is the additive noise.
The time-frequency distribution matrices for $\boldsymbol{b}(t)$ and $\boldsymbol{s}(t)$ are defined as $\boldsymbol{C}_b(t,f)$ and $\boldsymbol{C}_s(t,f)$, which, for example, are obtained by using any of the Cohen class time-frequency distributions; i.e.,

$$\boldsymbol{C}_b(t,f) = \int\int_{\infty}^{\infty} \Phi(\nu - t, \xi - f) \left[\int_{-\infty}^{\infty} \boldsymbol{b}(\nu+\tau/2)\,\boldsymbol{b}^T(\nu-\tau/2)e^{-2\pi i\xi\tau}d\tau\right]d\nu d\xi, \quad (3)$$

and

$$\boldsymbol{C}_s(t,f) = \int\int_{\infty}^{\infty} \Phi(\nu - t, \xi - f) \left[\int_{-\infty}^{\infty} \boldsymbol{s}(\nu+\tau/2)\,\boldsymbol{s}^T(\nu-\tau/2)e^{-2\pi i\xi\tau}d\tau\right]d\nu d\xi. \quad (4)$$

Here, $\Phi(t,f)$ is the convolution kernel, which determines the characteristics of the resultant Cohen class quadratic time-frequency distributions [6].
The matrix $\boldsymbol{C}_b(t,f)$ is an $M \times M$ matrix. Its diagonal elements are the auto-time-frequency distributions of the channel recordings and its off-diagonal elements are the cross-time-frequency distributions between different channel recordings. The matrix $\boldsymbol{C}_s(t,f)$ is a $P \times P$ matrix. Its diagonal elements are the auto-time-frequency distributions of the source activities and its off-diagonal elements are the cross-time-frequency distributions between different source activities.
Let us also define the matrices $\boldsymbol{\Upsilon}_b$ and $\boldsymbol{\Upsilon}_s$ as those obtained by averaging $\boldsymbol{C}_b(t,f)$ and $\boldsymbol{C}_s(t,f)$ over the target time-frequency region Ω for which the neural sources are localized; i.e. $\boldsymbol{\Upsilon}_b = \int\int_{\Omega} \boldsymbol{C}_b(t,f)dtdf$ and $\boldsymbol{\Upsilon}_s = \int\int_{\Omega} \boldsymbol{C}_s(t,f)dtdf$, where $\int\int_{\Omega}$ indicates the integral over the target time-frequency region.
We assume that the noise and signal are uncorrelated in the target region and the noise is white Gaussian. We thus finally derive the relationship

$$\boldsymbol{\Upsilon}_b = (\boldsymbol{L}_c\boldsymbol{\Psi})\boldsymbol{\Upsilon}_s(\boldsymbol{\Psi}^T\boldsymbol{L}_c^T) + \rho^2\boldsymbol{I} \quad (5)$$

where ρ^2 is the total noise power in the target region. We denote the noise-level eigenvectors of $\boldsymbol{\Upsilon}_b$ as $\boldsymbol{u}_j$ $(j = P_\Omega + 1, \ldots, M)$. Here P_Ω is the number of sources whose activity has time-frequency components in the target region. The matrices $\boldsymbol{L}_c$ and $\boldsymbol{\Psi}$ are full-column-rank matrices. Therefore, when the matrix $\boldsymbol{\Upsilon}_s$ is a full-rank matrix, Equation (5) leads to

$$\boldsymbol{L}_c^T\boldsymbol{u}_j = 0 \quad \text{for} \quad j = P_\Omega + 1, \ldots, M\ . \quad (6)$$

The above equation indicates that source locations can be obtained by checking the orthogonality between the sensor lead field $\boldsymbol{L}(\boldsymbol{x})$ and the noise-level eigenvectors of $\boldsymbol{\Upsilon}_b$. This orthogonality can be evaluated by calculating the following function,

$$J(\boldsymbol{x}) = 1/\lambda_{min}[\boldsymbol{L}(\boldsymbol{x})^T\boldsymbol{Z}_N\boldsymbol{Z}_N^T\boldsymbol{L}(\boldsymbol{x}), \boldsymbol{L}(\boldsymbol{x})^T\boldsymbol{L}(\boldsymbol{x})], \quad (7)$$

where a matrix $\boldsymbol{Z}_N$ is defined as $\boldsymbol{Z}_N = [\boldsymbol{u}_{P_\Omega+1}, \ldots, \boldsymbol{u}_M]$. In the TF-MUSIC algorithm, Eq (7) is calculated in a volume where sources can exist, and each location where $J(\boldsymbol{x})$ reaches a peak is chosen as the location of one source.

Evaluation of the source localization results

The distance between ECD location of P37m and of HFOs was calculated for the results from the SMD. The distance was again calculated between ECD location of P37m and of HFOs for the results from the TF-MUSIC algorithm. These two distances were compared and the accuracy of ECD location between the two methods were assessed.

Results

In wide-band recordings, the main P37m deflection was clearly identified in all 10 subjects. The ECDs of P37m peak (SMD P37m) were estimated at the somatosensory foot area in all subjects. After filtering with a 500-800 Hz band-pass filter, low amplitude high-frequency magnetic oscillations superimposed on P37m were detected in 5 out of 10 subjects. However, since the values of the correlation for the ECD sources of the HFOs were smaller than 0.86 in one subject, we calculated the ECDs of HFOs in only 4 subjects using the SMD method. With the SMD method, the ECD localizations for the high-frequency peaks and the underlying P37m were close with each other (Table 1). There were no significant statistical differences between the localizations for the x, y and z axes (paired t-test). The spectrogram was calculated for the frequency range above 400 Hz from the averaged somatosensory evoked magnetic fields. The region containing the HFOs was selected as the target regions of interest. A clear, isolated region was detected in 6 out of 10 subjects. The time-frequency region of interest started at 29-33 ms (30.8 ms±1.5) with 500-630 Hz (585 Hz±44.6) in frequency, and ended at 35-40 ms (38.3 ms±1.8) with 650-800 Hz (725 Hz±50.1) in frequency. These time ranges were coincident with the ascending and descending slopes of the P37m. Fig. 1(a) shows a typical record from one subject

where the ECDs of HFOs could be estimated by using both the SMD and the TF-MUSIC. Fig. 1(b) shows a typical result from another subject showing clear isolated region in the time-frequency spectrogram although the SMD algorithm failed to estimate the ECD localization due to a low signal-to-noise ratio with a low correlation value. We then applied the TF-MUSIC algorithm to these target regions. Typical TF-MUSIC localizer maps are shown in Fig.2. The contours in this figure show the relative values of the TF-MUSIC localization function projected onto the transverse, coronal and sagittal planes. Although the average distance of the dipole sources between the HFOs and the underlying P37m was not different between SMD method and TF-MUSIC algorithm, it should be noted that HFO dipole locations were estimated in 6 out of 10 subjects with the TF-MUSIC algorithm as against in 4 out of 10 subjects with the SMD method (Table 1).

Discussion and conclusion

In this study, the TF-MUSIC algorithm was applied to estimating the neural sources of the high-frequency magnetic oscillations evoked by posterior tibial nerve stimulation. The dipole locations of the HFOs were successfully estimated using the TF-MUSIC algorithm even when the estimations failed with the SMD method. This is mainly because the TF-MUSIC algorithm can selectively localize sources of interest when large amount of interferences exist. dipole strength of the HFOs is as small as one fourteenth of the N20m for median nerve stimulation[3]. In addition, it is widely known that somatosensory evoked potentials evoked by posterior tibial nerve stimulation are more difficult to record than those evoked by median nerve stimulation. Although we used averaging over nearly 10,000 stimulus presentations to obtain the desirable S/N, it is impossible to eliminate all magnetic noise such as external ambient noise, system noise and brain noise. Since such magnetic noise have no phase-locking to stimulus, the clear isolated activity detected in the averaged time-frequency spectrogram should be the signal free from the noise. In fact, the TF-MUSIC has theoretical as well as empirical advantages for eliminating noise from the evoked magnetic fields. With this algorithm, the time-frequency spectrogram of evoked magnetic response can be checked by visual inspection for inclusion in the analysis. Therefore, the TF-MUSIC algorithm is suitable for extracting a target response which have a uniform frequency-temporal profile such as HFOs.

References

[1] Yamada, T., Kameyama, S., Fuchigami, Y., Nakazumi, Y., Dickins, Q.S. and Kimura, J., Changes of short latency somatosensory evoked potential in sleep. Electroenceph. Clin. Neurophysiol., 1988, 70: 126–136.

[2] Curio, G., Mackert, B.M., Burghoff, M., Koetitz, R., Abraham-Fuchs, K. and Harer, W., Localization of evoked neuromagnetic 600 Hz activity in the cerebral somatosensory system. Electroenceph. Clin. Neurophysiol., 1994, 91: 483–487.

[3] Hashimoto, I., Mashiko, T. and Imada, T., Somatic evoked high-frequency magnetic oscillations reflect activity of inhibitory interneurons in the human somatosensory cortex. Electroenceph. Clin. Neurophysiol., 1996, 100: 189–203.

[4] Sakuma, K. and Hashimoto, I., High-frequency magnetic oscillations evoked by posterior tibial nerve stimulation. NeuroReport, 1999, 2 (in press).

[5] Sekihara, K., Nagarajan, S., Poeppel, D. and Miyashita, Y., Time-Frequency MEG-MUSIC algorithm. IEEE Trans. Medical Imaging., 1999, 18: 92–97.

[6] Cohen L., Time-Frequency Analysis: Theory and Applications, Prentice-Hall, Inc., Englewood Cliffs, New Jersey, 1994.

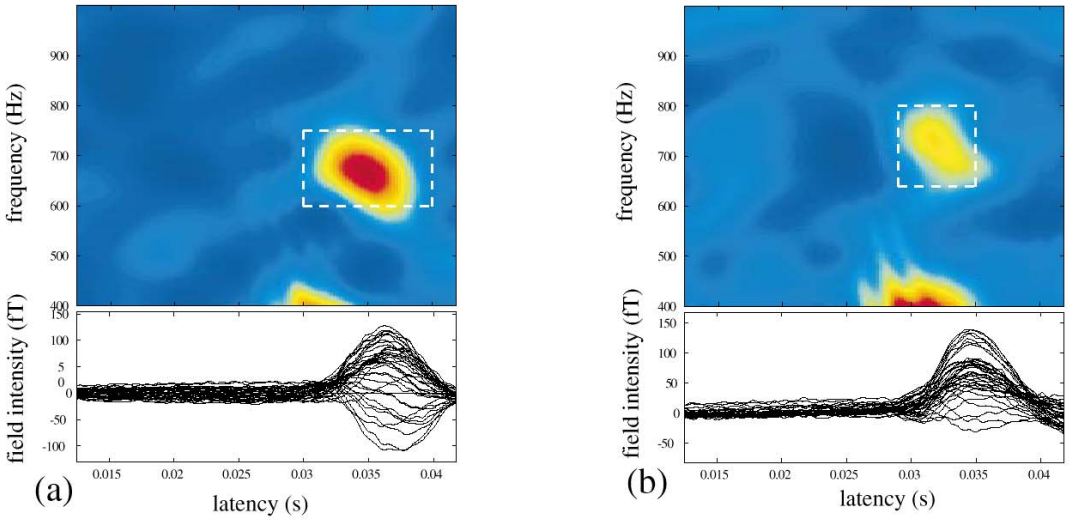

Fig. 1 Measured somatosensory-evoked fields and their spectrograms for two representative subjects: (a) subject#1 and (b) subject#2.

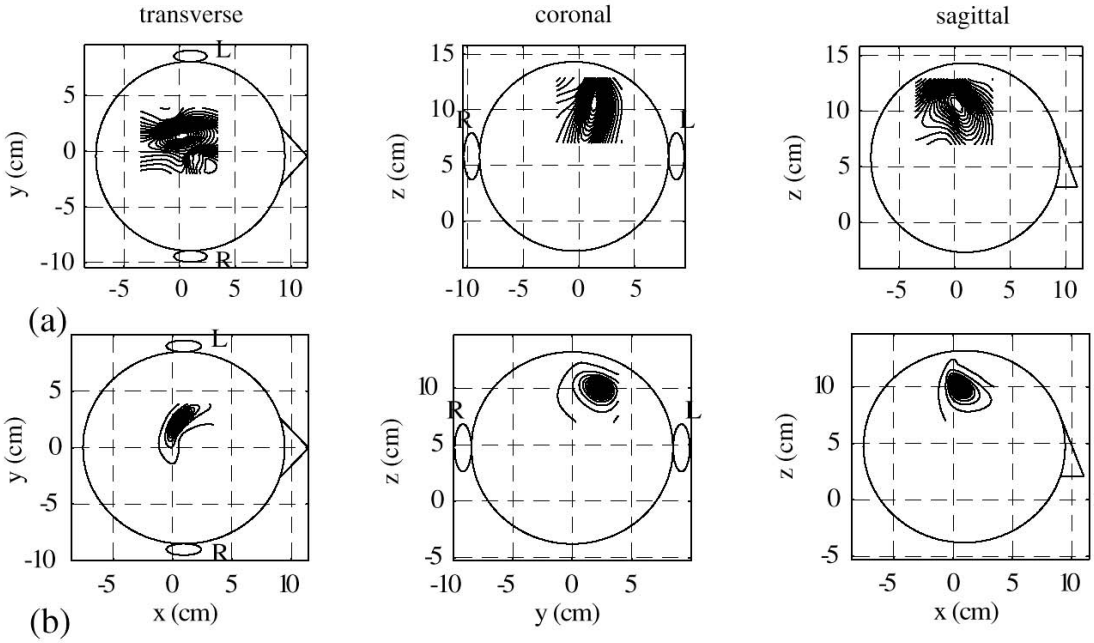

Fig. 2 TF-MUSIC results for the two representative subjects. The target regions were set as shown by the squares in Fig. 1. (a) Results from subject#1 and (b) results from subject#2.

	SMD P37m			SMD HFOs			TF-MUSIC HFOs			DISTANCE (cm)	
Subject	x	y	z	x	y	z	x	y	z	SMD	TF-MUSIC
KT	1.52	1.41	10.25	N.E	N.E	N.E	0.80	1.57	10.14	N.E	0.74
MK	1.09	1.89	10.29	1.03	2.41	9.44	−0.46	1.52	10.40	1.00	1.59
YI	0.90	1.35	10.73	0.68	1.36	10.33	1.65	2.26	10.50	0.46	1.20
KS	1.92	1.19	10.66	1.25	2.54	10.31	3.11	1.95	9.57	1.55	1.78
AG	−0.22	1.27	10.23	N.E	N.E	N.E	0.49	2.22	10.02	N.E	1.21
TO	0.17	1.36	10.95	−0.27	0.54	9.54	0.18	1.38	10.65	1.70	0.30
average										1.17	1.14
SD										0.57	0.55

n.s., not significant
N.E., not estimated

n.s.

n.s.

n.s.

Table 1 Individual source locations of P37m and HFOs and the distance between the locations of P37m and HFOs using the SMD and TF-MUSIC algorithm.

On the effective passive Conductivity of human Tissues at low Frequencies

Peters M.J., van Burik M.J., and Stinstra J.G.

Low Temperature Division, Faculty of Applied Physics, University of Twente, Enschede, The Netherlands

Introduction

The low-frequency electric conductivity of human tissues is of importance to study the electric activity generated within the human body, measured by for instance, the EEG, ECG or EMG. Commonly, the human body as a volume conductor is considered to be piece-wise homogeneous. The conductivity of a compartment, being the effective conductivity, is taken from literature. However, these values vary over a wide range. To narrow down the uncertainties, we will discuss the electric conductivity of human tissues for low frequencies (below 1000Hz) taking the architecture of the tissues into account.

Biological materials are inhomogeneous materials with two domains: the extracellular and the intracellular space. Although the cells are of microscopic size, still they are much larger than the ions in the extracellular space so that the extracellular fluid can be considered as a continuum. At low frequencies and small current densities, the currents tend to flow around the cell membranes rather than through them. Outside of the source region human tissue is assumed to be Ohmic. Particles suspended in a solvent are considered to be a relevant model of biological cells. Maxwell derived an expression for a dilute suspension of spheres within a uniform electric field. This expression has been experimentally tested for high concentrations of variously shaped objects and an agreement within 1% was found for concentrations up to a volume percentage of 90% [1]. However, measurements of the conductivity of the cortex of the brain did not fit so well with the theory of Maxwell. This was probably due to the fact that the human cortex as almost all biological tissues constitute of a dense packed medium. It was found that the conductivity of the cortex is in good agreement with an expression known as Archie's law [2]. This law was found empirically in geology. The conductivities of most water-saturated inhomogeneous rocks obey Archie's law [3]. In this paper expressions will be derived that can be used to determine the conductivity of tissues and they will be illustrated by several examples.

Method

First, an expression for the conduction of a dilute solution of spheres will be derived. The effective (i.e. macroscopic) electrical conductivity of suspensions in aqueous media of spherical particles (that do not have a permanent electric moment) has been derived by Maxwell.

A small sphere of radius R and conductivity σ_2 embedded in a homogeneous medium with conductivity σ_1 is considered. A uniform electric field is applied (see Fig. 1). An expression for the potential outside the sphere is found by solving the Laplace equation with the proper boundary conditions using Legendre polynomials. The origin of the co-ordinates (r, θ, φ) is at the centre of the sphere of radius R. This yields for the potential:

$$\varphi_1 = -\left(1+\frac{\sigma_1-\sigma_2}{2\sigma_1+\sigma_2}\frac{R^3}{r^3}\right)E_0 r\cos\theta \qquad r \geq R \qquad (1)$$

$$\varphi_2 = -\left(\frac{\sigma_1-\sigma_2}{2\sigma_1+\sigma_2}+1\right)E_0 r\cos\theta \qquad r \leq R \qquad (2)$$

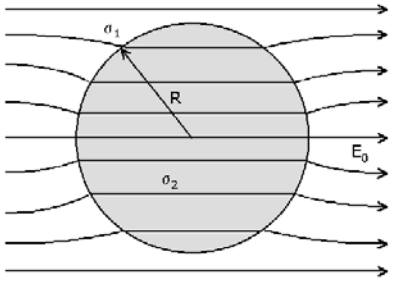

Figure 1: A spherical particle of conductivity σ_2 surrounded by a solvent with conductivity σ_1 placed in an original uniform electric field E_0

Within the sphere, the field is parallel and uniform. Outside the sphere, the field is the original field plus the field of a dipole at the centre of the sphere.

Next, the suspension is modelled by N small spherical particles of radius R and conductivity σ_2 that are distributed uniformly in a medium with conductivity σ_1 and are surrounded by a large spherical boundary of radius R'(R' >> R) as illustrated in Fig. 2. Two assumptions are made. The volume fraction occupied by the cells is assumed to be low, the average distance between them being larger than their dimensions and as a consequence the spheres do not effect the fields of the other spheres. The potential is the sum of the potentials due to a large number N of small homogeneously-distributed cells (the superposition principle) and integration yields:

$$\varphi_1 = -\left(N\frac{\sigma_1-\sigma_2}{2\sigma_1+\sigma_2}\frac{R^3}{r^3}+1 \right) E_0 r\cos\theta \qquad (3)$$

Instead of the microscopic point of view, we can look at the sphere from a macroscopic point of view. We have a spherical shaped medium consisting of an aqueous solution of spherical particles. The effective conductivity of the medium contained by a spherical boundary σ is defined as the conductivity that gives a potential outside of the sphere that is expressed by (1). Hence, the potential at a distance r > R' from the centre of the sphere describing the solution reads:

$$\varphi_1 = -\left(\frac{\sigma_1-\sigma}{2\sigma_1+\sigma}\frac{R'^3}{r^3}+1 \right) E_0 r\cos\theta \qquad (4)$$

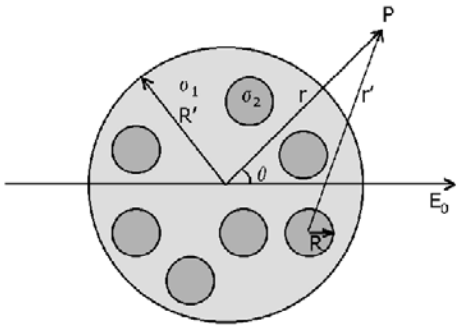

Figure 2: The model used for the derivation of the Maxwell mixture equation

Equating expressions (3) and (4), noting that

$$\frac{NR^3}{R'^3} = p \qquad (5)$$

is the volume fraction of small particles suspended in the large spherical boundary, we obtain the so-called Maxwell's mixture equation:

$$\frac{\sigma_1-\sigma}{2\sigma_1+\sigma} = p\frac{\sigma_1-\sigma_2}{2\sigma_1+\sigma_2} \qquad (6)$$

The spherical particles may have different sizes.
Reformulating relation (6) yields for the effective conductivity of the mixture

$$\sigma = \sigma_1\frac{(2\sigma_1+\sigma_2)-2p(\sigma_1-\sigma_2)}{(2\sigma_1+\sigma_2)+p(\sigma_1-\sigma_2)}, \qquad (7)$$

For substances with a very low p (e.g. amniotic fluid), the conductivity of the mixture increases linearly with p, because for a small p higher order terms in p can be neglected. In that case expression (7) reads:

$$\sigma = \sigma_1\left(1+3p\frac{\sigma_2-\sigma_1}{2\sigma_1+\sigma_2}\right) \qquad (8)$$

The Maxwell mixture equation was derived for a dilute solution of spherical particles, assuming that the distance between the particles is much larger than their size that each may be regarded as being under the influence of a uniform field. If we have a suspension of densely packed particles, the Maxwell mixture equation will not be valid anymore. Hanai [4] derived an equation for higher values of p (p > 0.4).
The derivation starts with equation (7) by incrementing the effective conductivity σ' with a fraction $\Delta\sigma'$. By adding particles to the suspension, the increase in the effective conduction can be expressed:

$$\sigma'+\Delta\sigma' = \sigma'\frac{(2\sigma'+\sigma_2)-2\frac{\Delta p'}{1-p'}(\sigma'-\sigma_2)}{(2\sigma'+\sigma_2)+\frac{\Delta p'}{1-p'}(\sigma'-\sigma_2)} \qquad (9)$$

After rearrangement and neglecting the second order term, the equation reads

$$\frac{2\sigma'+\sigma_2}{3\sigma'(\sigma'-\sigma_2)}\Delta\sigma' = -\frac{\Delta p'}{1-p'} \qquad (10)$$

Starting with the solvent, particles are added and the effective conductivity of the newly created suspension is calculated. Subsequently, particles are added to this new created suspension and so on. Hence, Hanai's equation is obtained by integration of both sides of expression (10):

$$\int_{\sigma_1}^{\sigma}\frac{2\sigma'+\sigma_2}{3\sigma'(\sigma'-\sigma_2)}d\sigma = \int_0^p -\frac{dp'}{1-p'} = \ln(1-p) \qquad (11)$$

yielding:

$$\frac{\sigma-\sigma_2}{\sigma_1-\sigma_2}\left(\frac{\sigma_1}{\sigma}\right)^{1/3} = 1-p \qquad (12)$$

At low frequencies and low current densities the currents will be in the extracellular space only as explained below. Assuming that intracellular currents are zero is equivalent to assigning a conductivity $\sigma_2 = 0$ to the cells. As a consequence expression (12) reads

$$\sigma = \sigma_1 (1\text{-}p)^m \qquad (13)$$

where m is 3/2 (for spherical particles). This expression is called Archie's law. The value of m depends on the shape of the particles. Its value is 3/2 for spherical particles. It is 2 for long cylinders with the axis perpendicular to the external field and it is 1 for cylinders with the axis parallel to the field.
For oriented ellipsoids with the field applied along the a-axis:

$$m = 1/(1 - L_a); \quad L_a + L_b + L_c = 1; \qquad (14)$$

where L_a is the depolarisation factor along the a-axis, see Fig.3 (for spheres $L_a = 1/3$) [5].
In a similar way to the derivation given above, Archie's law can also be derived for ellipsoidal particles that are randomly oriented in a dense packing. For an ellipsoid of revolution with semi-axes a, b and c where b = c, the value of m is displayed in Fig. 4 as a function of the ratio a/b. (The proper expressions can be obtained by taking the expressions derived by Boned and Peyrelasse [6] assuming that the cells are non-conducting.)

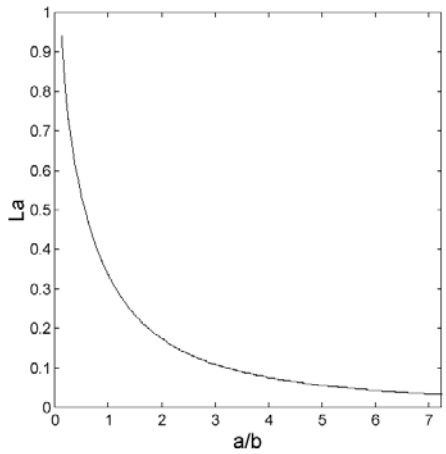

Figure 3:The depolarization factor in the direction of the a-axis for an ellipsoid of revolution with semi-axes a, b and c, where b = c.

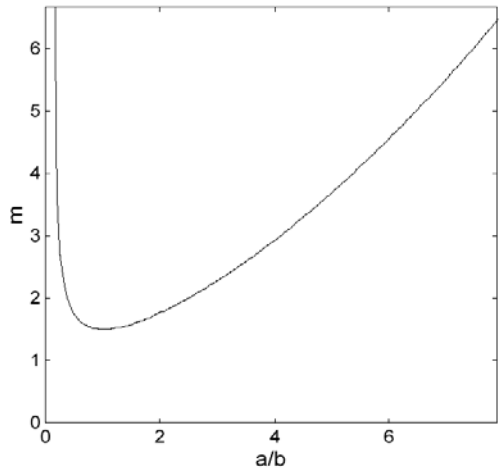

Figure 4: The exponent m in Archie's law against the ratio of the axes (a, b, c) of densely packed, randomly oriented, ellipsoids of revolution (b =c)

The assumption that at low frequencies and for low current densities, currents will only be present in the extracellular space, is based on model calculations involving a spherical model of the cell. In the model, a sphere of radius R with conductivity σ_3 is surrounded by a concentric spherical shell modelling the membrane with thickness d ($d << R$) and conductivity σ_2. The cell is suspended in a medium with conductivity σ_1.
Typical values of a cell are R = 15 µm; $\sigma_1 = \sigma_3 = 1{,}1$ S/m; $\sigma_2 = 10^{-8}$ S/m; d = 6 nm. The intracellular current density is a factor 10^5 smaller than the extracellular current density. The results are depicted in Fig. 5. The currents circumvent the cell. The current density at a distance from the cell smaller than the radius of the cell is disturbed by the cell.

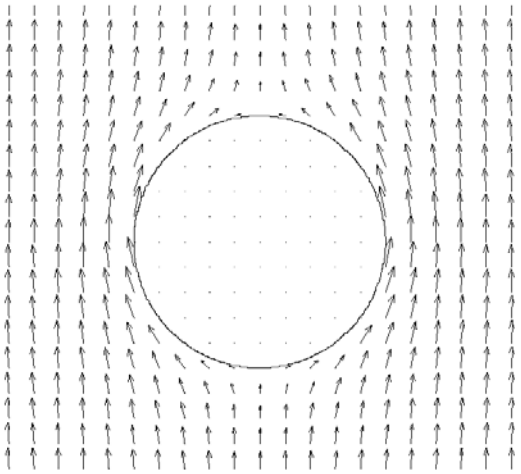

Figure 5: The current density around a cell. The intracellular current density is too small to be depicted.

Discussion

The theory discussed can be of help to diminish the uncertainties in the values of the conductivity presented in the literature. On the basis of the theory one should scrutinise the way the measurements were carried out and one should ensure that the findings are consistent. For instance, the extracellular space is often obtained from measurements of the conductivity using the Maxwell mixture equation, which is not appropriate if the volume fraction occupied by the cells is higher than 40 % [2].
The value of p can be deduced from the anisotropy factor. For instance, if we assume that the muscle fibres can be modelled as long cylinders with the same orientation, the ratio between the conductivity measured along the fibres σ_l and that perpendicular to them σ_t is according to Archie's law (1 - p). Taking the anisotropy factor $\sigma_l/\sigma_t = 10$ leads to the value p = 0.9. This value is in agreement with the value reported for the rat [7].
The applied field has to be uniform in the region where the effective conductivity is measured. Consequently, needle electrodes cannot be used to generate the current. Moreover, the potential measured by means of a needle electrode may be measured in the direct neighbourhood of the cell, where the potential is disturbed by the presence of the cell. For instance Gielen measured the conductivity of muscles by a small electrode (diameter 0.5 mm) and found an anisotropy factor that was about two, although they used a value for (1 - p) that was 10

[8]. In other words, they did not measure the effective conductivity but the local one.

According to Archie's law, the conductivity of tissues is linear with the conductivity of the solvent. The conductivity of the solvent is temperature dependent. Consequently, the conductivity should be measured at 37ºC.

Three examples that differ with respect to the volume fraction occupied by the cells will be shortly discussed. The first is the conductivity of amniotic fluid in which the concentration of phospholipids increases throughout gestation. As this concentration is low, the conductivity will be linear with the volume fraction occupied by the particles as follows from expression (7). Measurements are indeed in agreement with this expression [9].

The second example is the cortex of the brain that has a layered structure with a columnar organisation. Consequently, the cells in a small region will be subjected in the same way to the applied field. The conductivity of the cortex is in good agreement with expression (11) when m is about 3/2 [2]. The interstitial space in the brain is confined to narrow clefts 20-50 nm wide between the densely packed nerve and glial cells, the volume fraction p is about 80 %. As no significant concentration gradients exist between the cerebrospinal fluid and the interstitial fluid, one may assume that they have the same electrical conductivity. Using Archie's law and taking for the conductivity of the interstitial fluid that of the CSF (1.79 S/m), leads to an effective conductivity of the cortex of 0.16 S/m.

The third example is blood outside of the human body. Geddes and Sadler measured the conductivity for human blood at 25 kHz and 37 °C, having a hematocrit (the percentage of the volume of blood made up by red blood cells) ranging from 0 to 70 percent and found an exponential fit between the measured data and an exponential curve for $\rho = 53.2e^{0.022H}$ (H is the hematocrit) with a correlation coefficient of 0.989 [10]. The red blood cells are randomly orientated and densely packed. Fitting their data to Archie's law leads to an excellent fit for m = 1.44. The red cells are biconcave disks, each with a diameter of about 8 µm, a thickness of 2 µm at its edge, and a volume of about 94 μm^3. If we model the red blood cells as ellipsoids with a = 2 µm; b = c = 4 µm computation of the parameter m yields m = 1.57. This higher value can be understood by keeping in mind that the ellipsoids acting as our model are more streamlined than the real cells. Moreover, the low-frequency value will be somewhat lower than the value at 25 kHz due the α-dispersion.

We conclude that a better understanding of the influence of the architecture of the tissues on the conductivity, can help to choose consistent and reliable values to be used in volume conductor models.

References

[1] Cole, K.S., Li,C., Bak, A.F., Electrical analogues for tissues, Exp. Neurology, 1969, 459-473.

[2] Nicholson, C., Rice, M.E, The migration of substances in the neural microenvironment, Annals of the New York Academy of Sciences, Annals of the New York Academy of Sciences, 1986, 481: 55-71.

[3] Sen, P.N., Scala, C., Cohen, M.H., A self-similar model for sedimentary rocks with application to the dielectric constant of fused glass beads, Geophysics, 1981, 46: 781-795.

[4] Hanai, T., Theory of the dielectric dispersion due to the interfacial polarization and its application to emulsion, Kolloid Z., 1960, 171: 23-31.

[5] Boyle, M.H., The electrical properties of heterogeneous mixtures containing an oriented spheroidal dispersed phase, Colloid & Polymer Sci., 1985, 263: 51-57.

[6] Boned, C., Peyrelasse, J., Etude de la permittivite complexe d'ellipsoïdes disperses dans un milieu continu. Analyses theorique et numerique, 1983, Colloid & Polymer Sci., 1983, 261: 600-612.

[7] Kobayashi, N., Yonemura, K., The extracellular space in red and white muscles of the rat, Jap. J. Physiol., 1967, 17: 698-707.

[8] Gielen, F., Electrical conductivity and histological structure of skeletal muscle. Ph. D. Thesis, Universtity of Twente, The Netherlands, 1983.

[9] De Luca, F., Cametti, C., Zimatore, G., Maraviglia, B., Pachi, A., Use of low-frequency electrical impedance measurements to determine phospholipid content in amniotic fluid, Phys. Med. Biol., 1996, 41: 1863-1869.

[10] Geddes, L.A., Sadler, C., The specific resistance of blood at body temperature, Med. Biol. Eng., 1973, 11: 336-339.

Informed spatial basis functions in minimum norm solutions for the electromagnetic source localisation problem.

Phillips C.[1,2,3], Rugg M.D.[2], Friston K.J.[1]

[1]Wellcome Department of Cognitive Neurology, Institute of Neurology, UCL, London, UK ;
[2] Institute of Cognitive Neuroscience, UCL, London, UK;
[3]Cyclotron Research Centre, University of Liège, Liège, Belgium

Introduction

Linear inverse solutions have been applied extensively to solve the bioelectromagnetic inverse problem. In contrast to discrete dipole models, linear inverse solutions do not require any assumptions about the number of active sources and lead to a fully 3D representation of the electrical activity of the brain. However, the problem is underdetermined: there are many more parameters to estimate (relative to the number of dipole locations considered) than data available (relative to the number of electrodes). In order to ensure the uniqueness of the solution, existing linear methods generally apply constraints on the solution, for example: minimum 2-norm, maximum smoothness [1], optimal resolution [2], etc. These methods provide solutions with relatively poor spatial resolution because they neglect, wholly or in part, anatomical information relevant to the real source distribution.

Our method aims to model the spatial source distribution by using a set of basis functions. By appropriately defining these basis functions, we are able to include a priori information about the sources and our solutions will *de facto* belong to the subspace spanned by these basis functions. The priors enter as constraints on the covariance structure of the source power (over space), and are used to motivate the selection of a spatial basis set that maximises the information between the sources and their projection on that set. The orientation of each dipole is fixed and orthogonal to the cortical sheet, and therefore only the amplitude of the sources remains unknown. In a second step, we solve for the source distribution using a "classical" minimum norm method. Other methods could also be applied as the informed basis functions are generated before the computation of the solution.

Here we test our method using a realistic head model and noiseless instantaneous simulated data.

Method

The sources of the EEG signal are, in the absence of any data, assumed to conform to a fixed, uniform, three-dimensional distribution of current dipoles throughout the entire brain volume. Three strong assumptions are made about the sources: they are located in the grey matter, they are oriented orthogonal to the cortical sheet and, for a sufficiently dense dipole distribution, they present some locally coherent activity (or smooth activity along the cortical sheet) [3]. By fixing the orientation of each dipole, we can reduce the source localisation problem from a vectorial problem into a scalar problem. The two other assumptions, spatial smoothness and localisation within grey matter, are used to calculate the basis functions set.

The matrix K represents the smoothness along the cortical sheet. A current dipole represents the coherent electrical activity of the brain over a small volume. A grey/white matter coefficient is determined for each dipole such that its value is: 0 if the volume around the dipole contains only white matter, 1 if the volume contains only grey matter and a value between 0 and 1 otherwise. These coefficients are contained in the diagonal matrix G.

If other functional imaging results (e.g. the findings of a PET or fMRI study) are available, they may also help to solve the source localisation problem. This information has to be regarded as probabilistic [4] and therefore can be used to generate the basis functions set. It could also be introduced at the second step of the method, when the minimum norm solution is sought. These additional probabilistic constraints are either combined with G (if used to generate the basis functions) or represented by the matrix H (if introduced at the second step).

The source localisation problem can be stated as:

$$v = L\,j$$

where v is the electric potential at the electrodes, j the amplitude of each current dipole and L is the lead field linking j and v. The orientation of the current dipole is included in L so that j represents only the amplitude of the dipole.

To reduce the solution space j to k, we want j and k to be related by:

$$j = R\,k \quad \Leftrightarrow \quad R^T j = k$$

where R maximises the mutual information (MI) [5] between j and k:

$$\mathrm{MI}(j,k) = \mathrm{H}(j) + \mathrm{H}(k) - \mathrm{H}(j \cap k) = \mathrm{H}(k)$$

because $\mathrm{H}(j) = \mathrm{H}(j \cap k)$.

Information theory tells us that if k is a multinormal system then:

$$H(k) \propto \ln(|C_k|) = \sum \ln \lambda_i$$

where $C_k = k\,k^T$ is the variance/covariance matrix of k and λ_i its eigenvalues.

We then obtain:

$$MI(j,k) \propto \ln |R^T j\, j^T R| = \sum \ln \lambda_i$$

and the optimum R should be chosen as the eigenvectors of $j\,j^T$ corresponding to the highest eigenvalues λ_i.

We are now able to include our prior knowledge, K and G, about j:

- Prior 1, smoothness K: $j\,j^T = K^T K$ (correlation matrix).
- Prior 2, grey/white matter G: $j\,j^T = G^{T/2} K^T K G^{1/2}$.

Finally R is obtained by calculating the eigenvalue decomposition of $G^{T/2} K^T K G^{1/2}$ or preferably by using a singular value decomposition:

$$U S V^T = \mathrm{svd}(K G^{1/2})$$

and keeping the highest singular values in S, see fig. 1 and the corresponding vectors in V.

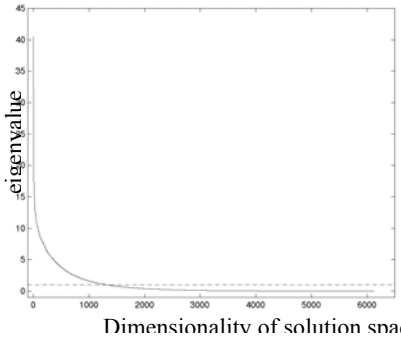

Figure 1, decreasing eigenvalues of $G^{T/2} K^T K G^{1/2}$

We can now reformulate the source localisation problem like this:

$$v = L_R\, k$$

where $L_R = LR$ and $k = R^T j$. To solve this latter problem we use a minimum norm method:

$$k = \arg\min_k \left\{ \|L_R k - v\|^2 + \lambda \|H R k\|^2 \right\}$$

We have assumed noiseless data, so the solution will be:

$$k = T_R v \text{ or } j = T v$$

where $T = R T_R$ and

$$T_R = \left(R^T H^T R H\right)^{-1} L_R^T \left[L_R \left(R^T H^T R H\right)^{-1} L_R^T\right]^{-1}$$

Application

We have applied the method described above using a realistic head model generated from structural MRI data. The lead field matrix L, the solution of the "forward problem", is calculated with the "boundary element method" [6] for a set of 61 quasi equidistant electrodes (see fig. 2) and 6122 dipoles spread within the brain volume on a regular three dimensional grid. The cortical surface is extracted for each hemisphere using the "BrainVoyager" software package [7], see fig. 3.

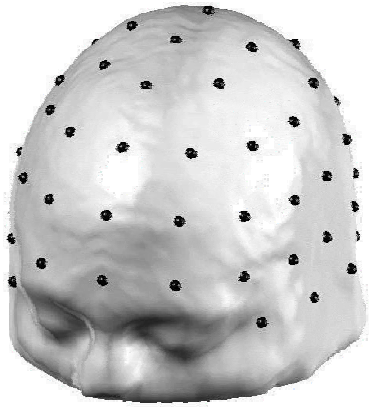

Figure 2, scalp surface with electrode locations

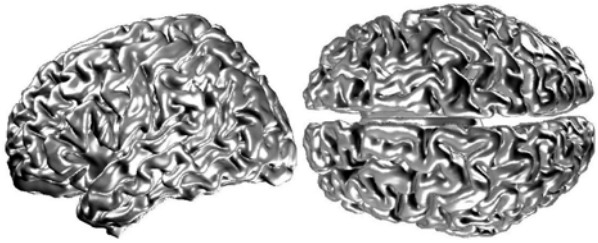

Figure 3, views of the cortical surface

The orientation of each dipole is defined to be normal to the closest cortical sheet patch, as shown in fig. 4, and is included in the lead field L.

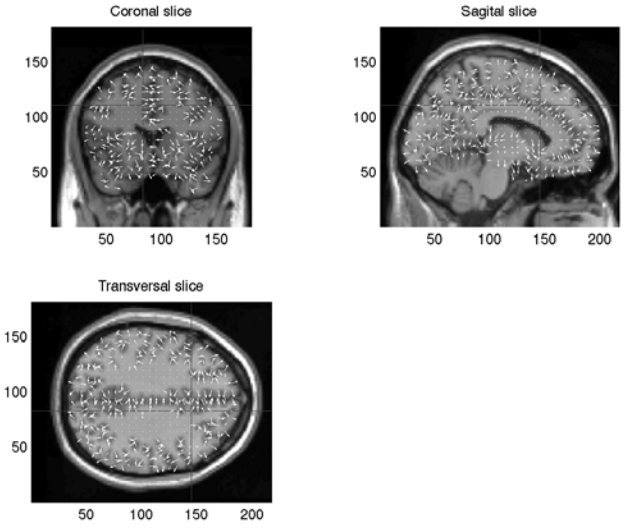

Figure 4, oriented dipoles in the grey matter.

We segment the MRI with the segmentation function of the SPM software package [8], and the grey matter image is averaged over each dipole cubic volume to

provide the grey/white matter coefficient of the matrix G, see fig. 5. To estimate the smoothness over the cortical sheet expressed by the matrix K, we use Dijkstra's algorithm [9] to measure the distance between any two points (here the closest cortical points to the dipoles) on a tessellated irregular surface.
With K and G we calculate the singular value decomposition $USV^T = \mathrm{svd}(KG^{1/2})$ and keep only the singular vectors of V corresponding to the normalised singular values greater than unity (see fig. 1). Eventually, from a solution space j of 6122 dimensions, we end up with a reduced solution space k of 1562 dimensions (a reduction of almost 85 percent), and the same number of orthonormal basis functions in R. Thereafter we can simply calculate the inverse solutions: T_R and T. We will refer to this solution as the "informed basis functions" (IBF) solution.
We also calculate a direct minimum norm (MN) solution without reducing a priori the solution space.

Results and discussion

We simulated sources that might be active in a typical cognitive ERP study, by assuming that the task activated left and right occipital cortex, left and right fusiform regions and a right frontal area. We define only one active dipole in each occipital region. For the left and right fusiform and the frontal regions we modelled distributed sources. Figure 6 shows the sources configuration. We used these sources to generate the EEG signal at each electrode and also to produce a simulated fMRI activation map, shown in fig. 7.
We first consider both MN and IBF solutions without the fMRI activation map, setting the matrix H to be the identity matrix. We reconstruct the 2 occipital sources as if they were simultaneously active, then the 2 fusiform sources together and finally the single frontal source, see fig. 8. Both method localise correctly the superficial sources (occipital and frontal) but fail to reconstruct the deep fusiform sources. Because smoothness is incorporated to constrain the basis functions, the IBF solution is smoother and more distributed than the MN solution. This latter solution tends to concentrate all the activity on a few superficial voxels.
We then use the simulated fMRI a priori to constraint the solution of the MN approach and at the second step for the IBF approach. Similarly, we reconstruct the 2 occipital sources as if they were simultaneously active, then the 2 fusiform sources together and finally the single frontal source, see fig. 9. Here all the sources are reconstructed accurately, including the deep fusiform sources.
In this preliminary work, therefore we have only used noise free simulated data. Under these optimal conditions, there is no need for much constraint and both MN and IBF methods yielded reasonable 3D solutions. The aim of the IBF method however is to allow the inclusion of any constraint on the solution. For example, further developments will incorporate temporal basis function [10]. These (with the spatial basis functions presented here) should be useful in the treatment of more realistic data that is time extended data mixed with real noise and background activity. In this case, spatio-temporal constraints are crucial to reconstruct even superficial sources.

Conclusions

We have introduced an original and general framework for solving the EEG source localisation problem that allows the inclusion of any a priori knowledge about the solution space. We have successfully applied our method on a spatially realistic model and data with a minimum norm approach. We tested our method on noiseless instantaneous simulated data. The results obtained show good spatial resolution and robust performance.
We plan to extend our method to more realistic, time extended data mixed with real noise and background EEG activity.

References

[1] Pascual-Marqui, R.D., Michel, C. and Lehman, D., Low-resolution electromagnetic tomography: a new method for localising electrical activity in the brain, Int. J. Psychophysiology, 1994, 18: 49-65.

[2] Grave de Peralta, R., Hauk, O., Gonzalez Andino, S., Vogt H and Michel C, Linear inverse solutions with optimal resolution kernels applied to electromagnetic tomography, Human brain mapping, 1997, 5: 454-467.

[3] Dale, A.M., Sereno, M.I., Improved localisation of cortical activity by combining EEG and MEG with MRI cortical surface reconstruction: a linear approach, J. Cogn. Neurosci., 1993, 5:162-176.

[4] Rugg, M.D., Convergent approaches to electrophysiological and haemodynamic investigations of memory, Hum. Brain Mapp., 1998, 6:394-398.

[5] Jones, D.S., Elementary information theory, Oxford, Carendon Press, 1979.

[6] Sarvas, J., Basic mathematical and electromagnetic concepts of the biomagnetic inverse problem, Phys. Med. Biol., 1987, 32: 11-22.

[7] Goebel, R., Brain Innovation Rainer Goebel, http://www.BrainVoyager.de.

[8] Ashburner, J. and Friston, K.J, Multimodal image coregistration and partitioning – a unified framework, NeuroImage, 1997, 6:209-217.

[9] Dijkstra, E.W., A note on two problems in connection with graphs, Numerische Mathematik, 1959, 1; 269-271.

[10] Phillips, C., Rugg, M.D. and Friston, K.J., A priori spatio-temporal basis functions in minimum norm solutions, HBM99 abstract, to be published in NeuroImage.

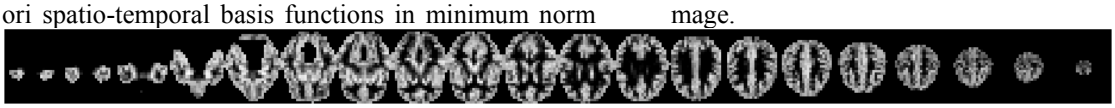

Figure 5, grey/white matter value susbampled for the dipoles location.

Figure 6, active sources: from top to bottom, occipital, fusiform and frontal sources.

Figure 7, a priori fMRI statistical map.

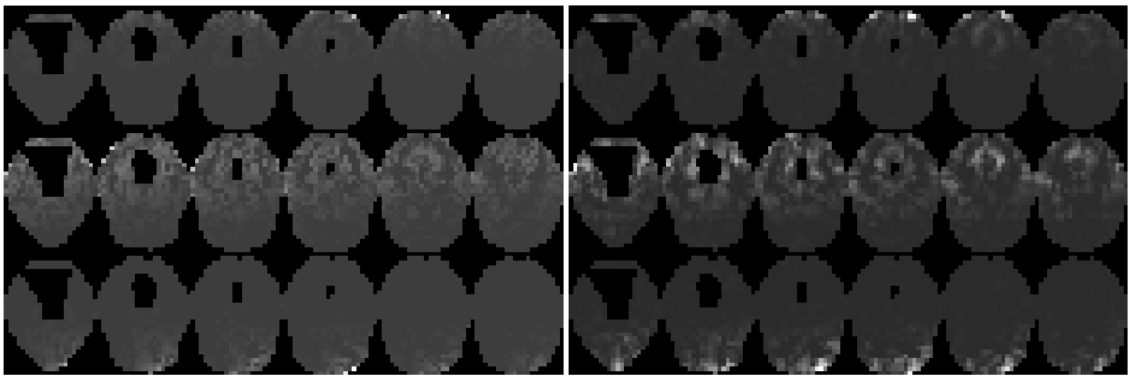

Figure 8, reconstruction of the sources without functional imaging a priori, left: simple minimum norm, right: informed basis functions and minimum norm; from top to bottom: occipital, fusiform and frontal sources.

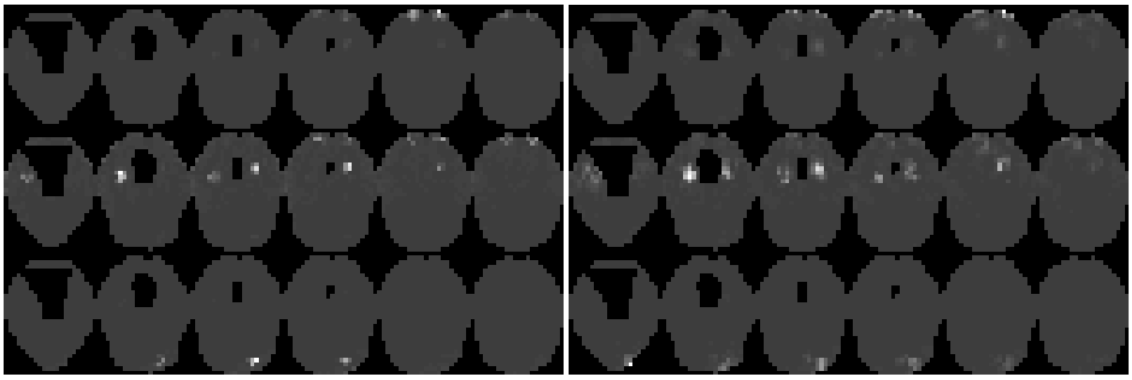

Figure 9, reconstruction of the sources with functional imaging a priori, left: simple minimum norm, right: informed basis functions and minimum norm; from top to bottom: occipital, fusiform and frontal sources.

Secondary Sources in the Skull

M.J. van Burik, M.J. Peters

Low Temperature Department, Faculty of Applied Physics,
University of Twente, Enschede, The Netherlands

1 Introduction

The head is not a homogeneous medium, on the contrary, it consists of many regions of different electric conductivity. One of the most dominant regions is the skull. The conductivity of this structure is typically a factor 20 to 80 lower than that of other tissues. Hence, it is a barrier for current flow to the scalp and as a result the EEG at the scalp is strongly attenuated and smeared out. If a hole is present in the skull, the potential across the scalp is influenced [1]. The objective of this paper is to investigate a skull with holes in it. This is done by using data from a patient that was undergoing epilepsy surgery. The patient has two trephine holes in the skull. Through these holes, subdural and depth electrodes were inserted. Normally, the intracranial electrodes are used for the measurement of the potential. In this case, the intracranial electrodes were used to induce a current in the brain and the resulting potential distribution at the scalp was measured. Since both the scalp EEG and the position intracranial electrodes are known, sufficient data is available to study the skull [2].

2 Method

In a patient that was undergoing epilepsy surgery, 14 bundles of electrodes were inserted through two trephine holes. On each of these reeds, either 6 electrodes (depth bundle) or 7 electrodes (subdural bundle) were available. The subdural reeds covered the left and right temporal and frontal lobes. The depth reeds were inserted directly underneath the holes and followed a line to the base of the skull. After the introduction of the electrodes, the holes were closed by bone plugs and the gap between the skull and plugs was filled with splinters of bone, blood and other liquids. Fig. 1 shows the reeds of electrodes and their positions on the inside of the skull and the surface of the brain. An MR and a CT scan were available of this subject. The MRI was made before the patient underwent the implantation of the electrodes. The CT scan was made shortly after the implantation, and showed the reeds of the electrodes clearly. As the MR and CT scan covered different volumes of the head and were oriented differently, they were fused using an algorithm developed by [5]. The CT scan was used to track the path of the inserted reeds. This was necessary to determine the positions of the electrodes on the reeds. By localizing the endpoint of each reed and following it towards the hole, the position of each electrode could be determined.

A 20 Hz-sinusoidal current was induced between contiguous pairs of intracranial contacts, while an EEG was being recorded through 21 scalp electrodes. Nineteen stimulation sites were used. The reference electrode was placed posterior to the line connecting the center of the two holes. Since the distance between the pairs of electrodes was small compared to the distance at which the potential was measured, it was assumed that the induced activity due to a pair of electrodes could be modeled by a current dipole. This dipole was placed halfway between the two stimulation electrodes, and oriented along the line connecting them.

The boundary element method is used for the computation of the volume conduction effects. In this method, the head is modeled by piecewise homogeneous compartments that are assumed to be isotropic

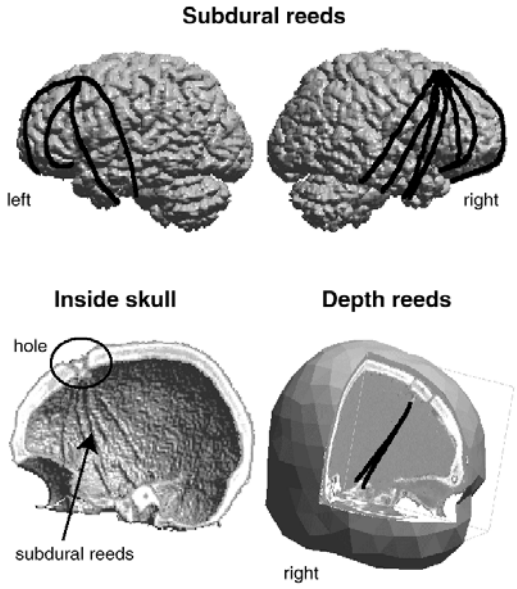

Figure 1: Top: positions of the subdural reeds shown on the rendered surface of the brain. Bottom left: inner surface of the skull with one of the holes and the subdural reeds. Bottom right: depth electrodes.

(e.g. [3, 4]). The potential at the scalp due to a dipole in the brain, can be calculated by taking into account the geometry of each interface and the conductivity of each compartment. Normally, the head is assumed to be consisting of three regions, i.e. the brain, the skull and the scalp, and their interfaces are described by surfaces constructed of triangular elements.

For the calculation of the volume conduction effects, the head is modeled by one homogeneous compartment. This model is constructed from the MRI and consists of 694 triangular elements (see Fig. 3). Using the boundary element method, the potential at the scalp surface due to each of the 19 implanted dipoles is calculated. Obviously, the potentials calculated using this model, do not match to the ones measured since the model used is not very realistic. For instance, it does not include the skull. The difference between the measured potential and the calculated potential due to the implanted dipole is accounted for by using fictitious sources. The fictitious sources simulate the influences of the skull and are in the following referred to as secondary sources. The secondary sources are set up at the nodes of a surface that was positioned halfway between the inner and outer surface of the skull, see Fig. 2 and Fig. 3. The inner and outer surfaces of the skull were extracted from the CT scan. The orientation of the secondary sources is in the direction of the normal vectors at the surface.

The measured potential distribution $\vec{\varphi}_{scalp}$ at the scalp is expressed as:

$$\vec{\varphi}_{scalp} = \vec{\varphi}_{dipole} + \mathbf{A}\vec{j}. \tag{1}$$

Here, $\vec{\varphi}_{dipole}$ is the potential distribution calculated at the scalp using the homogeneous boundary element model. Matrix $\mathbf{A}$ projects the strengths of the secondary sources $\vec{j}$ to a potential at the electrodes, $\vec{j}$ is a column vector with the strengths of the secondary sources at the nodes of the surface.

The ratio between the magnitude of the potential

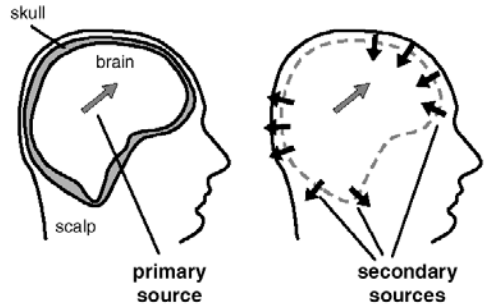

Figure 2: Left: Scheme showing a head model with three regions and a current source in the brain. Right: Equivalent situation using a homogeneous scalp model, secondary sources in the skull and the current dipole in the brain.

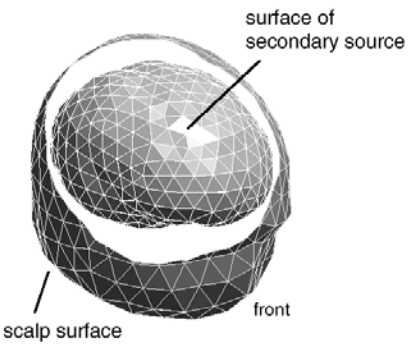

Figure 3: Part of the scalp surface shown together with the surface at which the secondary sources are placed.

due to the secondary sources in the homogeneous medium and that due to the dipole in the inhomogeneous medium, is a factor 2-3 [6]. Since in this case, the magnitude of the current dipole was unknown, it is assumed that the potential due to the secondary sources, is a factor 3 times the magnitude of the measured scalp potential.

The strengths of the secondary sources are estimated using:

$$\vec{j} = \mathbf{A}^{+}\left(\vec{\varphi}_{scalp} - \vec{\varphi}_{prim}\right) \tag{2}$$

where $\vec{\varphi}_{prim}$ is scaled such that $\|\vec{\varphi}_{scalp} - \vec{\varphi}_{prim}\|$ is 3 times $\|\vec{\varphi}_{scalp}\|$, and

$$\mathbf{A}^{+} = \left(\mathbf{A}^{t}\mathbf{A} + \lambda\mathbf{L}^{t}\mathbf{L}\right)^{-1}\mathbf{A}^{t}. \tag{3}$$

Here $\mathbf{L}$ is the surface Laplacian operator [7], $\mathbf{A}^{t}$ means the transpose of matrix $\mathbf{A}$ and λ is a regularization parameter, which was set equal to the smallest singular value of $\mathbf{A}$. The application of the surface Laplacian operator suppresses high spatial frequencies while low spatial frequencies are unaffected.

3 Results

Fig. 4 shows the results obtained for 4 different current dipoles. For each of the sources, the position of the dipole is shown in a coronal and sagittal view of the CT. The measured potential distribution, the potential distribution due to the current dipole, the potential distribution due to the secondary sources and the distribution of the estimated strengths of the secondary sources are shown as well. The first two dipoles shown are positioned subdurally, while the others were positioned on depth bundles. For the latter dipoles, the sagittal view of the CT images shows one of the holes that is present in the skull. The dipoles are pointing directly towards this hole.

The measured potential distribution at the scalp is smoother than the potential distribution due to the

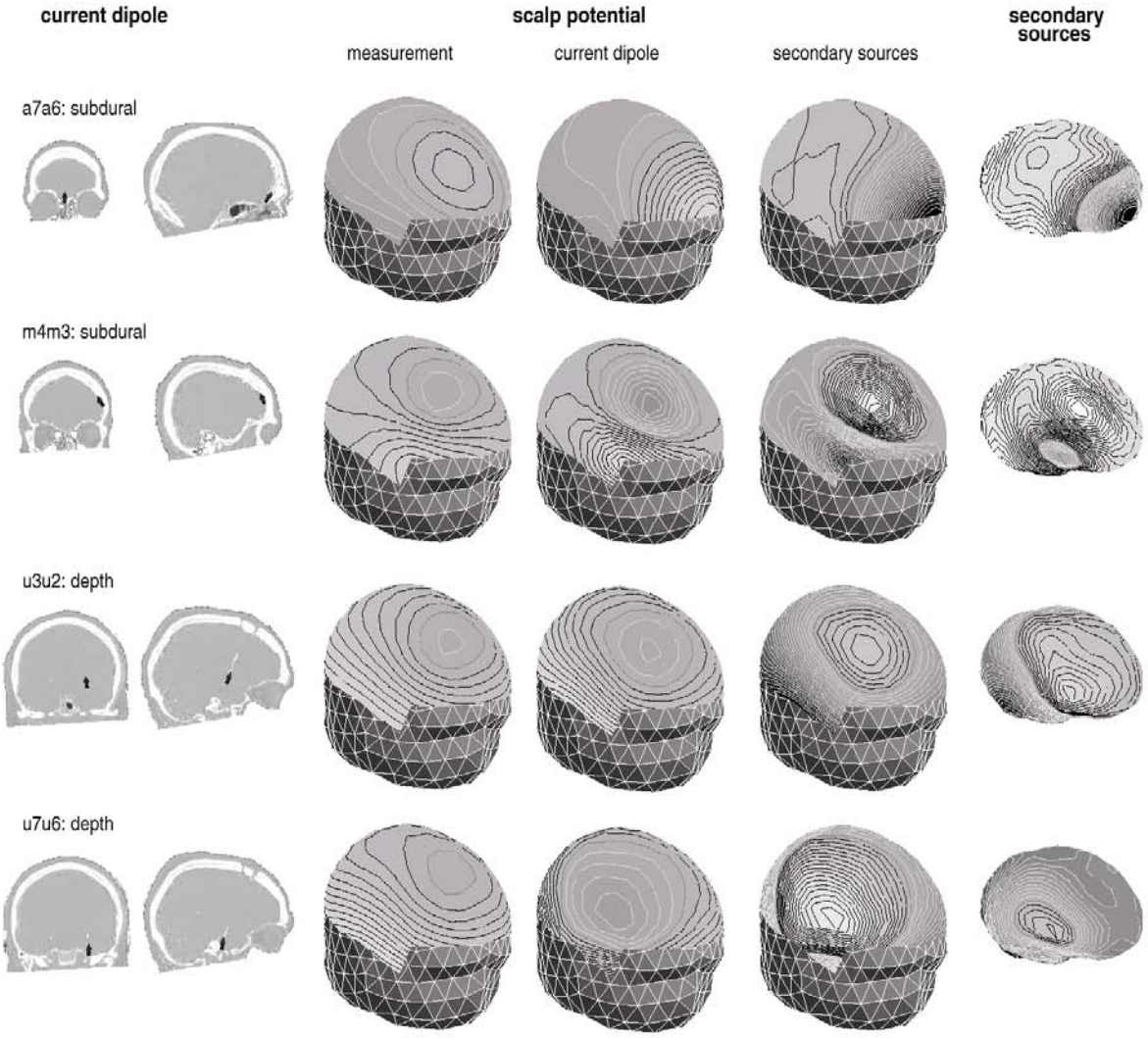

Figure 4: Left: The position of the current sources shown in a coronal and sagittal view of the CT. Middle three columns, from left to right: The measured potential, the potential due to the current source and the potential due to the secondary sources. For each source, the iso-potential lines are scaled equally for each distribution. Right: The distribution of the strengths of the secondary sources. For each distribution, a white line is used for negative values, a black line indicates positive values and the grey line corresponds to zero.

current dipole. Since the boundary element model did not incorporate the skull, the potential calculated from the dipole is less attenuated compared to the measured one. For dipoles a7a6 and u7u6, a clear shift of the measured potential distribution towards the holes is found. For the other two dipoles, the influence of the holes is less obvious.

The potential distribution calculated from the estimated secondary sources accounts for the difference between the measured potential and the potential calculated from the current dipole. The distribution of the secondary sources shows for dipole m4m3, a dipolar-like pattern around its position. For dipole a7a6 this pattern is less dipolar-like. For the dipoles u3u2 and u7u6 the distribution of the secondary sources shows pronounced extremes at the base of the skull (not shown in Fig. 4).

The distribution of the secondary sources for the other 15 dipoles show two different aspects (not shown here). While for some of the measurements distinct extremes are found underneath the two holes, are for other measurements clear extremes found at the base of the skull.

4 Discussion

A CT and MRI scan are used as basis for the geometrical modeling. Both the skull and the positions of the subdural and depth electrodes are clearly visible in a CT scan, whereas the scalp can be extracted from the

MRI. This allows for accurate modeling of the geometry. The CT images show that at the base of the skull, the skull is not homogeneous in thickness.

The estimated secondary sources simulate the volume conduction effects of the skull. Due to the poor conductivity of the skull, the potential distribution at the scalp is attenuated. To mimic this effect by means of the secondary sources, the secondary sources have to partly cancel the electric currents flowing as a result of the current dipole to weaken the potential at the scalp. For all dipoles shown, the potential distribution due to the secondary sources, shows a similar pattern to that due to the current dipole. Only, the sign of the potential distributions is opposite. As a result, the sum of the two distributions gives the measured potential distribution.

The patient has two trephine holes in the skull. At those positions, the potential distribution at the scalp in the vicinity of the holes shows pronounced extremes. This is seen in Fig. 4 and also found by means of simulations (see e.g. [1]). In the holes, more electric current flows. Hence, the secondary sources at those positions, are estimated such that the potential distribution over the holes is less damped or estimated such that the potential distribution over the holes is enhanced. The former is the case when the current dipole is pointing in the direction of one of the holes and its potential distribution already shows an extreme over it (dipole u3u2). The latter occurs when the potential distribution due to the current dipole is different from the one measured (dipole a7a6).

The formulation of the boundary element method can be interpreted as yielding the potential as if the entire space were uniform, but in addition secondary sources are set up at the interfaces between regions of different conductivity. These fictitious secondary sources that the boundary conditions are obeyed. The secondary sources have a current dipole intensity that is proportional to the step in the conductivity across an interface and the potential. Their orientations are in the direction of the normal vector at the interface. The skull has two interfaces; one on the inside (interface to the brain), one on the outside (interface to the scalp). As a consequence, secondary sources are placed at both interfaces. In this study, the secondary sources are located at a surface placed halfway between the inner and outer surface of the skull. These secondary sources simulate the effect of both interfaces. The estimated strengths of the secondary sources are different from the strengths of the secondary sources that would have been found when at both interfaces secondary sources are placed. However, to distinguish between the contribution of the secondary sources on either interface is very difficult since the surfaces are very close to each other.

References

[1] B. van den Broek, F. Reinders, M. Donderwinkel, and M.J. Peters, "Volume conduction effects in EEG and MEG", *Electroenceph. Clin. Neurophysiol.*, vol. 106, pp. 522–534, 1998.

[2] P. Nunez and K. Pilgreen, "The spline-laplacian in clinical neurophysiology: a method to improve EEG spatial resolution", *J. Clin. Neurophysiol.*, vol. 8, no. 4, pp. 397–413, 1991.

[3] M. Hämäläinen and J. Sarvas, "Realistic conductivity geometry model of the human head for interpretation of neuromagnetic data", *IEEE Trans. Biomed. Eng.*, vol. 36, no. 2, pp. 165–171, 1989.

[4] J. Meijs, O. Weier, M.J. Peters, and A. van Oosterom, "On the numerical accuracy of the Boundary Element Method", *IEEE Trans. Biomed. Eng.*, vol. 36, no. 10, pp. 1038–1049, 1989.

[5] P.A. van den Elsen, *Multimodality matching of brain images*, PhD thesis, Utrecht University, The Netherlands, 1993.

[6] J.C. Huang, C. Nicholson, and Y.C. Okada, "Distortion of magnetic evoked fields and surface potentials by conductivity differences at boundaries in brain tissue", *Biophys. J.*, vol. 57, pp. 1155–1166, 1990.

[7] G.J.M. Huiskamp, "Difference formulas for the surface Laplacian on a triangulated surface", *Journal of Computational Physics*, vol. 95, pp. 477–496, 1991.

The Electrically Silent Cardiac Magnetic Field

Fischer G. [1], Tilg B. [1], Modre R. [1], Fetzer J. [2], Rucker W. [2], Huiskamp G. [3], and Wach P. [1]

[1]Institute of Biomedical Engineering, Technical University Graz, Graz, Austria
[2]Institute for Theory in Electrical Engineering, University Stuttgart, Stuttgart, Germany
[3]Department of Clinical Neurophysiology, Utrecht University Hospital, Utrecht, Netherlands

Introduction

It is commonly assumed that biomagnetic fields contain additional information compared to bioelectric fields. Plonsey showed [1], that only the divergence of an impressed cardiac current density field (flux source) enters the calculation of the body surface potential. In contrast the magnetic field calculation is also affected by the curl of the impressed currents (vortex source).
The genesis of such an electrically silent vortex component can be illustrated by a simple example given in [2]. A nerve is modeled as a cylindrically strand of tissue with helical fiber architecture, electric conductivity along the fibers is assumed to be higher than across fiber direction. If an action potential propagates along the nerve, all azimuthal electric field components vanish due to the cylindrical symmetry of the problem. Therefore, the resulting electric potential field is also of cylindrical symmetry. The azimuthal current density on the other hand will not vanish due to the helical fiber structure. The magnetic field components associated with these azimuthal currents are called electrically silent, as they do not have an associated electric field component.
The human heart is of helix like or spiral like fiber architecture [3], but to the authors best knowledge no theoretical estimation exists at which order of magnitude electrically silent fields can be expected. In [4] the magnetic dipole moment of a cardiac vortex source has been determined experimentally. At rest results obtained during cardiac repolarization (peak of T-wave) varied from 48nAm^2 to 98nAm^2 in five normal subjects.
In the study presented first an eccentric spheres model is numerically investigated in order to compare the magnetic field components generated by flux sources to those generated by vortex sources. Within the spherical model of the left ventricle intramural rotating fiber orientation is assumed. Then investigations are extended to a realistically shaped torso model including fiber geometry. The body surface potential (BSP) map and the magnetic field map (MFM) are calculated for cardiac depolarization considering anisotropic conductivity within the myocardium. Finally these simulated data are used for an inverse estimation of the ventricular activation time map. For inverse calculation isotropic conductivity is assumed within the myocardium.

Method

Forward calculations are carried out numerically, applying BEM/FEM-coupling [5,6]. Within the cardiac mass the finite element method (FEM) is used in order to consider anisotropic volume conduction. FEM equations are based on the bidomain model. The torso enclosing the heart is modeled using the boundary element method (BEM). On the epi- and endocardial surfaces BEM and FEM are coupled by requesting continuity of the electric potential and of the surface normal components of the currents across these surfaces. Finite elements used are of tetrahedral shape, boundary elements are of triangular shape, both element types use linear basis functions. For all investigated models mesh generation was carried out using commercial software (Hyper Mesh®, Altair Computing Inc.).

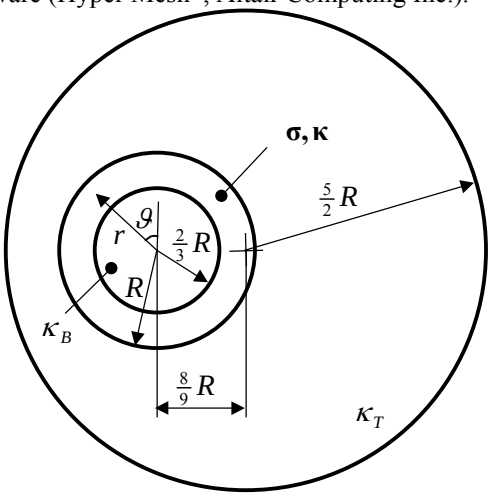

Figure 1: Eccentric spheres model, representing the left ventricle of anisotropic conductivity within the torso (R=4.5cm; κ_T=0.2 Sm^{-1}; κ_B=0.6 Sm^{-1}).

The spherical geometry shown in Fig. 1 can be interpreted as low order approximation of the investigated physical situation. The two inner spheres model the epi- and endocardial surface of the left ventricle, placed 2.75cm from the anterior chest wall. Intramural rotation of fiber angle α (i.e. the angle fiber encloses with lines of equal polar angle ϑ) is approximated by:

$$\sin\alpha = \frac{5}{6}\left(6\frac{r}{R} - 5\right), \qquad (1)$$

which is an approximation of the data shown in Fig. 12 A-D of [3]. Bidomain conductivities are chosen ac-

cording to [7]: longitudinal effective intracellular conductivity σ_l=0.240 Sm^{-1}, transversal effective intracellular conductivity σ_t=0.024 Sm^{-1}, longitudinal bulk conductivity κ_l=0.480 Sm^{-1}, transversal bulk conductivity κ_t=0.120 Sm^{-1}. A simple bipolar source distribution can be described by the transmembrane potential V_m:

$$V_m(\vartheta) = \Phi_0 \cos(\vartheta) - \Delta\Phi \,. \qquad (2)$$

By choosing Φ_0=50mV and $\Delta\Phi$=40mV the transmembrane potential V_m varies within the physiological reasonable interval (-90mV, 10mV).
5002 tetrahedrons are applied in order to model the left ventricular muscle, resulting in 1122 triangular boundary elements on the epi- and endocardial surface. The outer torso surface is modeled by 442 boundary elements. The total number of vertices is 1345. First the electric potential forward solution is computed and the radial component of the magnetic field is calculated at 130 observation points 12.5 cm above the outer spheres surface.
In order to quantify the contributions of the vortex sources to the extra corporal magnetic field, results are compared to those obtained when isotropic conductivity is assumed within the myocardium (here no vortex sources will occur). Care has to been taken on the choice of the isotropic conductivities. In an anisotropic medium conductivities transversal and longitudinal to fiber orientation differ. Therefore, for the isotropic model the chosen conductivities should be intermediate values of σ_t, σ_l and κ_t, κ_l. Such intermediate values σ, κ can be chosen by varying the conductivity scaling parameter q within the interval (0,1):

$$\sigma = q\sigma_l + (1-q)\sigma_t\,; \quad \kappa = q\kappa_l + (1-q)\kappa_t\,. \qquad (3)$$

In order to find the optimal isotropic intermediate conductivities σ and κ, q is varied in steps of Δq=0.01 for both electric potential and magnetic field calculations.
Next investigations are extended to a realistically shaped model of the torso. A model of a dog ventricle containing detailed description of fiber orientation throughout the whole of the muscle has been made available by the Auckland Bioengineering Research Group [3]. In [8] an activation sequence for this ventricle model has been calculated, using modified Beeler-Reuter membrane equations. The heart was placed in a realistic position within a torso model obtained from 24 MRI slices of a normal male volunteer. The heart model is based on data collected from a mongrel dog weighting about 35 kg. Therefore, all dimensions have been multiplied by 1.2 in order to enlarge it to about the size of an human heart. The average conductivity of the torso surrounding the heart was assumed to be 0.2 Sm^{-1}, bidomain conductivities are the same as used for the spherical model. The heart is modeled by 4923 tetrahedrons (1936 triangles on the surface), the outer torso surface is modeled by 1196 triangles. The whole model contains 1923 vertices. In forward calculations the electric potential at 65 electrodes on the outer torso surface and the magnetic field at 68 sensors are calculated for cardiac depolarization. Magnetic sensor axes are orientated almost normal to the anterior chest wall. Again the transmembrane potential was assumed to vary from -90mV to 10mV with a rise time of 1ms. Results are compared to those obtained by assuming isotropic conductivity within the myocardium. Here the parameter q is varied in steps of Δq=0.05.
Finally the errors which will occur in the inverse solution by neglecting anisotropic properties in inverse calculation are investigated. The epi- and endocardial activation time maps are estimated from simulated BSP and MFM data. For details on the inverse method see [9]. As the software applied for inverse calculation is restricted to the use of 8 noded quadrilateral boundary elements the torso had to be modeled a second time. Here, the model consists of totally 528 elements and 1586 vertices.

Results

For the spherical geometry calculations are carried out once considering anisotropic volume conduction and once simplified assuming isotropic conductivity. Results obtained by taking anisotropic conductivity into account are considered to be more realistic and therefore they are chosen as reference. The errors obtained by isotropic approximation are then described by the relative error:

$$RE = \frac{\|f_i - f_a\|}{\|f_a\|}\,. \qquad (4)$$

Here, f_a denotes the electric potentials calculated at 223 vertices on the outer sphere or the magnetic field components at 130 observation points respectively, considering anisotropic conductivity. f_i refers to data obtained assuming isotropic conductivity.

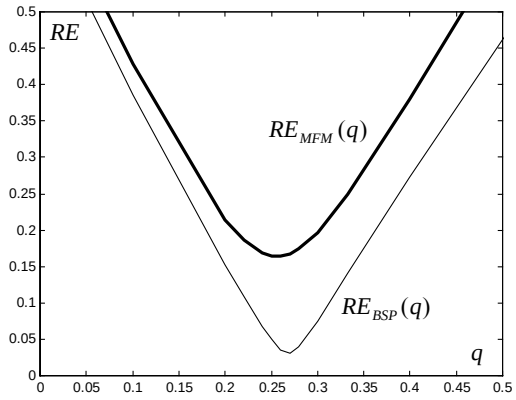

Figure 2: Relative error RE versus conductivity scaling parameter q for the magnetic field map (MFM) and the body surface potential (BSP). Errors in the magnetic field map are clearly higher due to the electrically silent field component.

In Fig. 2 the variation of RE versus the scaling parameter q in (3) is shown. For the BSP the best result is found at q=0.25 (RE=3.1%), for the MFM at q=0.26

(RE=16.4%). The higher errors in the magnetic field can be explained by the presence of electrically silent magnetic fields, which can not be taken into account by using an isotropic model. However, one can also estimate from these results, that in this case the electrically silent magnetic field components are about one order of magnitude smaller than the field produced by flux sources.

Taking the difference of the magnetic field maps computed with the anisotropic and the best isotropic model (q=0.26) one gets an estimation of the electrically silent MFM. Fitting a magnetic dipole field to this data the magnetic dipole moment of the vortex source is found by 70nAm^2 for this example.

For the realistically shaped torso model the best conductivity scaling parameter has been found by q=0.30 for both the BSP map and the MFM. In contrast to the results obtained for the spherical geometry, here in both cases relative errors are relatively high (BSP 53%, MFM 60%). Fig. 3 depicts the simulated time courses of the electric potential in electrode no. 6 for anisotropic (solid line) and isotropic (dotted line) conductivity. Results are in qualitative agreement, amplitudes are almost the same, but e.g. at t=60ms the simulated potentials differ more than 0.5 mV. This behavior was observed in almost all channels and is also reflected by the correlation coefficients (BSP 0.87, MFM 0.83).

For inverse calculations isotropic conductivity was assumed within the myocardium, q was chosen 0.30 (best isotropic model). The outer torso surface and the hearts surface are modeled applying quadrilateral boundary elements of second order. Note that for forward simulation and inverse calculation different approaches are used for calculating the lead field (triangular and quadrilateral elements; BEM/FEM coupling using linear basis functions and BEM using second order basis functions). Therefore, the quality of the lead field calculation has been checked by comparing the forward solutions obtained for q=0.30. Relative errors are about 20 %.

In order to study the influence of these errors on the inverse solution, first the activation time (AT) map is computed from the isotropic BEM/FEM forward solutions.

No noise was added to the simulated data for considering only the contribution of field calculation errors. For all computations the regularization parameter was chosen for minimal relative error, which is possible in theoretical studies only. Figure 4 depicts the AT map estimated from the anisotropic MFM forward solution. All characteristic events are found to be properly located (right and left ventricular breakthrough, late excitation of the heart base close to the aortic outflow tract). Similar results are found when source reconstruction is performed from the anisotropic BSP forward solution.

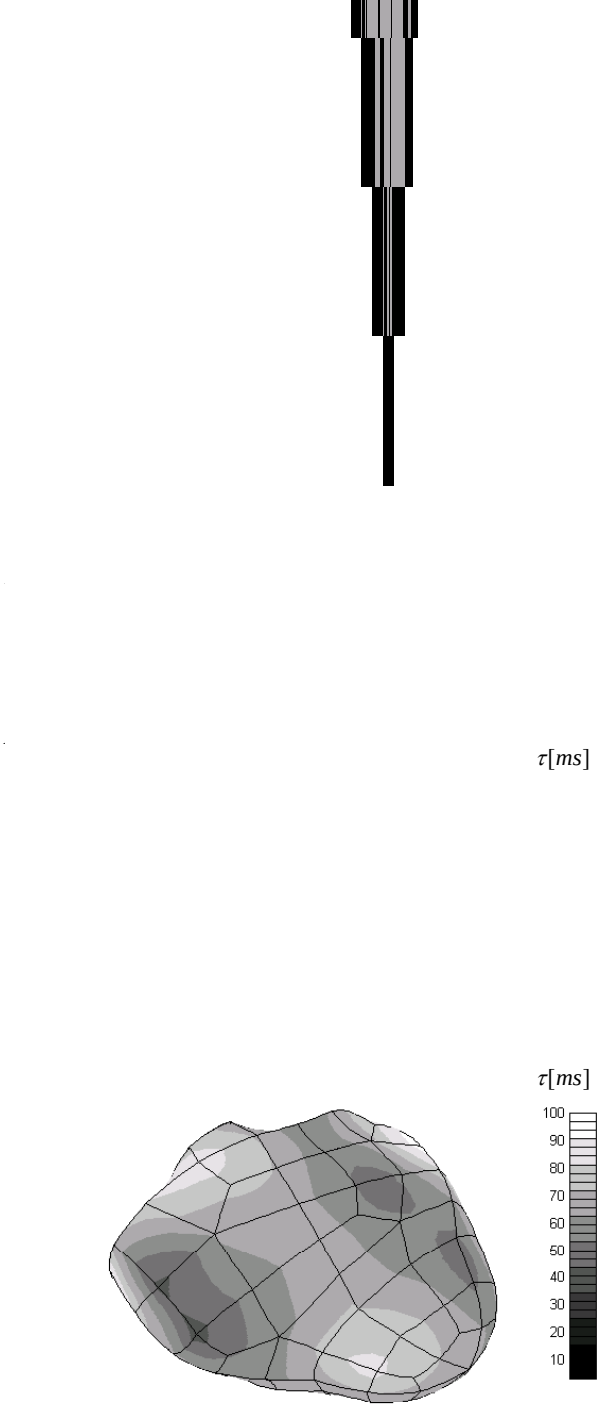

Figure 4: Reference activation time map (upper panel) based on data computed in [8] and inverse solution estimated from the anisotropic MFM forward solution (lower panel). The ventricles are shown in anterior view. Right and left ventricular breakthroughs are found to be properly located. Triangular and quadrilateral meshes are also plotted.

Discussion

The eccentric spheres model has been investigated in order to illustrate the genesis of an electrically silent magnetic field. Choosing physiologically reasonable dimensions, conductivities, fiber orientations and transmembrane potentials for the left ventricle, the computed dipole moment of the vortex source (70nAm^2) is in agreement with experimentally deter-

mined data ($48nAm^2$ to $98nAm^2$) [4]. However, results suggest that the field generated by vortex sources is almost one order of magnitude smaller than the field produced by flux sources. This can be explained by rotational intramural fiber angle variation [3]. The azimuthal current density components (which are associated with the silent field) on the epi- and endocardial surface have opposite sign. Therefore, their contributions cancel each other to small values.

It should be pointed out that similar to the example given in [2] fiber angle and source field within the spherical model of the ventricle are of axial symmetry. If the whole geometry was of axial symmetry it would be possible to approximate the body surface potential perfect by assuming isotropic conductivity within the myocardium. Here, the three spheres a placed eccentrically and thus the BSP can not be approximated with errors lower than 3 % by an isotropic model.

In reality fiber orientation, source field and geometry do not have any symmetry. In this case neglecting anisotropic tissue properties has a strong impact on the quantitative errors in the forward solution (over 50% for BSP and MFM). On the other hand qualitatively results are in good agreement.

Comparing the forward solutions obtained for isotropic models applying once first order BEM/FEM coupling and once second order BEM relative errors up to 20% are found. This clearly is a strong limitation but also an interesting aspect of this study. The relative large errors are caused by two effects:

- First, during depolarization the transmembrane potential rises quickly (within 1ms) from its resting value to plateau level. Assuming a medium spacing by boundary element vertices of 7mm and a propagation velocity for the excitation wave of $0.7ms^{-1}$, this means, that in the forward calculation no continuous propagation of the excitation wave is present but every 10ms a boundary node is 'switched on'. This means the excitation is not moving continuously but 'jumping' from one node to each other, exciting discontinuously relatively large parts of tissue. Therefore, the application of two different boundary element meshes having non matching vertices will lead to relatively large errors in the forward solution.
- Second, all applied boundary element formulations use the collocation form as method of residual weighting [10]. In [10] it is shown that this method in combination with linear triangles produces large errors when applied for electric potential calculation. This problem could be overcome by using the Galerkin form of residual weighting.

All characteristic events of cardiac activation could be reconstructed from simulated data considering anisotropic cardiac volume conduction. However, the relatively high errors in the computed forward solutions will impact the quality of the inverse solutions. Therefore, a quantitative analysis of the influence of neglecting anisotropic tissue properties in the inverse problem is left to further studies.

References

[1] Plonsey R. Capability and limitations of electrocardiography and magnetocardiography, IEEE Transactions on Biomedical Engineering, 1972, BME 19: 239-244.

[2] Roth B.J. and Wikswo J.P. Electrically silent magnetic fields, Biophysical Journal, 1986, 50: 739-745.

[3] Nielsen P.M.F., Le Grice I.J., Smaill B.H. and Hunter P.J. Mathematical model of geometry and fibrous structure of the heart, American Journal of Physiology, 1991, 260: H1365-H1378.

[4] Brockmeier K., Schmitz L., Chavez J.J.B., Burghoff M., Koch H., Zimmermann R. and Trahms L. Magnetocardiography and 32-lead potential mapping: repolarization in normals subjects during pharmacologically induced stress, Journal of Cardiovascular Electrophysiology, 1997, 8: 615-626.

[5] Fetzer J., Kurz S. and Lehner G. The coupling of boundary elements and finite elements for nondestructive testing applications, IEEE Transactions on Magnetics, 1997, 33:677-681.

[6] Fischer G., Tilg B., Modre R., Huiskamp G., Fetzer J., Rucker W. and Wach P. A bidomain model based BEM-FEM coupling formulation for anisotropic cardiac tissue, submitted to Annals of Biomedical Engineering.

[7] Roth B.J. Electrical conductivity values used with the bidomain model of cardiac tissue, IEEE Transactions on Biomedical Engineering, 1997, 44:326-238.

[8] Huiskamp G. Simulation of depolarization in a membrane-equations-based model of the anisotropic ventricle, IEEE Transactions on Biomedical Engineering, 1998, 45: 847-855.

[9] Tilg B., Wach P., Lesh M.D., Modre R., Fischer G., and Lafer G. Imaging surface activation time maps from magnetic field and body surface potential data, Proceedings of the BioMag98 Conference, Sendai, Japan (in press).

[10] Mosher J.C., Leahy R.M. and Lewis P.S. EEG and MEG: forward solutions for inverse methods, IEEE Transactions on Biomedical Engineering, 1999, 46: 245-259.

Acknowledgements

This work was supported by the Austrian Science Fund (FWF), grant P12267-MED and P11448-MED. The authors would like to thank Prof. J.P. Hunter for making the data of reference [3] available via ftp and Ch. Höller for preparing the quadrilateral BEM-models.

A Linearized Iterative Algorithm for Myocardial Activation Time Imaging

Modre R.[1], Tilg B.[1,2], Fischer G.[1], and Wach P.[1]

[1]Institute of Biomedical Engineering, Technical University Graz, Graz, Austria
[2]Section of Cardiac Electrophysiology, Department of Medicine, University of California, San Francisco, California, USA

Introduction

The noninvasive imaging of myocardial activation time sequences uses magnetocardiographic (MCG) or electrocardiographic (ECG) maps in combination with morphological data of the torso anatomy. Smoothing and attenuation effects in the torso volume cause the problem to be ill-posed [1]. In particular, the MCG and ECG data are related to electrical sources associated with the cardiac de- and repolarization via a linear operator whose inverse is discontinuous [2]. This discontinuous nature implies that any noise entering the process of measurement perturbs the inverse solution considering no regularization. Therefore different regularization techniques are used to control this problem [3, 4]. In the bidomain theory [5] the sources of the MCG and ECG are assumed to be the transmembrane potential. Identifying diagnostically useful parameters such as the set of activation times (onset of the transmembrane potentials), nonlinearity enters the problem because of the nonlinear relation between the transmembrane potential and the activation time [6]. In clinical cardiac electrophysiology this activation time imaging method should assist determining arrhythmogenic source patterns for catheter treatment (e.g., for focal and linear catheter ablation).

Method

Neglecting the effect of electrical anisotropy in the myocardium, which is valid for considering cardiac depolarization [6], an isotropic pseudo-subparametric boundary element method (BEM) with quadrilateral elements including the blood masses, the lungs and the outer torso surface was used to model the volume conductor [7].
The activation time pattern on the surface (endocardium and epicardium) of the ventricle is estimated applying the critical point theorem [2, 8] followed by an optimization routine for nonlinear problems (E04UCF, NAG Ltd. UK) minimizing the following cost function [9, 10]:

$$\Psi = \int_0^T \left\| A\varphi_m(t,\tau) - D(t) \right\|_2^2 dt + \lambda^2 \left\| \Delta\tau \right\|_2^2 \rightarrow \min \qquad (1)$$

The first part in (1) is the residual norm with the transfer matrix A describing the relationship between the transmembrane potential $\varphi_m(t,\tau)$ on the surface of the ventricle and the MCG or ECG data $D(t)$ [11]. The time interval [0,T] corresponds to the QRS wave in case of sinus rhythm activity, i.e., to ventricular depolarization.

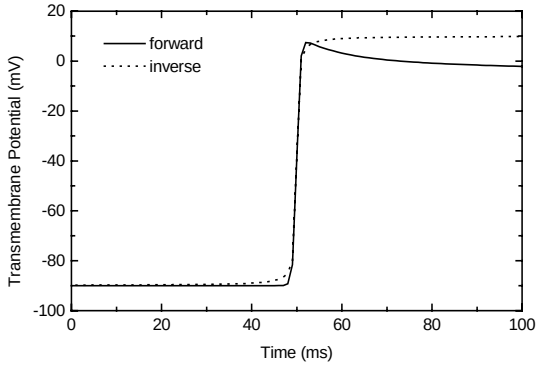

Figure 1: Time course of the myocardial surface transmembrane potential applied to the forward (solid line) and inverse (dotted line) problem.

A second order Tikhonov regularization method with the regularization parameter λ - the second part in the cost function - was applied to stabilize the inverse solution. In (1) λ is determined by the L-curve method [12]. The surface laplacian operator Δ [13] acts as a spatial smoothing operator on the activation time pattern. In the inverse formulation we described the transmembrane potential (see Fig. 1) at each source point on the surface of the ventricle by an analytical formula (2) with the parameters resting membrane potential a, action potential amplitude u, rise time w and activation time τ. All parameters except the activation time were assumed to be constant.

$$\varphi_m(t,\tau) = \frac{u}{2}\left\{1 + \frac{2}{\pi}\arctan\left[\pi\frac{t-\tau}{w}\right]\right\} + a \qquad (2)$$

In solving (1) the determination of λ can cause problems under real conditions. For instance, the corner in the L-curve can be smoothed due modeling errors. Therefore the uniqueness of the proper λ is not guaranteed. Under real conditions with an unknown noise level this can result in a non-optimal inverse solution. The motivation for this research study was to find an

algorithm allowing a more accurate determination of the proper λ. The following linearized iterative algorithm [14] was applied to the estimation of the activation time pattern on the epicardium and endocardium. Let τ_k (k = 0, 1, 2, …) be an approximation for the unknown solution - the activation time τ - of the nonlinear inverse ill-posed problem

$$F(\tau) = D \tag{3}$$

in which F is a nonlinear operator mapping the activation time τ onto the MCG or ECG data D. We linearized (3) in the point τ_k in order to obtain the linear problem

$$F(\tau_k) + F'(\tau_k) \cdot (\tau - \tau_k) = D \tag{4}$$

in which F' stands for the Frechet derivative of F. Equation (4) can also be written as

$$\begin{aligned} F_k = F'(\tau_k) \qquad & F_k \tau = D_k \\ & D_k = D + F_k \tau_k - F(\tau_k) \end{aligned} \tag{5}$$

which in general is again ill-posed [15]. In order to obtain a
regularized approximation τ_{k+1} for the linear ill-posed problem (5) we can apply any regularization method for linear ill-posed problems. Using second order Tikhonov regularization with the differential operator L and the regularization parameter λ_k the following regularized approximation can be achieved

$$\tau_{k+1} = (F_k^* F_k + \lambda_k^2 L^* L)^{-1} F_k^* (D_k) \tag{6}$$

The asterisk marks the adjoint operator. If we repeat this process we obtain an iteration method

$$\tau_{k+1} = \tau_k + \delta\tau_k \tag{7}$$

with the descent direction $\delta\tau_k$

$$\delta\tau_k = (F_k^* F_k + \lambda_k^2 L^* L)^{-1} F_k^* (D - F_k) - \lambda_k^2 F_k^* L^* L \tau_k$$

For growing k-values the iteration method (7) converges to a regularized approximation of the activation time pattern τ. In that case it is possible to extend regularization methods for linear to nonlinear inverse problems. The iteration process (7) is equivalent to the Gauss-Newton method for minimizing the cost function Ψ in (1).
The limit of the iteration is a solution of the corresponding Euler equation of this cost function Ψ.
The reference activation time map in Fig. 2 and Fig. 3 was estimated from sinus rhythm MCG data measured with the 68-channel cardiomagnetometer system at the Helsinki University Central Hospital (HUCH). This activation time map, which is in accordance with previously published results for the sinus rhythm in humans, was used to simulate synthetic MCG and ECG data. The forward and inverse formulation was based on a 62-channel ECG and 68-channel MCG mapping setup. As one can see from Fig. 1 a realistic time course for the transmembrane potential was used in the forward problem [16]. Gaussian noise was added to synthetic data with a signal-to-noise ratio of 35dB in order to take into account the unavoidable noise, which occurs in real MCG and ECG recordings.

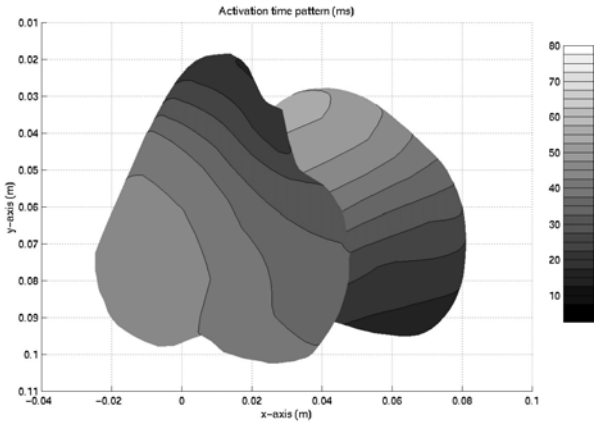

Figure 2: Reference activation time map (ms) on the endocardium. Isochrones are shown at steps of 5 ms.

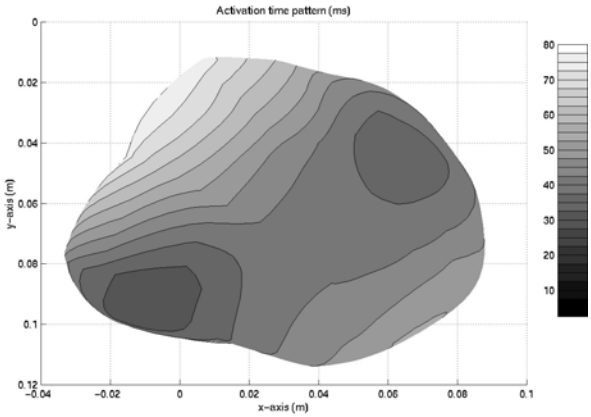

Figure 3: Reference activation time map (ms) on the epicardium. Isochrones are shown at steps of 5 ms.

Results

A relative root mean square (relRMS) error was applied as a measure for the localization accuracy and was defined by

$$\text{relRMS} = \frac{\left\| \tau - \tau ref \right\|_2}{\left\| \tau ref \right\|_2} \tag{8}$$

with the reference activation time τ_{ref} and the reconstructed activation time τ. In addition, a correlation coefficient (CC) was calculated by

$$CC = \frac{\sum_q \left(\tau(q) - \langle\tau\rangle\right) \times \left(\tau_{ref}(q) - \langle\tau_{ref}\rangle\right)}{\left\|\tau - \langle\tau\rangle\right\|_2 \times \left\|\tau_{ref} - \langle\tau_{ref}\rangle\right\|_2} \qquad (9)$$

In (9), < > denotes the mean value and the numerator is summed over the q nodes on the ventricular surface.

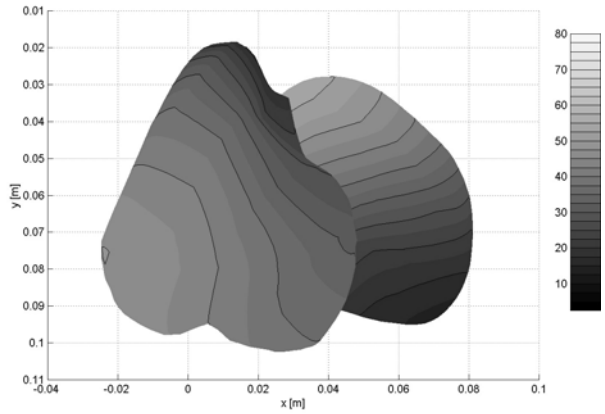

Figure 4: Activation time map (ms) on the endocardium estimated from synthetic MCG data. Isochrones are shown at steps of 5 ms.

From the synthetic MCG data applying the critical point theorem the CC was found to be 0.56 (relRMS = 0.37) for the epicardium and 0.3 (relRMS = 0.26) for the endocardium, respectively. Using the critical point solution as a starting vector for the linearized iterative method, the CC was improved from 0.56 to 0.98 (relRMS = 0.05) and from 0.30 to 0.99 (relRMS = 0.02). The estimated activation time pattern on the endocardium and epicardium is shown in Fig. 4 and Fig. 5. All critical events of the propagation sequence such as the breakthroughs on the left and right ventricle as well as the later depolarization of the heart base were found. The relRMS and CC of the inverse solution reconstructed from ECG data were in the same order. The CC was larger than 0.98 and the relRMS was less than 0.05.

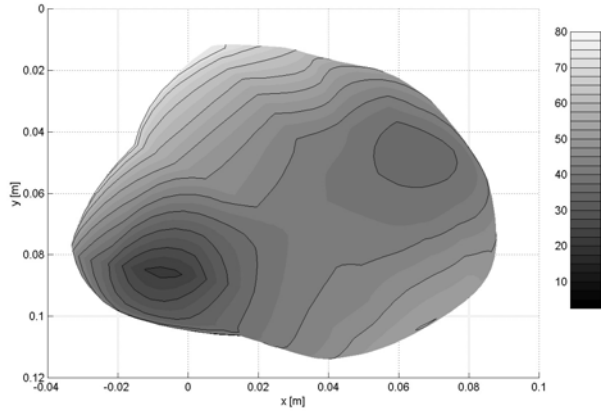

Figure 5: Activation time map (ms) on the epicardium estimated from synthetic MCG data. Isochrones are shown at steps of 5 ms.

Discussion

The results indicate that the proposed linearized iterative method enables the estimation of the activation time pattern on the epicardium and endocardium. The determination of the proper regularization parameter λ_k at each iteration step k in (7) is based on the L-curve [12]. Each point of the discrete L-curve corresponds with an inverse solution with a different λ_k. The corner of the characteristic L-shaped curve reflects the optimal inverse solution with the qualified λ_k.

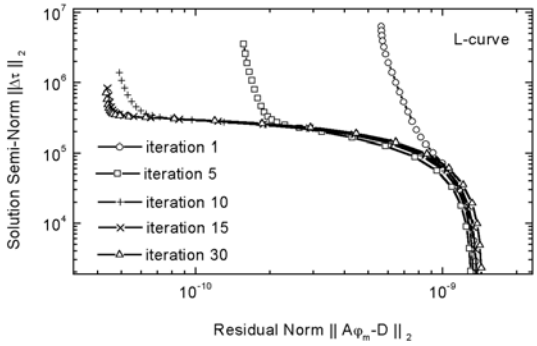

Figure 6: L-curve: log-log plot for different regularization parameters of the solution semi-norm $||\Delta\tau||_2$ versus the residual norm $||A\varphi_m\text{-}D||_2$ at iteration step k = 1, 5, 10, 15, 30.

In Fig. 6 L-curves for different iteration steps (1, 5, 10, 15 and 30 iterations) are depicted. The proper regularization parameter at each step corresponds with the largest curvature, i.e., with the corner of the individual L-curve.

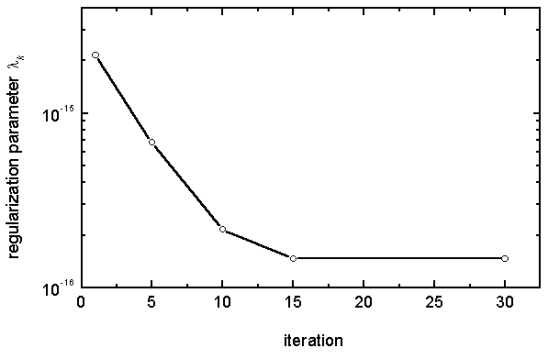

Figure 7: Proper regularization parameters λ_k corresponding to the corners of the L-curves at each iteration step k (see Figure 6) versus the index of iteration.

As shown in Fig. 7 λ_k does not change any more after a few iterations. The iteration process was continued using this final λ_k until the CC was near one between the subsequent inverse solutions τ_{k+1} and τ_k.

This method has several advantages over a nonlinear optimization routine minimizing the cost function in (1). In the nonlinear optimization approach Ψ has to be minimized for several λ's in order to get a parameterized L-curve for determining the corner. In the linear iterative approach the L-curve was calculated at each step of iteration with small computational efforts and the iterative process converged by few iterations.
Due to the linearization of the nonlinear ill-posed problem (3) it was possible to extend a regularization method from a linear to a nonlinear ill-posed problem. Such a method has a favorable behaviour on the determination of λ. In Fig. 8 the L-curves for the nonlinear and for the iterative linear method are shown.

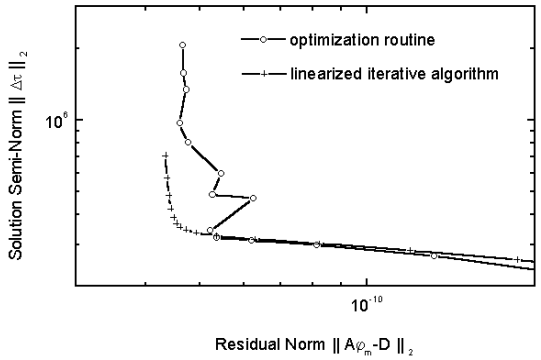

Figure 8: L-curve: log-log plot for different regularization parameters of the solution semi-norm $\|\Delta\tau\|_2$ versus the residual norm $\|A\varphi_m\text{-}D\|_2$ for the optimization routine and the linearized iterative algorithm.

In the linear approach the L-curve is very smooth and it is amazingly easy to determine λ_k for the 'best' inverse solution. In contrast the L-curve in the nonlinear approach is not smooth and it is difficult to determine the proper regularization parameter (Fig. 8).
In summary the proposed linearized iterative method for the electrocardiographic and magnetocardiographic inverse problem showed excellent computational performance and resulted in nearly the same inverse solution than the nonlinear approach. The procedere determing the proper λ is much easier in the linear algorithm. The validation of the inverse method with catheter mapping techniques will show whether these theoretical findings are also true for the inverse from ECG and MCG mapping data under clinical conditions.

References

[1] Rudy, Y., Messinger-Rapport, B.J. The inverse problem in electrocardiography: solutions in terms of epicardial potentials, Crit Rev Biomed Eng, 1988,16: 215-268.

[2] Greensite, F. The mathematical basis for imaging cardiac electrical function, Crit Rev Biomed Eng, 1994,22: 347-399.

[3] Engl, H.W., Hanke, M., Neubauer, A. Regularization of inverse problems, Dordrecht, Kluwer, 1996.

[4] Tikhonov, A.N., Arsenin, V.Y. Solutions of ill-posed problems, New York NY, Wiley, 1977.

[5] Henriquez, C.S. Simulating the electrical behavior of cardiac tissue using the bidomain model, Crit Rev Biomed Eng, 1993,21: 1-77.

[6] Tilg, B. Noninvasive functional cardiac electrical source imaging, Aachen, Shaker Verlag, 1998.

[7] Fischer, G., Tilg, B., Wach, P., Modre, R., Leder, U., Nowak, H. Application of high-order boundary elements to the electrocardiographic inverse problem, Comput Meth Prog Bio, 1999,58: 119-131.

[8] Huiskamp, G.J.M., Greensite, F. A new method for myocardial activation imaging, IEEE Trans Biomed Eng, 1997,44: 433-446.

[9] Huiskamp, G.J.M., Van Oosterom, A. The depolarization sequence of the human heart surface computed from measured body surface potentials, IEEE Trans Biomed Eng, 1988,35: 1047-1058.

[10] Wach, P., Tilg, B., Lafer, G., Fischer, G. Cardiac source imaging during de- and repolarization, In: Tilg, B., Wach, P. NFSI 97, Biomed Technik, 1997,42(Supplement 1): 269-272.

[11] Malmivuo, J., Plonsey, R. Bioelectromagnetism, Oxford, Oxford University Press, 1995.

[12] Hansen, P.C. Rank-deficient and discrete ill-posed problems, Philadelphia, SIAM, 1998.

[13] Oostendorp, T.F., Van Oosterom, A. The surface laplacian of the potential: theory and application, IEEE Trans Biomed Eng, 1996,43: 394-405.

[14] Tautenhahn, U. On a general regularization scheme for nonlinear ill-posed problems: II. Regularization in Hilbert scales, Inverse Problems, 1998,14: 1607-1616.

[15] Engl, H.W., Kunisch, K., and Neubauer, A. Convergence rates for Tikhonov regularization of nonlinear ill-posed problems, Inverse problems, 1989,5: 523-540.

[16] Wohlfart, B. A simple model for demonstration of STT-changes in ECG, Eur Heart J, 1987,8: 409-416.

Acknowledgements

This study was supported by the Austrian Science Fund grant no. P12267-MED. Measured MCG and MRI data were made available by the Laboratory of Biomedical Engineering, Helsinki University of Technology, Espoo, Finland.

Corresponding author:

Robert Modre
Department of Biophysics
Institute of Biomedical Engineering
Technical University Graz,
Inffeldgasse 18, 8010 Graz, Austria
Phone: ++43 316 873 7393
Telefax: ++43 316 465348
E-mail: modre@ibmt.tu-graz.ac.at
URL: http://www-db.tu-graz.ac.at

Influence of randomly displaced BSPM leads on theidentification of ventricular preexcitation sites

Jazbinšek V., and Hren R.

Institute of Mathematics, Physics and Mechanics, University of Ljubljana, Slovenia

Introduction

Radiofrequency (RF) catheter ablation has become a method of choice in curative treatment of pharmacologically refractory paroxysmal supraventricular tachycardias involving an accessory atrioventricular connection [1]. Prerequisite for the successful ablative treatment is the precise identification of an abnormal pathway. Several studies (see [2] and references therein) have indicated that the inverse solution of body surface potential recordings can offer noninvasive means for pre-interventional localization of preexcitation sites. The most often used approach to such a localization includes calculating the position of an equivalent single dipole source in a model of the human torso.

In our earlier simulation study [3], we have investigated various factors (e.g., thoracic inhomogeneities, measurement and modeling noise) that may affect the single dipole localizations in the clinical setting. Results of our study suggested that individualized torso geometries are required to localize the preexcitation activity within less than 20 mm. Although recent advances in development of imaging modalities has made possible to construct patient-specific geometry data, the accurate rendering of electrode positions (leads) on the torso surface is during actual recordings time consuming, labour intensive and often difficult to achieve. To facilitate clinical applications of the single dipole inverse solution, locations of recording leads are approximated using standardized arrays of nodes of individualized torso models. However, such standardized placements of leads are associated with modeling errors and their influence on single dipole inverse solution has not yet been evaluated.

Here, we used computer simulations to quantitatively assess how the localization accuracy may vary (i) with the random displacement of leads on the torso surface, (ii) with the time after the onset of preexcitation, (iii) with the measurement noise level, and (iv) with location of a given preexcitation site along the atrio-ventricular (A-V) ring. This work is viewed as an extension of our earlier simulation study [4] and its results may be potentially useful in improving the accuracy of localization of cardiac events using the single dipole inverse solutions.

Methods

Simulations

Our simulation study ("forward solution") followed methodology that was presented in detail elsewhere [3, 5, 6]. Briefly, we used an anatomical model of the human ventricular myocardium to simulate the activation sequence. From this realistic sequence, we calculated extracardiac potentials at the torso surface using the oblique dipole model of cardiac sources in combination with the boundary element method. To account for the influence of the torso's outer boundary on body surface potentials, we used a realistic male torso model [7] (Fig. 1). The model of the human ventricles was positioned in the torso model so as to best fit the heart's anatomical location documented by radiographic images [8].

To simulate displacement of leads on the torso surface, we generated a database of 7 torso models. We modified those nodes that corresponded to positions of 117 leads on a surface of the realistic male torso model (Fig. 1). For each lead position on the torso surface, we defined a local tangential plane and then displaced the lead along two mutually perpendicular directions on that plane. Random displacements were generated by uniform distribution on the interval $D \cdot \sqrt{6} \cdot [-0.5, 0.5]$, where D was a root-mean-square (RMS) value of a displacement on the tangential plane. We assigned D equal to 10 mm in all cases. Average ($\pm$SD) three-dimensional distance between displaced and reference leads was 9.4 ± 3.4 mm ($n = 7$). Fig. 2 shows locations of the displaced leads in one of the torso models.

Localizations

Using simulated maps as the input data, we performed localizations ("inverse solution") for a single dipole source in the realistic male torso model with standardized placement of leads following a Levenberg-Marquardt least-squares fitting algorithm [3, 4]. The initial estimate of the single dipole location was at the geometrical center of the heart. As a measure for accuracy of the localization we used the localization error, defined as the distance between the location of the best-fitting single dipole and the site of preexcitation in the ventricular model.

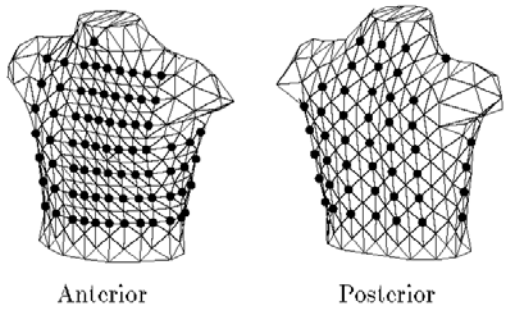

Figure 1: The anterior and posterior views of the realistic male torso model with the 117 standardized lead positions displayed. The outer boundary of the torso was tessellated with 700 triangles (352 nodes).

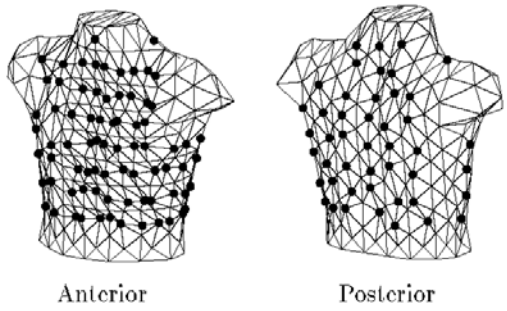

Figure 2: The anterior and posterior views of the torso model with randomly displaced leads.

Protocols

We initiated activation sequences at a total of 8 preexcitation sites located along right lateral (RL) and left lateral (LL) aspects of the AV ring of the epicardium (Fig. 3). In our earlier validation study [5], we have shown that the morphological features of simulated BSPM patterns (in particular, the position of extrema and the near-zero electric potentials) correspond well with those measured in patients with WPW syndrome. For each activation sequence and each torso model with randomly displaced leads, we simulated body surface potentials (at 117 sites) at 4-ms increments within the first 40 ms after the onset of preexcitation. To simulate measuring conditions, we calculated for each of 8 preexcitation sites, each time instant, and each torso model, body surface potentials with added random Gaussian noise at four different RMS levels: 5, 10, 20, and 50 μV. We generated 10 different noise distributions for each noise level. The inverse procedure was performed at 4-ms intervals for each of the 8 preexcitation sites using torso model with the standardized placement of leads.

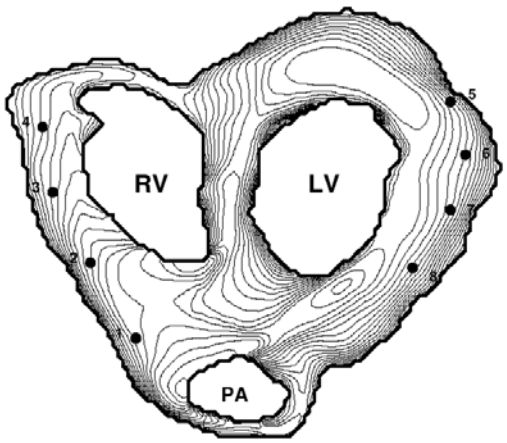

Figure 3: Basal view of the atrioventricular ring shown with 8 preexcitation sites. Sites 1–4 are right lateral (RL) preexcitation sites and sites 5–8 are left lateral (LL) preexcitation sites. Top 21 layers (at 1-mm increments) of the human ventricular model are shown. RV, right ventricle; LV, left ventricle; PA, pulmonary artery.

Results

Fig. 4 shows the average localization errors and their standard deviations calculated at each time instant from 4 individual errors for RL and LL preexcitation sites with no displaced leads and no noise present. For both RL and LL sites, the localization errors gradually increased through the preexcitation sequence (e.g., for RL sites, 3.3 ± 2.0 mm at 8 ms and 13.6 ± 4.0 mm at 28 ms after the onset) which is in agreement with the widespread notion that the single dipole can accurately represent the true cardiac sources only when the bioelectric activity of the heart is confined to small regions (diameter $\approx$ several mm). The average localization errors remained below 10 mm within the first 24 ms after the onset of preexcitation.

Fig. 5 shows the localization errors for RL and LL sites when torso models with displaced leads were used for the forward solution and the torso model with standardized placement of leads was used for the inverse solution. The localization errors for RL preexcitation sites were markedly larger than in the absence of displaced leads during the early phase of preexcitation (e.g., at 20 ms after the onset of preexcitation, 9 ± 4 mm versus 7 ± 1 mm). Later in the sequence, localization results suggest that the inaccuracies due to the size and shape of the activation wavefront dominate the localization accuracy. It appears that displacement of leads did not affect accuracy of localizations for LL sites (see below).

Fig. 6 illustrates the localization errors due to lead displacements alone. This figure was constructed by com-

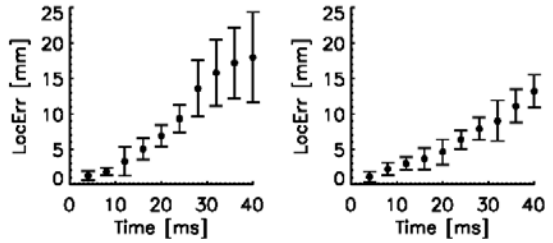

Figure 4: Average localization errors (in mm) shown as a function of time after the onset of preexcitation for RL and LL sites. The torso model with standardized placement of leads was used for both the forward and inverse solutions; no measurement noise was added. Error bars indicate ±standard deviation.

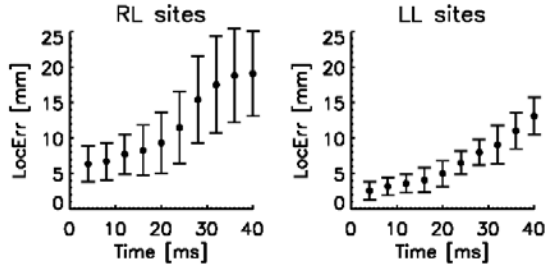

Figure 5: Average localization errors (in mm) shown as a function of time after the onset of preexcitation for RL and LL sites. Seven torso models with displaced leads were used for the forward solution and the torso model with standardized placement of leads was used for the inverse solution. Error bars indicate ±standard deviation.

paring localizations obtained from simulations using the torso models with displaced leads to corresponding localizations calculated from simulations using the torso model with standardized placement of leads. As can be expected, the localization error remained relatively constant throughout the preexcitation sequence (e.g., for RL sites, 6.4 ± 2.6 mm at 12 ms and 6.5 ± 3.7 mm at 28 ms after the onset). However, the separate impact of the lead displacement on the localization accuracy was significantly more pronounced for RL sites than for LL sites (e.g., at 20 ms after the onset, 6.0 ± 3.0 mm versus 2.1 ± 0.8 mm).

This observation is in agreement with forward simulations exploring pattern differences of BSPMs due to the displacement of leads. Using BSPMs calculated by the standardized placement of leads as the reference, we obtained significant differences in correlation coefficients between RL and LL sites (average correlations of 0.980 ± 0.012 versus 0.9971 ± 0.0004).

Figs. 7 and 8 show average and maximum localization errors calculated at each time instant for RL and LL preexcitation sites in the presence of four different lev-

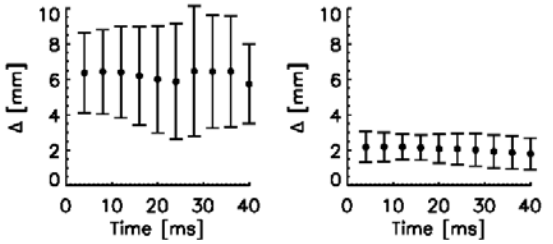

Figure 6: Average difference (Δ) for RL and LL preexcitation sites between localizations obtained from simulations using torso models with displaced leads and corresponding localizations calculated from simulations using the torso model with standardized placement of leads (reference). Error bars indicate ±standard deviation.

els of noise. Depending on the noise level, localization errors reached the minimum between 12 and 24 ms after the onset for RL sites, and between 16 and 32 ms after the onset for LL sites. For RL sites, maximum errors were 21, 22, 25, and 39 mm at 20 ms after the onset for RMS noise levels of 5, 10, 20, and 50 μV, respectively. For LL sites, maximum errors were 14, 17, 23, and 75 mm at 20 ms after the onset for RMS noise levels of 5, 10, 20, and 50 μV, respectively.

Our results suggest that the effect of measurement noise on localizations depended on a signal to noise (S/N) ratio defined as a ratio between RMS values of BSPMs and a given noise level. In fact, the measurement noise markedly influenced both forward and inverse solutions when S/N was less than 5.

Discussion

In this study, we investigated the effects of inaccuracies in determining the lead positions *and* measurement noise on the inverse solution that uses the single dipole source model. The findings of our study demonstrate that in the presence of measurement noise and lead displacement, average localization error was < 10 mm. At noise levels found during a typical BSPM recordings (≤ 5 μV), optimal time interval for localizations was between 12 and 20 ms after the onset of preexcitation.

In our recent study [5], we investigated various factors on localization accuracy and concluded that inaccuracies in rendering individualized torso boundaries result in average localization errors of 10–15 mm, with the maximum errors of 26–30 mm. Results of our present study showed that even when the electrical properties of the volume conductor are precisely known, the maximum localization error can be no better than 21 mm when the placement of leads is determined with an error of 10 mm.

Our study has some limitations. Firstly, we used anatomically detailed, but still idealized model of

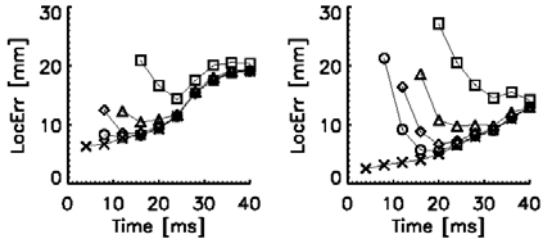

Figure 7: Average localization errors (in mm) shown as a function of time after the onset of preexcitation for RL and LL sites for four different RMS noise levels. Seven torso models with displaced leads were used for the forward solution and the torso model with standardized placement of leads was used for the inverse solution. ×–no noise, ○–5 μV, ◇–10 μV, △–20 μV and □–50 μV.

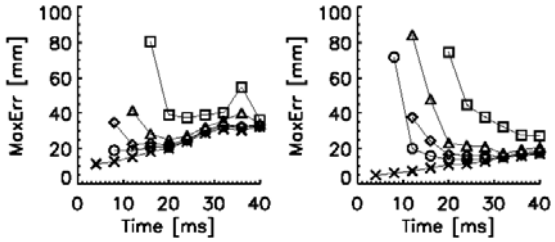

Figure 8: Average maximum errors (in mm) shown as a function of time after the onset of preexcitation for RL and LL sites for four different RMS noise levels. Seven torso models with displaced leads were used for the forward solution and the torso model with standardized placement of leads was used for the inverse solution. ×–no noise, ○–5 μV, ◇–10 μV, △–20 μV and □–50 μV.

the human ventricular myocardium. Secondly, we used homogeneous torso model. Thirdly, we simulated pure preexcitation sequences without interference from atrial repolarization or fusion with normal ventricular activation. Finally, our results were obtained for a specific 117-lead BSPM configuration. Overall, our study indicated that it is important to localize the preexcitation activity very early in the sequence (< 20 ms after the onset). Within this time interval, the bioelectric activity of the ventricles is confined to a single very small volume and the single dipole can accurately point to the preexcitation. In clinical applications, localizations thus depend on proper subtraction of the atrial repolarization from the electrocardiographic signals.

Acknowledgements

This study was supported by a grant (no. 3411-98-22 0558) from the Ministry of Science and Technology of Republic of Slovenia.

References

[1] Singer, I. Interventional Electrophysiology, Baltimore, Williams and Wilkins, 1997.

[2] Savard, P., Ackaoui, A., Gulrajani, R., Nadeau, R., Roberge, F., Guardo, R., and Dubé, B. Localization of cardiac ectopic activity in man by a single moving dipole. Comparison of different computation techniques, J Electrocardiol, 1985, 18:211–222.

[3] Hren, R., Stroink, G., and Horáček, B. Accuracy of the single dipole inverse solution in localizing ventricular preexcitation sites: a simulation study, Med. Biol. Eng. Comp., 1998, 36:323–329.

[4] Jazbinšek, V. and Trontelj, Z. On electrodes positioning in multichannel ECG, Biomed. Techn., 1997, 42 *(Suppl. 1)*:124–127.

[5] Hren, R., Stroink, G., and Horáček, B. Spatial resolution of body surface potential maps and magnetic field maps: a simulation study applied to the identification of ventricular preexcitation sites. Med. Biol. Eng. Comp., 1998, 36:145–157.

[6] Hren, R. Value of epicardial potential maps in localizing pre-excitation sites for radiofrequency ablation: A simulation study, Phys. Med. Biol., 1998, 43:1449–1468.

[7] Horacek, B. M. Digital model for studies in magnetocardiography, IEEE Trans. Magn., 1973, MAG-9:440–444.

[8] Hren, R. and Horáček, B. M. Value of simulated body surface potential maps as templates in localizing sites of ectopic activation for radiofrequency ablation, Physiol. Measur., 1997, 18:373–400.

Selective BOLD Activation of the Receptive Speech Area Using a Novel Passive Listening Paradigm

Lowe M.J., Lurito J.T., Mathews V.P., Phillips M.D., and M. Dzemidzic

Department of Radiology, Indiana University School of Medicine, Indianapolis, IN, USA

Introduction

Positron emission tomography (PET) and functional magnetic resonance imaging (fMRI) have been used extensively to study many facets of human language including auditory language comprehension [1] [2]. Language comprehension is classically localized to Wernicke's area. Although some controversy exist regarding the exact position and extent of Wernicke's area it is typically localised to the posterior portion of the superior temporal gyrus, which corresponds to the posterior portion of Brodman area (BA) 22. A variety of paradigms have been applied in both fMRI and PET studies to produce activation in Wernicke's area [3] [4] [5] [6] [1] [2] [7]. These paradigms typically produce activation in not only Wernicke's area but also a variety of cortical regions responsible for auditory and language processing. To the best of our knowledge no paradigm which produces selective activation of Wernicke's area has been published.

The purpose of the present study is to evaluate a novel paradigm for producing selective blood-oxygenation level dependent (BOLD) fMRI activation of Wernicke's area.

Method

Whole brain imaging of six strongly right-handed healthy subjects was performed on a 1.5 tesla (T) General Electric Echospeed scanner (GE Medical Systems, Waukeshau, WI, USA).

Two anatomic image data sets were acquired for the identification of activation sites by overlaying functional maps and for inter-subject image registration. Anatomic imaging consisted of 1) a 72 second long T_1-weighted spin echo axial scan with: repetition time = 500 ms; echo time = 20 ms; 15 slices, 7 mm thick with a 2 mm gap; matrix = 256x128; and field-of-view = 24x24cm and 2)a 577 second long 3D Spoiled Grass (SPGR) with repetition time =35 ms; echo time 8 ms; flip angle = 30^o, 124 contiguous axial slices with no gap and a thickness of 1.1-1.2 mm, matrix = 256x128; and field-of-view = 24x24 cm that covered entire brain. fMRI timeseries data were obtained in 160 repetitions using BOLD contrast whole brain acquisitions with same slices locations as T_1-weighted images with gradient echo echo-planar imaging (GE-EPI) parameters: repetition time = 2s; echo time = 50 ms; field-of-view = 24x24cm; matrix 64x64; bandwidth = 125 kHz; and flip angle = 90^o.

Stimuli were delivered in five 32 second control periods ("off"-state) alternated with four 32 second activation periods ("on"-state). In our case, this block paradigm gives a 16 image "off" – 16 image "on" boxcar reference function for expected activation pattern. Three different "on"/"off" paradigms were executed in the following order:

1. Listening to a simple narrative text from a popular novel (activation) interleaved with listening to an ambient scanner noise (control). This paradigm is labelled as forward versus noise (FvN).
2. Listening to (forward) narrative text (activation) interleaved with narrative text played backward (control). This pattern is referred to as forward versus backward (FvB).
3. Listening to narrative text played backward (activation) interleaved with the ambient scanner noise (control). We labelled this paradigm as backward versus noise (BvN).

The third functional scan was followed by a repeat of FvB in order to increase the statistical power and likelihood of getting at least one good FvB functional scan for every subject. Each of the scans was preceded by a reminder to subjects to remain still, close their eyes, and carefully listen to the text.

Stimuli were delivered via MRI compatible headphones (Avotec Inc., Jensen Beach, FL, USA) which consist of pneumatic stereo headphones with attached earplug-type carrier tubes that give approximately 30 dB sound attenuation. Stimulus delivery and sound attenuation capabilities are such that subjects are able to hear stimuli and instructions given at the level of conversational speech during the fMRI exam.

All subjects were immobilised during the data acquisition using a bite bar made from dental impression compound and mounted to the birdcage radio frequency (RF) coil with hard plastic secured by non-magnetic metal screws. This method is effective in controlling the gross head motion during relatively short (320 s) functional scans. All data sets were evaluated for patient motion and data sets which were motion corrupted were excluded from analysis. No motion correction was employed during the analysis of the data.

Functional data were spatially filtered by applying a Hamming filter which has been shown to give a three-fold signal-to-noise ratio enhancement with only a small degradation in spatial resolution when applied to each image of the time series [8].

The first eleven images were discarded to account for pre-saturation and hemodynamic delay effects [9]. In addition, the final five volumes were also excluded so that the data set would include exactly 144 time points (4.5 activation cycles) for each volume in the pixel.
The MRI time series at each pixel in the data was fit using the least squares fit to a boxcar reference function, a slope, and an intercept [10]. The ratio of the amplitude of this fit to its error gives a Student's t-statistic for each pixel. Pixels with a Student's $t > 3.5$ (significance level of 10^{-3}) were considered "active". Statistical maps were interpolated to 256x256x256 cubic voxels and transformed into Talairach space. Individual subject maps were summed on a pixel by pixel basis to produce combined subject maps

Results

All six subjects completed at least 1 motion free scan for each of the three "on/off" paradigms.
The FvN stimulus pattern (shown in Figure 1) produced activation in the left greater than right posterior portion of the superior temporal gyrus (posterior BA 22), symmetric activation in bilateral primary auditory cortex (BA 41 and 42) and anterior portion of the superior temporal gyrus (anterior portion of BA 22). Similar patterns were seen in both individual and combined data sets.
The BvN stimulus pattern (see Figure 1) produced the greatest activation in a symmetric fashion in bilateral primary auditory cortex that was seen in both the individual and combined subject data. Additionally minimal activation was noted in the anterior portion of the superior temporal gyrus corresponding to anterior BA 22 with slightly greater activation on the right than left. No significant activation was noted in the posterior superior temporal gyrus using the BvN pattern.
The FvB pattern produced prominent left sided activation of the posterior portion of the superior temporal gyrus in both the individual and combined data sets (see Figures 1,2 and 3). In the individual subject data there is robust selective activation in the posterior portion of the left superior temporal gyrus with only minimal activation in other portions of the brain. Activation of the posterior superior temporal gyrus was markedly asymmetric with only minimal activation noted on the right in the combined data set (right sided activation was seen in only 1 of the individual data sets). Activation was also noted in the anterior portion of the superior temporal gyrus corresponding to the anterior BA 22 on the left. This was seen both in the combined and individual subject data(see Figure 3). Additionally, left sided activation was seen in primary auditory cortex that was less prominent than that seen in the anterior and posterior portions of BA 22. Primary auditory cortex activation was seen only in the combined subject data. Note was also made of activation with in bilateral medial geniculate nuclei which was seen only in the combined subject data for the FvB paradigm.

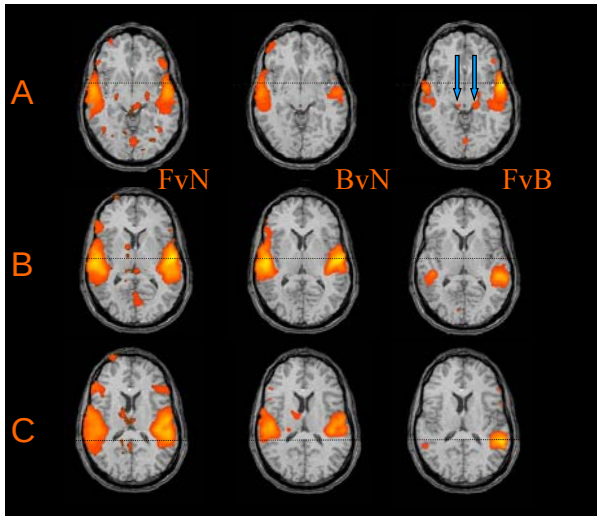

Figure 1: Combined subject activation maps for three different passive listening paradigms. Blue arrows demonstrate activation in the bilateral medial geniculate nuclei..

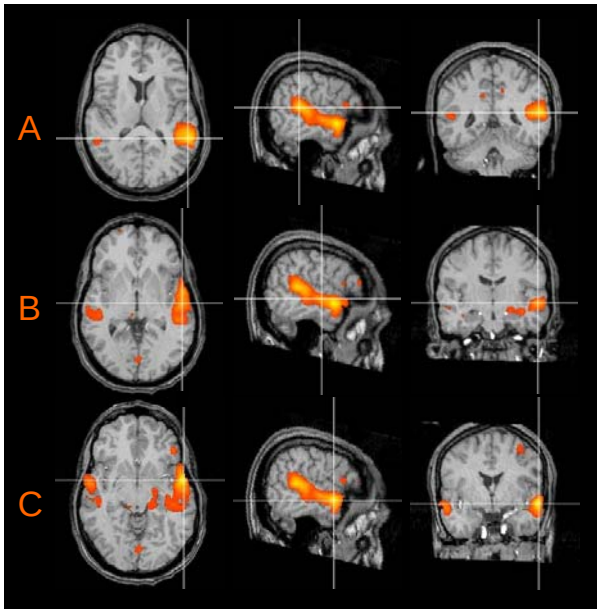

Figure 2: "Forward vs Backward Passive Listening"(FvB) activation map for the combined data set superimposed on 3D SPGR anatomic images.

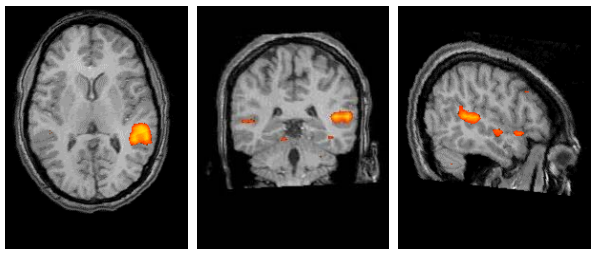

Figure 3: Three-plane display of a single subject activation map superimposed on high-resolution 3D SPGR anatomic images. Yellow-red color map indicates which pixels were considered active during FvB task

Discussion

The classical model for the anatomic organisation of language processing first described by Wernicke's localises the brain region for language comprehension in the posterior portion of the left superior temporal gyrus[11]. This region corresponds to the posterior portion of BA 22. This localisation was largely based on data from patients with strokes. Infarcts in the posterior superior temporal result in complete loss of language comprehension (receptive aphasia). Subsequent lesion studies have largely supported this result [12] [13] [14]. The results of the present study showing excellent selective activation of the left posterior temporal gyrus with the FvB language comprehension paradigm are consistent with the classic model for language processing and the results of subsequent brain lesion studies.

The results of PET and fMRI studies of language comprehension have been variable [3] [4] [5] [6] [1] [2] [7]. Studies have typically shown poor or no localisation of activity to the left posterior superior temporal gyrus [3] [4] [5] [6] [1] [2]. No published report has demonstrated the selective activation of the left posterior superior temporal gyrus seen in the present study. Several important differences exist between the paradigm used in the present study and those of prior investigators. The majority of these studies used single word comprehension rather than comprehension of narrative text [3] [4] [5] [6] [1] [2]. The relative difficulty and/or attention effects associated with comprehension of narrative text versus single words may account in part for the relatively selective activation of Wernicke's area seen in our FvB paradigm. A recent study that compared passive listening of native language versus non-native language narrative text also showed localised activity in the left superior temporal gyrus (as well as activity in other brain regions) suggesting that narrative text may provide better activation of regions responsible for language comprehension [7]. Typically, prior PET and fMRI investigation have not relied on passive listening, but rather have employed single word comprehension combined with a semantic task. The associated task performance may account in part for the lack of selective activation of the left superior temporal gyrus. Perhaps the most significant difference between the paradigm employed in the present study and those of others is in the selection of the appropriate control condition to be compared with the activation state. Prior studies have typically compared the activation state to scanner or background noise [3] [4] [5] [6] [1] [2]. Similar to our results in the FvN and BvN paradigms these studies usually showed fairly symmetric activation along the superior temporal gyrus and in some cases asymmetric activation of the posterior portion of the superior temporal gyrus. Although there is asymmetric activation of the posterior superior temporal gyrus is seen in the FvN paradigm with increase activity on the left, the degree of asymmetry is not as striking as the selective activation in the FvB paradigm. The use of backward narrative text as the comparison state provides an effective control for the all aspects of the acoustic component of the stimulus without providing understandable content. Thus allowing for relatively selective activation of brain regions related to auditory language comprehension.

Activation within the anterior portion of BA 22 on the left was also noted in the FvB paradigm. Other investigators have also demonstrated activation within this region with language comprehension tasks and the region is felt to serve as language association cortex [4].

Activation within the medial geniculate nuclei bilaterally was seen in the combined data from the FvB paradigm. No definite activation was seen in the medial geniculate nuclei in either the FvN or BvN paradigms. Although the medial geniculate has long been known to be an integral part of the auditory pathway, we know of no published data demonstrating mediate geniculate fMRI activation. It is unclear why activation in the present study was seen only in the FvB paradigm. The authors recognise that this finding requires further investigation.

It is clear that the paradigm presented in this study has several important advantages that make it immediately applicable clinically. The paradigm is simple and can be performed by virtually anyone. It requires relatively little in the way of special equipment or special training for either the patient or those administering the exam. It provides robust selective activation of Wernicke's area in individual subjects. Potential clinical applications would include pre-operative evaluation of temporal lobe seizure patients and identification of eloquent cortex prior to surgical removal of tumours or vascular malformations.

References

[1] Binder, J.R., Neuroanatomy of language processing studied with functional MRI. Clin Neurosci, 1997. 4(2): p. 87-94.

[2] Chertkow, H. and S. Murtha, PET activation and language. Clin Neurosci, 1997. 4(2): p. 78-86.

[3] Wise, R., F. Chollet, U. Hadar, K. Friston, E. Hoffner, and R. Frackowiak, Distribution of cortical neural networks involved in word comprehension and word retrieval. Brain, 1991. 114(Pt 4): p. 1803-17.

[4] Zatorre, R.J., A.C. Evans, E. Meyer, and A. Gjedde, Lateralization of phonetic and pitch discrimination in speech processing. Science, 1992. 256(5058): p. 846-9.

[5] Howard, D., K. Patterson, R. Wise, W.D. Brown, K. Friston, C. Weiller, and R. Frackowiak, The cortical localization of the lexicons. Positron emission tomography evidence. Brain, 1992. 115(Pt 6): p. 1769-82.

[6] Warburton, E., R.J. Wise, C.J. Price, C. Weiller, U. Hadar, S. Ramsay, and R.S. Frackowiak, Noun and

verb retrieval by normal subjects. Studies with PET. Brain, 1996. 119(Pt 1): p. 159-79.

[7] Nakai, T., K. Matsuo, C. Kato, M. Matsuzawa, T. Okada, G.H. Glover, T. Moriya, and T. Inui, A functional magnetic resonance imaging study of listening comprehension of languages in human at 3 tesla-comprehension level and activation of the language areas. Neurosci Lett, 1999. 263(1): p. 33-6.

[8] Lowe, M.J. and J.A. Sorenson, Spatially filtering functional magnetic resonance imaging data. Magn Reson Med, 1997. 37(5): p. 723-9.

[9] Bandettini, P.A., Jesmanowicz, A., Wong, E.C., Hyde, J.S., Processing strategies for time-course data sets in functional MRI of the human brain, Magn. Res. Med., 1993, 30: 161-173..

[10] Lowe, M.J. and D.P. Russell, Treatment of baseline drifts in fMRI time series analysis. J Comput Assist Tomogr, 1999. 23(3): p. 463-73.

[11] Wernicke, C., Der Aphasische Symptomencomplex: Eine psychologishe Studie auf anatomischer Basis. 1874, Breslau: Cohn and Weigert.

[12] Bogen, J.E. and G.M. Bogen, Wernicke's region--Where is it? Ann N Y Acad Sci, 1976. 280: p. 834-43.

[13] Geschwind, N., Problems in the anatomical understandings of the aphasias., in Contributions to clinical neuropsychology, A.L. Benton, Editor. 1969, Aldine: Chicago. p. 107-128.

[14] Coughlan, A.K. and E.K. Warrington, Word-comprehension and word-retrieval in patients with localized cerebral lesions. Brain, 1978. 101(1): p. 163-85.

Acknowledgements

The authors would like to thank our technologists, Julie B. Sims and Rich Fain for their help in performing the experiments.

On the organisation of the SII human somatosensory cortices: preliminary results with fMRI and electrical peripheral nerve stimulation

Della Penna S.[1], Del Gratta C.[1,2], Ferretti A. [1], Franciotti R.[1], Tartaro A.[2], Torquati K.[1] Bonomo L.[2], Rossini P.M.[3,4] and Romani G.L.[1,2]

1-Institute of Advanced Biomedical Technologies, University of Chieti, Chieti, Italy; 2-Department of Clinical Sciences and Biomedical Imaging, University "G. D'Annunzio", Chieti, Italy; 3-IRCCS "San Giovanni di Dio", Istituto Sacro Cuore di Gesù, Brescia, Italia; 4-AFaR-CRCCS "Isola Tiberina", Rome, Italy.

Introduction

Direct electrical stimulation of the exposed human brain during neurosurgery of drug-resistant epilepsies firstly demonstrated the presence of stimulus-evoked paresthesis when the stimulator tip was located on the superior bank of the Sylvian fissure and/or nearby convexial cortex [1]. This cortical area has been named since secondary somatosensory (SII); it shows a relatively rough topographical organization, is adjacent to primary auditory cortex and receives sensory inputs from both ipsi- and cotralateral hemibodies [2,3]. In fact, animal studies showed that receptive fields of the majority of SII neurons are bilateral; this probably provides an early integration of somatosensory information from both sides of the body. Such an hypothesis explains why in monkeys bilateral SII lesions affect severely their ability to learn from tactile stimuli, as well as their intermanual transfer of somatosensory information [4,5]. Electromagnetic brain responses to sensory stimuli in intact and awake humans, consistently demonstrated the existence of generator sources bilaterally located adjacent to the Sylvian fissure [6].
Functional Magnetic Resonance is a non-invasive functional imaging technique able to identify an event-related increase in oxygen consumption in discrete brain regions with a very good spatial resolution.
Aim of the present study was to investigate the ability of fMRI to localize the SII areas, and possibly reveal their somatotpic organization, in healthy humans following upper and lower limb sensory stimulation.

Method

BOLD contrast images were obtained in order to reveal oxygenated blood perfusion in activated brain areas, following electrical stimulation of median and tibial nerve.
We examined two healthy volunteers (male, aged 24 and 32). The protocol was approved by the local ethics comitee and both subjects gave their informed consent.
The MRI scans were performed with a SIEMENS MAGNETOM VISION 1.5 T scanner with echo-planar imaging capability. The scanning volume of functional images consisted of 22 bicomissural transaxial slices, 3 mm thickness, no gap, 128 × 128 matrix, FOV 250 mm, and covered the upper part of the brain from vertex to, and including, the upper bank of the temporal lobes. The functional imaging sequence was an EPI FID with TR = 0.8 ms and TE = 54 ms. Functional images were acquired according to a block paradigm, with alternating groups of 10 volumes each, in the stimulus and control condition respectively, with an interval between the starting of two consecutive images of 5s. In addition, a morphological image was acquired, with the same geometrical parameters as the functional, and a T1 weighed SE sequence (TR = 350 ms, TE = 15 ms). Finally a high resolution (FOV 250× 250, 256 × 256 matrix, 1 mm thickness, no gap, flip angle 12 degrees, TR 9.7 ms, TE 4 ms) image of the whole brain was acquired by means of a MPRAGE sequence.
Electrical stimuli were generated by means of a modified, battery powered, optically decoupled GRASS stimulator, driven by a HP 8116A pulse function generator operating outside the scanner shielded room and connected to the former via a low-pass filter. The stimuli were rectangular pulses, 0.4 ms in duration, at a frequency of 1.9 Hz and were manually controlled by an operator at the scanner consolle in order to be delivered during the appropriate paradigm blocks. Unilateral stimuli were delivered, by means of a pair of non magnetic, 3 cm spaced, Cu-Sn electrodes, via a twisted and shielded pair of wires, to the median nerve at the wrist and to the tibial nerve at the medial malleolus respectively; the stimulus intensity was adjusted clearly above the motor threshold, but with a painless intensity.
Analysis of functional images was performed using MEDx software by Sensor Systems. First, artifacts due to brain motion were reduced by means of AIR motion correction algorithm. When residual brain motion was considered satisfactory (fluctuations of the image centre of intensity below 0.2 mm), statistical brain activation images were generated by a Student t-test of the stimulus condition group of images versus the control group, and Z-score activation maps were obtained. Activated voxels were selected by means of a clustering algorithm. The mean intensity image of all the motion-corrected functional images was registered (AIR) to the high resolution morphological image, which was subsequently transformed into Talairach space. The transformation resulting from the combination of the

former two registrations was used to project the activation Z-score maps into Talairach coordinates. Finally, the clustered Z-score maps were thresholded and superimposed on the high resolution, Talairach transformed, morphological images.

Results

In all the subjects that we studied, activation was clearly seen in the superior parietal lobes contralaterally to the stimulated limb, and bilaterally in the inferior parietal lobes, in the supratemporal region, at the level of the Sylvian fissure.
The activated areas in the superior parietal cortex included areas that could be identified with the SI somatosensory area (Brodmann areas 1,2,3,5), and in which the activation was consistent with the homuncular organization of this cortex area, the upper limb representation being more lateral and more anterior, and the lower limb representation being more medial and more posterior. In addition, a more posterior, significantly activated area was observed, wich could be identified with Brodmann area 7.
The activated areas in the supratemporal region could be identified with the SII somatosensory cortices. They were investigated from two points of view: 1) the somatotopy of the area organization, by comparing the location and extension of the upper and lower limb representation areas, and 2) the extension of the ipsi- and contralateral activated areas, by comparing the numbers of activated voxels in different areas.
Table 1 indicates the Talairach coordinates, and the extension, of the statistically most significant clusters of activation in SI and SII areas for subject DAGI, for left and right, median and tibial nerve stimulation.

		R tib	L tib	R med	L med
SI	X	0	13	-34	47
	Y	-57	-56	-34	-20
	Z	63	63	49	50
	ΔX	6	11	10	2
	ΔY	5	7	4	1
	ΔZ	5	7	8	2
SII ipsilateral	X	45	-46	45	-48
	Y	-15	-26	-20	-22
	Z	9	10	0	13
	ΔX	18	4	9	5
	ΔY	8	4	6	3
	ΔZ	10	5	5	3
SII Contralateral	X	-39	46	-40	48
	Y	-28	-16	-26	-17
	Z	14	10	6	8
	ΔX	5	23	7	17
	ΔY	5	9	6	6
	ΔZ	4	8	6	8

Table1: Talairach coordinates, and extension, of the most significant clusters of activation in the parietal cortex of subject DAGI.

The extension of the clusters is calculated as the difference between the extrema of each cluster along the three coordinate axes. Distances are expressed in millimeters. Table 2 indicates the distances between the most significant clusters of activation elicited respectively by median and tibial nerve stimulation on the same side, in areas SI, SII ipsilateral to the stimulated side, and SII contralateral to the stimulated side. The distances are calculated from Talairach coordinates, and are expressed in millimeters.

	Right side stimulation	Left side stimulation
SI	43	34
SII Ipsilateral	10	5
SII Contralateral	8	3

Table2: Distance between the most significant clusters of activation elicited respectively by median and tibial nerve stimulation of the same side, in SI and SII areas of subject DAGI.

Table 3 indicates the volume (as measured by the number of activated voxels) of the activated regions in SII for left and right, median and tibial nerve stimulation.

	Right median	Left median	Right tibial	Left tibial
Iipsi-lateral	156	425	666	177
Contra-lateral	647	852	238	719

Table 3: Number of activated voxels in the SII area of left and right hemispheres, for left and right, median and tibial, nerve stimulation in subject DAGI.

Figure 1 shows a number of slices in the Talairach transformed high resolution image with, superimposed, the co-registered, statistically significant, activated regions of SII, elicited by the stimulation of the left median and tibial nerves.
Figure 2 shows, in more detail, in a selected slice, the SII activated regions, elicited by right median and tibial nerve stimulation. Note the clearcut somatotopy.

Discussion

Due to technical problems in the electrical peripheral nerve stimulation within the MRI, functional studies of the somatosenry system have been mostly performed using mechanical tactile stimulation that activates only selected mechanoreceptors. Recently, Spiegel et al. [7] compared fMRI activations elicited by electrical me-

trical median and tibial nerve stimulation, in SI as well as in SII cortices.

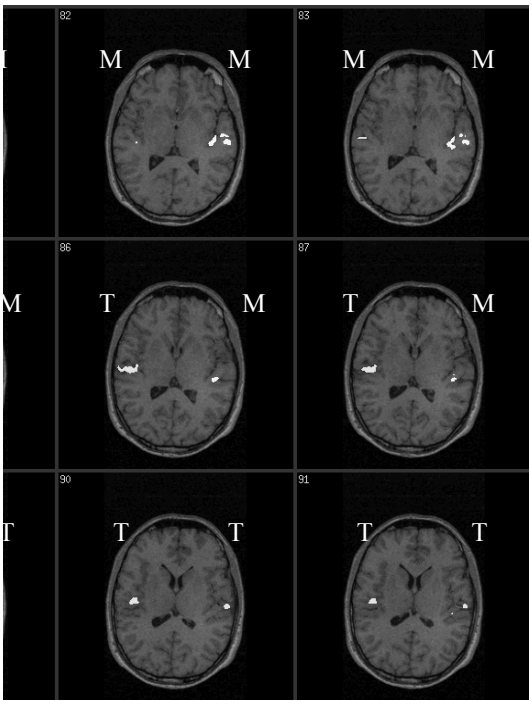

*lution, Talairach projected image with superimposed the statis-
the stimulation of the left median and tibial nerves. The slices
stral. Left hemisphere is on the right and vice versa. Letters M
ely. Somatotpy is clearly visible, the tibial nerve representation
on.*

Figure 2: (Next page lower panel) Subject DAGI: 1slice from the high resolution, Talairach projected image with superimposed the statistically significant, activated regions of SII, elicited by the stimulation of the right median and tibial nerves. . Left hemisphere is on the right and vice versa. The activations are enlarged for clarity, to show the spatial relationships between the different representation areas. Somatotopy is again clearly visible, the tibial nerve representation being more posterior than the median nerve representation, in the contralateral hemisphere. Note that in the ipsilateral hemisphere, the organisation seems to be more complicated, with an area of overlap of the the median and tibial nerve representation areas.

Figure 1 shows, in the case of one subject, for left side stimulation, that the region activated by tibial nerve stimulation is more rostral than the region activated by median nerve stimulation. Figure 2, corresponding to right side stimulation, also shows a different location of upper and lower limb representations in SII, the lower limb being more posterior than the upper limb in the hemisphere contralateral to stimulated side. In the hemisphere ipsilateral to the stimulated side, the organisation is not as clearly marked: although distinct regions are activated by upper and lower limb stimulation respectively, these regions partially overlap and show a more complicated spatial relationship.

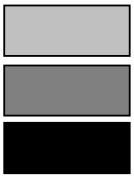

Median nerve

Tibial nerve

Overlapping region

A comparison of the intensities of activation in the SII areas may be obtained by evaluating the size of the activated regions in the various stimulus conditions. From Table 2 it can be seen that in three cases over four, the activated region is larger in the contralateral SII area. Focusing attention on each single hemisphere, it can be seen that, for median nerve, as well as for tibial nerve stimulation, the size of the activated area is larger when the hemisphere is contralateral to the stimulus. These results are consistent with those obtained by means of MEG [8] that indicate more intense dipolar sources in contralateral SII.
To our knowledge this is the first report in which somatotopy of the secondary somatosensory cortex is revealed by means of fMRI.

References

[1] Penfield, W., and Jasper, H. Epilepsy and the Functional Anatomy of the Human Brain, Boston, Little, Brown, and Company, 1954.

[2] Woolsey, C., Erickson, T., and Gilson, W. Localization in somatosensory and motor areas of human cerebral cortex as determined by direct recording of evoked potentials and electrical stimulation, J. Neurosurgery, 1979, 53:476-506.

[3] Allison , T.G.M., Wood, C., Williamson, P., and Spencer, D. Human cortical potentials evoked by stimulation of the median nerve. II Cytoarchitectonic areas generating long-latency activity, J. Neurophysiol., 1989, 62:711-722.

[4] Ridley, R., and Ettlinger, G. Further evidence of impaired tactile learning after removals of the second somatic sensory projection cortex (SII) in the monkey, Exp. Brain Res., 1978, 31:475-488.

[5] Picard, N., Lepore, F., Ptito, M., and Guillemot, J.-P. Bilateral interaction in the second somatosensory area (SII) of the cat and contribution of the corpus callosum. Brain Res., 1990, 536:97-104.

[6] Hari, R., and Kaukoranta, E. Neuromagnetic studies of the somatosensory system, Progr. Neurobiol., 1985, 24:233-256.

[7] Spiegel, J., Tintera, J., Gawehn, J., Stoerer, P., and Treede, R.-D. Functional MRI of human primary somatosensory and motor cortex during median nerve stimulation, Clin. Neurophysiol., 1999, 110:47-52.

[8] Hari, R., Karhu, M., Hämäläinen, M., Knuutila, J., Salonen, O., Sams, M., and Vilkman, V. Functional organisation of the first and second somatosensory cortices: a neuromagnetic study, European Journal of Neuroscience, 1993, 5:724-734.

The use of single event fMRI and fuzzy clustering analysis to examine haemodynamic response timecourses in supplementary motor and primary motor cortical areas.

[1, 4] Cunnington R., [2] Windischberger C., [1] Deecke L., and [2, 3] Moser E.

[1] Department of Neurology, University of Vienna, Vienna, Austria
[2] NMR Unit, Institute for Medical Physics, University of Vienna, Vienna, Austria
[3] Centre for Magnetic Resonance Imaging, General Hospital of Vienna, Vienna, Austria
[4] Department of Psychology, Monash University, Melbourne, Australia

Introduction

The roles of premotor, supplementary motor and primary motor cortical areas in the organisation and control of voluntary movement have been studied using many different methods, all of which have differing strengths and weaknesses. Electrophysiological studies, examining cortical activity recorded from the scalp surface, have shown that a slowly increasing negative potential, termed the Bereitschaftspotential, precedes movement onset by 1 to 2 seconds [1]. This increasing pre-movement activity is thought to reflect processes associated with movement preparation involving mainly the supplementary motor area (SMA); however, it is difficult to accurately localise the cortical source of this pre-movement activity from surface potentials. Studies of regional cerebral blood flow, using PET, have shown activation of both the SMA and primary motor cortex during voluntary movement compared with rest, and activation mainly in the SMA when movements are imagined (assumed to involve similar processes of movement preparation), but not actually executed [2, 3]; however, this technique lacks the temporal resolution to make conclusions regarding the roles of various cortical areas in processes preceding movement onset.

Functional MRI provides better spatial resolution for localising sources of activation, and has the potential to provide better temporal resolution than PET; however, most studies of motor activation to date have used relatively long image repetition times and box-car type designs alternating between periods of rest and activation, thereby providing little improvement in temporal resolution compared with previous PET studies.

Echo planar functional MRI, using fast repetition times, has the potential to reveal haemodynamic response characteristics for single events or actions [4], however new methods for analysing such data are required. Standard fMRI designs which use relatively long repetition times and consist of alternating rest and activation periods are commonly analysed by correlation with a simple box-car reference function. Single-event fMRI data can also be analysed by correlation with some modelled reference function [5]; however, such an approach requires prior knowledge of the expected time and duration of the haemodynamic response, which is not always available. Alternately, average timecourses within predefined anatomical regions of interest can be examined. A study by Richter et al. [6], using time-resolved fMRI to examine the temporal characteristics of the haemodynamic response to a single movement, was able to separate activation occurring during periods of movement preparation compared with movement execution. By examining average timecourses within regions of interest, activity of the SMA and premotor cortex were found to be similar during both preparation and execution periods, whereas activity of the primary motor cortex was reduced during movement preparation. Similarly, a study by Wildgruber et al. [7] examined average haemodynamic response timecourses within the supplementary motor area and primary motor cortex (as predefined regions of interest) associated with single self-paced finger movements, showing that activation within supplementary motor area begins significantly earlier than that in primary motor cortex.

Such studies using region of interest analyses have provided important information regarding differences in activation of areas for which involvement in particular tasks is already known. This analysis approach, however, does not take full advantage of the ability of high resolution function MRI to localise activity without relying on prior assumptions of activity sources.

Fuzzy clustering analysis [8] is a model-free analysis method which separates different timecourses present within a data set into clusters such that variability of timecourses within clusters is minimised and variability between clusters is maximised. In this way, fuzzy clustering analysis is able to separate timecourses associated with the activation task from those associated with artefact (e.g. physiological artefact associated with heart beat or respiration [9]) or drift, and can show the extent to which voxels within the whole brain space acquired show task-related haemodynamic response timecourses. The analysis of results, therefore, is not restricted only to particular regions of interest, nor only to particular timecourse characteristics.

The aim of this study was to examine activation associated with single movements of the 5^{th} finger with both high temporal and spatial resolution. Single slice EPI images were acquired with both 64^2 and 128^2 matrix sizes with fast repetition rate (80 ms and 160 ms

respectively between consecutive images). Fuzzy clustering analysis was then used to extract different timecourses and to separate task-related activation of supplementary and primary motor cortical areas from physiological artefact.

Method

Five right-handed healthy subjects (age 18-30 years) were examined on a 3 Tesla Medspec S300 (Bruker Medical, Ettlingen, Germany) equipped with a whole-body gradient system and a birdcage head coil. Imaging was performed using a phase-corrected single-shot gradient-echo blipped EPI sequence. A single slice of 5mm thickness and FOV 256 by 256 mm was acquired using two different matrix sizes: 64^2 (4x4 mm) pixel (RBW=100kHz; TR=80 ms; 750 repetitions) and 128^2 (2x2 mm) pixel (RBW=200kHz; TR=160 ms; 375 repetitions). Echo time (TE=40 ms) and total acquisition time (60 s) were always constant. Head motion artefacts were minimised by using a head-shaped pillow and a strap fixed across the forehead.
Subjects performed a single extension of the 5^{th} finger of the right hand. This movement was selected since previous work of our group has found extension of the 5^{th} finger to give greater functional activation of supplementary and primary motor cortical areas than extension of the index finger [10]. The movement was made by subjects in response to an auditory "go" signal presented via headphones exactly 20 s after the start of image acquisition.
Functional data was analysed using fuzzy clustering as implemented in EvIdent 3.34 (IBD, NRC, Winnipeg, Canada). Initially 50 clusters were formed representing 50 different patterns of voxel intensity variation over time. These timecourses were then subjectively judged as representing artefact or task-related activation patterns.

Results and Discussion

Fuzzy-clustering analysis was able to identify timecourses relating to physiological artefacts, such as heart beat and respiration, as well as activation timecourses relating to the finger movement task. Artefactual timecourses were most apparent in the 64^2 matrix size images in which the repetition time, or effectively the sampling rate, was higher. Often such artefact obscured all task-related activation.
Figure 1 shows a typical example of physiological artefact extracted by fuzzy clustering analysis. As can be seen in the image, voxels showing such artefact were generally not clustered together in discrete anatomical regions, but spread apparently randomly across the brain. Peaks with a frequency of approximately 1 Hz most likely reflect heart beat while lower frequency variation of approximately 10 s per cycle most likely reflect respiration. Such voxel intensity variations are most likely caused by physiological motion of the brain associated with cardiac pulsation and venous pressure changes with respiration [9]. Pulsatile blood flow in arteries directly alters the phase and magnitude of the MR signal of the vessels due to spin history effects, as well as causing the brain to pulsate due to arterial pressure changes; both effects cause voxel intensity changes according to heart rate. Respiration also causes pulsation (expansion and contraction) of the brain as cranial blood volume and venous pressure change according to changes in thoracic pressure with inspiration and expiration.

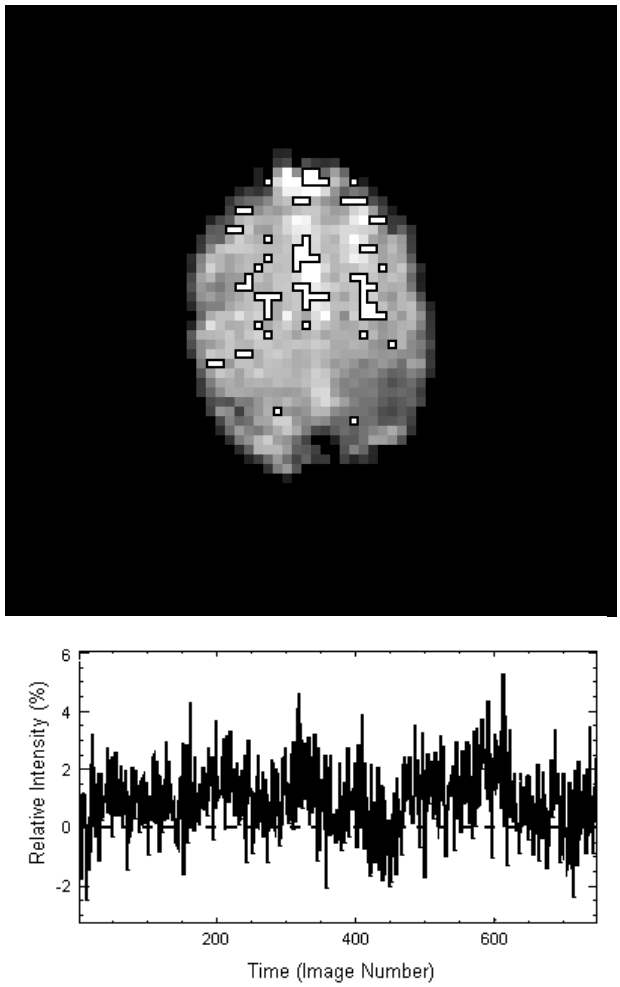

Figure 1: A typical timecourse representing physiological artefact for a 64x64 matrix image. The marked pixels in the image above show the areas correlated with the timecourse. High frequency and lower frequency variations associated respectively with heart rate and respiration are apparent in the timecourse.

Despite the dominance of such physiological artefact, timecourses representing task-related activation were also found by fuzzy clustering analysis. Only preliminary results of task-related changes for a single subject are reported here.
Figures 2 and 3 show task-related activation timecourses which were found in contralateral primary motor and supplementary motor areas. The slice orientation is not parallel with the AC-PC plane, but is angled forward such that the central sulcus (primary somatosensory cortex) is near the posterior edge of the slice.

Pixels within contralateral primary motor and supplementary motor areas correlated with the respective timecourses are marked in white and overlaid on the mean EPI images. Images of both matrix sizes clearly showed task-related intensity changes representing the haemodynamic response (or blood oxygen level changes) within supplementary motor and contralateral primary motor areas to a single extension of the 5th finger.

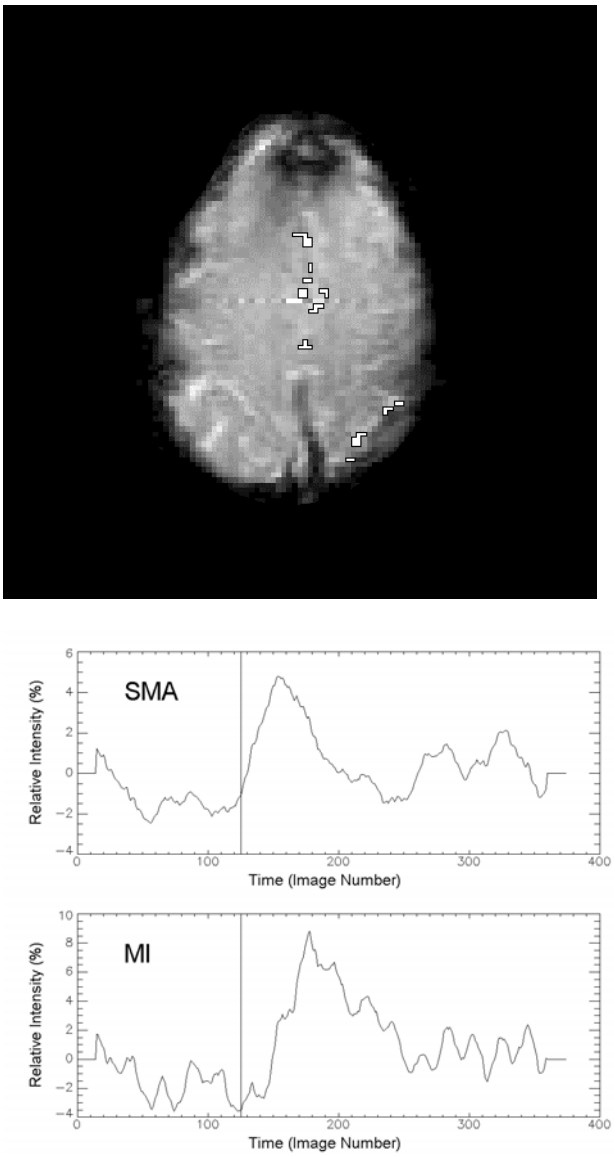

Figure 2: 128^2 matrix image and timecourses comparing task related activation in supplementary motor area (SMA) and primary motor cortex (MI).
100 images represents 16 s duration and the vertical line represents the time of movement of the 5th finger.

The 128^2 matrix image (Figure 2), with higher spatial resolution and lower effective sampling rate (longer repetition time), showed the haemodynamic response within supplementary motor area to begin at or immediately prior to the movement. Given that the haemodynamic response of the brain to brief stimuli, as measured by fMRI, is delayed by approximately 5 s relative to the underlying neural activation [4], this clearly represents activation of the supplementary motor area beginning prior to movement onset. Moreover, the haemodynamic response within primary motor cortex clearly begins later than that within supplementary motor area. This is consistent with the findings of Wildgruber et al [7], that activation of the supplementary motor area precedes that of primary motor cortex, and further supports the theory that the supplementary motor area is important for processes associated with the preparation and planning for forthcoming movements and is therefore functionally upstream from primary motor cortex [1].

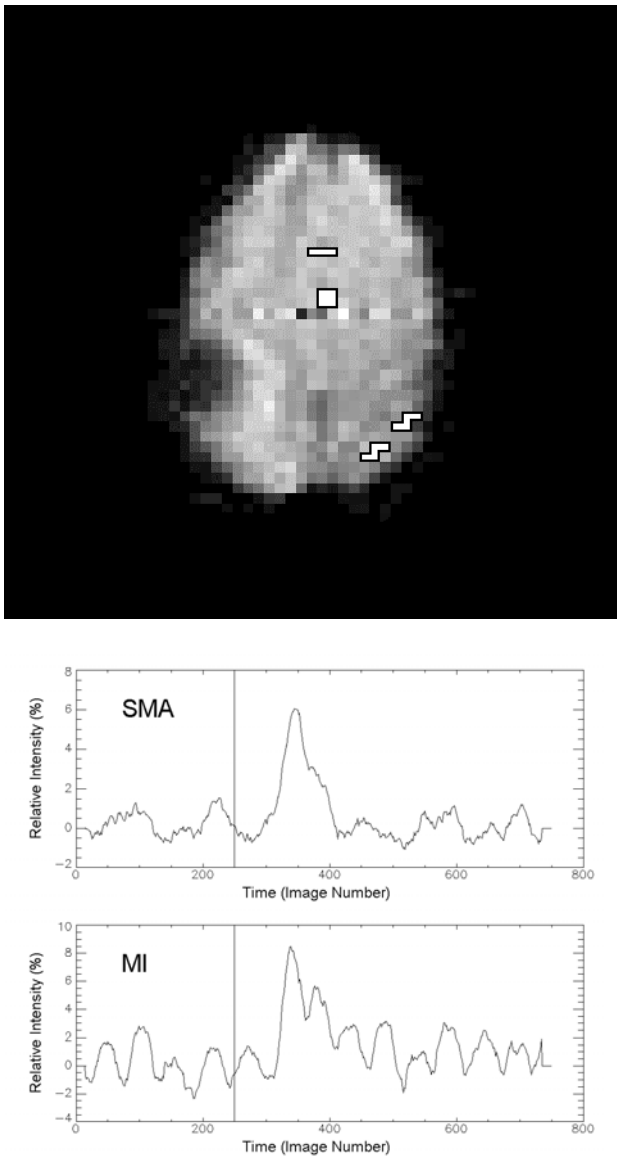

Figure 3: 64^2 matrix image and timecourses comparing task related activation in supplementary motor area (SMA) and primary motor cortex (MI).
200 images represents 16 s duration and the vertical line represents the time of movement of the 5th finger.

The 64^2 matrix image showed timecourses more affected by artefact due to the higher effective sampling rate (faster repetition time). Timecourses representing the haemodynamic response within supplementary motor and contralateral primary motor areas were apparent; however, due the additional artefact it is difficult to make statements regarding onset times of these activation patterns. Haemodynamic responses within both areas appear to begin together, and both also appear to begin later and show a shorter duration than for the 128^2 matrix image.

There is no theoretical reason for these two MRI matrix sizes and repetition rates to result in different measured haemodynamic response patterns; therefore, apparent differences may be due either to artefact or variability of the response over different trials. This raises an interesting issue regarding inter-trial variability which becomes apparent when it is possible to determine activation patterns for single trials. The haemodynamic response to the same repeated stimulus within primary cortical areas (motor and visual) is found to be highly consistent [4]; however, the consistency of the haemodynamic response within secondary and association areas, reflecting higher-order cognitive processes, has not been examined and most likely varies considerably with varying task performance or with differing strategies or cognitive set employed by subjects which may vary over repeated trials.

Such possible "psychological" variability may provide important information when examining brain function; however, when the aim of an fMRI study is simply to localise a particular function, variability perhaps provides grounds for averaging in order to improve the activation signal for the function of interest.

Conclusions

Using single event fMRI with high repetition rates and fuzzy clustering analysis, haemodynamic response timecourses representing activation of supplementary motor and primary motor cortical areas for a single extension of the 5^{th} finger were found. Activation of the supplementary motor area appeared to begin prior to movement onset and preceded that of primary motor cortex.

Much physiological artefact arising from heart beat and respiration was also apparent and may be improved by averaging across repeated trials; however, inter-trial variability in activation patterns may provide important information and the ability to detect such activation patterns in single trials is a major benefit of this methodology. Single event fMRI, in conjunction with fuzzy-clustering analysis, is therefore a powerful technique which is able to detect event-related activation patterns for single trials with both high temporal and spatial resolution.

References

[1] Deecke L., and Kornhuber H.H. An electrical sign of participation of the mesial 'supplementary' motor cortex in human voluntary finger movement. Brain Research, 1978, 159:473-476.

[2] Roland P.E., Larsen B., Lassen N.A., and Skinhoj E. Supplementary motor area and other cortical areas in organization of voluntary movements in man. Journal of Neurophysiology, 1980, 43:118-136.

[3] Stephan K.M., Fink G.R., Passingham R.E., Silbersweig D., Ceballos Baumann A.O., Frith C.D., and Frackowiak R.S. Functional anatomy of the mental representation of upper extremity movements in healthy subjects. Journal of Neurophysiology, 1995, 73:373-386.

[4] Kim S.G., Richter W., and Ugurbil K. Limitations of temporal resolution in functional MRI. Magnetic Resonance in Medicine, 1997, 37:631-636.

[5] Friston K.J., Josephs O., Rees G., and Turner R. Nonlinear event-related responses in fMRI. Magnetic Resonance in Medicine, 1998, 39:41-52.

[6] Richter W., Andersen P.M., Georgopoulos A.P., and Kim S.G. Sequential activity in human motor areas during a delayed cued finger movement task studied by time-resolved fMRI. Neuroreport, 1997, 8:1257-1261.

[7] Wildgruber D., Erb M., Klose U., and Grodd W. Sequential activation of supplementary motor area and primary motor cortex during self-paced finger movement in human evaluated by functional MRI. Neuroscience Letters, 1997, 227:161-164.

[8] Scarth G., McIntyre M., Wowk B., and Somorjai R. Detection of novelty in functional images using fuzzy clustering. Proceedings ISMRM, 1995, 1:238.

[9] Hu X., Le T.H., Parrish T., and Erhard P. Retrospective estimation and correction of physiological fluctuation in functional MRI. Magnetic Resonance in Medicine, 1995, 34:201-212.

[10] Erdler M., Windischberger C., Cunnington R., Edward V., Streibl B., Gartus A., Moser E., Deecke L., and Beisteiner R. Quantification of supplementary motor area activation with movements of different practice levels using functional magnetic resonance imaging at 3T. Biomedizinsche Technik, 1999, [this volume].

Quantification of Supplementary Motor Area activation with movements of different practice levels using Functional Magnetic Resonance Imaging at 3T

Erdler M. 1, Windischberger C. 2, Cunnington R. 1, Edward V. 1, Streibl B. 1, Gartus A. 1, Moser E. 2, Deecke L. 1 and Beisteiner R. 1

1 Department of Neurology, 2 NMR-Group – Institute for Medical Physics, General Hospital and University of Vienna, Vienna, Austria

Introduction

It is well known that the supplementary motor area is more active and more critically involved in processing complex movements, which are more difficult to execute, than simple ones. The stronger increase of the slow negative electrical activity in EEG over the supplementary motor area while executing complex movements compared to simple movements was demonstrated [1, 2] as well as the increase of regional cerebral blood flow in the supplementary motor area while performing various complex movements [3]. Similar results were shown with a comparison of a simple finger opposition task and a complex sequential finger opposition task [4] and a simple compared to a complex finger tapping task [5]. Stimulating the supplementary motor area with repetitive transcranial magnetic stimulation caused errors only in the most complex task compared to more simple movement sequences [6]. There are many factors that make a movement more or less difficult to execute, like speed and accuracy, involvement of number of joints and muscles, modes of movement selection, but also the degree of experienced practice. The effect of short and long term practice of movements on the activity of the supplementary motor area was described in several studies [e.g. 7]. It was demonstrated that supplementary motor area activity decreases with higher levels of practice. The goal of this study was to investigate whether differential supplementary motor area activation also reflects the different degrees of training which are experienced by the different fingers of a hand during daily life.

Methods

Six right handed healthy subjects (mean age 26) took part in the experiment. Subjects had to perform repetitive tapping of the 2nd and the 5th finger paced by the scanner noise at a constant frequency of 1.6 Hz. The tapping was performed in a blocked design with a block duration of 20 s. Subjects had to execute the tapping either of the 2nd or the 5th finger in blocks with alternating order. Blocks of finger tapping were separated by blocks of rest. One measurement included 4 trials, each trial consisting of 65 consecutive time points and 6 finger tapping blocks (3 blocks tapping of the 2nd finger and 3 blocks tapping of the 5th). One trial lasted for 260 s. Fig 1 shows the design of one trial graphically.

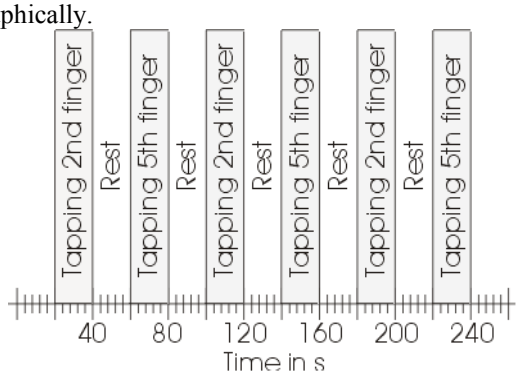

Fig 1: Design of one trial

The measurements were carried out on a 3 Tesla BRUKER Medspect S300 scanner using a phase-corrected blipped gradient echo single shot EPI sequence (TE/TR = 84/4000 ms, 128*128 matrix, 256*256FOV. 13 adjacent axial slices with a slice thickness of 3 mm were measured. Images were realigned using AIR v3 with 3D sinc interpolation [8]. Data were analyzed using a correlation technique with a threshold of 0.6. Active pixels in the supplementary motor area were counted in each measured slice separately for the 2nd and the 5th finger tapping.

Results

The number of active pixels in the supplementary motor area was larger when tapping the 5th finger compared to tapping the 2nd finger in all 6 subjects. Table 1 shows the detailed results for each subject.

Subject #	# of active pixels in SMA, 2nd finger	# of active pixels in SMA, 5th finger
1	4	52
2	2	6
3	9	13
4	2	18
5	2	29
6	2	11

Tab1: Number of active pixels in SMA are given for 2nd finger tapping and 5th finger tapping

The mean number of active pixels for tapping of the 2nd finger was 3.5 and for the 5th finger 21.5, yielding a mean difference of 18 active pixels. Over all subjects the cumulated number of active pixels in the supplementary motor area was 21 for the 2nd finger tapping and 129 for the 5th finger tapping, which corresponds to a 6 fold increase in pixel counts. A t-test confirmed a significant group difference ($t(5) = 2.58$, $p < 0.05$). Figs 2 (2a & 2b) and 3 (3a & 3b) show the results for two of the subjects (Fig 2 = subject 1, Fig 3 = subject 2). Activated pixels in the supplementary motor area and the primary motor cortex are colored. The figures for the two subjects show one representative slice for 2nd finger tapping (Figs 2a and 3a) and 5th finger tapping (Figs 3a and 3b). It can clearly be seen that more pixels are activated in the supplementary motor area when tapping the 5th finger.

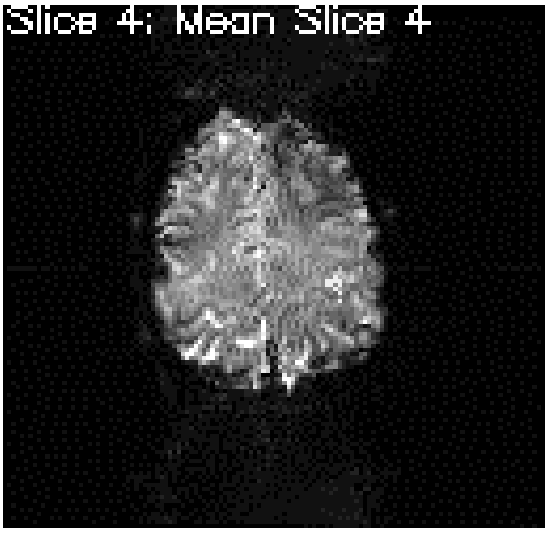

Fig 2a: 4th slice of one subject during the 2nd finger tapping task. Activated pixels in the SMA and MI are colored.

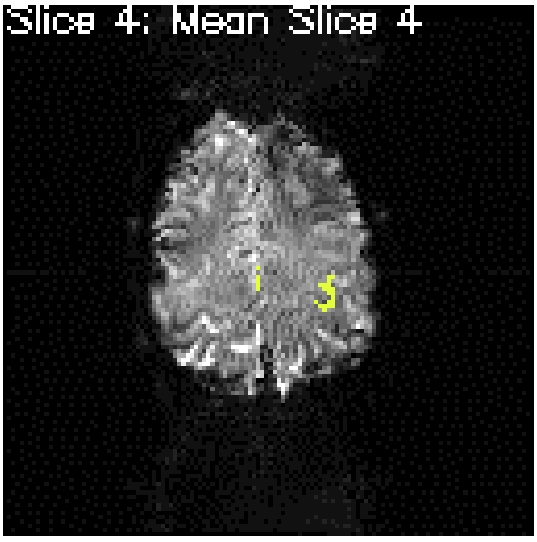

Fig 2b: 4th slice of the same subject during the 5th finger tapping task.

Fig 3a: 3rd slice of the second subject during the 2nd finger tapping task. Activated pixels in the SMA and MI are colored.

Fig 3b: 3rd slice of the same subject during the 5th finger tapping task.

Discussion

The main result of this study is the significant difference in area of activation for the 2nd finger tapping task and the 5th finger tapping task. This confirms findings of previous studies stating the dependence of activation of the supplementary motor area on movement complexity and difficulty [1-6]. One of the reasons for making the performance of a movement difficult is the lack of practice [7]. Due to the fact that the index finger is much more used in daily life than the fifth finger and tapping procedures are more frequently performed with the index than the little finger, rhythmic tapping movements are usually experienced as being more difficult when using the little finger. This lack of specific practice demands a higher level of motor control since the optimum activation of appropriate sets of muscles

with appropriate intensity and optimized coordination for such movements is not adequately accessible. This is reflected by increased areas of fMRI activation within the supplementary motor area but also the primary sensory motor cortex, recordable despite type of movement and movement frequency were exactly the same with both fingers. In general the finding demonstrates a high sensitivity of high field fMRI for subtle activation changes in small brain areas as induced by small variations of movement type.

References

[1] Lang, W., Zilch, O., Koska, C., Lindinger, G., Deecke, L. Negative cortical DC shifts preceding and accompanying simple and complex sequential movements. Exp Brain Res, 1989, 74: 99-104.

[2] Lang, W. Cheyne, D. Kristeva, R., Beisteiner, R., Lindinger, G., Deecke, L. Three dimensional localization of SMA activity preceding voluntary movement. A study of electric and magnetic fields in a patient with infarction of the right supplementary motor area. Exp Brain Res, 1991, 87 (3): 688-695.

[3] Orgogozo, J,M,, Larsen, B. Activation of the SMA during voluntary movements in man suggests it works as a surpramotor area. Science,1979, 206: 847-850.

[4] Shibasaki, H., Sadato, N., Lyshkow, H., Yonekura, Y., Honda, M., Nagamine, T., Suwazono, S., Magata, Y., Ikeda, A., Miyazaki, M., Fukuyama, H., Asato, R., Konishi, J. Both primary motor cortex and supplementary motor area play an important role in complex finger movement. Brain, 1993, 116: 1387-1398.

[5] Rao, S.M., Binder, J.R., Bandettini, P.A., Hammeke, T.A., Yetkin, F.Z., Jesmanowicz, A., Lisk, M.S., Morris, G.L., Mueller, M.D., Estkowski, R.T.R., Wong, E.C., Haughton, M.D., Hyde, J.S. Functional magnetic resonance imaging of complex human movements. Neurology, 1993, 43: 2311-2318.

[6] Gerloff, C., Corwell, B., Chen, R., Hallett, M., Cohen, L.G. Stimulation over the human supplementary motor area interferes with the organization of future elements in complex motor sequences. Brain, 1997, 120: 1587-1602.

[7] Hund-Georgiadis, M; von-Cramon, DY. Motor-learning-related changes in piano players and non-musicians revealed by functional magnetic-resonance signals. Exp Brain Res, 1999, 125 (4) : 417-425

[8] Woods, RP., Grafton, ST., Holmes, CJ., Cherry, SR., Maziotta, JC. Automated image registration: I. General methods and intrasubject, intramodality validation, J of Comp Ass Tomography, 1998, 22 (1): 139-152.

Acknowledgements

This work was supported by the FWF research grant P12451 MED.

Functional Discrimination of Thalamic Nuclei Using BOLD Contrast fMRI at 1.5 T

Dzemidzic M., Lowe M.J., Mathews V.P., Lurito J.T., and Phillips M.D.

Department of Radiology, Indiana University School of Medicine, Indianapolis, IN, USA

Introduction

Functional magnetic resonance imaging (fMRI) techniques have been extensively used in investigating functionality of various cortical areas. However, these techniques can also be applied to the studies of neuronal activation in small gray matter structures of the thalamus, basal ganglia, and brainstem. The thalamus is located superior to the brainstem and is composed of numerous nuclei differentiated by their fibrous connections to different brain regions. Some of the thalamic nuclei have spatial dimensions approaching 10 mm^3. Chen *et al.* reported that that the lateral geniculate nucleus (LGN) of the thalamus and pulvinar of the thalamus could be discriminated using fMRI techniques at 4 tesla (T) [1]. Guimares *et al.* successfully used functional magnetic resonance imaging at 1.5 T to detect subcortical auditory activation in the medial geniculate nucleus (MGN) [2].

In this work we demonstrate that adjacent thalamic nuclei can be clearly discriminated using blood-oxygenation level dependent (BOLD) fMRI at 1.5 T. Six normal subjects were studied in a protocol designed to detect thalamic activation in simple auditory and visual tasks. The hypothesis is that the medial geniculate nucleus of the thalamus will be activated in the auditory task while the lateral geniculate nucleus of the thalamus will be detected in the visual task. The physical dimensions of these two adjacent thalamic nuclei are approximately equal to the spatial resolution of the acquired functional images (3.5 mm^3) thus illustrating the spatial specificity of the BOLD fMRI technique in subcortical structures. In addition, the LGN-MGN separation distance is comparable to the in-plane spatial resolution of the acquired data, which constitutes a test of the spatial resolving power for BOLD fMRI method at 1.5 T

Method

Time series BOLD-weighted data were obtained on a 1.5 T General Electric Echospeed scanner (GE Medical Systems, Waukeshau, WI, USA), with gradient echo-planar (GE-EPI) parameters: repetition time = 2.25 s; echo time = 50 ms; field-of-view = 24cmx24cm; matrix 64x64; bandwidth = 125 kHz; flip angle = 90^o. An experienced neuroradiologist chose a single, 3.5-mm thick, axial slice through the lateral and medial geniculate nuclei. The slice was selected on a whole head 3D Spoiled Grass (3D SPGR) T_1-weighted scan taken at the beginning of the scanning session. The imaging parameters for this high-resolution anatomical scan were the following: repetition time = 35 ms; echo time = 12 m ms; field-of-view = 24cmx24cm; matrix = 256x128; bandwidth = 32 kHz; flip angle = 30^o; slice thickness = 1.1 mm, and 124 contiguous axial slices.

BOLD functional magnetic resonance imaging amounts to searching for regionally specific signal fluctuations due to changes in venous blood susceptibility that are typically under 2 % at 1.5 T [3]. These small signal changes between control and activation images can be easily overwhelmed by subject head motion leading to possibly severe imaging artefacts. Head motion restraint must be comfortable but sufficiently rigid to prevent the transfer of small body movements to the cranium. We use a bite bar made from dental impression compound and mounted to the birdcage radio frequency (RF) coil with hard plastic secured by non-magnetic metal screws. Since visual and auditory stimulus delivery equipment operates within the magnetic field it is essential that it does not cause RF noise. Visual stimuli are delivered via a MRI-compatible stereoscopic visual system (Avotec Inc., Jensen Beach, FL, USA) with fiberoptic goggles mounted to the birdcage head coil with a custom holder. In addition to providing stimulus delivery, the auditory system also offers hearing protection necessary in the extremely noisy (~ 130 dB) scanner environment generated by echo-planar pulse sequence. Avotec pneumatic stereo headphones with attached earplug-type carrier tubes give approximately 30 dB sound attenuation and are interfaced to a microphone, stereo and computer systems.

Subjects were presented paradigms following 36 second “off” - 36 second “on” pattern giving a 16 image “off” - 16 image “on” boxcar reference function for expected activation pattern. A single complete GE-EPI scan lasted 648 seconds and consisted of a quarter cycle of rest, followed by 8.5 rest/activation cycles, and concluded by a quarter cycle of rest. Two auditory and two visual functional MRI scans were performed for each subject. The auditory stimuli consisted of fragments of narrative text (activation) interleaved with the ambient scanner noise (control). Visual stimuli consisted of periods of black background with a colored fixation point (control) and a background of a checkerboard pattern switching at 8 Hz with a colored fixation point (activation). Requiring the subjects to press a button on a response pad every time the color of the fixation point changed ensured the fixation during the scan. The fixation point was programmed to change colors at random intervals throughout both control and switching checkerboard presentations. The visual pres-

entation was achieved by using the Stim presentation software (Neuroscan Inc., Sterling, VA, USA).
The large bandwidth of the echo-planar data acquisition necessary to obtain the desired functional image also enhances the presence of high spatial frequency noise. Filtering of this noise component can significantly improve the signal-to-noise ratio of the reconstructed images. However, low-pass filters dramatically attenuate very small signals. In the case where the activated region has a spatial extent larger than four pixels in radius, a good general-purpose filter that does not appreciably affect the amplitude of the activation signal is the Hamming filter. Application of a Hamming spatial filter to each image of the time series improved the temporal coefficient of variance (COV_t) to 0.7%, almost a threefold improvement in noise signature with only a small loss of spatial resolution [4]. The MRI time series at each pixel in the data was fit using the least squares fit to a boxcar reference function, a slope, and an intercept [5].
It is well known that it is necessary to account for a delay between the start of an activation cycle and the onset of BOLD activation signal [6]. In addition, the first few images are acquired before a steady state with respect to proton spin saturation is achieved. After the pilot studies we concluded that discarding the first eleven volumes adequately accounts for pre-saturation and hemodynamic delay effects. The final five volumes were also excluded so that the final GE-EPI data set would consist of exactly 8.5 activation cycles with 272 time points for each pixel in the volume. Fig. 1, that shows MR signal intensity while the subject was performing a visual task, very nicely illustrates activation pattern with alternating control and activation periods.

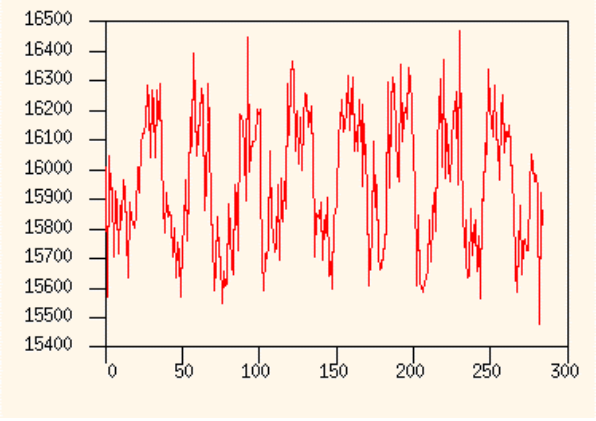

Figure l: Magnetic resonance signal intensity in an individual visual scan is shown as a function of image volume for a pixel in the primary visual cortex. MR time series includes 288 image volumes, out of which 272 volumes (exactly 8.5 activation cycles) are used to generate activation maps.

The ratio of the amplitude and the error of the fit to the reference function required to assign a Student's t-statistic for each pixel was used to generate activation maps. The percentage signal change was determined from the ratio of the amplitude to the intercept of the line determined from the fit.
Due to hemodynamic nature of the BOLD signal and the intrinsic coupling to the vasculature near activated parenchymal tissue, the region of activation extends in the region surrounding the activated structure. The extent of this depends on the details of the vasculature, signal-to-noise ratio, spatial resolution of image acquisition, and other factors. If the BOLD signal is a good indicator of the spatial location of activated parenchyma, then, the region of signal maximum will be the best indication of most activated parenchyma.
In a low signal-to-noise environment it can be misleading to simply identify a pixel with a maximum effect as indicating the maximum signal. In order to get an unbiased measure of the primary location of an activated region, we performed a cluster analysis to evaluate the extent of the activation within a defined region-of-interest and then used the centroid of the cluster as the location of the primary activation. A cluster was defined as all spatially contiguous pixels above a confidence level of c. The significance of a detected cluster is a function of the cluster size and the confidence level for inclusion in the cluster [7]. For the signals reported here, c=0.95 (i.e., Student's t >1.65) was used. The centroid is then calculated according to

$$x_c = \frac{\sum_i x_i s_i}{\sum_i s_i} \qquad \text{Eq.(1)}$$

where x_i is the x-coordinate of the *i*th pixel in the cluster and s_i is the detected BOLD signal amplitude of the *i*th pixel. The y coordinate of the centroid, y_c, is calculated by substituting y_i for x_i in Eq. 1.

Results

The most significantly activated regions (Student's t >3.5) for a single subject performing visual and auditory tasks during a single session are shown in the center and right panels of Figure 2, respectively. A yellow-red color map rendered onto a high-resolution T_1-weighted anatomical image indicates positive correlation with the reference function where the yellow corresponds to the highest significance.
The primary visual and auditory cortices are very strongly activated during the respective scans. It is important to note the slice chosen for Fig. 2 is located inferior to the primary visual cortex and thus the cortical activation does not extend more posteriorly as it would if more superior slices were chosen.
White arrows indicate that the lateral geniculate nucleus (LGN) is detected bilaterally in the visual study and is not present during the auditory study while the opposite holds true for the medial geniculate nucleus (MGN). The location of the axial slice, illustrated by a

black line in the coronal plane, is shown in the left panel of Figure 2.

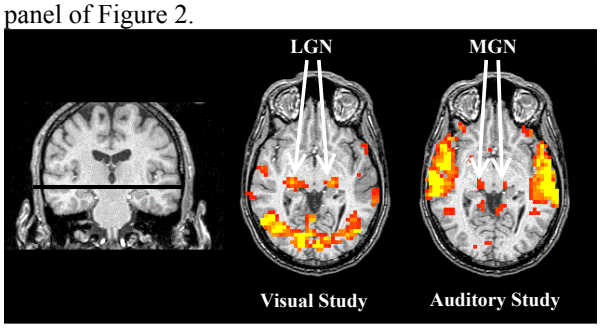

Figure 2: Activation maps for one subject performing visual and auditory tasks in a single imaging session. The maps are superimposed on 3D SPGR anatomic data. LGN = lateral geniculate nucleus of the thalamus, MGN = medial geniculate nucleus of the thalamus.

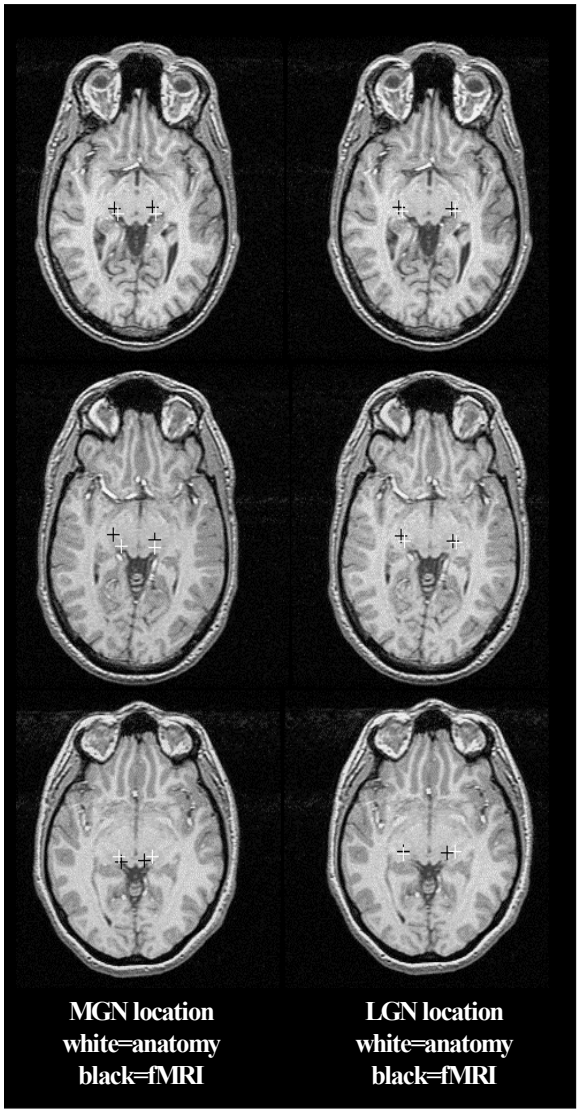

Figure 3: High-resolution T1-weighted anatomic data for three different subjects. Black and white crosses indicate MGN and LGN location (left and right panels, respectively) as determined from the functional data and by identifying these two thalamic nuclei on high-resolution T1-weighted anatomical data.

Discussion

Excellent agreement between the LGN and MGN locations as extracted from the functional data and as identified on the high-resolution 3D SPGR images by an experienced neuroradiologist is illustrated by Figure 3. A comparison between the anatomic (white cross) and functional (black cross) locations of the MGN (left panel) and LGN (right panel) is displayed for three different subjects. Although the centroid position is not coincident with the anatomic location in every case, it is important to note that in every case, the activated *region* included the anatomic location.
The slice containing the thalamic nuclei must be selected very carefully and consistently in order to minimize inter-subject variations. In addition, it is essential that subject's head orientation in the scanner be straight. If this requirement is not fulfilled, a single 3.5-mm slice may include the lateral geniculate nuclei and medial geniculate nuclei only partially or unilaterally. The success of our experiment was facilitated by the use of high quality stimuli delivery systems and proper motion restraint, leading to high quality, motion-free data acquisition. Finally, applying the Hamming spatial filter considerably enhanced detection of the thalamic activation.

Conclusion

In this work we have shown that BOLD contrast functional MRI technique can be successfully applied to discriminate adjacent thalamic nuclei at 1.5 tesla.

References

[1] Chen W., Cato, T., Zhu, X.H., Strupp J., Ogawa, S., and Ugurbil, K., Mapping of lateral geniculate nucleus activation during visual stimulation in human brain using fMRI, Magn. Reson. Med., 1998, 39: 89-96.

[2] Guimaraes, A.R., Melcher, J.R., Talavage, T.M., Baker, J.R., Ledden, P., Rosen, B.R., Kiang, N.Y., Fullerton, B.C., and Weisskoff, R.M., Imaging subcortical auditory activity in humans, Hum. Brain Mapp., 1998, 6: 33-41.

[3] Kwong, K.K., Belliveau, J.W., Chesler, D.A., Goldberg, I.E., Weiskoff, R.M., Poncelet, B.P., Kennedy, D.N., Hoppel, B.E., Cohen, M.S., Turner, R., Cheng, H.M., Brady, T.J., and Rosen, B.R., Dynamic magnetic resonance imaging of human brain activity during primary sensory activation, Proc. Natl. Acad. Sci., 1992, 89: 5675-5679.

[4] Lowe, M.J. and Sorenson, J.A, Spatially filtering functional magnetic resonance imaging data, Magn. Reson. Med., 1997, 37: 723-729.

[5] Lowe, M.J. and Russell, D.P., Treatment of baseline drifts in fMRI time series analysis, J. Comp. Assist. Tomogr., 1999, 23: 463-473.

[6] Bandettini, P.A., Jesmanowicz, A., Wong, E.C., Hyde, J.S., Processing strategies for time-course data sets in functional MRI of the human brain, Magn. Res. Med., 1993, 30: 161-173.

[7] Forman, S.D., Cohen, J.D., Fitzgerald, M., Eddy, W.F., Mintun, M.A., Noll, D.C., Improved assessment of significant activation in functional magnetic resonance imaging (fMRI): use of a cluster-size threshold, Magn.Reson. Med., 1995, 33: 636-647.

Acknowledgements

This work has been supported by the Whitaker foundation. We would also like to thank our technologists, Julie B. Sims and Rich Fain for their help in performing the experiments.

Application of Eigenspace Beamformer to Virtual Depth-Electrode Measurement Using MEG

Sekihara K.[1], Peoppel D.[2], Miyashita Y.[1,2]

[1]JST Mind Articulation Project, Tokyo, Japan
[2]University of Maryland, College Park, USA
[3]School of Medicine, University of Tokyo, Tokyo, Japan

Introduction

The conventional approach for the source-moment evolution time course is based on the linear-estimation method. This method works well when information on all the source locations can be obtained. However, if this information is not available, the method generally fails to provide correct results. In many practical situations, it is very rare to obtain the information on all the source locations.

We have developed an efficient method for estimating the time course of a neural activity at a predetermined location. The developed method requires only the location of the source of interest and does not require the locations of other sources. Therefore, in contrast to the linear-estimation method, it is applicable to situations where there are interfering sources with unknown locations in addition to the sources of interest. Using this method, it is possible for an MEG sensor array to perform like a virtual in-vivo depth electrode.

The developed method consists of two steps: estimating the orientation of a neural source, then estimating its moment evolution time course. The second step uses a technique referred to as the eigenspace beamformer [1][2], which gives a higher signal-to-noise ratio than that obtained from the well-known minimum-variance beamformer [3]

Method

Definitions Let us define the magnetic field measured by the mth detector coil at time t as $b_m(t)$, and a column vector $\boldsymbol{b}(t) = [b_1(t), b_2(t), \ldots, b_M(t)]^T$ as a set of measured data where M is the total number of detector coils. A total of P current sources are assumed to generate the neuromagnetic field, and the locations of these sources are denoted as $\boldsymbol{x}_1, \boldsymbol{x}_2, \ldots, \boldsymbol{x}_P$. The moment magnitude of the pth source at time t is defined as $s_p(t)$, and the source magnitude vector is defined as $\boldsymbol{s}(t) = [s_1(t), s_2(t), \ldots, s_P(t)]^T$. A spherical homogeneous conductor is assumed, and two tangential components, the ϕ and θ components, of the dipole-source moment are considered. The orientation of the pth source is defined as its normal vector $\boldsymbol{\eta}_p(t) = [\eta_p^{\phi}(t), \eta_p^{\theta}(t)]^T$, where $||\boldsymbol{\eta}_p(t)|| = 1$. We also define a $2P \times P$ matrix that expresses the orientations of all P sources as $\boldsymbol{\Psi}$ such that

$$\boldsymbol{\Psi} = \begin{bmatrix} \boldsymbol{\eta}_1 & 0 & \cdots & 0 \\ 0 & \boldsymbol{\eta}_2 & \cdot & \vdots \\ \vdots & \cdot & \ddots & 0 \\ 0 & \cdots & 0 & \boldsymbol{\eta}_P \end{bmatrix}.$$

We assume that the orientation of each source is time independent in this paper.

The lead field vectors for the ϕ and θ components of the source at $\boldsymbol{x}$ are defined as $\boldsymbol{l}^{\phi}(\boldsymbol{x}) = [l_1^{\phi}(\boldsymbol{x}), l_2^{\phi}(\boldsymbol{x}), \cdots, l_M^{\phi}(\boldsymbol{x})]^T$ and $\boldsymbol{l}^{\theta}(\boldsymbol{x}) = [l_1^{\theta}(\boldsymbol{x}), l_2^{\theta}(\boldsymbol{x}), \cdots, l_M^{\theta}(\boldsymbol{x})]^T$. Here, $l_m^{\phi}(\boldsymbol{x})$ and $l_m^{\theta}(\boldsymbol{x})$ express the mth sensor output induced by the unit-magnitude source moment directed in the ϕ and θ directions, respectively. We define the lead field matrix for the source at $\boldsymbol{x}$ as $\boldsymbol{L}(\boldsymbol{x}) = [\boldsymbol{l}^{\phi}(\boldsymbol{x}), \boldsymbol{l}^{\theta}(\boldsymbol{x})]$, which represents the sensitivity of the sensor array at $\boldsymbol{x}$. The composite lead field matrix for the entire set of P sources is defined as

$$\boldsymbol{L}_c = [\boldsymbol{L}(\boldsymbol{x}_1), \boldsymbol{L}(\boldsymbol{x}_2), \cdots, \boldsymbol{L}(\boldsymbol{x}_P)]. \qquad (1)$$

The relationship between $\boldsymbol{b}(t)$ and $\boldsymbol{s}(t)$ is then expressed as

$$\boldsymbol{b}(t) = (\boldsymbol{L}_c\boldsymbol{\Psi})\boldsymbol{s}(t) + \boldsymbol{n}(t), \qquad (2)$$

where $\boldsymbol{n}(t)$ is the additive noise.

Estimation of the source orientation To estimate the magnitude of the source moment, we first need to estimate the orientation of the source, assuming that the source orientation is unchanged during a certain time interval. This assumption is reasonable because the source orientation is, in principle, determined by the anatomical structure of a brain, which does not change over the measurement period. The method described in this section is based on the MUSIC algorithm; the method was originally developed for estimating the polarization of wavefronts received by an array of antennas in radar-signal processing [4].

Let us define the measurement covariance matrix as $\boldsymbol{R}_b$; i.e., $\boldsymbol{R}_b = \langle \boldsymbol{b}(t)\boldsymbol{b}^T(t) \rangle$. Let us define the matrices $\boldsymbol{E}_S$ and $\boldsymbol{E}_N$ as $\boldsymbol{E}_S = [\boldsymbol{e}_1, \cdots, \boldsymbol{e}_P]$ and $\boldsymbol{E}_N = [\boldsymbol{e}_{P+1}, \cdots, \boldsymbol{e}_M]$, where $\{\boldsymbol{e}_j\}$ with $j = 1, 2, \cdots, M$

are the eigenvectors of $\boldsymbol{R}_b$. The column span of $\boldsymbol{E}_S$ is called the signal subspace and that of $\boldsymbol{E}_N$ is called the noise subspace.
The MUSIC algorithm makes use of the relationship,

$$(\boldsymbol{\Psi}^T \boldsymbol{L}_c^T)\boldsymbol{e}_j = 0 \ \text{ for } \ j = P+1, \cdots, M. \quad (3)$$

This implies that the lead field matrix with the correct source orientation at the true source location is orthogonal to any $\boldsymbol{e}_j$, where $j = P+1, \cdots, M$; i.e., it is orthogonal to the noise subspace. The source orientations can thus be obtained by utilizing this orthogonality relationship between $\boldsymbol{L}(\boldsymbol{x})\boldsymbol{\eta}$ and $\boldsymbol{E}_N$. That is, the optimum estimate of $\boldsymbol{\eta}$ is one that minimizes the following measure of this orthogonality;

$$J(\boldsymbol{\eta}, \boldsymbol{x}) = \frac{[\boldsymbol{\eta}^T \boldsymbol{L}^T(\boldsymbol{x})]\boldsymbol{E}_N \boldsymbol{E}_N^T [\boldsymbol{L}(\boldsymbol{x})\boldsymbol{\eta}]}{[\boldsymbol{\eta}^T \boldsymbol{L}^T(\boldsymbol{x})][\boldsymbol{L}(\boldsymbol{x})\boldsymbol{\eta}]}. \quad (4)$$

This minimization problem can be solved by using the generalized-eigenproblem formulation. Namely, the optimum orientation $\hat{\boldsymbol{\eta}}_{opt}(\boldsymbol{x})$ satisfies the relationship,

$$[\boldsymbol{L}^T(\boldsymbol{x})\boldsymbol{E}_N \boldsymbol{E}_N^T \boldsymbol{L}(\boldsymbol{x})]\hat{\boldsymbol{\eta}}_{opt}(\boldsymbol{x}) = \lambda_{min}[\boldsymbol{L}^T(\boldsymbol{x})\boldsymbol{L}(\boldsymbol{x})]\hat{\boldsymbol{\eta}}_{opt}(\boldsymbol{x}), \quad (5)$$

where λ_{min} indicates the minimum eigenvalue of this generalized eigenvalue problem. Therefore, the optimum estimate of the source orientation is obtained by finding the eigenvector corresponding to the minimum eigenvalues of Eq. (5). Note that solving this equation requires information only on the pointing location $\boldsymbol{x}$.

Estimation of the source moment Once the orientation is estimated, we can proceed to estimating the source moment. We have focused on the class of techniques referred to as a beamformer, in which the source-moment magnitude can be estimated using

$$\hat{s}(t) = \boldsymbol{w}^T \boldsymbol{b}(t), \quad (6)$$

One well-known beamformer is the minimum-variance distortion-less beamformer.

$$\boldsymbol{w}_m(\boldsymbol{x}) = \frac{\boldsymbol{R}_b^{-1}\boldsymbol{l}(\boldsymbol{x})}{\boldsymbol{l}^T(\boldsymbol{x})\boldsymbol{R}_b^{-1}\boldsymbol{l}(\boldsymbol{x})}. \quad (7)$$

Here, $\boldsymbol{l}(\boldsymbol{x})$ is the lead-field vector at $\boldsymbol{x}$ and it is obtained using $\boldsymbol{l}(\boldsymbol{x}) = \boldsymbol{L}(\boldsymbol{x})\hat{\boldsymbol{\eta}}_{opt}$.
This minimum variance beamformer has been one of the most popular methods of this kind in various signal-processing fields. However, the method is sensitive to errors which are inevitable in actual MEG measurements, as was shown in our experiments.

The eigenspace beamformer provides an estimate with an signal-to-noise ratio (SNR) higher than that from the minimum-variance beamformer in practical situations. Let us decompose the measurement covariance matrix $\boldsymbol{R}_b$ into its signal and noise subspace components; i.e.,

$$\boldsymbol{R}_b = \boldsymbol{E}_S \boldsymbol{\Lambda}_S \boldsymbol{E}_S^T + \boldsymbol{E}_N \boldsymbol{\Lambda}_N \boldsymbol{E}_N^T. \quad (8)$$

Here, defining the jth eigenvalue of $\boldsymbol{R}_b$ as λ_j, we define the matrices $\boldsymbol{\Lambda}_S$ and $\boldsymbol{\Lambda}_N$, as

$$\begin{aligned} \boldsymbol{\Lambda}_S &= \text{diag}[\lambda_1, \ldots, \lambda_P], \\ \boldsymbol{\Lambda}_N &= \text{diag}[\lambda_{P+1}, \ldots, \lambda_M], \end{aligned} \quad (9)$$

where diag$[\cdots]$ indicates a diagonal matrix whose diagonal elements are equal to the entries in the parenthesis. Using Eqs (7) and (8), and defining $\mu = 1/[\boldsymbol{l}^T(\boldsymbol{x})\boldsymbol{R}_b^{-1}\boldsymbol{l}(\boldsymbol{x})]$, the filter for the minimum-variance beamformer can be expressed as

$$\boldsymbol{w}_m = \mu \boldsymbol{R}_b^{-1}\boldsymbol{l}(\boldsymbol{x}) = \mu \boldsymbol{\Gamma}_S \boldsymbol{l}(\boldsymbol{x}) + \mu \boldsymbol{\Gamma}_N \boldsymbol{l}(\boldsymbol{x}), \quad (10)$$

where

$$\boldsymbol{\Gamma}_S = \boldsymbol{E}_S \boldsymbol{\Lambda}_S^{-1} \boldsymbol{E}_S^T, \qquad \boldsymbol{\Gamma}_N = \boldsymbol{E}_N \boldsymbol{\Lambda}_N^{-1} \boldsymbol{E}_N^T.$$

In Eq. (10), the second term on the right side, $\mu\boldsymbol{\Gamma}_N \boldsymbol{l}(\boldsymbol{x})$, should ideally be equal to zero because the lead-field vector $\boldsymbol{l}(\boldsymbol{x})$ is orthogonal to $\boldsymbol{E}_N$ at the true source locations. Various factors, however, prevent this term from being zero, and a non-zero $\mu\boldsymbol{\Gamma}_N \boldsymbol{l}(\boldsymbol{x})$ causes serious SNR degradation. Therefore, the eigenspace beamformer uses only the first term of Eq. (10) to calculate the filter weight $\boldsymbol{w}_e$; i.e.,

$$\boldsymbol{w}_e = \mu_e \boldsymbol{\Gamma}_S \boldsymbol{l}(\boldsymbol{x}) = \frac{\boldsymbol{\Gamma}_S \boldsymbol{l}(\boldsymbol{x})}{\boldsymbol{l}^T(\boldsymbol{x})\boldsymbol{\Gamma}_S \boldsymbol{l}(\boldsymbol{x})}, \quad (11)$$

where the normalization constant μ_e is $\mu_e = 1/[\boldsymbol{l}^T(\boldsymbol{x})\boldsymbol{\Gamma}_S \boldsymbol{l}(\boldsymbol{x})]$ so that the constraint $\boldsymbol{w}_e^T \boldsymbol{l}(\boldsymbol{x}) = 1$ is satisfied.

SNR consideration The SNR for the minimum-variance beamformer, $\text{SNR}_{(\text{MV})}$, is given by [5]

$$\text{SNR}_{(\text{MV})} = \frac{P_s}{\sigma^2} \frac{[\boldsymbol{l}^T(\boldsymbol{x})\boldsymbol{\Gamma}_S \boldsymbol{l}(\boldsymbol{x})]^2}{[\boldsymbol{l}^T(\boldsymbol{x})\boldsymbol{\Gamma}_S^2 \boldsymbol{l}(\boldsymbol{x}) + \boldsymbol{l}^T(\boldsymbol{x})\boldsymbol{\Gamma}_N^2 \boldsymbol{l}(\boldsymbol{x})]}, \quad (12)$$

where P_s is the average power of the signal-moment magnitude defined by $P_s = \langle s(t)^2 \rangle$, and σ^2 is the noise variance. The SNR for the eigenspace beamformer, $\text{SNR}_{(\text{ES})}$, is expressed as

$$\text{SNR}_{(\text{ES})} = \frac{P_s}{\sigma^2} \frac{[\boldsymbol{l}^T(\boldsymbol{x})\boldsymbol{\Gamma}_S \boldsymbol{l}(\boldsymbol{x})]^2}{[\boldsymbol{l}^T(\boldsymbol{x})\boldsymbol{\Gamma}_S^2 \boldsymbol{l}(\boldsymbol{x})]}. \quad (13)$$

It is readily apparent that if we can use an accurate noise subspace estimate and an accurate lead-field

vector, the term $\boldsymbol{l}^T(\boldsymbol{x})\boldsymbol{\Gamma}_N^2\boldsymbol{l}(\boldsymbol{x})$ is equal to zero, and $\mathrm{SNR}_{(\mathrm{MV})}$ and $\mathrm{SNR}_{(\mathrm{ES})}$ are exactly equal.
It is, however, generally difficult to attain the relationship, $\boldsymbol{l}^T(\boldsymbol{x})\boldsymbol{\Gamma}_N^2\boldsymbol{l}(\boldsymbol{x}) = 0$ due to an error in estimating sources or an error associated with using an analytical conductor model. Let us define the overall error contained in $\boldsymbol{l}(\boldsymbol{x})$ as $\boldsymbol{\varepsilon}$. Assuming that $\| \boldsymbol{l}(\boldsymbol{x}) \|^2 \gg \| \boldsymbol{\varepsilon} \|^2$, we can get

$$\mathrm{SNR}_{(\mathrm{MV})} \fallingdotseq \frac{P_s}{\sigma^2} \frac{[\boldsymbol{l}^T(\boldsymbol{x})\boldsymbol{\Gamma}_S\boldsymbol{l}(\boldsymbol{x})]^2}{[\boldsymbol{l}^T(\boldsymbol{x})\boldsymbol{\Gamma}_S^2\boldsymbol{l}(\boldsymbol{x}) + \boldsymbol{\varepsilon}^T\boldsymbol{\Gamma}_N^2\boldsymbol{\varepsilon}]}. \quad (14)$$

Note that, in the denominator of the right side of the above equation, the norm of the matrix $\boldsymbol{\varepsilon}^T\boldsymbol{\Gamma}_N^2\boldsymbol{\varepsilon}$ has an order of magnitude proportional to $\| \boldsymbol{\varepsilon} \|^2 / \lambda_N^2$, where λ_N represents one of the noise-level eigenvalues of $\boldsymbol{R}_b$. The eigenvalue λ_N is usually significantly smaller than the signal-level eigenvalues. Therefore, Eq. (14) indicates that even when the error $\| \boldsymbol{\varepsilon} \|$ is very small, the term $\boldsymbol{\varepsilon}^T\boldsymbol{\Gamma}_N^2\boldsymbol{\varepsilon}$ may not be negligibly small compared to the first term in the denominator of Eq. (14).

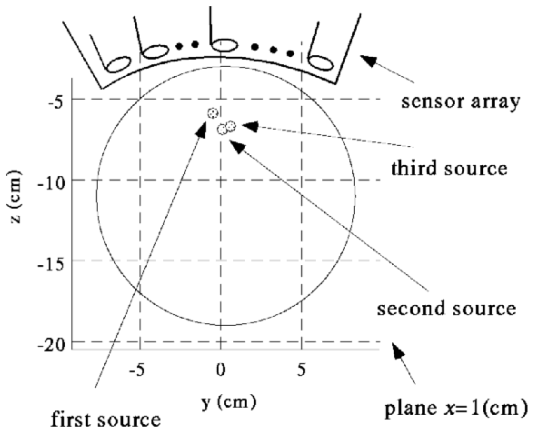

Figure 1: The source and detector configuration.

Numerical experiments

Data generation We conducted a series of numerical experiments to test the validity of our arguments in the previous section. A coil alignment of the 37-channel Magnes™ biomagnetic measurement system (Biomagnetic Technologies Inc., San Diego) was used in these experiments. Three signal sources were assumed to exist on a plane defined as $x = 1.0$ cm. The locations of the first to the third sources are $(1.0, -0.5, -5.9)$, $(1.0, 0.1, -6.9)$, and $(1.0, 0.6, -6.7)$ cm, respectively. The source and detector configuration is shown schematically in Fig. 1.

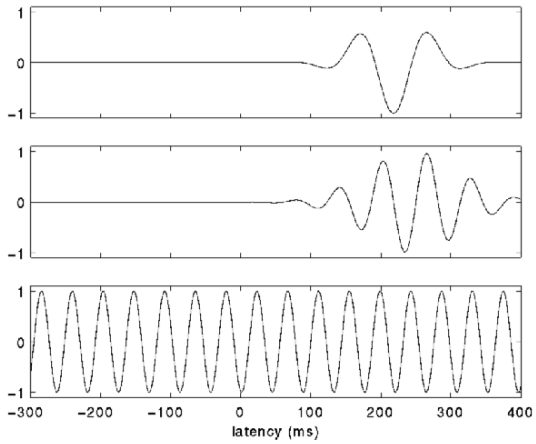

Figure 2: The moment time courses of the three sources. Time courses from the first to the fourth sources are shown from the top to the bottom, respectively.

The magnetic field was generated at 1-ms intervals from -300 to 400 ms. The moment time courses of the three sources assumed in our numerical experiments are shown in Fig. 2. Here, the first and second sources were the sources of interest; their time courses were to be estimated. The third source simulated background interference that was incoherent to the target sources. Gaussian noise was added to the generated magnetic field to make the final signal-to-noise ratio (SNR) to be 18. Here, the SNR was defined by the ratio of the Frobenius norm of the signal-magnetic-field data matrix to that of the noise matrix.

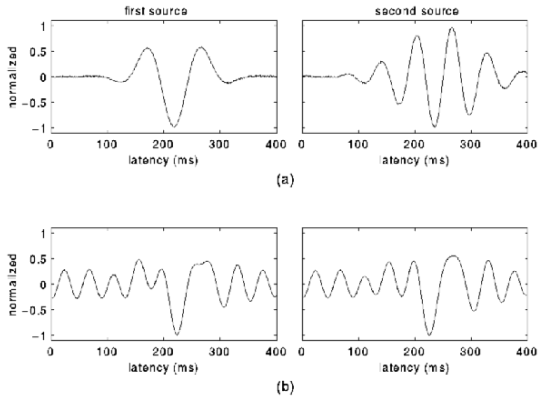

Figure 3: The results of the linear-estimation method. (a)When all the locations of the three active sources were taken into account. (b)When only the locations of the source to be measured was taken into account.

Application of the linear-estimation method We first applied the linear-estimation method to the

generated data set. We assumed that the locations of all three active sources were known and the composite lead field matrix was calculated using these locations. The estimated time courses of the first and second sources are shown in Fig. 3(a). The time courses were nearly perfectly estimated in this case. It is, however, very rare in actual applications that the locations of all active sources are known. We thus assumed that when estimating the time course of one source, the locations of the other two sources were unknown. In this case, the composite lead-field matrix consisted only of a single lead-field matrix at a target location. The results of estimating the first- and second-source time courses are shown in Fig. 3(b). Here, the linear-estimation method could not separate the time courses of the three sources and the results confirm that the linear-estimation method fails unless information on the locations of all sources is available. This is the starting point of the investigation presented in this paper.

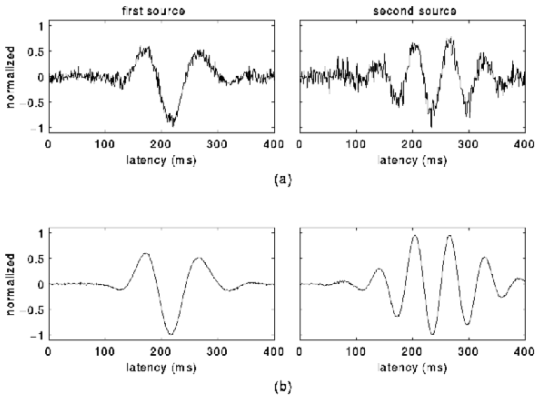

Figure 4: The results of applying (a) the minimum-variance and (b) eigenspace beamformer methods.

Application of minimum-variance and eigenspace beamformer methods We then applied the minimum-variance and the eigenspace beamformer methods. The results of estimating the time courses of the first and second sources are shown in Fig. 4. Both methods were able to estimate the correct time courses. The SNR with the eigenspace beamformer was considerably higher than that with the minimum-variance beamformer, clearly demonstrating its superiority over the minimum-variance method. This SNR degradation in the minimum-variance beamformer results probably arises from the use of the sample covariance matrix as mentioned in the previous section.

The regularized version of the minimum-variance beamformer has been also used in which the weight vector is calculated using

$$\boldsymbol{w}_m(\boldsymbol{x}) = \frac{(\boldsymbol{R}_b + \gamma \boldsymbol{I})^{-1}\boldsymbol{l}(\boldsymbol{x})}{\boldsymbol{l}^T(\boldsymbol{x})(\boldsymbol{R}_b + \gamma \boldsymbol{I})^{-1}\boldsymbol{l}(\boldsymbol{x})}, \qquad (15)$$

where γ is the parameter for this Tikhonov regularization. It has been reported [6] that the regularized minimum-variance beamformer can provide a trade off between the output signal-to-noise ratio and the spatial resolution. Therefore, the noise in the results in Fig. 4(a) can be reduced by choosing an appropriate γ. The results from the regularized minimum-variance beamformer are shown in Fig. 5. Here, the regularization parameter was set to have nearly the same amount of noise as in the results from the eigenspace method. In this figure, it can clearly be observed that the waveform of the third source is overlapped with that of the second source due to the degraded spatial resolution. The comparison between Figs. 4(b) and 5 again indicated the superiority of the eigenspace beamformer over the regularized minimum-variance beamformer in that the eigenspace beamformer can attain the SNR improvement without sacrificing its spatial resolution.

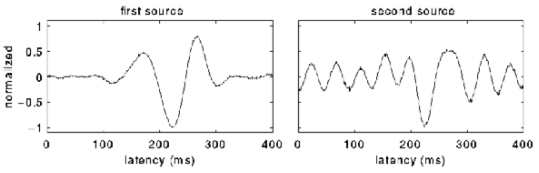

Figure 5: The results of applying the regularized minimum-variance beamformer.

References

[1] Van Veen, BD. Eigenstructure based partially adaptive array design, IEEE Trans. Antenn. Propagat., 1988, 36:357–362.

[2] Yu JL, Yeh CC. Generalized eigenspace-based beamformers, IEEE Trans. Signal Process., 1995, 43:2453–2461.

[3] Van Veen BD, Buckley KM. Beamforming: a versatile approach to spatial filtering, IEEE ASSP Magazine, 1988, 5:4–24.

[4] Ferrara Jr. ER, Parks TM. Direction finding with an array of antennas having diverse polarizations, IEEE Trans. Antenn. Propagat., 1983, 31:231–236.

[5] Chang L, Yeh CC. Performance of DMI and eigenspace-based beamformers, IEEE Trans. Antenn. Propagat., 1992, 40:1336–1347.

[6] Vrba J. Evaluating MEG functional brain imaging performance, Workshop on "The art of EEG/MEG Source Analysis", Düsseldorf, June, 1999.

Cortical oscillatory activity assessed by combined EEG and MEG recordings and High-Resolution ERD methods

Edlinger[1] G., Bastiaansen[2] M., Brunia[2] C., Neuper[1] C., Pfurtscheller[1] G.

[1]Department of Medical Informatics, Institute for Biomedical Engineering, and Ludwig Boltzmann Institute for Medical Informatics and Neuroinformatics, Graz University of Technology, Austria
[2] Psychonomics section, Tilburg University, Tilburg, Netherlands

Introduction

Event-related desynchronization is a phenomenon of the awake brain and was quantified for the first time by Pfurtscheller and Aranibar [1]. ERD of alpha band rhythms can be seen as a correlate of activated cortical neurons and was reported during sensory, motor and cognitive processing.
In evoked potential/field studies the responses of the brain activity with respect to the stimuli are phase locked to the event. In order to improve the signal-to-noise ratio (SNR) trials of EEG/MEG recordings are averaged with respect to the event. Source localization procedures or cortical imaging methods are then applied to the averaged potentials/fields. However, in event-related desynchroni-zation studies the response of the brain (*i.e.* the induced rhythmic activity) to the stimuli is not phase locked to the event. Therefore, simple amplitude averaging of trials with respect to the event can not be done properly to improve the SNR. To overcome this problem the non-stationary Event-Related Desynchronization analysis (ERD) was introduced [1]. The outcome of the ERD analysis resembles in some way an averaged evoked response signal with a temporal profile depending on the mean power ratio between the EEG in the actual measurement interval and a reference interval.
It is assumed that most of the ongoing EEG observed on the scalp (by EEG recordings) or outside the head (by MEG recordings) is due to superficially located neo-cortical sources [2],[3]. Dipole layers can describe the sources. Based on findings by [4] mainly radially orientated dipole-layers (with respect to the cortical surface) contribute to the observed ERD/ERS. Combined EEG and MEG recordings have (at least theoretically) higher information content for identifying brain source activity than single EEG and MEG recordings [5]. In order to investigate the usefulness of simultaneous EEG and MEG recordings the topographical differences in EEG and/or MEG maps based on simple self-paced finger movements are investigated. High-resolution ERD methods based on a distributed cortical source space [6] combining biomagnetic and bioelectric data are applied to the acquired data sets.

Method

M/EEG recordings
A total of six subjects participate in the study. Subjects were instructed to perform movements of all 4 fingers (except thumb) or complex sequences of finger movements. Results for the more complex movements will be presented elsewhere. Optical sensors detected all finger movements. EEG from 36 scalp electrodes and MEG from 151 first order gradiometers (CTF systems) were measured simultaneously at the MEG center KNAW in Amsterdam, Netherlands. The sampling frequency was 250 Hz and high- and lowpass filter cut-off frequencies were set to 0.5 and 50 Hz. The instant of the movement is termed time 0.

MRI recordings & source space model
In order to correctly integrate M/EEG recordings and MRI, fiducal markers (for M/EEG recordings small coils and for MRI recording oil capsules (vitamin E) are placed at fixed landmarks (the nasion and the 2 preauricular points). The positions of the gradiometers and electrodes were measured in the coordinate system defined by the landmarks. Realistically shaped head models containing smoothed brain, skull and scalp compartments were constructed (see figure 1 for sensors configuration). The brain surface was deflated by 10 mm and dipolar sources were positioned at each node of the discretized surface yielding a distributed source space. For that source space electrical and magnetical lead fields were computed using the boundary element method for a three-compartment head model.

Source strength reconstruction
Dipolar source moments were reconstructed by linear estimation method (LE) for single EEG, single MEG and combined M/EEG recordings. Matrix inversion of electric and magnetic lead fields were done via a truncated singular value decomposition. Truncation levels were estimated by the Akaike information criterion [7]. Lead field normalization was performed according to [8] and the fusion of electric and magnetic lead field matrices according to [5]. An overall scaling of the conductivity values as described by [5] was not performed. The High-Resolution ERD results obtained by

LE are compared to results obtained via the spline surface Laplacian method [9].

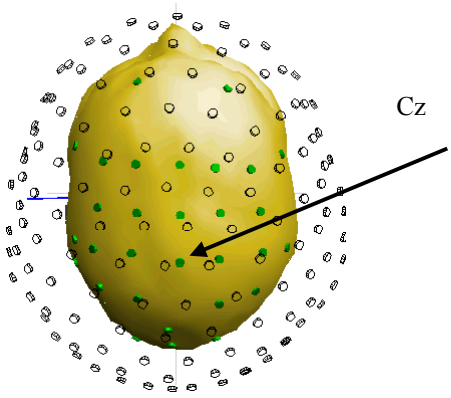

Figure 1: Top view of electrode and gradiometer configuration for subject S1. Small filled cylinders indicated 36 electrode positions on the realistically scalp surface, small transparent cylinders indicate 151 gradiometer positions.

High-Resolution ERD method

In order to estimate the High-Resolution ERD results all artifacts controlled M/EEG raw data were digitally band-pass filtered between 8-13 Hz. Then 3*827 dipolar source strengths were reconstructed for 827 dipolar sources located in the upper hemisphere. Reconstructed source strengths were squared and averaged across trials. In order to further reduce variance in the data an averaging over 32 subsequent time steps was performed. All squared and averaged amplitudes were referenced to the source activity during a resting interval between –2500 to -1500 ms before movement. The steps involved quantifying High-Resolution ERD results can be seen from figure 1. Detail on ERD quantification can be found in [1,4]

Results

All subsequent figures show typical ERD distributions obtained for subject S1. Figure 2 shows a sequence of LP maps for simple index finger movements between -1152 msec before movement to 256 msec after the movement in steps of 128 msec. Red color coded areas indicate ERD and blue color coded areas indicate event-related synchronization. As can be seen from figure 2, the ERD starts around -1000 msec before the actual movement over the left (contra-lateral) sensorimotor area and gets bilateral during and after the movement. Figure 3 gives the corresponding High-Resolution ERD maps based on single EEG source strength reconstruction. However, the desynchronization over the ipsilateral side around instant 0 is more pronounced than in LP maps. Figure 4 gives High-Resolution ERD maps based on single MEG recordings. What is interesting is that ERD starts only about -200 msec before actual movement and the focus of maximal ERD after movement is found more laterally than in single EEG based maps. Figures 5 and 6 give High-Resolution ERD results for combined M/EEG data processing. ERD of radial components of dipolar source activity (figure 5) starts about -1000 msec before movement. Compared to single EEG results, the focus of maximal ERD is circumscribed.

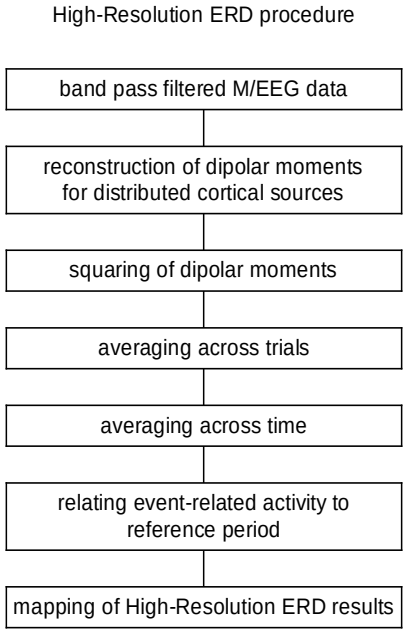

Figure 1: Computational steps for quantification of High-Resolution ERD.

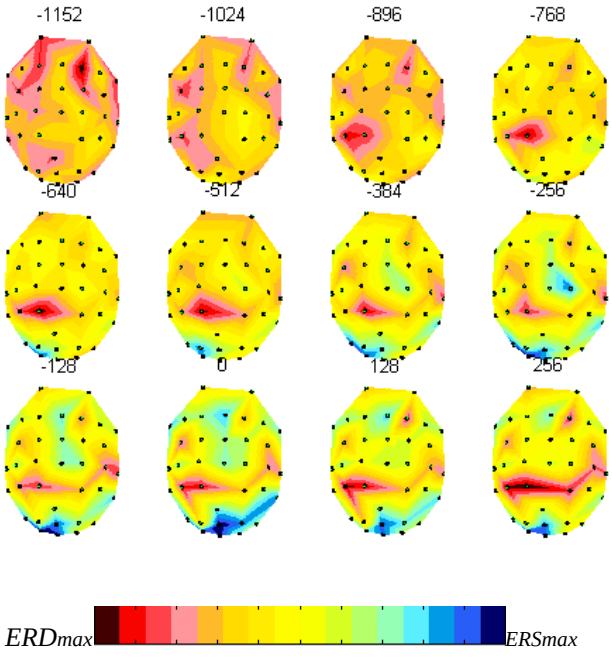

Figure 2: ERD results for LP during right finger movement. Maps are viewed from above. The nose points to the top of the page and time steps are indicated at the top of each map. Time 0 corresponds to

the movement onset. Small disks indicate electrode positions.

Results for the tangential component of combined M/EEG data processing show very similar topography compared to single MEG based results. ERD starts only about –200 msec before movement and maximal ERD values are lower for than for single MEG results.

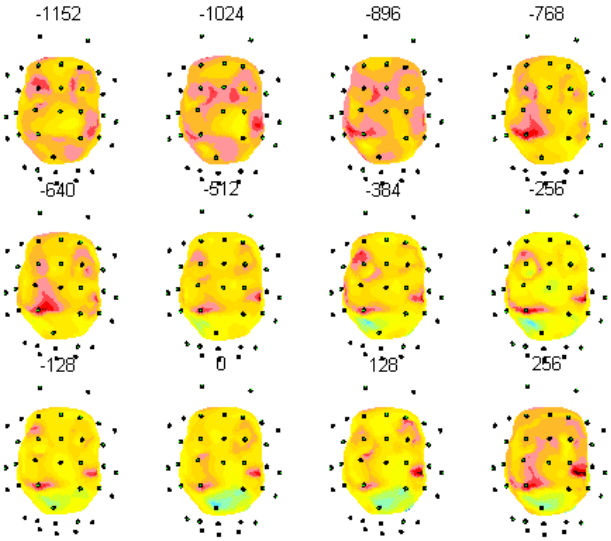

Figure 3: High-resolution EEG results for LE during right finger movement. Results for radial source components are given over the realistic source space in terms of relative power changes of dipolar moments.

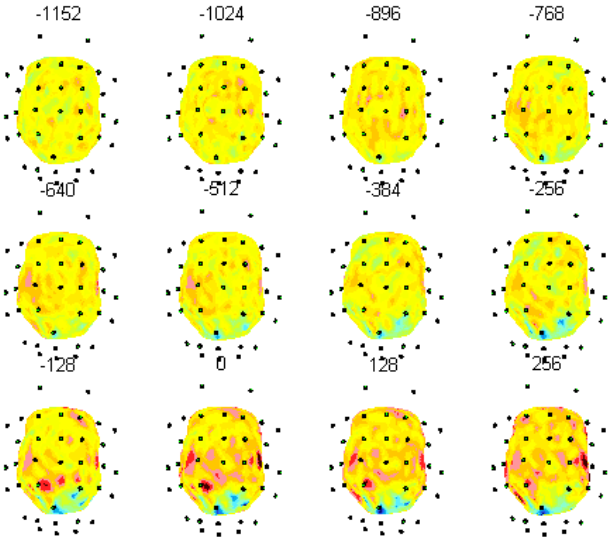

Figure 4: High-resolution MEG results for LE during right finger movement. Results for tangential source components are given over the realistic source space in terms of relative power changes of dipolar moments

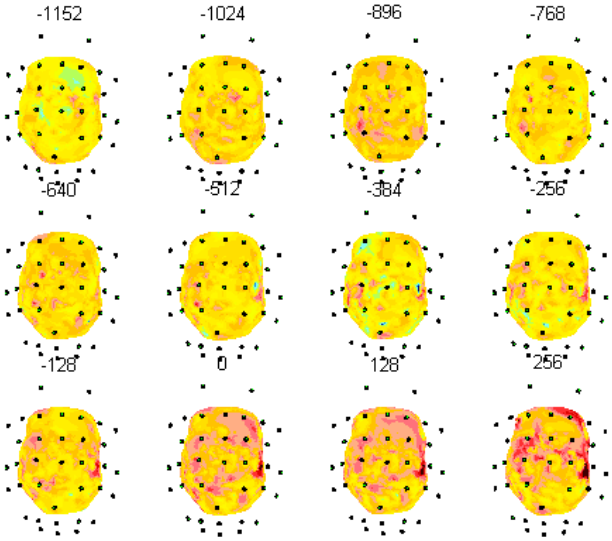

Figure 5: High-resolution M/EEG results for LE during right finger movement. Results for radial source components are given over the realistic source space in terms of relative power changes of dipolar moments.

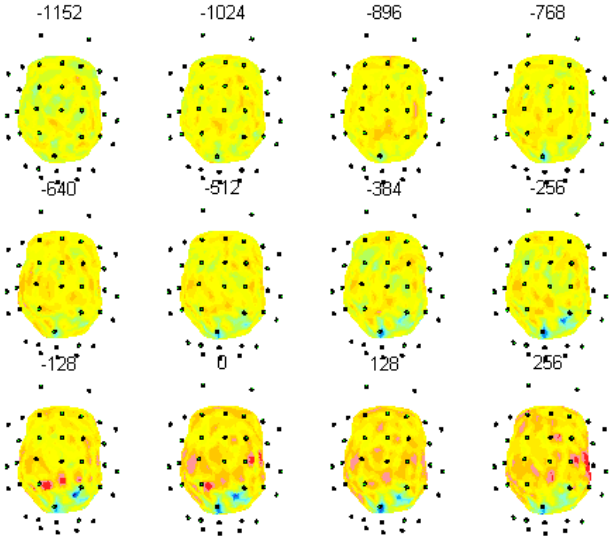

Figure 6: High-resolution M/EEG results for LE during right finger movement. Results for tangential source components are given over the realistic source space in terms of relative power changes of dipolar moments.

Discussion

It was assumed that most of the spontaneous brain activity measured by surface electrodes or by gradiometers most probable results from superficial cortical

brain activity. Cortical dipole layers can describe the sources of this activity. These layers are orientated normally to the cortical surface (which does not mean that these sources are orientated in the normal direction of the scalp surface). Sources orientated normally to the surface of the scalp (radial sources) can be hardly detected by MEG recordings. Hence, one reason for the lack of ERD in the tangential direction (along the surface of the smoothed brain compartment) observed in single MEG and combined M/EEG recordings around -1000 msec before movement might be that only radially orientated source areas are activated. However, during the execution of movement a more complicated source configuration is activated which is not only radially orientated. High-Resolution ERD results for single EEG, single MEG and combined M/EEG recordings show similar results. However, the foci of maximal ERD values are more circumscribed for combined M/EEG source reconstruction. This result can be expected, as more sensors are available detecting brain activity. However, the fusion of electric and magnetic lead field matrices is based on the reconstruction of dipolar source components in 3 orthogonal direction. The number of unknowns is increased by a factor of 3 compared to e.g. a reconstruction of the cortex potential distribution described by van Oosterom and Oostendorp [10] and the advantage of having additional sensors is reduced again. However, it is not possible to directly estimate the cortex potential distribution based on MEG recordings. Further assumption about the source space have to made as shown by [11] for the reconstruction of the transmembrane potential in electro- and magnetocardiography. Similar ideas have to be put forward for the estimation of the epicortex potentials based on M/EEG recordings.

Acknowledgements

This work was supported by the Austrian “Fonds zur Förderung wissenschaftlicher Forschung”, project P11571 and P12407.

References

[1] Pfurtscheller, G. and Aranibar, A. Event-related cortical desynchronization detected by power measurements of scalp EEG., Electroencephalogr. Clin. Neurophysiol., 1977,42:817-826.

[2] Nunez, P. Electric fields of the brain. 1981. Oxford University Press.

[3] Nunez, P. Neocortical dynamics and human {EEG} rhythms. 1995. Oxford University, New York.

[4] Pfurtscheller, G., Stancák, A. Jr, and Neuper, C. Post-movement beta synchronization. A correlate of an idling motor area?, Electroencephalogr. Clin. Neurophysiol., 1996,98:281-293.

[5] Fuchs, M., Wagner, M., Wischmann, H. A., Köhler, T., Theissen, A., Drenckhahn, R., and Buchner, H. Improving source reconstructions by combining bioelectric and biomagnetic data., Electroencephalogr. Clin. Neurophysiol., 1998, 107:93-111.

[6] Hämäläinen, M. S. and Ilmoniemi, R. J. Interpreting magnetic fields of the brain: Estimates of current distributions. Helsinki University of Technology. J. TKK-F-A559. 1984.

[7] Akaike, H. A new look at the statistical model identification. IEEE Trans.Automat.Contr. 1974: 19, 716-723.

[8] van Burik, M., Knösche, T., Edlinger, G., Neuper, C., Pfurtscheller, G., and Peters, M. Post-movement beta oscillations studied with linear estimation., Electroencephalogr. Clin. Neurophysiol., 1998,106:195-198.

[9] Babiloni, F., Babiloni, C., Carducci, F., Fattorini, L., Onorati, P., and Urbano, A. Spline Laplacian estimate of EEG potentials over a realistic magnetic resonance-constructed scalp surface model., Electroencephalogr. Clin. Neurophysiol., 1996,98:363-373.

[10] Oosterom, A and Oostendorp, T. On computing pericardial potentials and current densities in inverse electrocardiography. J.Electrocardiography 1992:25,102-106.

[11] Geselowitz, D. A bidomain model for anisotropic cardiac muscle. Ann.Biomed.Eng. 1983:11, 191-206.

Cardiomagnetic Source Imaging Studies with Focal and Distributed Source Models

Nenonen J. [1,2], Pesola K. [1,2], Lötjönen J. [1,2], Lauerma K. 4, Hänninen, H. [2,3], Korhonen, P. [2,3], Mäkijärvi, M. [2,3], Fenici, R. [5], and Katila, T. [1,2]

[1]Laboratory of Biomedical Engineering, Helsinki University of Technology, 02015 HUT, Espoo;
[2] Medical Engineering Centre, BioMag Laboratory, [3] Division of Cardiology, and [4] Department of Radiology, Helsinki University Central Hospital, 00290 Helsinki, Finland
[5]Clinical Physiology _ Biomagnetism Center, Catholic University of Rome, Italy

Introduction

During the recent years, magnetocardiographic (MCG) source imaging has received increasing interest [1, 2]. The ability to locate current sources combined with precise timing of events is valuable both in basic research and in clinical studies [3, 4]. Presently, the MCG is employed at some hospitals to test and further develop its clinical use [5, 6].

The BioMag Laboratory at the Helsinki University Central Hospital (HUCH) is equipped with state-of-the-art facilities both for basic research and for clinical applications in functional neuro- and cardiomagnetic studies. The cardiac measurement systems – the 67-channel MCG and the 123-channel body-surface potential mapping (BSPM) equipment – have been described in detail elsewhere [7]. Combined with fast data transfer to the Helsinki University of Technology (HUT) and the signal and image processing methods developed at HUT, the facilities give a good framework for cardiomagnetic source imaging research. In the following, we describe briefly such studies in association with the ongoing patient studies.

First, we outline how individualized boundary-element torso models are constructed from medical image data. We have developed nearly automated methods to segment the objects of interest from magnetic resonance (MR) or X-ray images, as well as a novel triangulation software to tessellate the surfaces of the objects.

Next, we discuss testing of the ability of MCG to locate point-like sources. Artificial current-dipole sources have been utilized, both in phantom experiments and in studies with a pacing catheter placed inside the heart during the MCG recordings. In addition, we show results obtained with distributed source models, such as minimum-norm estimates on the epicardial surface, and double-layer sources in reconstructing activation sequences on the heart surfaces.

In our studies, the 'golden standard' for the inverse solutions is provided by clinically validated invasive data recorded before MCG measurements. In many cases, the BSPM was performed simultaneously with the MCG recordings, and similar source analysis was carried out both from the MCG and the BSPM data.

Methods

Patient studies

Presently, more than 200 cardiac patients are studied annually with the multichannel MCG and BSPM systems. In most patients undergoing catheter ablation or other invasive investigations, to obtain a reliable validation for the cardiomagnetic inverse problem, also MR imaging has been performed. In this paper, we focus on three patient groups:

1. Fifteen patients have been studied with a non-magnetic pacing catheter, inserted in the heart during routine electrophysiological studies. MCG and BSPM data were used to compute the parameters of a freely moving current dipole, during the 2-ms stimulus and during the cardiac response evoked by the stimulus. The catheter positions recorded on fluoroscopic X-ray images provided the golden standard for the non-invasive dipole localizations.
2. Nine patients suffering from chronic ischemia have been studied. The MCG and the BSPM data were recorded at resting state, and during ergometer exercise to induce acute ischemia. In these patients, the golden standard was provided by the metabolic information in positron emission tomography (PET) images, indicating the viable tissue suffering from the chronic ischemia.
3. Four arrhythmia patients undergoing open-chest surgery have been studied. Activation isochrones were reconstructed from the MCG and BSPM data, and the results were compared directly with the epicardial activation maps recorded during the surgery.

In all patients described above, anatomical MRI was performed with a 1.5-T superconducting magnet device (Magnetom Vision, Siemens AG) at the Department of Radiology of HUCH. MR images were applied for extracting accurate representation of the individual geometry of the thorax and the heart, as well as in combining the functional MCG and ECG results accurately with the cardiac anatomy.

Individualized torso models

In the boundary-element method (BEM), the body is approximated as a piecewise homogeneous volume conductor, and only the boundary surfaces where the electric conductivity changes are tessellated. In general, most accurate inverse solutions are achieved when the BEM geometries are generated for each patient individually using medical imaging data. We have developed methods to create triangulated torso models from MR images [8], and also from two orthogonal X-ray projections [9].

The segmentation is based on a prior model, which in this case is the set of triangulated surfaces of the thorax, the lungs and the heart. The prior model is elastically deformed to fit onto the volume (MRI) data or manually extracted edges (X-ray images). The segmentation takes about 1 minute (Sun Ultra10), depending on the number of objects and the method to preserve the geometrical prior knowledge. In our subjects, the method has produced satisfactory results with few interactive corrections of small magnitude.

After segmentation of the thorax, the heart and the lungs, their surfaces are automatically triangulated to reconstruct inhomogeneous BEM torso models [10]. In general, equilateral triangles are formed, with equal solid angles as seen from the center of the heart. An example of such triangulations is seen in Fig. 1.

Source models

Inverse studies with artificial current generators were performed using a freely moving current-dipole source in individual BEM torso models [1]. Non-linear least squares fit was utilized to define all six dipole parameters simultaneously. The initial dipole location in the MCG localizations was selected 12 cm below the MCG channel exhibiting the largest surface gradient, $\partial \mathbf{B}_z/\partial x$, $\partial \mathbf{B}_z/\partial y$ (see Fig. 1c).

Minimum-norm estimation (MNE) [2] provides a more general inverse solution for the primary-current density in terms of the lead fields $\mathbf{L}_k$: $\mathbf{j}^* = \sum_{k=1}^{m} \omega_k \mathbf{L}_k$. The lead fields are provided by the forward solution to the selected volume-conductor and sensor geometry, while the weights ω_k are obtained from the measured data, $\mathbf{b}$, at each time instant.

Special care has been taken to optimally regularize the inverse solutions. For example, the current-density solution, $\mathbf{j}$, based on the MNE becomes $\mathbf{j} = (L^T L + \lambda R^T R)^{-1} L^T \mathbf{b}$, where L is a matrix of the dot-products between the lead fields, R is the regularization operator, and the regularization parameter λ defines the weight of the side constraint $R^T R$ (see [11]). We have applied the L-curve method and the Tikhonov regularization, both with an identity matrix (zero-order) and a Laplacian matrix (second-order) regularization operator.

Besides single-layer sources, such as $\mathbf{j}^*$ above, uniform double-layer sources have been tested with our data. The transfer coeffiecients (i.e., the lead fields) from each point on the endo- and epicardial surfaces to the MCG/BSPM sensors are utilized in defining the sequence of cardiac excitation during the QRS complex (see, e.g., [12]).

Results

Phantom studies

A physical thorax phantom was used to test the MCG localization of accurately defined sources. Seven test dipoles were lying at distances between 25 and 145 mm from the anterior surface of the phantom filled with saline solution. The 95 % confidence intervals were defined for the MCG localization results, ranging from 1 mm for the sources nearest to the sensors, to 25 mm for the deepest sources [13].

In other studies with a pacing catheter in the same phantom, MCG and BSPM data were acquired [14]. When the catheter was at 38 mm from the anterior surface, the MCG and BSPM localization accuracies were, respectively, 2±1 mm and 4±1 mm. When the dipole was placed at 88 mm from the anterior surface, the localization accuracies decreased to 7±4 mm (MCG), and 10±2 mm (BSPM). Thus, both MCG and BSPM exhibited similar capability to locate dipolar sources.

Cardiac evoked fields

Altogether, fifteen patients have undergone MCG and BSPM studies for locating non-invasively the position of a non-magnetic catheter inside the heart [15, 16, 17]. A catheter specially designed to produce no magnetic disturbances was inserted into the heart of the patients after routine electrophysiological studies in the Cardiovascular Laboratory of HUCH. The tip of the catheter provides an exactly defined current-dipole source. The patients were transferred to the BioMag Laboratory where the catheter was used to stimulate the heart during MCG and BSPM recordings.

In the first five patients, comparison of the MCG location with the catheter positions documented on X-ray fluoroscopy showed the mean 3D difference of 11±4 mm [15]. In a later series of ten patients, both MCG and BSPM were simultaneously recorded. The MCG locations were in even better agreement with the fluoroscopy reference, with the mean 3D difference of 6±2 mm [16]. However, the BSPM localization accuracy was significantly poorer, 25±4 mm [17].

In all fifteen patients the MCG locations were in good agreement with the catheter position documented on the X-ray fluoroscopy images. Furthermore, the localizations obtained during earliest myocardial depolarization within a few milliseconds after the catheter stimulus were within few millimeters from the results during the stimulus spike. These studies provide further support for verifying that the MCG method can provide accurate localizations.

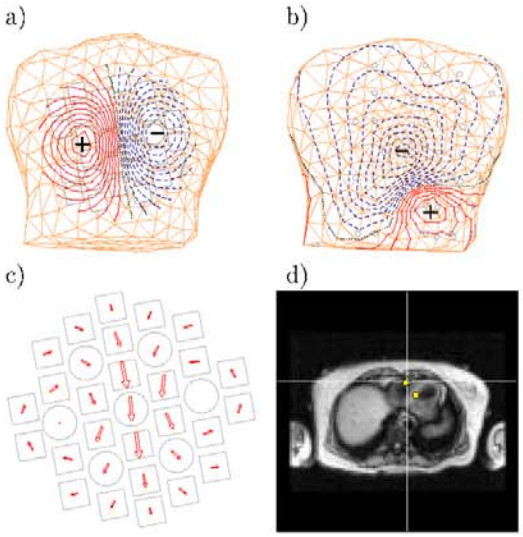

Figure 1: *a) Cardiac evoked field induced by a non-magnetic pacing catheter. b) The corresponding cardiac evoked potential about 5 ms after the stimulus. c) An arrow map corresponding to the magnetic-field distribution in a). The largest arrow at the center denotes the largest surface gradient, and provides the starting position for the non-linear least squares dipole fit. d) MCG and BSPM localization result superimposed on a transaxial MR image of the heart. The MCG result was correctly located in the apex of the right ventricle, while the BSPM result shows about 2 cm too deep position.*

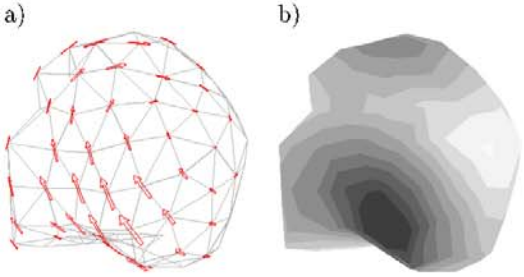

Figure 2: *An example of MNE reconstructions in a patient suffering from chronic ischemia, after supine ergometer exercise. The triangulated surface of the left ventricle is displayed from the frontal direction. a) MNE arrows, b) the distribution of the MNE magnitude, evaluated at the ST-segment enhanced by induced injury currents. The darkest area exhibits the largest injury current density at the septal region.*

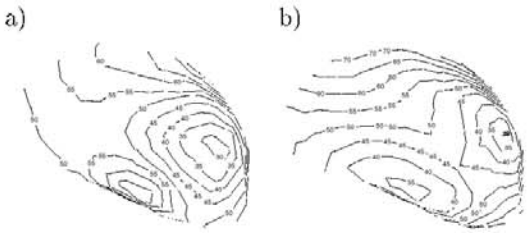

Figure 3: *Reconstruction of activation isochrones a) from MCG, and b) from BSPM data. The triangulated epicardial surface is displayed from the frontal direction. Both MCG and BSPM reconstruction were in excellent agreement with invasively recorded isochrones of a sinus-rhythm heart beat.*

Reconstruction of injury current distribution

We have applied the current-density reconstruction in estimating the primary current distributions underlying MCG signals measured from patients suffering from acute or chronic ischemia [11]. An example of MNE estimates confined on the triangulated outer surface of the left ventricle (LV) is presented in Fig. 2. The use of measured MCG data enables a more reliable comparison of the regularization methods than the use of simulated data only. The MNE estimate tends to move towards the sensors, but a proper regularization of the estimate was found to focus the estimates around the true source location [11]. A match of 77% was obtained between MCG and PET results, when viable and scar regions (PET) were compared with the CDE magnitude determined by the MCG [11].

Reconstruction of activation isochrones

Both MCG and BSPM data were applied in reconstructing isochrones during the QRS complex on the endo- and epicardial surfaces of the heart in four patients undergoing cardiac surgery. Bipolar epi- and endocardial potential recordings were performed to guide the surgery, displayed as activation isochrones in a directly comparable form with the inverse solutions. Both MCG and BSPM computations showed a striking similarity between estimated and measured isochrones [12]. An example is displayed in Fig. 3.

Discussion

The localization accuracy of our patient studies ranges from about 5 to 25 mm, depending mainly on the signal-to-noise ratio of the measurement. In addition, low beat-to-beat variations were obtained in studies with the non-magnetic pacing catheter, suggesting that the localization results are valuable for providing advance information in pre-ablative evaluation of the patients.

Our segmentation and triangulation methods are nearly

automated, and they can be applied to any volume data. Besides MCG and BSPM, the methods would be particularly useful to extract the brain, the skull and the scalp for neuromagnetic studies.
However, it is still difficult to combine the inverse solutions accurately with cardiac anatomy. Movement of the chest and the heart complicates this registration problem, particularly if the MCG and MRI sessions are not performed during the same day. More advanced methods need still to be developed for accurate combination of the MCG and BSPM results with the clinical data obtained, e.g., during invasive catheter studies, and with medical imaging data.
Reconstructions of source distributions have shown promising results which can add useful information of the electrophysiological activation related to cardiac diseases. Still, the clinical usefulness of such methods remains to be validated in future studies with a larger number of cases.
Finally, our results were achieved with a SQUID sensor array consisting of planar and axial gradiometers. So far, differing sensor array types and configurations have been an obstacle to compare the MCG results of different research centres. Recently, however, we have experimentally validated methods to reliably convert signals from one sensor presentation to another one [18]. With such transformations, multicenter patient studies in the future can be maximally utilized in bringing the MCG methods toward routine clinical use.

References

[1] Nenonen, J. Solving the inverse problem in magnetocardiography, IEEE Eng. Med. Biol., 1994, 13: 487–496.

[2] Hämäläinen, M.S., Nenonen, J. Magnetic source imaging. In: Webster, J., Ed. Encyclopedia of Electrical Engineering, Vol. 12. Wiley & Sons. New York, 1999, pp. 133–148.

[3] Stroink, G., Moshage, W., Achenbach, S. Cardiomagnetism. In: Andrä, W., Nowak., H., Eds. Magnetism in Medicine. Wiley VCH, Berlin, 1998, pp. 136–189.

[4] Leder, U., Haueisen, J., Huck, M., Nowak, H. Non-invasive imaging of arrhythmogenic left-ventricular myocardium after infarction. The Lancet, 1998, 352: 1825.

[5] Mäkijärvi, M., Brockmeier, K., Leder, U., Lesh, M., Moshage, W., Nakaya, Y., Nenonen, J., Nowak, H., Oeff, M., Stroink, G., Fenici, R. New trends in clinical magnetocardiography. In: Aine, C., et al., Eds. Advances in Biomagnetism Research: Biomag96. In press.

[6] Nowak, H. Biomagnetic instrumentation. In: Andrä, W., Nowak., H., Eds. Magnetism in Medicine. Wiley VCH, Berlin, 1998, pp. 88–135.

[7] Nenonen, J. Multimodal cardiac source imaging studies in the BioMag Laboratory. Biomed. Technik, 1997, 42: 29–32.

[8] Lötjönen, J., Reissman, P.-J., Magnin, I.E., Katila, T. Model extraction from magnetic resonance volume data using the deformable pyramid. Medical Image Analysis, in press.

[9] Lötjönen, J., Magnin, I.E., Nenonen, J., Katila, T. Reconstruction of 3D geometry using 2D profiles and a geometric prior model. IEEE Trans. Med. Im., in press.

[10] Lötjönen, J., Reissman, P.J., Magnin, I.E., Nenonen, J., and Katila, T. A triangulation method of an arbitrary point set for biomagnetic problems. IEEE Trans. Magn., 1998, 34: 2228–2233.

[11] Pesola, K., Hänninen, H., Lauerma, K., Lötjönen, J., Mäkijärvi, M., Nenonen, J., Takala, P., Voipio-Pulkki, L.-M., Toivonen, L., Katila, T. Current density estimation on the left ventricular epicardium: A potential method for ischemia localization. This volume.

[12] Pesola, K., Oostendorp, T., Nenonen, J., Korhonen, P., Lötjönen, J., Toivonen, L., Katila, T. Uniform double layer solutions for magnetocardiographic and body surface potential mapping data. Proc. of the 11th Internat. Conf. on Biomagnetism (Sendai, Japan), 1998.

[13] Pesola, K., Tenner, U., Nenonen, J., Brauer, H., Katila, T., Leder, U. Multichannel magnetocardiographic measurements with a physical thorax phantom. Med. Biol. Eng. Comput., 1999, 37:2–7.

[14] Fenici, R., Pesola, K., Mäkijärvi, M., Nenonen, J., Tenner, U., Fenici, P., Katila, T. Nonfluoroscopic localization of an amagnetic catheter in a realistic torso phantom by magnetocardiographic and body surface potential mapping. PACE, 1998, 21: 2482–2491.

[15] Fenici, R., Nenonen, J., Pesola, K., Korhonen, P., Lötjönen, J., Mäkijärvi, M., Toivonen, L., Poutanen, V.P., Keto, P., and Katila, T. Nonfluoroscopic localization of an amagnetic stimulation catheter by multichannel magnetocardiography. PACE, in press.

[16] Fenici, R., Pesola, K., Korhonen, P., Mäkijärvi, M., Nenonen, J., Toivonen, L., Fenici, P., Katila, T. Magnetocardiographic pacemapping for nonfluoroscopic localization of intracardiac electrophysiology catheters. PACE, 1998, 21: 2492–2498.

[17] Pesola, K., Nenonen, J., Fenici, R., Lötjönen, J., Mäkijärvi, M., Fenici, P., Korhonen, P., Lauerma, K., Valkonen, M., Toivonen, L., Katila, T. Bioelectromagnetic localization of the pacing catheter in the heart. Phys. Med. Biol., in press.

[18] Burghoff, M., Nenonen, J., Trahms, L., Katila, T., Conversion of magnetocardiographic recordings between two different multichannel SQUID devices. Submitted.

Spatial and Temporal Changes during the QT-Interval in the Magnetic Field of Patients with Coronary Artery Disease

Van Leeuwen P.[1], Hailer B.[2], Lange S.[3], Donker D.[4], Grönemeyer D.[3]

[1] Department of Biomagnetism, EFMT, Bochum, Germany
[2] Department of Internal Medicine, Philippusstift, Essen, Germany
[3] Institute for Microtherapy, University of Witten/Herdecke, Bochum, Germany
[4] Department of Cardiology, University Hospital Maastricht, Maastricht, Netherlands

Introduction

In the diagnosis of coronary artery disease (CAD), a number of standard noninvasive methods, such as ECG, nuclear imaging and echocardiography can be applied at rest and under stress. However, they have varying sensitivity and specificity, are not always practically applicable and may be associated with risk.
Recently, electrocardiographically determined QT interval dispersion (QTd), seen as reflecting underlying disturbances of ventricular recovery, has been proposed as method to detect ischemic heart disease [1] although conflicting results have also been reported [2]. Among other things, this may be due to the fact that only twelve leads are available in the standard ECG for the determination of QTd. This limitation can be offset by the use of body surface potential mapping (BSPM). Using BSPM, anomalous potential distributions during repolarization have been noted which were not apparent in 12-lead ECG [3]. Furthermore, the qualitative and quantitative investigation of potential maps has given new insight into CAD induced changes in spatial and temporal aspects of such maps [4].
Analogous to BSPM, magnetocardiography (MCG) can be used to noninvasively register cardiac activity at multiple sites over the heart. In the work presented here, we explore several spatial and temporal approaches in the analysis of the cardiac magnetic field in patients with coronary artery disease.

Methods

We investigated a total of 62 subjects: healthy subjects without a history or evidence of cardiovascular disease (normal group N), patients without prior myocardial infarction and with normal ECG and echocardiogram at rest but with significant narrowing (≥75%) of at least 1 coronary artery (CAD group) as well as patients with prior myocardial infarction (MI group). Some patient characteristics are listed in Table 1.
Magnetocardiograms (MCG) were recorded in all subjects for 60 s at rest using a 37-channel Siemens Krenikon system (Erlangen, Germany) with a 1-200 Hz bandpass and a sampling rate of 1 kHz. The probe (diameter 19 cm) was positioned as close to the frontal thorax as possible, directly over the heart. The recordings were performed in a shielded room (Vakuumschmelze, Hanau, Germany).

	N	CAD	MI
n	20	22	20
male	6	15	14
age (years)	53±7	59±10	56±10
EF (%)		73±6	61±12
0/1/2/3 vessels		0/9/7/6	2/12/5/1
inferior/anterior MI			15/5

Table 1: Patient characteristics

The single beats of each subject's recorded data were averaged in order to improve the signal to noise ratio and the averaged beat was evaluate using the methods described below.
Magnetic field maps (MFM) were reconstructed and examined over the QRST interval on the basis of 1) field strength (sum of the absolute values of the maximum and minimum magnetic field strength values); 2) field orientation (the angle formed by the line joining the centers of gravity of the positive and negative magnetic field values and the right-left line across the torso); 3) field width (the distance between the centers of gravity). The values of these three parameters were calculated for the time normalized course of the QT interval of each subject.
For a random subset of subjects (10 subject per group), the orientation and strength of equivalent current dipoles (ECD) were calculated at selected times between Q onset and T offset. Using the semi-infinite homogeneous volume conductor model, ECDs were calculated at Q onset, R upstroke, R peak, R downstroke, T apex and T offset. R upstroke was defined at the time instant of one quarter of the QR interval, R downstroke at three fifths of the RJ interval. Dipole orientation in the xy plane as well as source strength were determined as the average of the calculated values over 5 ms for each time point and subject.
Furthermore, QT interval duration was determined in all channels for all 62 subjects. QTd was calculated as the difference between the longest and shortest QT interval. The spatial variability of the QT interval duration was examined by plotting the QT duration value in each channel relative to the position of the channel in the sensor array. The spatial homogeneity of this variability as

well as the overall shape of the pattern formed by the distribution of the QT intervals was quantified using the normalized Smoothness Index SIn [5].

Results

Of the spatial features of the magnetic field, the courses of the normal subjects were similar at specific times during de- and repolarization (e.g. orientation, see Fig. 1, top panel). For the majority of the MI patients and many of the CAD patients there were clear deviations from the courses of the control subjects at specific times. For example, the patient groups showed the most marked differences in MFM orientation: in particular, they diverged from the normal course during the T wave, in particular at T apex and T offset (see Fig. 1, lower panels). On the basis of >10% deviations from the normal course, the sensitivity of MFM orientation was 85% and 68% respectively for the MI and CAD groups, the specificity 90%. Those CAD patients who consistently showed fewer deviations from the normal values were less likely to have multivessel disease. MFM strength and width did not discriminate as well between the normal subjects and the patients, the corresponding values for strength being: sensitivity 55%, 43%, specificity 90% and for width: sensitivity 75%, 41%, specificity 95%.

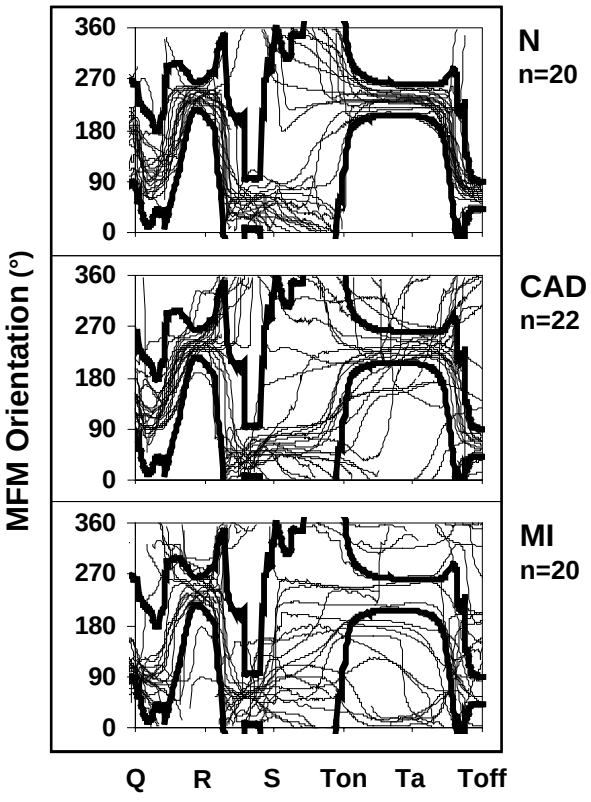

Fig. 1: Individual normalized time courses of MFM orientation over the QT interval for the normal group (N) as well as CAD and MI patients. The course of the 95% confidence limits of the normal values are shown in bold lines.

Examination of ECD strength and orientation at the selected times during the QT interval showed that the orientation again was similar for normal subjects. In all patients of the MI group and most in the CAD group, it deviated from the normal values at least one of the time points, in particular at T maximum and T offset (Fig. 2). Using the mean ± 2 SD values of the normal subjects as a normal range, sensitivity was 100% for MI and 80% for CAD, specificity was 90%. In comparison, the ECD strength values of the patient groups did not display consistent differences to those of the normals.

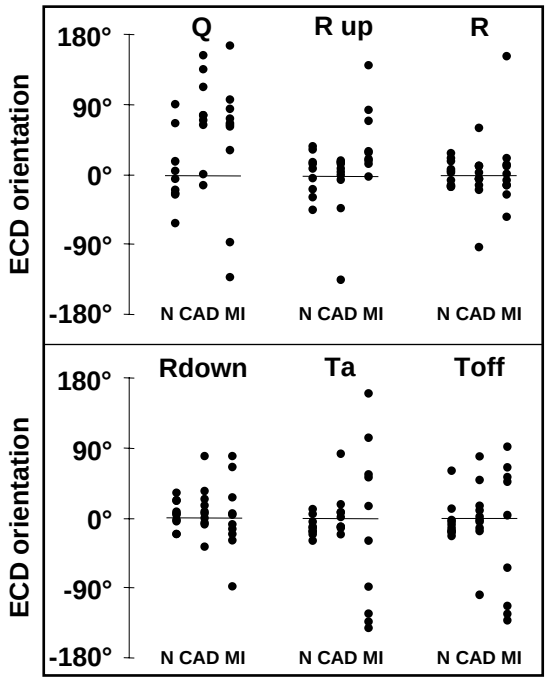

Fig. 2: ECD orientation at selected times during the QT interval (Q onset, R upstroke, R peak, R downstroke, T apex and T offset). All angles are rotated such that the values of the normal subject center on 0°.

Of the temporal features, QT dispersion values for the normal subjects calculated on the basis of the MCG signals was around 50 ms which is comparable to values as determined on the basis of ECG. The MCG QTd values of both patient groups were significantly higher than those of the normals (both $p<0.005$, see also Fig. 3), whereas for ECG-based QTd, no differences could be found between the groups.

When taking the spatial distribution of QT interval duration into account, the normal subjects consistently showed similar patterns with longer QT interval duration at the lower right and upper left as well as minor differences in duration at most neighboring channel sites. The patients deviated from these patterns, demonstrating greater local variability in QT duration in neighboring sites as well as a shift or change in the overall pattern found the normals (Fig. 4). Using SIn to quantify these differences in spatial QT dispersion, discrimination be-

tween the normal and CAD and MI groups improved ($p<0.001$ and $p<0.0001$, respectively; see also Fig. 3).

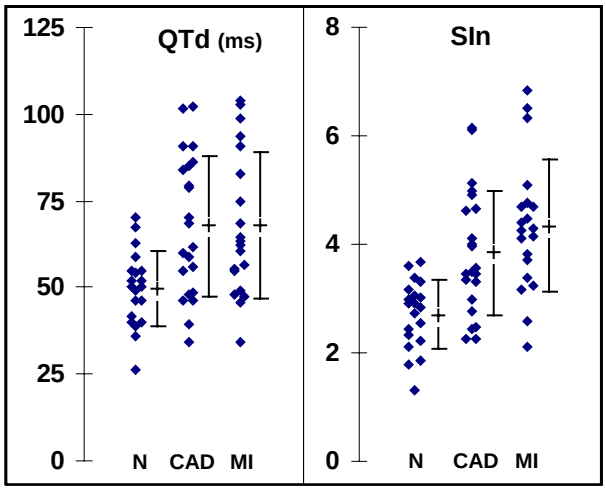

Fig. 3: QT dispersion (QTd) and normalized Smoothness Index (SIn; arbritary units) values as well as group means ± SD for the normal subjects (N) and patients with coronary artery disease without and with myocardial infarction (CAD and MI, respectively).

Discussion

Various spatial and temporal features of the MCG may be examined during the QT interval to reveal differences between healthy subjects and patients with CAD. Of the magnetic field map characteristics, orientation during repolarization seems particularly sensitive to disease-induced changes. This is consistent with findings showing that magnetic iso-integral maps are more sensitive in the ST-T interval in patients after MI [6]. Also, body surface potential mapping may identify patients with CAD who have no changes in 12-lead ECG at rest [7]. Here we found that both the map features and variability in QT duration were altered in a large portion of patients who displayed no changes in ECG.

From the point of view of clinical relevance, it seems to be most important that, on the basis of the MCG data recorded at rest, patients with CAD without prior MI could be separated from normal subjects with reasonable sensitivity and high specificity although all CAD patients had a normal ECG at rest. In prior studies such a separation using a noninvasive method such as ECG and echocardiography was generally only possible within in the context of stress induction [1].

The results presented here cannot be explained in terms of the presence of relevant ischemia because all of these patients had a normal left ventricular function without regional wall abnormalities as determined on the basis of echocardiography. One may speculate that the observed variations follow from changes in electrophysiological processes which result from early subtle changes in cellular mechanisms caused by alterations in coronary flow. This would imply that changes in MCG could appear even earlier in the cascade of ischemia than wall motion disturbances or electrical changes in 12-lead ECG.

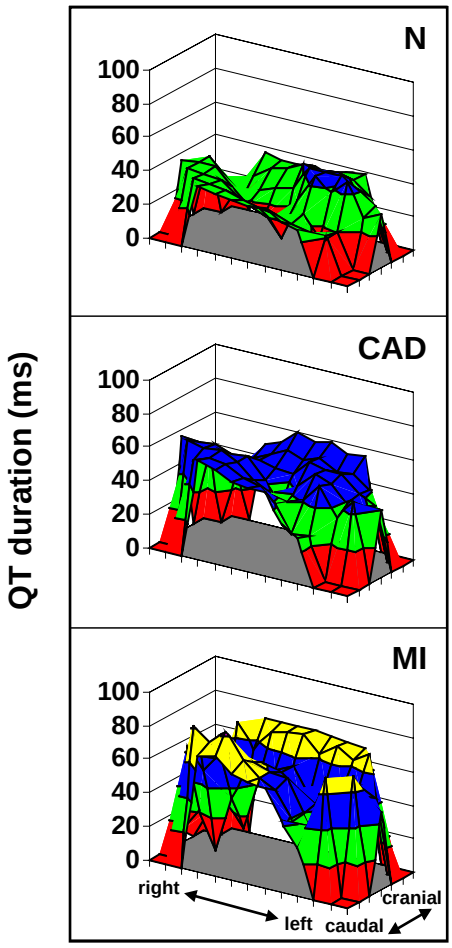

Fig. 4: QT duration plotted as a function of the 37 MCG channel locations for a normal subject (N) as well as a subject with coronary artery disease without myocardial infarction (CAD) and a subject with myocardial infarction (MI).

Summing up, in the results presented here, we found that both the map features and variability in QT duration were coherently altered in a large portion of patients who displayed no changes in ECG. Furthermore, in the patient groups, the degree of deviation from the results of the normal subjects tended, on the whole, to be dependent on the severity of CAD. In these respects, the results of the various approaches in the analysis of the data were consistent. This implies that MCG at rest may be useful in the identification of patients with CAD not only after suffering myocardial damage due to MI but also those with normal left ventricular function but documented hemodynamically relevant stenosis of the coronary arteries.

References

[1] Sporton, S.C., Taggart, P., Sutton, P.M., Walker, J.M., Hardman, S.M. Acute ischaemia: a dynamic influence on QT dispersion, Lancet 1997, 349:306-309.

[2] Grimm, W., Steder, U., Menz, V., Hoffmann, J., Maisch, B. Effect of amiodarone on QT dispersion in the 12-lead standard electrocardiogram and its significance for subsequent arrhythmic events, Clin Cardiol 1997, 20:107-110.

[3] Stilli, D., Musso, E., Macchi, E., Manca, C., Dei Cas, L., Vasini, P., Taccardi, B. Body surface potential mapping in ischemic patients with normal resting ECG, Can J Cardiol 1986, Suppl A:107A-112A.

[4] Montague, T.J., Witkowski, F.X. The clincal utility of body surface potential mapping in coronary artery disease, Am J Cardiol 1989, 64:378-383.

[5] Van Leeuwen, P., Hailer, B., Wehr, M. Spatial distribution of QT intervals: an alternative approach to QT dispersion, PACE 1996, 19:1894-1899.

[6] Lant, J., Stroink, G., ten Voorde, B.J., Horacek, B.M., Montague, T.J. Complementary nature of electrocardiographic and magnetocardiographic data, J Electrocardiol, 1990, 23:315-322.

[7] Green, L.S., Lux, B.L., Haws, C.W. Detection and localization of coronary artery disease with body surface mapping in patients with normal electrocardiograms, Circulation, 1987, 76:1290-1297.

Current density estimation on the left ventricular epicardium: A potential method for ischemia localization

Pesola K.[1,2], Hänninen H.[2,3], Lauerma K.[4], Lötjönen J.[1], Mäkijärvi M.[2,3],Nenonen J.[1,2], Takala P.[1,2], Voipio-Pulkki L.-M.[5], Toivonen L.[2,3], and Katila T.[1,2]

[1]Laboratory of Biomedical Engineering, Helsinki University ofTechnology, Espoo, Finland;
[2]Medical Engineering Centre, BioMag Laboratory, [3]Division of Cardiology, [4]Division of Radiology, Helsinki University Central Hospital, Helsinki, Finland;
[5]Turku University Central Hospital, Turku, Finland

Introduction

The localization of ischemic regions in the heart is a potential clinical application for magnetocardiography (MCG). Non-invasive localization and determination of the size of ischemic areas is clinically of significant importance. The use of point-like source models, such as a single current dipole, is not feasible in ischemia localization as the ischemic regions can be large. Thus, distributed source models need to be applied in solving the inverse problem.

In this study, a discrete equivalent current density was applied on the epicardial surface of the left ventricle (LV). A similar model has been applied previously, e.g., in locating epicardial current sources [1,2] and in detecting decreased current amplitude in myocardial infarction (MI) patients [3]. Triangulated boundary element (BE) torso models, acquired from magnetic resonance imaging (MRI), were used to model the volume conductor. The BE models also contained the outer surface, i.e., the epicardial surface of the LV. The current density estimates were solved from magnetic field data using Tikhonov regularization. Simulated MCG data with realistic amount of measurement noise were used to study different regularization operators. In addition to simulations, current density estimation (CDE) was applied in 13 coronary artery disease (CAD) patients. The calculated estimates were compared with the clinical reference information about the LV function.

Methods

The measured magnetic field values and the current distribution inside the heart can be linked together via the *lead fields* $\mathbf{L_i}$:

$$b_i(\mathbf{r}) = \int_{V'} \mathbf{L_i}(\mathbf{r}\,') \cdot \mathbf{j}(\mathbf{r}\,')\, dv' \,. \qquad (1)$$

The subscript i refers to the i^{th} sensor, b_i denotes to the magnetic field at the observation point $\mathbf{r}$, and $\mathbf{j}$ is the primary current distribution. Before estimating $\mathbf{j}$, the reconstruction region (surface or volume) needs to be selected. In our calculations, the discrete reconstruction points were placed on the left ventricular epicardial surface at the centers of the triangles. Next, the sensor lead fields were calculated by placing unit dipoles in each coordinate direction to each source point $\mathbf{r}\,'$. In the calculation of the lead fields, the properties of the volume conductor were taken into account. Discretization of Eq. 1 produces a matrix equation

$$\mathbf{b} = L\mathbf{j} \,, \qquad (2)$$

where the matrix $L_{m\times 3n} = (\mathbf{L_1}, \cdots, \mathbf{L_m})$ is composed of the lead fields, vector $\mathbf{j}_{3n\times 1}$ contains the unknown source strengths, and n is the number of source points. The conventional minimum norm solution of an underdeterministic matrix equation, such as Eq. 2, can be expressed as

$$\mathbf{j} = L^{\dagger}\mathbf{b} = L^T(LL^T)^{-1}\mathbf{b} \,, \qquad (3)$$

where $L^{\dagger}$ is the pseudo-inverse of L. Eq. 3 relates directly to the so-called *minimum norm estimate* $\mathbf{j}^*$ [4] which is defined as a linear combination of the lead fields

$$\mathbf{j}^* = \sum_{i=1}^{m} \omega_i \mathbf{L_i} = \boldsymbol{\omega}^T L \,. \qquad (4)$$

The coefficients ω_i are solved from the magnetic field values using the inner product matrix Γ:

$$\boldsymbol{\omega} = \Gamma^{-1}\mathbf{b} = (LL^T)^{-1}\mathbf{b} \,. \qquad (5)$$

Therefore, the transpose of the minimum norm estimate equals to the solution in Eq. 3, namely: $\mathbf{j}^{*T} = L^T\boldsymbol{\omega} = L^T(LL^T)^{-1}\mathbf{b}$.

In practice, the unknown current distribution $\mathbf{j}$ cannot be directly solved from Eq. 3 because the lead fields of adjacent sensors are nearly linearly dependent on each other. Therefore, the inner product matrix (LL^T) has a low numerical rank, and the classical solution will be contaminated by noise. The matrix inversion can be stabilized with truncation of the singular value decomposition where the smallest singular values of the inner product matrix are replaced by zeros [4].

In this study, Tikhonov regularization was selected as the means for obtaining meaningful solutions for $\mathbf{j}$. In this type of regularization, a side constraint is added to the original minimization problem. The function to be minimized can then be written as

$$\|L\mathbf{j} - \mathbf{b}\|^2 + \lambda\|R\mathbf{j}\|^2 \longrightarrow min \,, \qquad (6)$$

where $\|\cdot\|$ is the Euclidean norm, R is the regularization operator and λ is a parameter which controls the weight given to the minimization of the side constraint. With the side constraint, *a priori* knowledge can be used in the calculation. The use of a side constraint changes the classical solution towards the applied side constraint.

The regularization operator R can be implemented in several ways. We have used the identity matrix I (zero-order regularization) and a simple discrete approximation of the surface Laplacian (second-order regularization) where the center triangle was weighted with value −3, and the three neighboring triangles were weighted with value 1 [5]. The use of the identity matrix tends to minimize the norm of the current density estimate whereas the surface Laplacian avoids steep changes in the estimate. The solution to the minimization problem in Eq. 6 can be written as

$$\mathbf{j} = (L^T L + \lambda R^T R)^{-1} L^T \mathbf{b}\,, \qquad (7)$$

or alternatively

$$\mathbf{j} = (R^T R)^{-1} L^T (L(R^T R)^{-1} L^T + \lambda I)^{-1} \mathbf{b}\,, \qquad (8)$$

provided that the regularization operator R has a full rank $3n$. Both solutions involve the inversion of $3n \times 3n$ matrix, therefore increasing the computational demands with increasing number of source points. However, if the identity matrix is used as the regularization operator, Eq. 8 reduces to $\mathbf{j} = L^T(LL^T + \lambda I)^{-1}\mathbf{b}$ which contains only an inversion of $m \times m$ matrix.

Selecting a value for the regularization parameter λ in the case $R = I$ by means of the L-curve method has been formulated previously [1]. With L-curve, a balance between the minimization of the residual and the side constraint in Eq. 6 can be found as the value of λ is varied. The L-curve method was used in zero-order regularization to select a value for λ. However, with measured data, the L-curve method sometimes resulted in multiple maxima in the curvature function which is used in finding the corner point of the L-curve. In second-order regularization, the λ values were selected by investigating the quality of the calculated estimates.

Simulated MCG data with a realistic amount of measurement noise were used to study different regularization operators. In addition to simulations, the CDE was applied in 13 CAD patients. Four of the patients with no previous MI had a single vessel coronary disease with a significant stenosis (> 50 %) in one of the main coronary arteries. Nine patients had regional or global left ventricular dysfunction caused by severe chronic myocardial ischemia, previous MI, or both. For the latter patient group, positron emission tomography (PET) was used as the 'golden standard' in separating MI scar areas from regions of viable myocardial tissue.

In MCG measurements, acute ischemia was induced by exercise testing with a non-magnetic stress ergometer, pedaled in supine position. The measurements

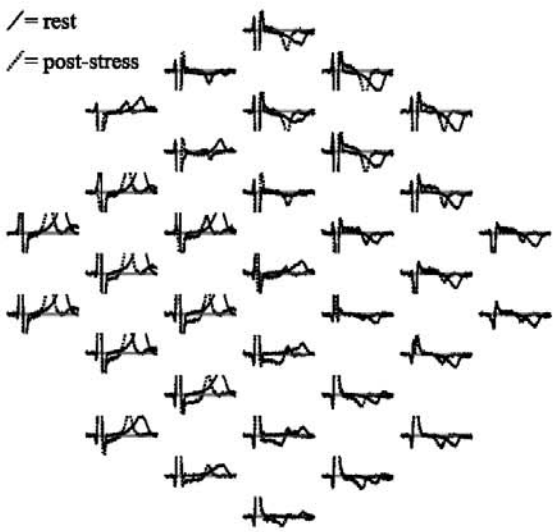

Figure 1: Signal-averaged MCG data at rest (solid line) and after stress (dotted line), presented with 33 simulated axial sensors.

were performed at rest and after stress with the 67-channel cardiomagnetometer in BioMag Laboratory at Helsinki University Central Hospital (HUCH). The ST-segment of the cardiac cycle was selected for the data analysis. An example of the changes in the MCG during the ST-segment and the T-wave, induced by stress testing, is shown in Fig. 1. The ST-segment difference signals of averaged post-stress and rest MCG recordings were used in computing current density estimates. In the calculations, individualized realistic LV and torso models were used. The torso and LV surfaces were tessellated with approximately 700 and 100 triangles, respectively. The torso was assigned a constant electrical conductivity of 0.2 S/m. In single vessel CAD patients, CDEs were compared to the assumed ischemic regions estimated from the coronary angiograms. In the other patient group, the calculated CDEs were compared to the reference information obtained from the PET images. No current density should build up in scar regions, and regions of high CDE amplitude should correspond to the viable areas.

Results

In simulation studies, zero- and second-order regularizations were tested by placing distributed sources on a triangulated epicardial surface of the LV. The source locations were selected to represent the myocardial regions vascularized by the three main coronary arteries: 1) septal and anterior regions supplied by the left anterior descending coronary artery (LAD), 2) lateral region supplied by the left circumflex coronary artery (LCX), and 3) posterior surface of LV supplied by the right coronary artery (RCA). The sources were constructed by placing dipoles at the centroids of se-

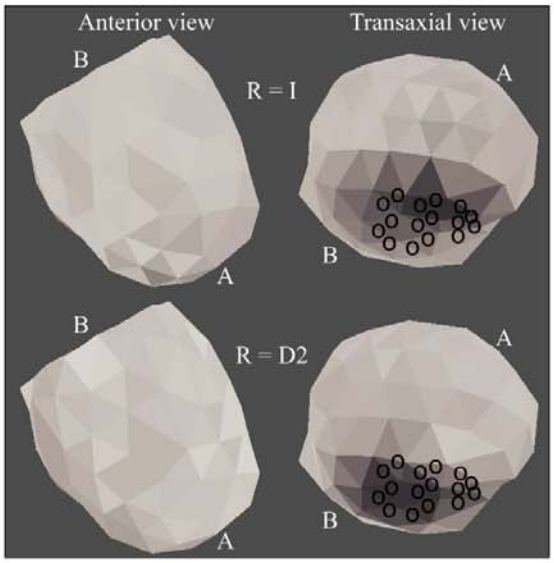

Figure 2: CDEs calculated for the RCA simulation with zero-order (upper row) and with second-order regularization (bottom row). The actual positions of dipoles used in generating the data are marked with black circles. The amplitude of CDEs is coded with gray scale values. (A = apex, B = base)

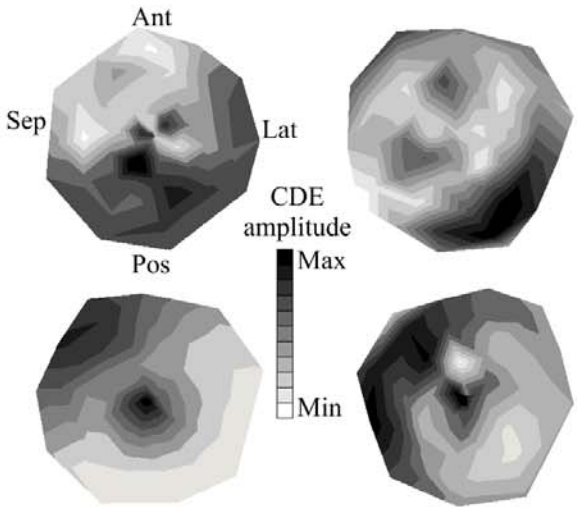

Figure 3: CDEs for two RCA patients (upper row) and for two LAD patients (bottom row), visualized with polar maps. The CDE amplitude for each patient is coded with gray scale values.

lected triangles. CDEs were then calculated with zero- and second-order regularizations. For the LAD simulation, the results with both types of regularization operators were similar. For the LCX simulation, differences between the operators started to appear. The largest differences were obtained for the RCA simulation. The calculated CDEs for the RCA simulation are shown in Fig. 2. It can be seen that for $R = I$, the calculated CDE is not focused around the source area but is shifted towards the anterior surface of LV. This shift is caused by regularization which tries to minimize the norm of the solution. However, for $R = D2$, the calculated estimate is correctly centered in respect to the source region. The quality of the estimate is increased as the use of the surface Laplacian doesn't try to minimize the amplitude of the solution but simply to avoid steep changes. From the results obtained with simulated data it was concluded that more reliable CDEs will be obtained with $R = D2$ which was then used in calculating CDEs from measured MCG data.

In the first part of the patient study, CDEs were calculated from the ST-segment difference signals of four single vessel CAD patients. In single vessel CAD, the injury currents should restrict only to the myocardial regions supplied by the stenosed coronary artery. Two of the single vessel CAD patients had significant stenosis in the LAD, and the other two had significant stenosis in the RCA. The calculated CDEs are shown in Fig. 3 where a polar map has been used to visualize the results. In the polar map, the epicardial surface of LV is stretched to form a circle, the apex being at the center. Therefore, the whole LV surface can be seen from the same view, but some anatomical information is lost. The polar map can be divided into four regions according to the coronary anatomy: anterior, lateral, posterior, and septal regions. The regions are indicated in Fig. 3. From the results presented in Fig. 3, it can be seen that in the CDEs calculated for the RCA patients, the amplitude is largest in the posterior and in the lateral parts of LV. In the second RCA patient, there are small areas of increased CDE amplitude near the apex but the largest amplitude is found at the posterior/lateral side of LV. This site matches to the expected ischemic myocardial regions in patients with a stenosis in the RCA. For the LAD patients, in contrast, the CDEs are focused in the apex, in the anterior and in the septal regions of LV, thus matching to the myocardial regions supplied by the LAD. Therefore, an increase in CDE amplitude is found to correlate with the expected ischemic myocardial regions supplied by the stenotic coronary artery in single vessel CAD patients.

In the second part of the patient study, the CDE was applied in 9 three-vessel CAD patients with regional or global LV dysfunction caused by severe chronic myocardial ischemia, previous MI, or both. PET images were used in separating the areas of viable myocardial tissue from the scar regions. The PET shows the uptake of ^{18}F-2-deoxyglucose (FDG) which is increased in chronically ischemic myocardial areas, and is negligible in scar areas. In MCG measurements, exercise testing was used to induce acute ischemia in the cardiac tissue, thus possibly increasing the amplitude of the ischemic signal. Also in this patient group, the CDEs were calculated from the ST-segment difference signals. The calculated CDEs were compared with the

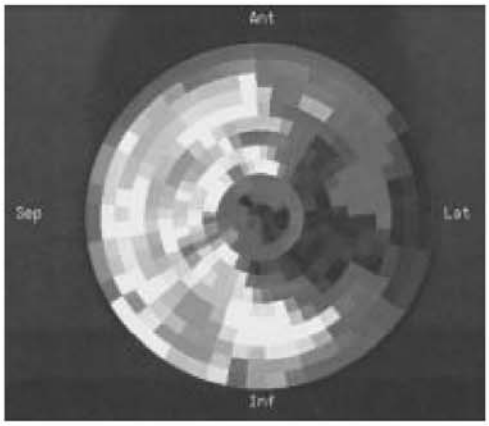

Figure 4: The PET result of a three-vessel disease CAD patient showing a scar in the lateral region.

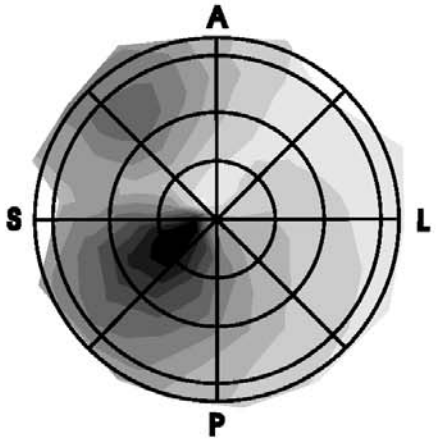

Figure 5: The CDE corresponding to the PET result in Fig. 4 (scale as in Fig. 3).

reference information obtained from PET images. The comparison was performed by dividing the polar map of LV into eight sectors: two anterior, two lateral, two septal, and two posterior sectors. Each sector was further divided into three short axis planes: apex, mid, and base. Thus, the comparison was carried out in 24 segments which by PET were determined to be either viable tissue or scar. The scale of the CDEs was divided into half to indicate low and high CDE amplitude. Therefore, a match was obtained if a low CDE amplitude was detected in a scar segment, or a high CDE amplitude in a viable segment. An example of the PET images is shown in Fig. 4. The PET result in Fig. 4 indicates that there is a lateral scar area (dark region). The anteroseptal, septal and posteroseptal regions show normal to increased uptake of FDG, thus indicating viable myocardium. The corresponding CDE, calculated for the same patient, is presented in Fig. 5 where the division of the polar map into 24 segments is also shown. The CDE in Fig. 5 shows increased amplitude in the anteroseptal, septal and posteroseptal regions, thus matching well with PET. A decreased CDE amplitude is found in the lateral region which was found to be a scar area. The overall results of the comparison between PET data and calculated CDEs for all 9 chronic ischemia patients showed an average match of 77 % between the segments of high and low amplitude in CDEs, and the viable and scar areas in PET, respectively. Therefore, the classification (scar or viable tissue) obtained from the calculated CDEs was correct in approximately 18/24 segments.

Discussion

Localization of ischemia is a promising, clinically important application for magnetocardiography. In this study, current density estimation (CDE) was found to localize extended source regions in simulations. Satisfactory results were obtained using a simple discrete approximation of the surface Laplacian as the regularization operator. In patient studies, regions of high CDE amplitude were found to correlate with the ischemic areas in single vessel CAD patients. For CAD patients with previous MI and severe chronic ischemia, the areas of low CDE amplitude were found to match with scar regions whereas a high CDE amplitude was found to correlate with areas of viable, ischemic cardiac tissue. Therefore, current density estimation is a potential method for localizing both myocardial ischemia in single vessel CAD patients, as well as more complex chronic ischemia in three-vessel CAD patients.

References

[1] Pesola, K., Nenonen, J., Fenici, R., and Katila, T. Comparison of regularization methods when applied to epicardial minimum norm estimates, Biomedizinische Technik, 1997: 42 (Suppl. 1): 273-276.

[2] Ferguson, A.S., Vardy, D., et al. A regularized minimum norm method for calculating distributions of source currents on epicardial surfaces, In: Baumgartner, C., et al. Biomagnetism: Fundamental Research and Clinical Applications, Elsevier Science/IOS Press, 1995.

[3] Leder, U., Pohl, H.P., et al. Noninvasive biomagnetic imaging in coronary artery disease based on individual current density maps of the heart, Int. J. Cardiol., 1998, 64:83-92.

[4] Hämäläinen, M., and Ilmoniemi, R. Interpreting magnetic fields of the brain: minimum norm estimates, Med. & Biol. Eng. & Comput., 1994, 32: 35-42.

[5] Huiskamp, G. Difference formulas for the surface Laplacian on a triangulated surface, J. Comp. Phys., 1991, 95:477-496.

Validation of Noninvasive Functional Cardiac Electrical Source in a 43-year old Male Patient

Tilg B.[1,2], Modre R.[1], Fischer G.[1], SippensGroenewegen A.[2], Mlynash M.[2], Roithinger F.X.[2], Reddy G.[3], Roberts T.[3], Wach P.[1], Lesh M.D.[2], and Steiner P.R.[2]

[1]Institute of Biomedical Engineering, Technical University Graz, Graz, Austria
[2]Section of Cardiac Electrophysiology, Department of Medicine, [3]Department of Radiology,
University of California San Francisco, San Francisco, California, USA

Introduction

The combined recording of the torso anatomy (e.g., with magnetic resonance imaging (MRI)) with electrocardiographic (ECG) or magnetocardiographic (MCG) mapping data enables the non-invasive imaging of the primary electrical sources in the human heart. In the forward problem the source-field relationship is investigated. The primary sources in the cardiac muscle are the spatio-temporal transmembrane potential φ_m distributions [14]. In modeling cardiac source structures both isotropic and anisotropic model types are considered. In the isotropic case the forward and inverse formulation can be reduced to a two-dimensional field and scalar potential problem. In general for this kind of problem the boundary element method (BEM) is applied [3, 6, 7, 12, 13]. The consideration of electrical anisotropy requires the extension to a three-dimensional volumetric formulation, in most cases numerically handled with the Finite Element Method (FEM) [4]. During depolarization the assumption of electrical isotropy in the myocardium is valid. For repolarization the consideration of electrical anisotropy (fiber structure) is an important factor for the source-field relationship [14]. For source imaging during depolarization the two-dimensional isotropic formulation is applicable. In the inverse problem parameters describing features of φ_m (e.g., the activation time (AT) defined as the onset of the φ_m (phase 0)), equivalent primary sources (e.g., a single current dipole (SCD) mathematically related to a φ_m pattern over a patch of activated cardiac tissue) or the epicardial (pericardial) potential pattern are estimated. The epicardial potential as well as the potential on all other conductivity interfaces (and therefore also at the ECG electrode positions) are related to φ_m by an integral equation [3]. The relation between the MCG at the sensor positions and φ_m is given by an integral representation [12, 13]. The most established inverse formulations are imaging of the AT map on the entire surface of the heart (endo- and epicardium) and epicardial potential pattern [2, 7, 6, 9, 12]. The first approach is based on the uniform dipole layer (UDL) theory assuming electrical isotropy in the myocardium. In the epicardial potential formulation from the estimated potentials the AT map can be derived on the epicardium only. For this, electrical isotropy in the myocardium has not to be assumed. A further estimation of the AT map on the endo- and epicardium would require the solution of an additional inverse problem. For this, the assumption of electrical isotropy must be introduced or a volumetric inverse problem has to be solved. Beside the surface AT inverse approach, SCD fitting algorithms were developed during the last two decades. The AT imaging methods permit the reconstruction of single focal, multiple focal and of more distributed activation patterns. Further, these methods can distinguish between areas with early and late activation. The SCD approach allows imaging of single focal source patterns only. Potential clinical application of the ECG and MCG inverse problem are imaging of premature and pre-excited ventricular activation.

The application of non-invasive source imaging to clinical data requires a detailed validation of the inverse method. So far, only a synthetic validation of source imaging was performed using computer models, tank models, and phantom models. Recently, an open chest validation study in humans for the AT inverse approach was presented [8]. However, closed-chest validation in humans has not yet been reported. Such a closed chest validation is an essential step in bringing the ECG and MCG inverse method into clinical application. The AT inverse approach can be validated applying a recently developed electroanatomical catheter mapping system [1, 11]. CARTO™ enables the imaging of the endocardial spatio-temporal potential and AT map. In this study we compared non-invasively estimated and measured sinus rhythm AT maps on the endocardium of the right ventricle (RV) in one patient.

Method

A 43-year old male without structural heart disease underwent an electrophysiological study for paroxysmal atrial fibrillation. From this patient the CARTO™ map, the 62-channel ECG and 37-channel MCG map and the torso anatomy ((cine) MRI) was recorded.

CARTO™ map

A 123-point endocardial sinus rhythm AT map of the RV was measured with an electroanatomical catheter mapping system (Biosense/Johnson&Johnson [1]). From the 123 endocardial points the three-dimensional location (in the device co-ordinate system) and the potential was recorded. From the potential the local AT was determined. This non-fluoroscopic mapping system consists of a location pad positioned under the bed

of the patient, two catheters with a sensor and reference catheter, a mapping system and a Silicon Graphics computer. The location pad generated a magnetic field of low intensity. In the distal part of the mapping catheter a sensor is mounted. This sensor gives information about the position and the rotation of the distal catheter segment. From the distal tip of the catheter an unipolar or bipolar potential signal can be recorded whose timing is related to a reference signal. In this way, ATs are obtained in relation to the position of the catheter in the heart. Sequential recording of several points by dragging the catheter along the endocardium allows a real-time construction of the three-dimensional map. In addition to the mapping catheter, a second catheter is instrumented with a sensor. The spatial information from this catheter is used to detect small changes in intracardiac position due to respiration or movement of the patient. In the acquisition software, these small changes of the reference catheter are used to correct the spatial information of the mapping catheter. The mapping and the reference catheter are positioned in the heart under fluoroscopic guidance [11]. Figure 4 depicts the CARTO™ sinus rhythm map of the RV from an anterior-posterior view.

62-channel ECG map

The ECG mapping data was simultaneously recorded with the CARTO™ map in the catheter laboratory. The ECG mapping system (Amsterdam, The Netherlands) is an on-line portable dual-computer acquisition and analysis system with data transmission by optical fibre. A radiotransparent carbon electrode array was used to record unipolar ECG data from 62 torso sites (anterior chest: 41, posterior chest: 21) relative to the Wilson's terminal as a reference. Sampling rate was 1000.0 Hz with a 14-bit AD converter. Amplifier specifications allowed for a peak-to-peak noise level of $2 \cdot 10^{-6}$V [10].

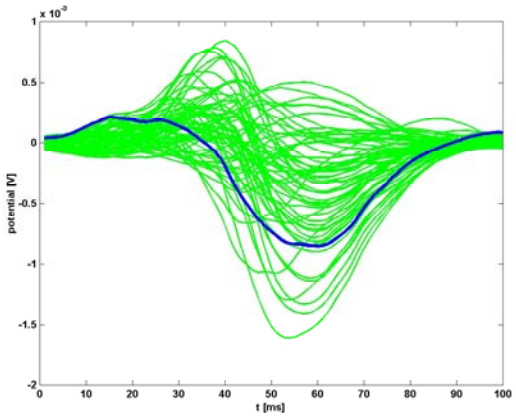

Figure 1: Single beat QRS complexes for sinus rhythm activity of the 62 ECG channels in a butterfly plot. The thick line represents the potential for channel no. 12 (Wilson lead V1).

37-channel MCG map

The MCG was measured on the anterior chest surface with a 37-channel first-order axial gradiometer magnetic field mapping system (MagnesII®, Biomagnetic Technologies) in a shielded room at three different locations (anterior chest close sternum, anterior chest close xiphoid, left lateral chest). Sampling rate was 1041.7Hz with a 16-bit AD converter. The noise level of the system is specified in the order of $10 \cdot 10^{-15}$T/√Hz.

(Cine) MR imaging

The torso was imaged with a 1.5 Tesla MR scanner (Signa™, General Electrics). From the torso 40 axial and 10 coronal cross-sections were recorded with a slice thickness of $10 \cdot 10^{-3}$m. Additionally, for the modeling of the surface of the heart the cardiac muscle was imaged in a ECG-gated (cine) breath-hold oblique imaging mode with $7 \cdot 10^{-3}$m slice thickness and seven phases during the cardiac cycle (with a phase delay of $35 \cdot 10^{-3}$s). Vitamin E markers (diameter $5 \cdot 10^{-3}$m) were used to determine the electrode positions from the axial MR scans. Additional markers were positioned on the sternum, xiphoid and on the left and right rib cage. A subset of these markers was used to couple the MR, CARTO™, ECG and MCG data. The MR co-ordinate system was used as the actual co-ordinate system for the inverse formulation.

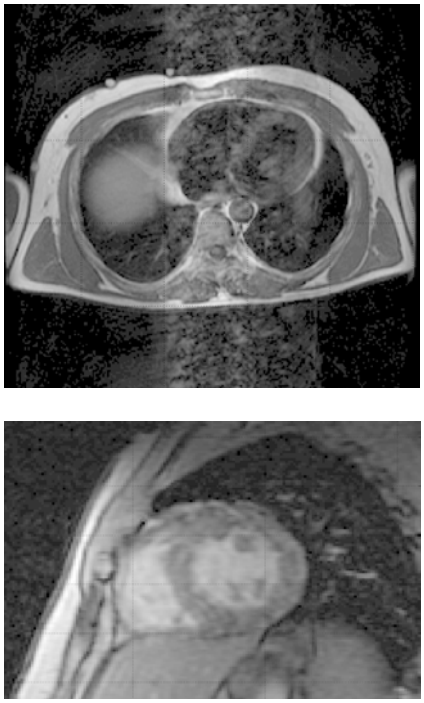

Figure 2: The outer torso surface and the surfaces of the two lungs were modeled from axial scans (upper panel). Two markers can be seen in this slice on the right anterior chest wall. The surface of the ventricle was modeled from oblique cine MR scans (R-wave triggered). The lower panel depicts a cross-section at $45 \cdot 10^{-3}$s (late diastole).

Inverse problem

The activation time pattern on the surface (endocardium and epicardium) of the ventricle was estimated applying the critical point theorem (CPT) [7] followed by a subsequent optimization routine for non-linear problems (E04UCF, NAG Ltd. UK) minimizing the following cost function [12]:

$$\Psi = \int_0^T \left\| \mathbf{A}\,\varphi_m(t,\tau) - D(t) \right\|_2^2 dt + \lambda^2 \left\| \Delta\tau \right\|_2^2 \rightarrow min \qquad (1)$$

A is the transfer matrix, which describes the relation between $\varphi_m(t,\tau)$ on the surface of the ventricle (endo- and epicardium) and the ECG or MCG data D(t). The surface laplacian operator Δ acts as a spatial smoothing operator with the second order Tikhonov regularization parameter λ. The time interval [0,T] corresponds to the QRS wave in case of the sinus rhythm, i.e., to ventricular depolarization. In E04UCF a sequential quadratic programming method with a quasi-Newton update of the Hessian matrix is implemented. In the inverse formulation we described φ_m at each source point on the surface of the ventricle by an analytical template function with the parameters resting membrane potential a (=-0.09V), action potential amplitude u (=0.10V), rise time w (=$2 \cdot 10^{-3}$s), and activation time τ. All parameters except the activation time were assumed to be constant. An isotropic pseudo-subparametric BEM including the blood masses, the lungs and the outer torso surface was used to model the volume conductor [3]. The following conductivities of the torso compartments were used in the inverse formulation: 0.2 Sm^{-1} (torso), 0.05 Sm^{-1} (lungs), and 0.6 Sm^{-1} (blood masses) [6]. The entire volume conductor was modeled with 528 pseudo-subparametric high-order boundary elements (BEs). The endocardial surface of the RV was meshed with 70 BEs (212 nodal points). The AT pattern was estimated from the ECG and MCG data on the entire surface of the ventricle (246 BEs, 744 nodal points). Both cardiac geometries (CARTO™, cine MR (oblique mode)) were collected during the end-diastolic phase.

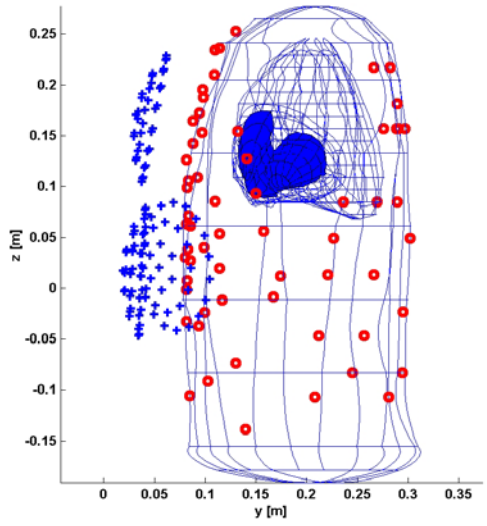

Figure 3: Inhomogeneous boundary element torso model from a left lateral view with the ventricular surface modeled from cine oblique MR cross-sections at $45 \cdot 10^{-3}$s after the peak of the R-wave. 41 and 21 ECG mapping electrodes (O) are located on the anterior and posterior chest wall. Three MCG data recordings (run 1, run 2, run 3) were performed with the 37-channel first-order axial gradiometer mapping system. The locations of the pickup coils for the three runs are indicated by crosses (+).

Results

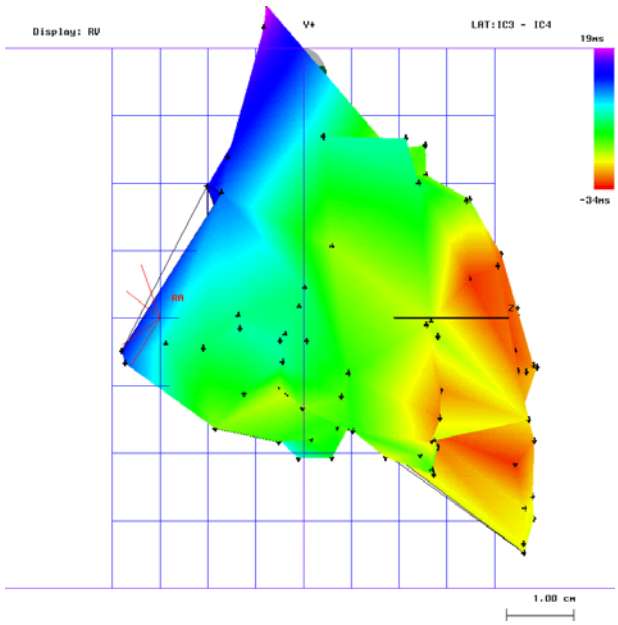

Figure 4: Measured endocardial AT map of the RV during sinus rhythm activity in an anterior-posterior view. The (raw data) AT map is in the CARTO™ coordinate system. Early endocardial activation occurred at the anterior side of the apex of the RV. Later, the propagation wave spread towards the heart base and the RV outflow tract. The measured AT interval was $51 \cdot 10^{-3}$s.

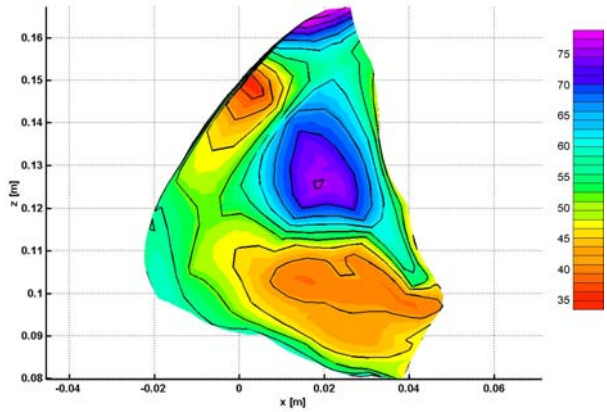

Figure 5: Critical point solution (with an effective rank of 22) of the endocardial AT map of the RV during sinus rhythm activity in an anterior-posterior view reconstructed from 62-channel ECG mapping data (single beat). The reconstructed AT interval was $47 \cdot 10^{-3}$s. Isochrones are shown in steps of $5 \cdot 10^{-3}$s.

The reconstructed and invasively recorded endocardial AT sequence of the RV showed good qualitative agreement (Figure 4, 6). The measured and estimated AT interval was 51 and $54 \cdot 10^{-3}$s, respectively. The CPT solution for the AT map is shown in Figure 5. An

effective rank of 22 of the single beat ECG data matrix was considered. As shown in [7] the CPT is less powerful on the endocardium. But the main pattern (breakthroughs, late activation) of the epicardial AT pattern was properly imaged by the CPT. The final inverse solution in Fig. 6 was quantitatively compared with the (raw data) CARTO™ map. The correlation coefficient (CC) for this AT map was determined with 0.84. The endo- and epicardial AT pattern of the left ventricle was found to be in accordance with previously published results [5]. The inverse solutions from ECG and MCG data were also quite similar.

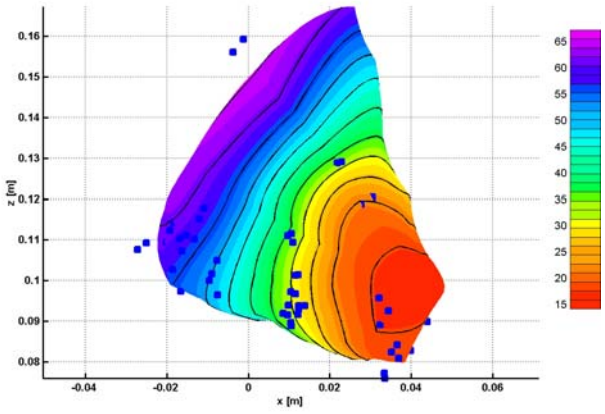

Figure 6: Final (critical point algorithm and subsequent optimization of equation (1)) endocardial AT map of the RV during sinus rhythm activity in an anterior-posterior view reconstructed from 62-channel ECG mapping data (single beat) with CC=0.84. The reconstructed AT interval was $54 \cdot 10^{-3}$s. Isochrones are shown in steps of $5 \cdot 10^{-3}$s. The points of the CARTO™ map transformed into the MR co-ordinate system are shown as squares (■).

Discussion

A recently introduced electroanatomical catheter mapping system offers the possibility for a closed-chest validation of the electro- and magnetocardiographic inverse problem [1]. The favourable results achieved for sinus rhythm activity let one to expect that similar agreement can be obtained with ectopic or pre-excited ventricular activation. This clinical reference data set enables the investigation of important questions for a future clinical application of non-invasive electrical source imaging, e.g., the number of sensors and the accuracy of the volume conductor model necessary to achieve certain localization accuracy.

References

[1] Ben-Haim, S.A., Osadchy, D., Schuster, I., Gepstein, L., Hayam G., and Josephson, M.E. Nonfluoroscopic, in vivo navigation and mapping technology. Nature Medicine, 1996, 2: 1393-1395.

[2] Cuppen, J., and van Oosterom, A. Model studies with inversely calculated isochrones of ventricular depolarization. IEEE Transactions on Biomedical Engineering, 1984, 31: 652-659.

[3] Fischer, G., Tilg, B., Wach, P., Modre, R., Leder, U., and Nowak, H. Application of high-order boundary elements to the electrocardiographic inverse problem. Computer Methods and Programs in Biomedicine, 1999, 58(2): 119-131.

[4] Fischer G., Tilg B., Modre R., Fetzer J., Rucker W., Huiskamp G., and Wach, P. The electrically silent cardiac magnetic field. In these proceedings.

[5] Durrer, D., van Dam, R., Freud, G., Janse, M., Meijler, F., and Arzbaecher, R. Total excitation of the isolated human heart. Circulation, 1970, 41: 899-912.

[6] Hren, R., Zhang, X., and Stroink, G. Comparison between electrocardiographic and magnetocardiographic inverse solutions using the boundary element method. Medical & Biological Engineering & Computing, 1996, 34: 110-114.

[7] Huiskamp, G., and Greensite, F. A new method for myocardial activation imaging. IEEE Transaction on Biomedical Engineering, 1997, 44: 433-446.

[8] Ostendorp, T., Pesola, K. Non-invasive determination of the activation time sequence of the heart: validation by comparison with invasive human data. In: Computers in Cardiology 1998, New York, NY, USA, IEEE, 25: 313-316.

[9] Oster, H.S., Taccardi, B., Lux, R.L., Ershler, P.R., and Rudy, Y. Electrocardiographic Imaging. Noninvasive characterization of intramural myocardial activation from inverse-reconstructed epicardial potentials and electrograms. Circulation, 1998, 97: 1496-1507.

[10] SippensGroenewegen A., Peeters H.A.P., Jessurun E.R., Linneback A.C., Robles de Medina E.O., Lesh M.D., and van Hemmel N.M. Body surface mapping during pacing at multiple sites in the human atrium. Circulation, 1998, 97: 369-380.

[11] Smeets, J.L., Ben-Haim S.A., Rodriguez L.-M., Timmermans C., and Wellens, H.J. New method for nonfluoroscopic endocardial mapping in humans - accuracy assessment and first clinical result. Circulation, 1998, 97: 2426-2432.

[12] Tilg, B. Noninvasive functional cardiac electrical source imaging. Thesis for Habilitation, Technical University Graz, Aachen, Verlag Shaker, 1998.

[13] Wach, P., Tilg, B., Lafer, G., Nenonen, J., and Katila, T. Modeling of the cardiac forward and inverse problem - magnetic source imaging from magnetocar-

diographic data. Medical & Biological Engineering & Computing, 1996, 34(1): 35-36.

[14] Yamashita, Y., and Geselowitz, D. Source-field relationships for cardiac generators on the heart surface based on their transfer coefficients. IEEE Transactions on Biomedical Engineering, 1985, 32: 964-970.

Acknowledgements

This work was supported by the Austrian Science Fund grant J1506-MED (Erwin Schrödinger scholarship), by the NIH grant RO1-HL55227 and by the UCSF REAC Harris Fund. The authors would like to thank Terry Ransbury and Suzanne Honma for their technical assistance.

Magnetocardiography under Clinical Conditions

Erné, S.N.[1], Kammrath, H.G.[1], Ziolkowski, M.[2], Tenner, U.[1], Müller, H.-P.[1]

[1]Division for Technical Bioelectromagnetism, Central Institute for Biomedical Engineering, Ulm University, D – 89069 Ulm, Germany
[2]Szczecin Technical University, Al. Piastow 19, PL - 70310, Szczecin, Poland

Introduction

During the last years several algorithms and analysis procedures were developed for the evaluation of biomagnetic and bioelectric data. To obtain clinical validation, an Magnetocardiography (MCG) system especially designed for clinical studies on large patient number has been installed in Ulm (Figs. 1-3) [1].

Fig. 1: Global view of the facility. The shielding performance is described in [2].

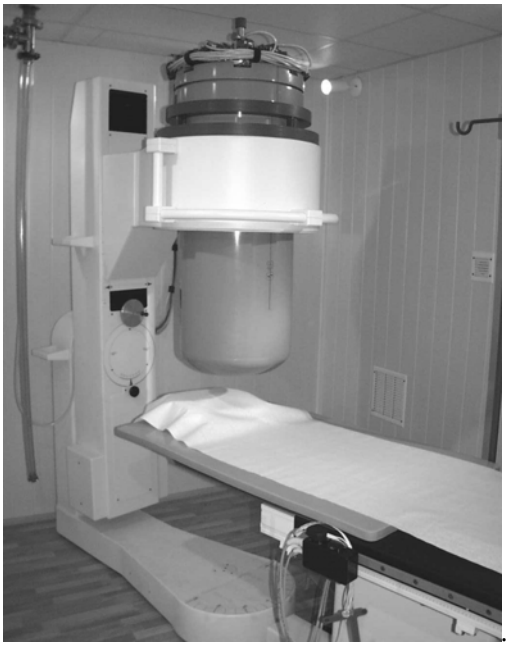

Fig. 2: MCG measurement device.

Fig. 3: Operator Console

Standardized application software has been developed that simultaneously combines and merges established time series algorithms as well as spatio-temporal analysis algorithms from high resolution electrocardiogram (HR-ECG) with their extensions to MCG data.

Method

The MCG system installed at the Ulm University is specifically designed for clinical application and routine use and this implies that a large number of patients are to be investigated. To reach this goal, the system design meets the requirements of reliability and high field sensitivity. The MCG sensor system is operating inside the magnetic shielded room described in [2]. The sensor system consists of a planar dewar, containing a complex architectural structure with sensors distributed over three levels. The first level, i.e. the primary measurement plane holds 55 SQUID sensors. The sensing elements are integrated magnetometers with a square shape of 12.7 mm in diagonal. The sensors are uniformly distributed over the inner surface of the dewar, according to a hexagonal geometry, covering a circular surface of about 230 mm in diameter. The measurement plane is 18 mm from the outer dewar bottom. Nineteen additional SQUIDs are mounted on the second level and are used as reference channels 90 mm from the measurement plane. On the third level there is a magnetometric triplet located 70 mm from the reference plane to control the active shielding system. Operating in the shielded environment the system shows on all channels a white noise level better than 10 fT/√Hz at 10 Hz. A software-gradiometer set-up is

easily performed by subtraction of the background field sensed by selected reference channels from the signal of each primary channel.
The patient handling set-up is made of non magnetic material and is an emulation of the standard set-up for clinical cardiac electrophysiology (fig. 4).
For cardiac measurements a map of 55 magnetic channels, three orthogonal electrocardiographic (ECG) leads and a breathing channel are used.
For a raw patient positioning a set of laser markers is used. These markers are set up to point on positioning coils on the ends of a cross which is fixed at the sternum. The dewar is tilt at an angle of 10° to get aligned to the thorax surface. The measurement system is positioned at a distance of about 10 mm from the thorax. This procedure allows for a position of the central sensor approximately 120 mm caudal of manubrium sterni and 50 mm left of the sternum, so that mainly the field normal to the thorax surface is measured. The patient positioning unit (PPU) determines the patient position relative to the sensor array using three coils on the cross that is fixed along the sternum of the patient. The PPU measurement takes only few seconds before the five minutes MCG measurement starts. As example for the 55-channel MCG, the normal heart beat of a volunteer is illustrated in fig. 4.

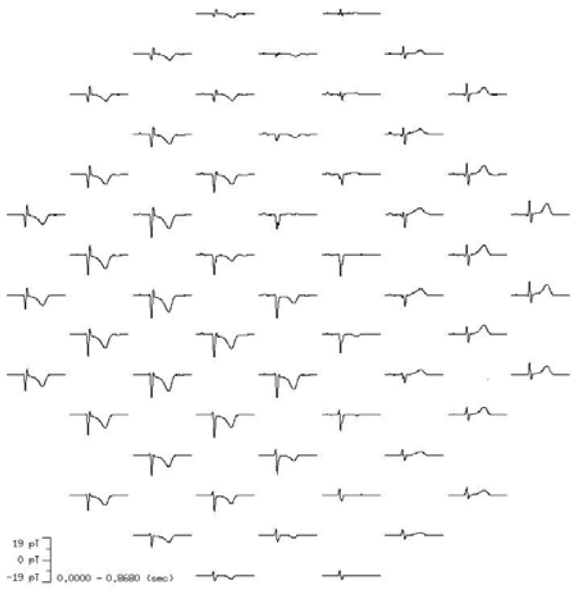

Fig. 4: Example of an averaged heart beat (100 beats). The signals were recorded simultaneously at 55 positions.

Digital filtering at a cut-off frequency of 250 Hz is applied by digitizing the MCG signals at a sampling rate of 1 kHz.
The recorded raw data are stored on compact discs and afterwards are automatically preprocessed by the analysis software, described below.
The MRT data are needed for an accurate representation of the individual geometry of the thorax and the heart surfaces for volume conductor modeling. The MRT images are recorded in a superconducting magnet device (Magnetom Vision 1.5 T Siemens, Erlangen) using a body array coil. Electrocardiographic leads used for cardiac gating. With a normal T_1-spin-echo-sequence, implemented as a standard technique of the Siemens software pulse-sequences, transverzal images are obtained from apex to base in order to cover the entire heart and the thorax. For a useful volume conductor modeling 64 slices in transverzal direction with extension 512 x 512 pixels should be detected. Then, the voxel size would be about 1 x 1 mm^2 in the transverse slices with a slice thickness of about 5 mm. Thus, a field of view of 51.2 x 51.2 cm^2 in the transverzal slices and 32.0 cm perpendicular is recorded. With an echo time T_E of about 15 ms and a repetition time $T_R >$ 800 ms, according to heart beat gating a total measurement time of about 15 min can be reached.

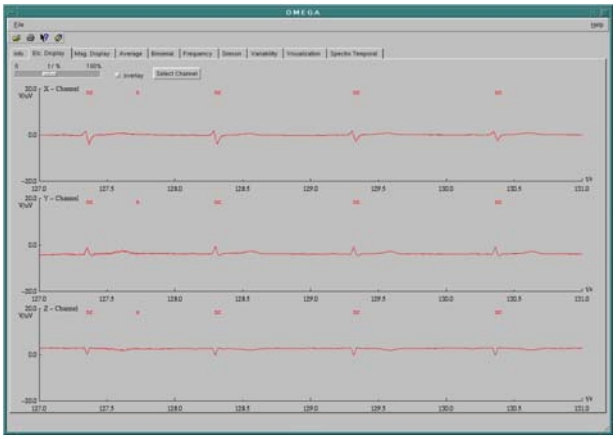

Fig. 5: Channel display for ECG signals. The 3 orthogonal leads are displayed.

At the beginning the Biomagnetic Analysis Console (BAC) software was used for MCG signal analysis [3]. Now, the standard analysis tool is the Open Magnetic and Electric Graphic Analysis (OMEGA) software [4]. The OMEGA software contains established time series analysis algorithms with their extensions to MCG and ECG (Figs. 5,6) data as well as tools for the localization of cardiac electromagnetic sources.

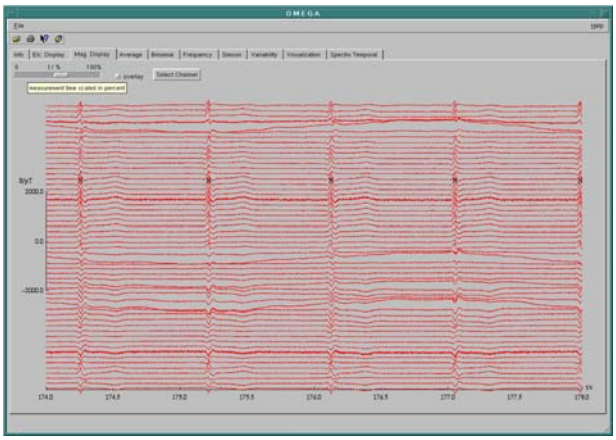

Fig. 6: Multichannel display for 55 MCG signals.

The OMEGA software is using different analysis algorithms under exactly defined mathematical conditions on the same data set to pursue synergetic interactions. Therefore, medical information for clinical applications and diagnostics can be obtained.
The OMEGA software was developed object oriented to run on UNIX workstations as well as on PCs. To obtain flexibility and expandability the program is divided into different parts:

- reader tools for MCG or high resolution ECG data sets
- preprocessor tool
- analysis tools
- reader tools for CT or MRT images
- 2D/3D visualization tools
- graphic user interface

As analysis methods are included frequency analysis, binomial filtering, Simson analysis, heart beat variability, principal component analysis, smoothness test and further analysis algorithms (Figs. 7-10) as well as the visualization of the field distribution (Fig. 7).

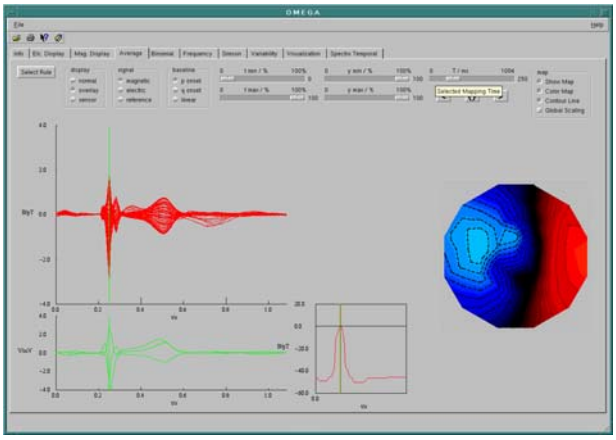

Fig. 7: Averaged data display. The MCG and ECG signals are displayed as overlay plots. On the right side a contour plot of the magnetic field for a defined time point (see the line in the overlay plot) is displayed.

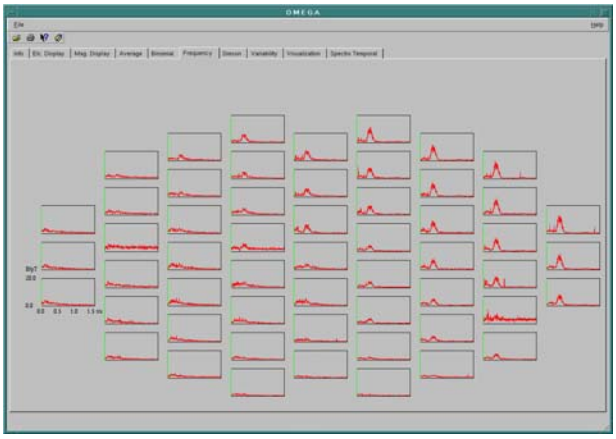

Fig. 8: Example for a time series analysis tool: Frequency analysis.

Spatio-temporal analysis and current source localization methods are implemented as well. These methods are using localized (dipole) sources or distributed sources. Tools for generating 3D models obtained from MRT are included, 2D/3D visualization of the results of the electromagnetic source reconstruction in the morphologic environment is also possible (Fig. 11).

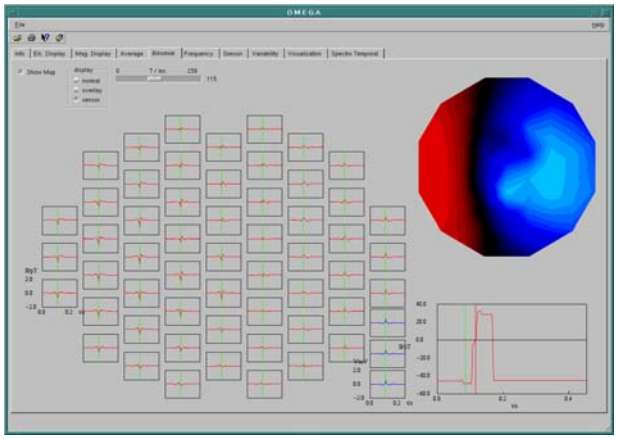

Fig. 9: Example for a time series analysis tool: Binomial filtering analysis.

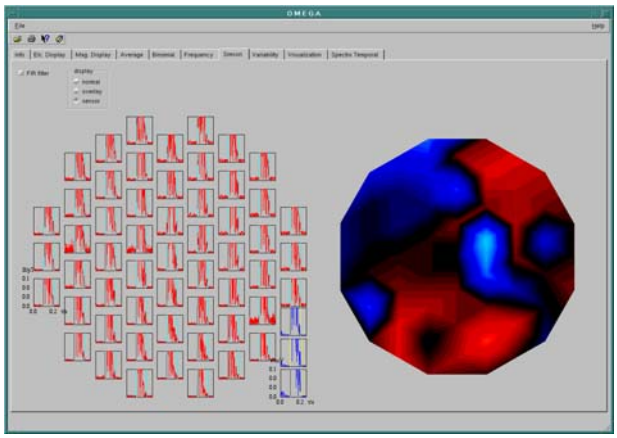

Fig. 10: Example for a time series analysis tool: Simson analysis.

Visualization in medicine is usually linked up to CT-or MRT-images. The information received using these techniques can be displayed as a set of 2D images or combined 3D blocks with volumetric rendering methods. In numerical modeling of biomagnetic fields in the human body, the basic goal is not only to show the anatomical structure but also to present calculated electromagnetic fields and localized sources in the morphological environment.
OMEGA provides the possibility to present calculated fields, i.e. the electromagnetic information, in combination to the anatomy. The working scene for the presentation of the electromagnetic fields and the anatomical objects (boundary element method (BEM) meshes, MRT slices, CT slices) is a rotating 3D-cube controlled by so called virtual trackball, which enables the rotation in any direction. The scalar fields can be displayed

in a form of isocontours or equifilled regions and the vector fields can be shown as a set of solid cones.
Common dipole reconstruction methods work with non-linear least-squares parameter estimations for solving the inverse problem. This method needs costly computations if instead of an analytical volume conductor (sphere, halfspace, ellipsoid, etc.) realistic geometry models are involved.

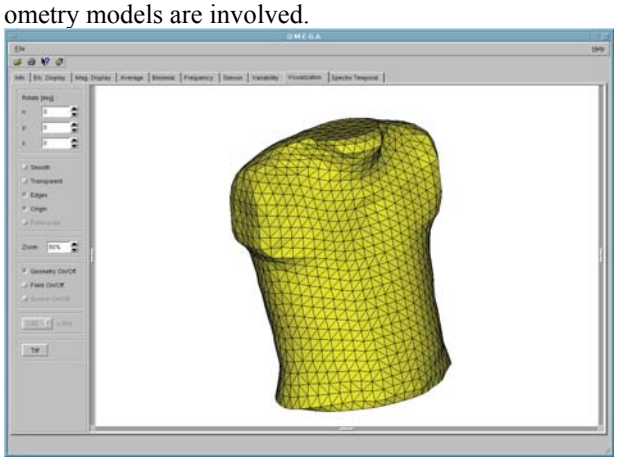

Fig. 11: Visualization of the localization results on a BEM modeled torso. The BEM torso consists of some 500 triangles.

The OMEGA software contains a linear iterative algorithm for dipole localization. This algorithm provides the possibility of computing dipole localization in analytically described surfaces as well as in realistic triangulated surfaces in a time which is in a useful range for routine applications of biomagnetism. The method is described in [5].
The goal in solving the biomagnetic inverse problems, is to calculate the source current density distribution producing the magnetic signals measured outside the body. The method that is implemented in OMEGA to realize this task is based on the minimum-norm approach [6]. Weighting matrices to eliminate depth bias of localized sources and to correct the lead field matrix with the field deviations [7] are used. The Tikhonov-like regularization [8] is used in the process of solution for balancing noise influence. The source space where the current distribution is reconstructed can be defined as a regular 3D grid of current dipoles locations or can be described as a 2D surface arising from physiological constrains.

Results

Within a training study more than 100 MCG measurements have been performed. The volunteers have been selected having no reported cardiac diseases. During the course of the training study the measurement protocol was iteratively improved. An optimized recording strategy and an optimized measurement position for the patient has been defined and can be set up within a few minutes, so that an MCG measurement can be performed within 10 minutes.

Discussion

The OMEGA software has been developed to provide an easy, reproducible and fast analysis and visualization possibility for electric and magnetic data sets in combination with the image data sets of the corresponding anatomy.
A special feature of OMEGA is the open structure prepared for implementation of further analysis algorithms and new techniques of visualization.
When clinical measurements are considered there is a need to observe a large number of patients and thus short measurement time, fast data analysis and large storage capability. A validation of the results of magnetocardio-graphy at a clinical level, allowing a clinical routine use of MCG in the contest of clinical work in cardiology is on the way. A clinical system has to perform a standard MCG measurement within a global time of about 15 minutes per patient, leading to a possible throughput of 30 patients per day. The results of the study on more than 100 subjects to iteratively improve the measurement protocol and the system logistic have shown that these performances are realistic for the Argos 55 system. Of course, for a clinical validation the analysis routines have to be tested on a large data base.

References

[1] Erné, S.N., Müller H.-P. Magnetocardiographic technology: state of the art, Proceedings of 8th International Congress on Holter and Noninvasive Electrocardiology, ISHNE98, Ulm, Germany, 1998.
[2] Pasquarelli, A., Kammrath, H., Tenner, U. and Erné, S.N. The new Ulm magnetic shielded room, Proceedings of BIOMAG98, Sendai, Japan, 1998.
[3] Martin, K., Erné, S.N., Law, C., Mallick, J., Tatar, B., Multiple modality biomagnetic analysis system, 10th International Conference on Biomagnetism, BIOMAG '96, Santa Fe, USA, 1996.
[4] Tenner, U., Kammrath, H., Erné, S.N., OMEGA Open Magnetic and Electric Graphic Analysis, 8th International Congress on Holter and Noninvasive Electrocardiology, ISHNE98, Ulm, Germany, 1998.
[5] Del Gratta, C., Erné, S.N., Edrich, J. A Linear iterative algorithm for dipole localization. In Baumgartner, C., et al., Biomagnetism: Fundamental research and Clinical Applications, Elsevier Science, 1995.
[6] Nenonen, J.T., Hämäläinen, M.S., Ilmoniemi, R.S., Minimum-norm estimation in a boundary-element torso model, Medical & Biol. Engineering & Computing, 43-48, 1994.
[7] Brauer, H., Kosch, O., Tenner, U., Arlt, A., A modified linear estimation approach for solving biomagnetic inverse problems. IEEE Transactions on Magnetics, 32, 1298-1301, 1996.
[8] Tikhonov, A.N., Arsenin, V.Y., Solutions of Ill-possed Problems, New York, Wiley, 1977.

Topographic Presentation of the Dipolar Content of Cardiac Electric Field

Bacharova L.[1], Chorvat D. [1], Mateasik A. [1], Titomir L.I. [2]

[1]International Laser Center, Bratislava, Slovakia
[2]Institute of Problems of Information Transmission RAS, Moscow, Russia

Introduction

The electrocardiographic signal provides the unique information about the status and activity of the heart, as a generator of cardio-electric field. In current clinical practice, it is mostly registered by the means of a standard 12-lead system and presented as scalar electrocardiograms. However, the information obtained in this way is characterized by a considerable redundancy, and the conceptual model used for the interpretation is complicated.

The advantage of physically corrected orthogonal leads is the biophysically based approach and a relatively small volume of input data, allowing meaningful mathematical treatment. An important prerequisite for optimal evaluation is their proper mathematical treatment and adequate graphic representation.

The aim of this study was demonstrate a biomathematical model for the topographic presentation of orthogonal electrocardiograms and to present reference values of dipolar electrocardiograms of ventricular depolarization.

Method

In dipolar electrocardiotopography (DECARTO), orthogonal ECG signals are transformed by means of a simple mathematical model to represent the equivalent generator of the cardiac electric field as a uniform double layer with time varying size and location on a spherical surface approximating the ventricular wall, called the image sphere (Figure 1) [1]. Ventricular activation is represented by time series of maps of activated points on the image surface. More compact, but also easily perceived visualization of the same data may be obtained in the form of summary maps of cardiac excitation, or chronotopocardiograms. Decartograms can be presented in a form of discrete spherical image surface in a shape of rectangle, other planar projection of sphere, or in 3D visualization, including animation of activated areas on the image surface (Figure 2).

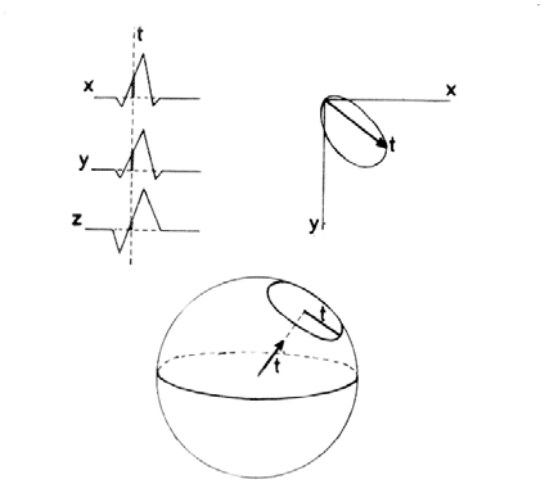

Figure 1: Top left: Scheme of x, y, z signals of orthogonal electrocardiograms. Thick lines represents the scalar components of the instantaneous spatial vectorcardiographic QRS vector in time t. Top right: Scheme of a frontal plane vectorcardiographic loop; the arrow represents an instantaneous vector in time t. Bottom: Construction of area of activated points on the spherical image surface.

The reference values fot topographic presentation of orthogonal electrocardiogram were calculated from a sample of healthy population (total number 123 subjects, 54 women, 69 men). Presented data are for the Frank orthogonal electrocardiogram. Decartograms are presented in the form of a rectangle (matrix of 11 lines, 24 columns). For each point of this matrix the value of relative frequency (probability) of its occurrence in activated state is given in a sample of healthy population.

Results

Figure 3 shows areas of activation with $p > 0.05$ probability and with maximum probability on instantaneous decartocardiotopograms.

a)

b)

c)

d)

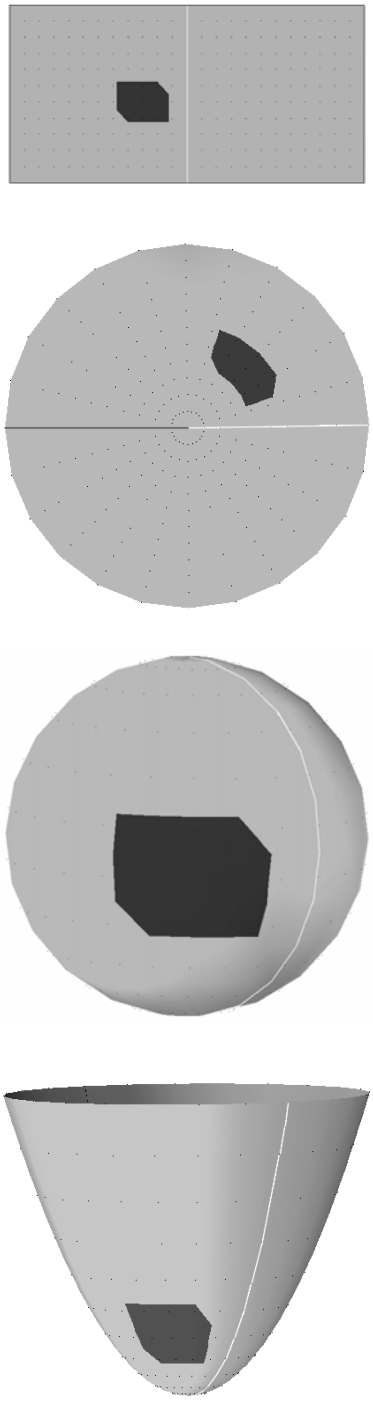

Figure 2: Examples of decarto projections and visualizations: a) rectangular projection, b) azimuthal equidistance projection, a view from the apex, c) spherical image surface, d) paraboloidal image surface.

An ordinary set of discrete elements (points) on the image surface may be treated as consisting of two fuzzy subsets at any instant time, those of activated and those of non-activated elements [2]. If each element of the reference spherical surface is attributed the probability of being activated at a given instant of time as its characteristic membership functions, we obtain the reference fuzzy subset of activated elements at time t. The cardiac electric activity of a subject may then be expressed as a time series of fuzzy subsets, each representing the activated elements of the spherical image surface at a predetermined instant of time with membership functions obtained from the reference fuzzy subsets. After having computed individual sums of membership functions in our reference sample for each 10^{th} milliseconds of QRS duration, we may define the criteria of normality in terms of fuzzy mathematics.

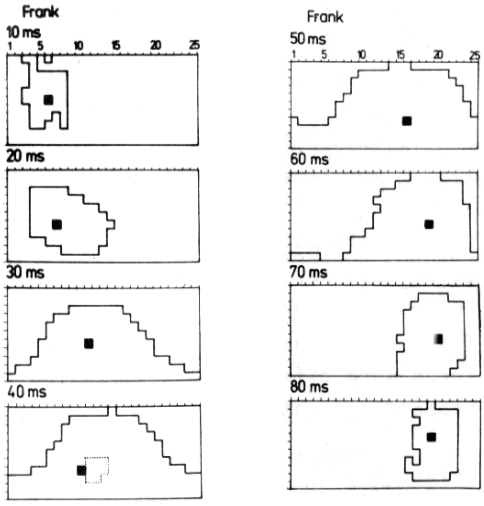

Figure 3: Areas of activated points on the spherical image surface with p > 0.05 probability (empty) and with maximum probability (black) during QRS complex from 10 ms to 80 ms, obtained for Frank lead system in healthy subjects. Each point on the sphere is represented by a square on the rectangular surface. Lateral borders: right mid-axillary line, 1 – 12 anterior, 13 – 25 posterior hemisphere.

Discussion

A sample of 123 healthy subjects originally included in the study of normal vectorcardiographic variability [3] served for constructing probability topograms of the activation sequence represented on a spherical image surface [4]. The localization of areas of activation with p > 0.05 probability was in good agreement with the localization of positive potential distribution on body surface potential mapping in a healthy subject [5]. Areas of maximum probability moved during ventricular depolarization from the right paramedial mid-area to the left, downwards and posteriorly. This movement is in good agreement with the myocardial activation sequence as represented by the spatial vectorcardiogram, as well as with the experimental data on the current field measured in the close vicinity of the isolated dog heart [6].

Medical diagnostics is decision making in fuzzy environment and so fuzzy sets help to handle our data in mathematical modeling, as well as in diagnostic utilization of the changes of cardiac electric field.
Visualization of physically corrected orthogonal ECG lead signals as vectorcardiographic loops and determination of the spatial localization of instantaneous vector end-points enable the physician to find the bridge in his conceptual model between characteristics of myocardial activation propagation and abstract representation of the cardiac electric field. Treatment of the same signals as dipolar electrocardiotopograms aids in finding topographical relations between body surface electrical events and the activation process in the myocardium. This approach aids also in understanding and analysis of body surface potential maps obtained by separate procedures.
In conclusion, decartocardiograms visualize the sequence of activation and a sequence of activated points on a spherical surface closely enveloping the heart. The localization of the activated areas determined by spatial orientation of the vector, and the extend of the activated area at given instant of time is proportional to the module of the vector related to the maximum spatial vector magnitude. Decomposition of the information about the spatial localization of a vector end-point into the area of defined localization and size makes it possible to use advanced mathematical methods, which is especially important in the evaluation of normal and borderline pathological findings.

References:

[1] Titomir, L.I., Ruttkay-Nedecky,I.: Chronotopocardiography: A new method for presentation of orthogonal electrocardiograms and vectorcardiograms. Int J Bio-Medical Computing, 1987, 20: 275 – 282.

[2] Rutkay-Nedecky, I.: Decision making in boundary problems of computerized electrocardiology using fuzzy sets. In: Computers in Cardiology, Los Alamitos, California, IEEE Computer Society Press, 1992.

[3] Bacharova, L., Melotova, J.: Reference areas of the localization of QRS instantaneous vector end-points in Frank lead systém for computerized evaluation. Bratisl. Lek. Listy 1986: 86: 603 – 611 (In Slovak).

[4] Bacharova, L., Melotova, J., Ruttkay-Nedecky, I.: Reference values of dipolar electrocardiotopogram of QRS complex. Bratisl. Lek.Listy 1991: 92, 402 – 409. (In Slovak)

[5] Taccardi, B.: Distribution on heart potentials on the thoracic surface of normal human subjects. Circ. Res. 1963: 12, 341 – 352.

[6] Taccardi, B., Musso, E., De Ambroggi, L.: Current and potential distribution around an isolated dog heart. In: Rijlant, P., Ruttkay-Nedecky, I., Schubert, E. (eds.): The electric field of the heart, Bruxelles, Presses Academiques Europeennes, 1972.

Functional Mapping of Speech Evoked Brain Activity by Magnetoencephalography and its Clinical Application

Möller M.[1], Kober H.[2], Ganslandt, O.[1], Nimsky, Ch.[1], Vieth J.B.[2], and Fahlbusch, R.[1]

[1]Department of Neurosurgery, University of Erlangen–Nürnberg, Erlangen, Germany
[2]Biomagnetism Group, University of Erlangen–Nürnberg, Erlangen, Germany

Introduction

Magnetoencephalography (MEG) is a new tool able to investigate sources of brain activity with high spatial and temporal resolution which allows to evaluate even higher cognitive functions like speech processing [3,7,12]. In this study we tried to investigate the time course of cortex activation of speech processing and to localize their sources in a first step. Secondly we wanted to make these localizations available for clinical application. Functional mapping of speech eloquent areas is of high value for patients with brain tumors adjacent to the sensory (Wernicke) or the motor speech area (Broca) as they bear a high risk of postoperative speech deficits. To identify the speech dominant hemisphere still the invasive Wada test [13] is necessary. Functional mapping of eloquent areas is realized by intraoperative corticography in local anesthesia in some centers [10]. In recent years first results of noninvasive methods based on different physiologic mechanisms like MEG [3,7,12], fMRI [1,14,15] and PET [8,15] for mapping speech relevant areas and determining the speech dominant hemisphere were presented. Our aim was to preoperatively identify the speech dominant hemisphere and localize the speech relevant brain areas noninvasively by means of MEG. According to surgery of tumors in the central region by functional neuronavigation [2,5] in our department we wanted to make the MEG localizations intraoperatively available for the surgeon by displaying the Broca or Wernicke area in the operation microscope.

Method

We investigated 11 healthy subjects (9 male, 2 female, age range between 20 and 35 years) and 16 patients (13 male, 3 female, between 10 and 69 years) with brain tumors adjacent to the Wernicke or Broca area. 12 patients suffered from permanent or incidental speech disorders during seizures. All subjects and 14 patients revealed right handedness, two patients were clearly left handed, tested by the Edinburgh Handedness Inventory [6]. Measurements were performed simultaneously over both hemispheres with a 2x37 channel biomagnetic system (Magnes II, Bti, USA) in a magnetically shielded dark room. To prevent movement artifacts we embedded the subjects in a vacuum cushion. During the data acquisition we visually displayed meaningful pictograms on a screen in the first measurement. The subjects task was to name the pictograms silently in the mind. In a second measurement monosyllabic words were presented which the subject had to read silently. About 300 meaningful stimuli were randomized with 150 meaningless stimuli displayed for 800 ms with an interstimulus interval of 2531 ms and a variation of 500 ms. Eye movements and the ECG signal were simultaneously monitored. Motion and eye movement artifacts were manually removed. The recorded data was digitally notch-filtered at 50 Hz. To enhance the speech-relevant magnetic signals the averaged meaningless data set was subtracted from the meaningful [3]. Latencies showing a clear single dipole were manually selected separately for each averaged data set. For source localization we used the single dipole model as well as the current localization by spatial filtering (CLSF) [11] which is able to resolve multiple at one moment simultaneously active sources. We calculated a laterality index (LI) taking the strength (S) of speech activated sources between left and right cortex activation into account to determine the speech dominant hemisphere individually for each patient:

$$LI = (\text{left } S - \text{right } S) / (\text{left } S + \text{right } S)$$

Positive LI values indicate left, negative values right hemisphere dominance. MEG results were superimposed on individual MR images by a contour fit program [4]. The MEG localizations of the Wernicke or Broca area were intraoperatively displayed in the microscope eye pieces of a neuronavigation system (MKM, Zeiss, Germany) in three patients up to now.

Results

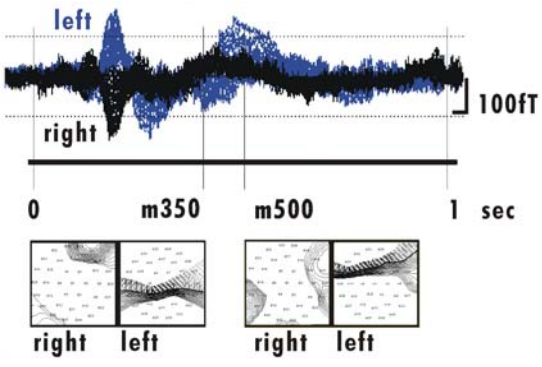

Figure l: Averaged data set of 2x37 channels over the right (black) and the left (gray) hemisphere showing the time course for 1 sec after onset of meaningful stimuli. The maps show a clear single dipole pattern in the left but no dipole in the right hemisphere for both selected latencies of 350 ms and 500 ms.

The analysis of the time course of cortex activation showed a first strong response after 150 ms in both hemispheres caused by activation of the visual cortex. We also found early activation in the right fusiform gyrus at 170 ms. The first strong speech related temporal response could be found at a latency of around 350 ms after stimulus onset which could be localized in the posterior part of the left superior temporal gyrus and supramarginal gyrus, the sensory speech area (Wernicke). At a latency of around 500 ms a second source was activated which could be localized in the left inferior frontal gyrus, the motor speech area (Broca).

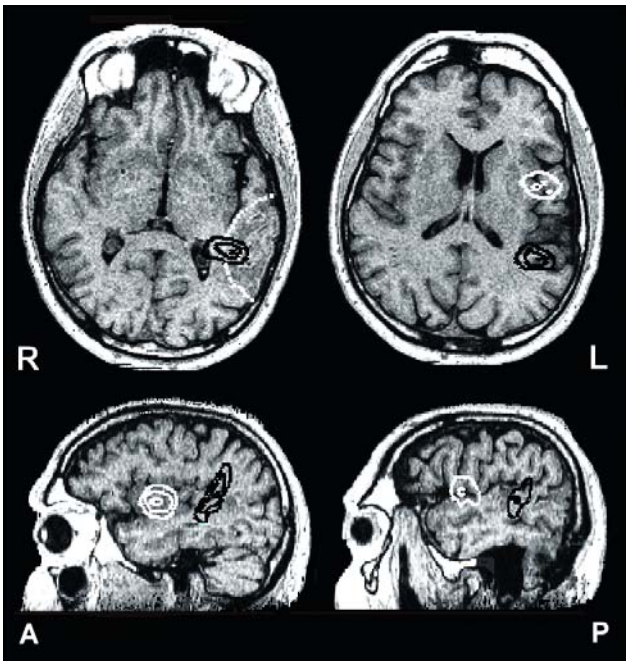

Figure 2: Patient (khd, male, 45 years old) with a left temporal glioblastoma grade IV (WHO) (segmented with white dots). Localization of sources of m350 in the posterior part of left superior temporal gyrus (Wernicke) and m500 in the left inferior frontal gyrus (Broca).

We also found right side activation of the posterior temporal lobe and the inferior frontal gyrus whereas these sources were not as strong as those in the left hemisphere. Further activity could mainly be located in the left inferior temporal gyrus, in the left superior frontal gyrus and insula. In all subjects and in 15 of 16 patients the left Wernicke area was clearly identified, the Broca area could be located in the left hemisphere in 10 subjects and in 12 patients. The laterality index of Wernicke and Broca signal intensity identified speech dominance in the left hemisphere in all investigated subjects and in 15 patients. 12 patients underwent tumor surgery, in three patients MEG localizations were displayed together with the tumor contour in the neuronavigation system and used as intraoperative landmarks. Postoperatively no patient suffered from an increase of preoperatively existing speech impairment.

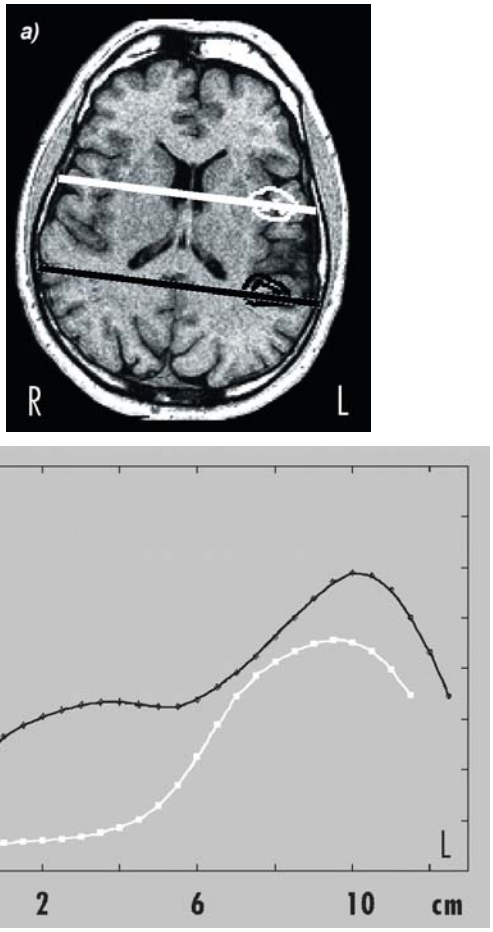

Figure 3a,b: Patient (khd): a) Source intensity measured along a line between right and left hemisphere crossing the Wernicke (black bar) and the Broca (white bar) area demonstrated in a graph b) showing clear dominance of the left hemisphere for sources of Wernicke (black line) and Broca (white line) with a laterality index of +0,9.

Discussion

Functional mapping of speech related brain areas by MEG is a completely noninvasive method and seems to be a fast and accurate tool to investigate both the time course and the localization of sources of cortex activation during speech processing. In neurosurgical application these localizations can preoperatively help estimating the risk of postoperative speech disorder in patients with brain tumors in the vicinity of speech eloquent areas and the surgical approach can be planned in a better way. Future studies are necessary to validate MEG localizations by comparison with alternative modalities as fMRI and PET – which do not directly reflect neuronal activity like MEG but indirectly show blood flow and metabolite consumption differences between activation and rest conditions - as well as with direct cortical stimulation. This invasive and burdening procedure cannot unequivocally localize the Wernicke and Broca area because the stimulation of a variety of cortex areas may lead to speech arrest [9]. By comparing the strength of activation of MEG

located sources of the left and the right hemisphere the hemispheric dominance can be determined. Investigation of a greater number of subjects should result in findings similar to that of Wada [13] describing that in 96% of the right handed and in 70% of the left handed humans the speech dominance is located left hemispheric. In patients the MEG results also have to be confirmed by the invasive Wada test results in future investigations. The intraoperative use of MEG localizations in a neuronavigation system can support the orientation in the operation field. Tumors can be resected more radically without damaging the intraoperatively displayed speech related areas which reduces the risk of postoperative speech disorders.

References

[1] Frost, J.A., Binder, J.R., Springer, J.A., Hammeke, T.A., Bellgowan, P.S.F., Rao, S.M. and Cox, R.W. Language processing is strongly left lateralized in both sexes. Evidence from functional MRI, Brain, 1999,122: 199-208.

[2] Ganslandt, O., Fahlbusch, R., Nimsky, Ch., Kober, H., Möller, M., Steinmeier, R., Romstöck, J., and Vieth J. Functional neuronavigation with magnetoencephalography: outcome in 50 patients with lesions around the motor cortex, Neurosurgical Focus, 1999,6: Article 3.

[3] Kamada, K., Kober, K., Saguer, M., Möller, M., Kaltenhäuser, M., and Vieth, J. Responses to silent *kanji* reading of the native japanese and german in task subtraction magnetoencephalography, Cognitive Brain Research, 1998,7: 89-98.

[4] Kober, K., Grummich, P., and Vieth, J. Fit of the digitized head surface with the surface, reconstructed from MRI-Tomography. In: Baumgartner, C., Deeke, L., Stroink, G., and Williamson, S.J. Biomagnetism: Fundamental Research and Clinical Applications, Amsterdam, Elsevier, 1995, pp 309-312.

[5] Nimsky, Ch., Ganslandt, O., Kober, H., Möller, M., Ulmer, S., Tomandl, B. and Fahlbusch, R. Integration of functional magnetic resonance imaging supported by magnetoencephalography in functional neuronavigation, Neurosurgery, 1999,44: 1249-1256.

[6] Oldfield, E.C. The assessment and analysis of handedness: the Edinburgh inventory, Neuropsychologia, 1971,9: 97-113.

[7] Papanicolaou, A.C., Simos, P.G., Breier, J.I., Zouridakis, G., Willmore, L.J., Wheless, J.W. Constantinou, J.E.C., Maggio, W.W., and Gormley W.B. Magnetoencephalographic mapping of the language-specific cortex, Journal of Neurosurgery, 1999,90: 85-93.

[8] Paulesu, E., Frith, C.D. and Frackowiak, R.S.J. The neural correlates of the verbal component of working memory, Nature, 1993,362: 342-344.

[9] Penfield, W., and Roberts, L. Speech and brain mechanisms, Princeton, Princeton University press, 1959.

[10] Reulen, H.J., Schmid, U.D., Ilmberger, J., Eisner, W. and Bise, K. Tumorchirurgie im Sprachkortex in Lokalanästhesie, Der Nervenarzt, 1997,68: 813-824.

[11] Robinson, S.E. and Rose, D.G. Current source image estimation by spatially filtered MEG. In: Hoke, M., Erné, S.N., Okada, Y.C., and Romani, G.L. Biomagnetism: Clinical Aspects, Amsterdam, Elsevier, 1992, pp 761-765.

[12] Salmelin, R., Hari, R., Lounasmaa, O.V. and Sams, M. Dynamics of brain activation during picture naming, Nature, 1994,368: 463-465.

[13] Wada, J. and Rasmussen, T. Intracarotis injection of sodium amytal for the lateralization of cerebral speech dominance: Experimental and clinical observations, Journal of Neurosurgery 1960,17: 266-282.

[14] Wildgruber, D., Kischka, U., Ackermann, H., Klose, U. and Grodd, W. Dynamic pattern of brain activation during sequencing of word strings evaluated by fMRI, Cognitive Brain Research, 1999,7: 285-294.

[15] Xiong, J., Rao, S., Gao, J.H., Woldorff, M. and Fox, P.T. Evaluation of hemispheric dominance for language using functional MRI: a comparison with positron emission tomography, Human Brain Mapping, 1998,6: 42-58.

Acknowledgements

This study was supported in part financially by the Johannes and Frieda Marohn Foundation (Erlangen, Germany).

Scalp current density (SCD) mapping of cerebral activity during object and space selection in humans

Alberto Zani[1,2], Carmela Avella[1], Stefania Lilli[2], Alice Mado Proverbio[1,2]

[1]Cognitive Electrophysiology Lab, Istituto di Psicologia del CNR, Roma, Italy
[2]Cognitive Electrophysiology Lab, Department of Psychology, University of Trieste, Trieste, Italy

Introduction

Rather recently, the combining of high spatial and temporal resolution characterizing neuroimaging and electrophysiological techniques, respectively, has provided new evidence on the cerebral localization and the timing of attentional processing of visual information [1, 3]. Relatively independent brain mechanisms have been found to subserve the selection of spatial and non-spatial features of visual information, the so called 'dorsal' and 'ventral' streams originally proposed by Mishkin and Ungerleider. From the electrophysiological point of view, the research mostly focused on the possible attentional modulation of the very early stages of sensory processing, and the involvement of striate and/or extra-striate areas of the occipital lobes at this early time of information processing. For long time, it was advanced that the selection of a location in space only had the power to modulate the sensory processing of visual information, as proved by the larger P1 component elicited by the stimuli falling at this relevant location. More recently, however, data have been provided showing that a modulation of early latency components (i.e., PN80, P1, N115) also occurrs during the selection of single objects' non-spatial features, such as spatial frequency and color [4, 5, 2]. At present, not much knowledge is available in literature about the longer latency ERP components reflecting neural mechanisms subserving visual space and object selection beyond the stages of sensory processing. In the present study we investigated neural selection mechanisms for object and space separately by recording event-related potentials (ERPs) of the brain in humans with an relatively high-density electrode montage (i.e., 32 channels) mostly placed at the back of the scalp.

Methods

Subjects

20 college students, 10 females and 10 males (one half in Experiment 1 and the other half in Experiment 2) participated in this study as paid volunteers. All were right handed and had normal or correct-to-normal vision.

Stimuli and procedure

The same stimuli (equiluminant black-and-white gratings presented in the two upper hemifields of the visual display) were presented in two different tasks in which participants had to attend and respond selectively to either one spatial frequency (*object selection*) independent of its location or one location (*space selection*) independent of stimulus spatial frequency.

Participants sat in a sound attenuated and electrically shielded cubicle dimly illuminated. They faced a high resolution TV screen located outside the cubicle. Participants were instructed to maintain fixation on a little cross permanently present in the center of the visual display during stimulation. Two sinusoidal luminance modulated vertical gratings were used as stimuli. At the viewing distance of 114 cm they produced stimulation of 1 and 7 cycles per degree and subtended 2.5° of visual angle. Gratings were randomly and sequentially presented in pattern-onset mode for 80 msec at one of two peripheral locations of the upper visual hemispace centered at 4.5° degree of eccentricity from the vertical meridian and 2.5° above the horizontal meridian. Inter-stimulus interval randomly varied between 800 and 1000 msec. Stimuli were replaced by a gray background which had an equal average luminance to avoid flash stimulation. Stimuli and experimental parameters were kept identical in the two experimental conditions, which varied only for the task requirements. Before each run participants were instructed about the attention condition which consisted in paying covert attention selectively to one particular spatial location independent on stimuli spatial frequency in Experiment 1 or to one particular spatial frequency independent of spatial location in Experiment 2. They were also asked to press a button to the given target with the index finger of the left or right hand thus enabling their reaction times (RT) to be recorded.

EEG recording

The electroencephalogram (EEG) was continuously recorded from 30 scalp sites using tin electrodes mounted in an elastic cap. The electrodes were located at frontal (Fp1, Fp2, FZ, F3, F4, F7, F8), central (CZ, C3, C4), anterior temporal (T3, T4), posterior temporal (T5, T6), parietal (PZ, P3, P4), and occipital (OZ, O1, O2, OL, OR) scalp sites of the International 10-20 System. Additional electrodes were placed at non-standard electrode sites halfway between the standard ones. For example, CP5, CP6 at centro-parietal areas, PO3, POz, PO4 at parieto-occipital areas and IN3, INz, IN4 at Inion inferior lateral occipital areas. Balanced linked ears were used as reference. Horizontal and vertical eye movements were also monitored. EEG and EOG were digitized for 100 msec prior and 600 msec following stimulus onset at a rate of 512 samples /s.

Results

Reaction times (RTs) were about 100 ms faster in the location than the frequency selection task (see Fig. 1).

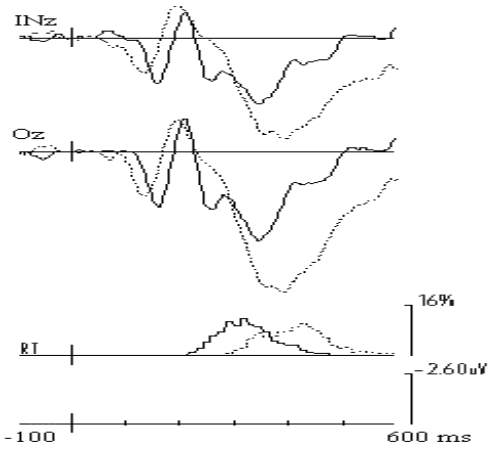

Figure 1. RT distributions and examples of ERPs to relevant stimulation in the object (dashed line) and space (solid line) selection tasks.

Different morphologies characterized ERPs obtained in the two selection modes over the posterior regions of the scalp. ERPs for space selection were characterized by a prominent Pl peaking at about 140 msec, followed by a tiny N1 and a very early P300 component (see Figure 2). Conversely, ERPs for object selection showed an early PN80 deflection followed by a prominent selection negativity (SN) and a delayed late positive component (LPC) (see Figure 3).

Consistent with previous studies, attention modulation showed early attention effects in both types of selection mechanisms. In particular, in the spatial location task, attention modulated Pl amplitude as early as 100 ms at extra-striate sites (see figure 2) [5], as shown by scalp current density (SCD) maps, whereas in the frequency selection task, attention modulation started as early as 60-80 msec at both striate and extra-striate areas (see figure 3) [4].

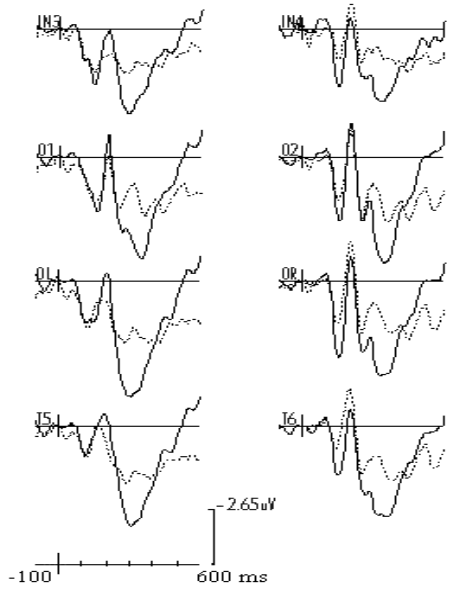

Figure 2. Examples of grand-average ERPs to space relevant (solid line) and irrelevant (dashed line) 7 cpd RVF stimuli recorded at back electrode sites.

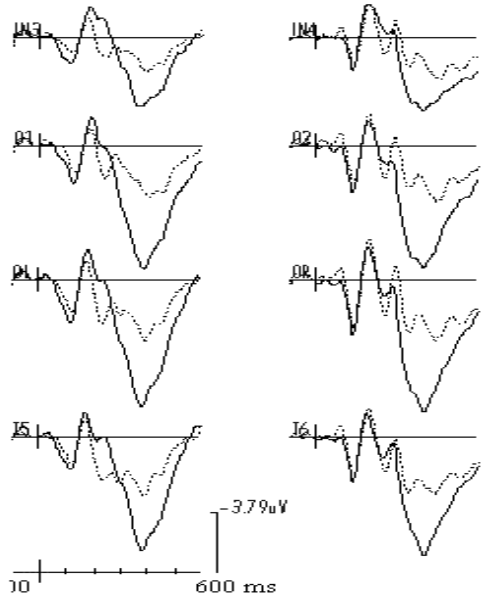

Figure 3. Examples of grand-average ERPs to object relevant (solid line) and irrelevant (dashed line) 7 cpd stimuli falling at the RVF recorded at back electrode sites.

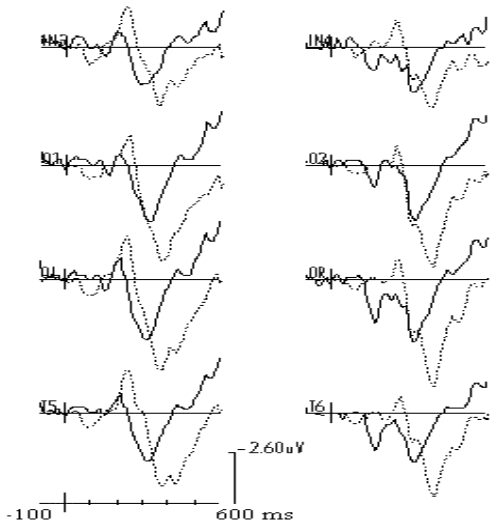

Figure 4. Examples of difference waves for space (solid line) and object (dashed line) selection at some electrodes of the back scalp.

These effects can be observed clearly in the difference waves shown in figure 4. Spatio-temporal SCD mapping of the difference waves in the P1-PN80 range for the two attention modes showed topographies centered at lateral-occipital sites (extra-striate areas) for space selection, and at mesial-occipital, posterior-temporal, and parietal-occipital sites (striate and extra-striate areas) for object selection, as shown in figure 5. SCD mapping in the SN latency range for object selection showed a neat focus centered at the inferior-lateral-occipital electrode sites at Inion level (IN3/IN4) pro-

gressively shifting in time toward the lateral-occipital (OL/OR) and posterior-temporal (T5/T6) locations (see Figure 5). Conversely, in the same latency range SCD maps for space selection showed the beginning of the LPC centered at the same sites as for the object selection (see again Figure 4).

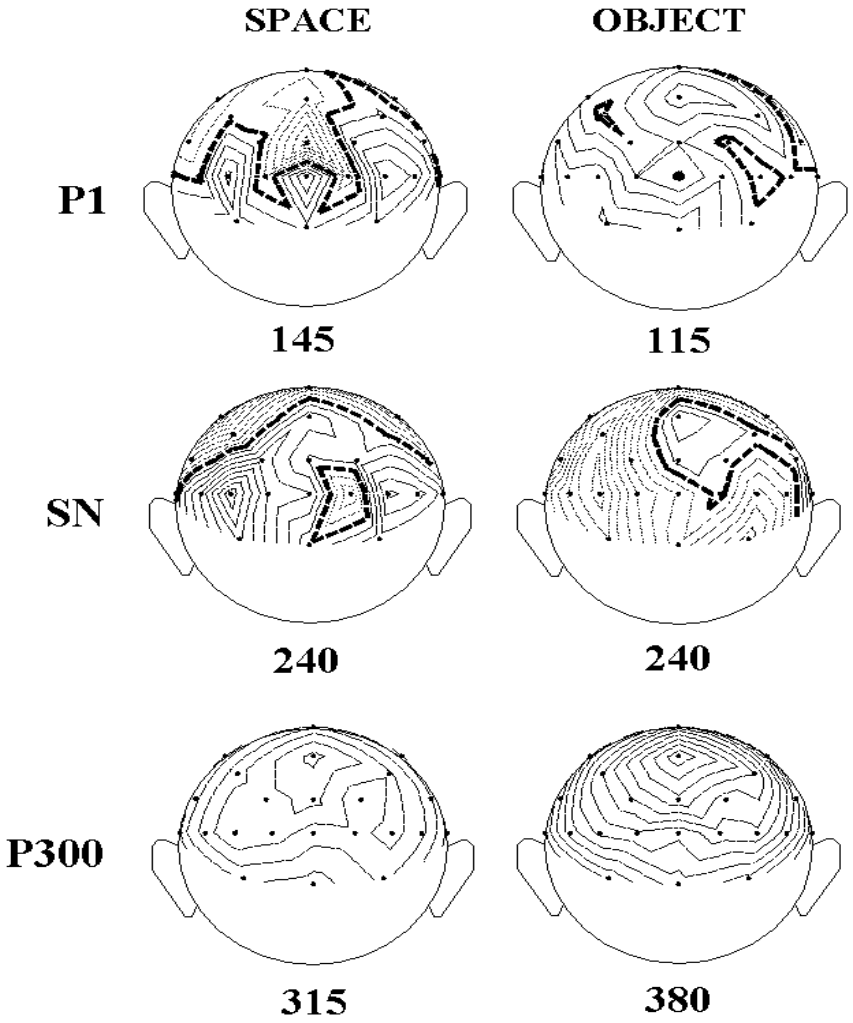

Figure 5. SCD maps of brain activity as a function of space and object selection at the P1, and SN peak latencies in the difference waves obtained subctracting the irrelevant from the relevant condition. The thin solid and dotted lines reflect a positive and negative current density, respectively, whereas the thick solid lines reflect the zero level. A same scale, varying in steps of ± 18,285 uV/m^2, was used for both attention conditions. For the P300 peaks isocontour voltage maps are displayed. A same scale, varying in steps of ± 18,285 uV, was used for both attention conditions.

Discussion

The present findings further support the view of two anatomically and functionally relatively distinct neural mechanisms for space and object selection. As a whole, these mechanisms seem to be related to the activation of the "dorsal" and "ventral" streams of neural information processing. When engaged in the separate selection of a
space location or a stimulus object, the brain independently activates one of the two specifically localized systems. In both kinds of selection, the data suggest that this activation already occurs at early sensory processing stages. However, during object selection attentional modulation occurs at an earlier latency level than during space selection.

The present findings are somewhat different from those obtained during a space and object feature-conjunction selection task where it was found that the selection of an object within a space location was carried out in parallel but not independently from one another [e.g., 5]. A finding that was consistent with the view of a so called "object-based space selection" advanced on the

basis of recent findings in studies founded on single units intra-cerebral recordings in monkeys.
Overall, the present findings strongly support the view that the early latency modulation of neural processing mechanisms might be task-specific. When separate spatial and non-spatial features selection is required, these systems may be activated separately and independently from one another. Conversely, when a conjoined selection is demanded in an attentional task, they are both activated in parallel. The data also support the view [4, 5] that this parallel activation is not simply additive in nature but reflect complex interactions between these independent neural attentional systems.
As for the longer latency processing, our findings suggest that object selection is more source demanding than location selection. This might be reflected by the elicitation of a prominent SN in the former selection mode. SCD maps also showed that this more demanding processing might be carried out by extra-striate areas of the occipital lobes of the brain.
That object selection may be more source demanding than space selection was also strongly suggested by our findings at later stages of visual information processing. Indeed, our data showed a much larger and later LPC for object than location selection. Notwithstanding this difference in the timing and the entity of brain activation at this stage of processing, SCD mapping indicated that there might be no differences in the topography of brain activation in the two selection modes.

References

[1] Cabeza, R., and Nyberg, L., Imaging cognition: An empirical review of PET studies with normal subjects, J. NCogn. Neurosci., 9: 1-26.

[2] Heinze, H.J., Mangun, G.R., et al., Combined spatial and temporal imaging of brain activity during visual selective attention in humans, Nature, 1994, 372:543-546.

[3] Hillyard, S.A., and Anllo-Vento, L., Event-related potentials in the study of visual selective attention, Proc. Nat. Acad. Sci. USA, 1998, 95: 781-787.

[4] Zani, A. and Proverbio, A.M. ERP signs of early selective attention effects to check size, EEG Clin. Neurophysiol., 1995, 95: 277-292.

[5] Zani, A. and Proverbio, A.M., Attention modulation of early components of ERPs to lateralized gratings in the upper and lower visual quadrants, J. Psychophysiol.,1997, 11: 21-32.

Acknowledgements

The present study was supported by a grant of the Biological and Medical Sciences Board of CNR to Alberto Zani.

Spatio-temporal mapping of electrocortical activity during selective processing of colour and shape in humans

Alice Mado Proverbio[1,2], Fabiana Burco[1], Alberto Zani[1,2]

[1]Cognitive Electrophysiology Lab, Department of Psychology, University of Trieste, Trieste, Italy
[2]Cognitive Electrophysiology Lab, Istituto di Psicologia del CNR, Roma, Italy

Introduction

High spatial resolution neuroimaging techniques have indicated that different brain regions are activated during selective processing of shape and/or colour: i.e., bilateral temporal regions (areas 22) parietal region (area 39), left dorsal occipital region (area 18) and bilateral parahippocampal regions for the former, and bilateral occipital regions (areas 18 and 19) for the latter [1,2]. Studies of selection of colour or combinations of colour and other features (e.g., check size [3], orientation [4]) with high temporal resolution event-related potentials (ERPs) have indicated the timing of colour selective modulation, starting as early as 100 msec post-stimulus in form of a P130, continuing with a prominent selection negativity (SN) and a broadly distributed P300. This is consistent with the view of early selection effects for non-spatial stimulus features [5]. Dipole modelling analysis applied to the high-resolution electrode montage localised the sources of the early P130 and SN at the dorsolateral occipital and ventral occipital (close to the collateral sulcus) regions [3], respectively, consistently with neuroimaging findings.
In the present study, we further investigated colour selective processing indirectly tapping at the conjoined selection of colours and objects by introducing "prototypical" and "non-prototypical" objects and animals. This was done from an ecological point of view.

Methods

Subjects
Eight college students (4 females and 4 males) ranging in age from 18 to 24 years participated in this study as paid volunteers. All were right handed as attested by a self-report laterality questionnaire, had a right eye dominance and a normal or correct-to-normal vision. None of them were familiar with the purpose of the investigation.

Stimuli and procedure
ERPs were recorded from the scalp of healthy young volunteers who viewed and selectively attended different sorts of pictures of familiar objects and animals presented in different colours (a 'prototypical' one - e.g., a green crocodile - and other samples of the same shape in different colours - e.g., pink and blue crocodiles) in the central visual field of a PC monitor. Volunteers had to select and respond to the pictures either on the basis of the colour (*colour selection*) independent of their shape, or on the basis of the shape represented (*object selection*) independent of its colour. They were instructed to push a button as fast and accurately as possible to targets appearance with the index fingers of the left or right hand, thus allowing reaction times (RTs) to be recorded.

EEG recording
EEG was continuously recorded with a 32 channel montage using tin electrodes mounted in an elastic cap. Electrode impedance was kept below 5 KOhm. Linked earlobe served as reference lead. To ensure that fixation was maintained the horizontal and vertical oculogram (EOG) was also monitored. The EEG and the EOG were amplified with a half-amplitude band pass of 0.1-70 Hz and 0.01-70 Hz, respectively. Grand-average ERPs were separately computed for the various attention conditions and tasks. Before averaging a computerised artefact rejection and baseline correction procedure were performed. RT values, as well as latency and amplitude measures of the major ERPs component were analysed by means of multifactorial repeated-measures ANOVAs.

Results

RTs to targets were faster in the colour than the object selection task (389 vs. 407 msec), although hits percentage (about 99%) did not differ in the two conditions. Furthermore, false alarm rate was significantly greater when stimuli were shown in the prototypical object or shape, thus suggesting a strict interaction between the processing mechanisms of the two features.

In agreement with behavioural data, ERP results indicated that selection of the two dimensions occurred in parallel but not independently of one another, and affected the amplitude of the occipital-temporal P1 (P110), N1 (N166) and SN (N278) components, and the central-parietal P300 one (see Figure 1 and Figure 2).

Overall, object selection produced larger and later N2 and P300 components, as opposed to colour selection. Very interestingly, Selection Negativity responses to colour selection were significantly affected by object content but not viceversa. More specifically, when engaged in selecting a colour (e.g., green) and a shape (object or animal) was displayed that "prototypically" had that colour in nature (e. g., a green crocodile), volunteers' SN responses resulted signficantly larger than when the shape presented was not "prototypical" in that colour (e.g., a green lamb) specially over the left hemisphere (see Figure 1).

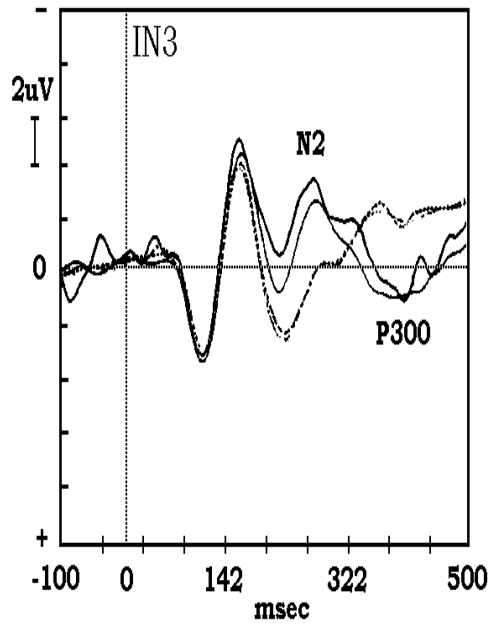

Figure 1. Grand-average ERPs to target (solid line) and non-target stimuli (dashed line) recorded at left inion site (IN3). ERPs to pictures displayed in the prototypical colour (thick lines) showed a much larger N2 component.

Spatio-temporal mapping revealed that for colour selection SN displayed two foci bilaterally centred at ventral mesial- and lateral-occipital sites (IN1, IN3 and IN2, IN4), whereas for shape selection this component was more diffusely bilaterally distributed at ventral (IN1, IN3, and IN2, IN4) and dorsal mesial- and lateral-occipital, and posterior temporal sites (O1, OL, T5, and O2, OR, T6).

Figure 3 shows scalp distribution of N278 component to targets in the two attend-colour and attend-object experimental conditions. It can be noted that the negative occipital deflection was much larger to object than colour targets, especially over the left hemisphere.

The P300 component, which was much larger to target than non-target pictures, had also a different generator in the attend-object compared to the attend-colour condition. Indeed, the positive focus was stronger and more anteriorly distributed when pictures had to be selected on the basis of their shape rather than colour, probably suggesting that this condition was more source demanding or needed more voluntary control (see maps of Figure 3.)

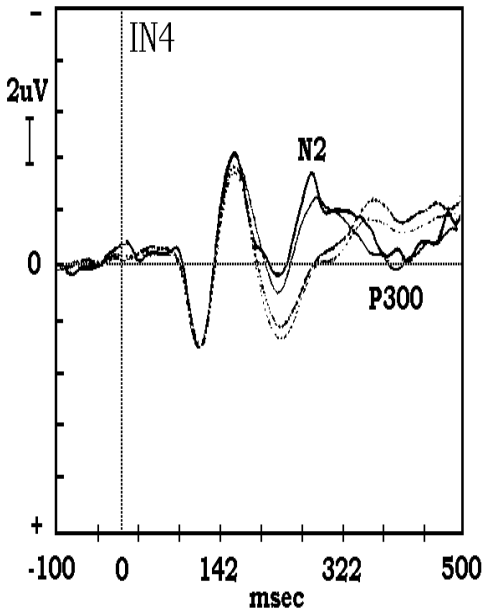

Figure 2. Grand-average ERPs to target (solid line) and non-target stimuli (dashed line) recorded at right inion site (IN4). ERPs to pictures in the prototypical colour are in thick lines, while ERPs to pictures in other colours (universal) are in thin lines.

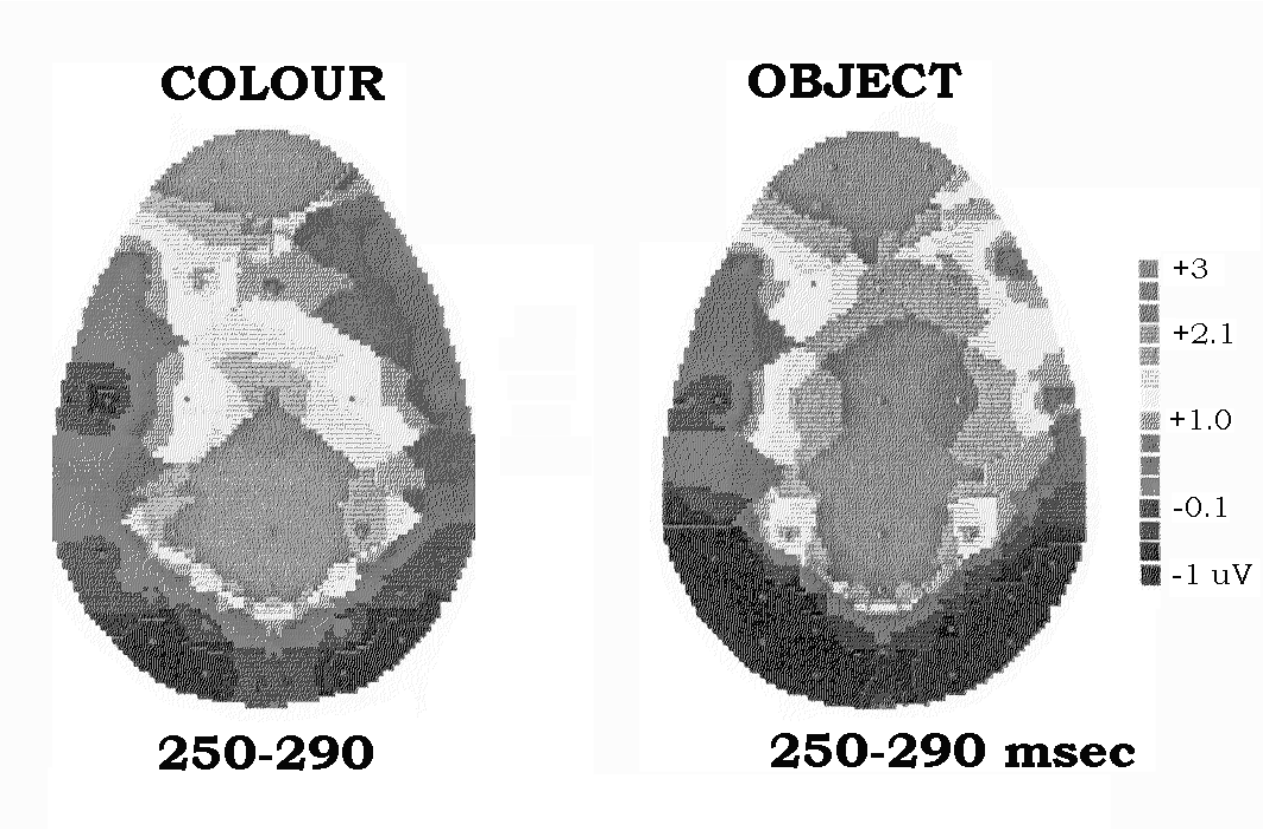

Figure 3. Isocontour voltage maps of brain evoked potentials to targets in the colour (left) and object (right) selective attention tasks. The time window from 250 to 290 msec is in the 'selection negativity' latency range.

Mapping of 'prototypical colour' attentional difference waves (i.e., prototypical minus universal) displayed a large focus centred at ventral lateral-occipital sites in the latency range of the occipital component N278. The focus was mostly asymmetrically spread toward the left hemisphere at posterior temporal and lateral occipital areas (see Figure 4).

Discussion

Both RT and ERP results indicated that the colour dimension is selected faster and easier than the shape dimension [6,7]. However, since the two features were presented in conjunction in the present experiment, we found that the spatial content (shape) of an object might speed up and facilitate the colour-based selection of the same object when the colour was prototypical of that shape, whereas vice versa did not occur. These data suggest a strong interaction between the two mechanisms subserving shape and colour selection.
ERP high density mapping of brain activity indicated that the selection of the colour dimension of familiar pictures (i. e., objects prototypically matched as far as colour and shape) strongly activates posterior temporal and extra-striate areas of the left hemisphere.
Those areas showed to be very sensitive to the so called prototypicity effect, thus providing the possible locus of conjoined colour and shape processing of real objects in human visual cortex.

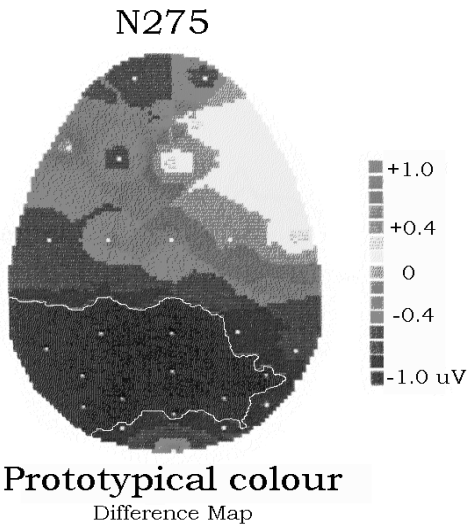

Figure 4. Isocontour voltage maps of brain evoked activity obtained by subtracting the response to targets of all colours (universal) from that to targets displayed in the prototypical colours (prototypical).

References

[1] Corbetta, M., Miezin, F.M., Shulman, G.L., and Petersen, S.E., Attentional modulation of neural processing of shape, colour, and velocity in humans. Science, 1990, 248: 1556-1559.

[2] Proverbio, A.M., Minniti, A. and Zani, A. Electrophysiological evidence of a perceptual precedence of global vs. local visual information. Cognitive Brain Research, 6: 321-334.

[3] Karayanidis, F., and Michie, P.T., Evidence of visual processing negativity with attention to orientation and color in central space. Electroencephalogr Clin Neurophysiol, 1997, 103: 282-297.

[4] Anllo-Vento, L., Luck, S.J., and Hllyard, S.A., Spatio-temporal dynamics of attention to color: Evidence from human electrophysiology. Hum Brain Map, 1998, 6: 216-238.

[5] Zani, A., and Proverbio, A.M., ERP signs of early selective attention effects to check size. Electroencephalogr Clin Neurophysiol, 1995, 95: 277-292.

[6] Hillyard, S.A. and Münte, T. F. Selective attention to colour and location: An analysis with event-related brain potentials. Perception and Psychophysics, 1984, 36(2): 185-198.

[7] Eimer, M. An event-related potential (ERP) study of transient and sustained visual attention to colour and form. Biological Psychology, 1997, 44 (3): 143-160.

Acknowledgements

This research was funded by MURST grants to the Department of Psychology of University of Trieste. We would like to thank Stefania Lilli for her kind support.

Clinical DC applications using MEG: Moving the curtains aside

Bowyer, S.M.

Henry Ford Hospital, Detroit, MI

Direct Current Magnetoencephalography (DC-MEG) is the somewhat misused term describing MEG observations of extremely low frequency phenomena (frequencies below 0.01Hz). "Steady field" is another term used to describe DC changes which occur in the cellular environment over a long period of time [1]. Biomedical data analysis is usually conducted using a variety of filters, band passes, notch filters, and high or low-pass filters. These filters act like curtains, blocking out signals that, until now, have been considered unimportant. The information contained in these signals however, may be useful in the clinical evaluation of a number of neurological disorders such as Migraine [2,3], Epilepsy [4], Stroke [5], TIA [6], Anoxia [7,8], and Nerve and Muscle injury [9]. Modern Electroencephalographic (EEG) recordings are not capable of resolving the DC signal, due to electrode/skin interface noise. Until recently, Electrocorticographic (ECoG) has been the only reliable method for observing extremely slow signals from the brain; however this requires direct contact with the cortical surface. MEG has emerged as an alternative modality capable of observing DC signals arising from the human brain, in a non-invasive manner.

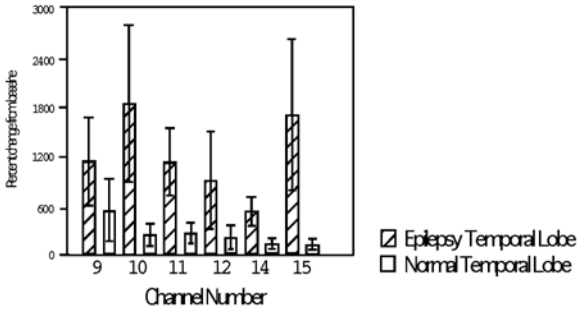

Fig 1. The percent change from baseline in temporal lobe Epilepsy subjects compared to their non-epileptic lobe.

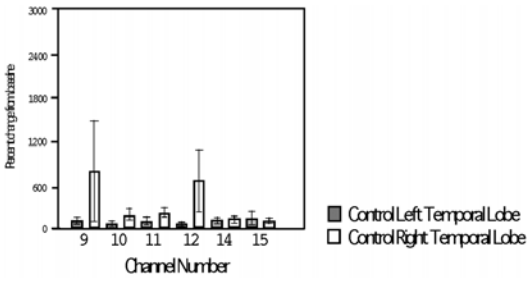

Fig 2. The percent change from baseline in non-epileptic subjects, right temporal lobe compared to their left lobe.

Cohen, in 1969, used the magnetometer to measure the DC fields of the heart using an induction coil near a subject's chest [10]. In 1970 the DC fields from the heart were again measured using a SQUID magnetometer [11]. Cohen described two types of DC fields: normal electrophysiological processes and injury currents. He went on to measure the DC fields of many parts of the body [1]. Curio et al. (1993) found observable DC-MEG signals arising from nerve and muscle injuries [9]. Using rats, Chen et al (1992) detected DC MEG signals arising from ischemia [5], and Takinashi et al (1991), detected DC MEG signals during anoxia [7]. In 1998, in studies of human subjects, both Saligram et al.[4] and Wübbler et al.[12] used changes in position of the subject to extract the DC amplitude of the underlying DC field. Figure 1 shows data acquired, by Saligram et al.[4]. She found the percent change from the baseline in the DC-MEG filed shifts in temporal lobe epilepsy subjects was higher on the epileptic temporal lobe then on the normal temporal lobe and higher then the DC-MEG fields measured in controls.. Figure 2 shows no statistical significance in percent changes from baseline of the DC-MEG fields when comparing the right and left lobes of subjects without epilepsy. The focal DC shifts from Epileptic patients are a result of focal seizures. These studies have all increased our understanding of the DC MEG changes that arising from the cellular environment during epilepsy.

Magnetoencephalography (MEG) has become a non-invasive tool to detect neuroelectrical phenomena related to neurological disturbances, such as migraine [2,3,13]. Our lab has been using DC-MEG since 1987, when KMA Welch predicted that if SCD was the underlying mechanism of migraine, then MEG technology could be used to detect migraine [14]. Spreading Cortical Depression (SCD) is believed to play an important role in the pathogenesis of migraine [2,13,18]. During SCD, hyperexcited neurons in the cortical surface fire and then become electrically silent. This band of hyperexcited neurons propagates across the cortical surface at a rate of 3-7 mm/minute.

At Henry Ford Hospital in conjunction with Oakland University, our group (HFH-OU) has been using a 7-channel Neuromagnetometer, to conduct DC-MEG studies [2,4,5,7,13,15,16,17] for the past 11 years. In migraine patients, data revealed a reduction of spontaneous

EEG and MEG activity during migraine with aura [13]. Gardner-Medwin et al. (1991) measured DC magnetic fields from rabbit cortex in vivo to better understand MEG signals during SCD [17]. Recently we used a micro squid at the VA Hospital in New Mexico to

characterize and compare the MEG signals from a gyrencephalic and a lissencephalic brain during propagation of SCD [19,20]. We found, in these animals, that MEG signals occur when a band of hyperexcited neurons travels into sulci or fissures during an SCD-like event [19,20].

Currently we are using DC-MEG to investigate human migraine subjects. DC-MEG waveforms arising during spontaneous migraine-with-aura and evoked migraine auras were measured. We saw DC-shifts in spontaneous and evoked migraine auras using two different types of SQUID neuromagnetometers, a 7-channel Neuromagnetometer (BTi model 607) which utilized Gradiometers and 148-channel Neuromagnetometer (BTi Magnes 2500WH) equipped with Magnetometers. These signals were consistent with those expected to arise during the propagation of an underlying hyperexcited wave, such as those observed during SCD induced in animal models. These DC-MEG shifts were not seen in the controls. The MEG field patterns seen in the evoked data were of similar morphology to those observed in the spontaneous data and we interpreted them as arising from similar underlying electrical activity.

Using IHS criteria for migraine, 14 Migraine patients and 9 Controls (interviewed by neurologist) participated in the study. Neuromagnetic fields were measured during visual stimulation of the occipital cortex from all of these subjects. Six ictal migraine patients were also studied during their spontaneous migraine-with-aura. The magnetic field detectors were placed perpendicular to the occipital cortex, over the inion. Data was collected with the 7-channel neuromagnetometer while visual stimulation was performed on 5 migraine subjects and 3 controls with pattern reversal of a black and red circular checkerboard at 5Hz. Visual stimulation was changed to a black and white circular checkerboard at 8 Hz and performed on 9 migraine subjects and 6 controls in the 148-channel system. The stimulus was changed to increase contrast and to focus on linear neurons. Subjects of the 148-channel system were studied in the supine position with their heads held firmly in place by a plastic head holder. Subjects in the 7-channel system were studied while kneeling forward with their heads held in a support frame. All data was collected at 250 samples per second, band passed at 0-50 Hz. During visual stimulation, data was collected for eighteen minutes from both controls and migraine subjects, whereas data was collected for thirty minutes from migraine subjects experiencing spontaneous aura. Environmental noise was subtracted from the MEG data during post-processing analysis.

Aura was induced in 11 of the 14 migraine subjects and in none of the 9 controls. Subjects indicated that these auras were similar to those they normally experience with their migraine. DC MEG shifts were observed in migraine subjects during evoked Migraine-with-aura. DC MEG shifts were also observed in migraine subjects during spontaneous Migraine-with-aura. No DC MEG shifts were seen in control subjects.

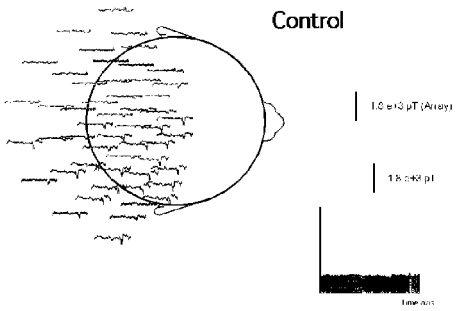

Fig 3. MEG signals from control subject during visual stimulation, acquired with the 148-channel neuromagnetometer system.

Figure 3 displays the occipital MEG channels collected during 300 seconds of visual stimulation from a control subject. Data was collected for 18 minutes and no shifts were seen in the data. Small spikes seen in the data are from patient movement.

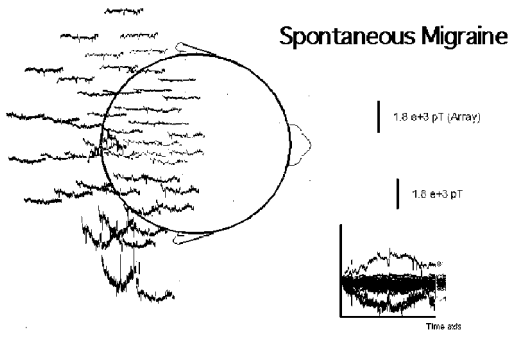

Fig 4. MEG signals from Migraine subject during spontaneous Migraine-with-aura Recorded using the 148-channel neuromagnetometer.

Figure 4 displays 300 seconds of MEG data during a spontaneous Aura over the occipital area. Data collection began approximately 3 minutes after the aura had started. Large amplitude MEG signals were seen arising from the right hemisphere. The large negative component seen in 3 channels and a positive component seen in the channels over the midline indicated that there was neuroelectrical activity occurring under these channels.

Figure 5 displays 300 seconds of DC MEG data collected during a visually evoked migraine aura. The DC MEG shifts can be seen arising from the right occipital cortex. The pattern of DC shifts seen during spontaneous migraine (Fig. 4) is similar to the pattern seen during induced migraine (Fig. 5)

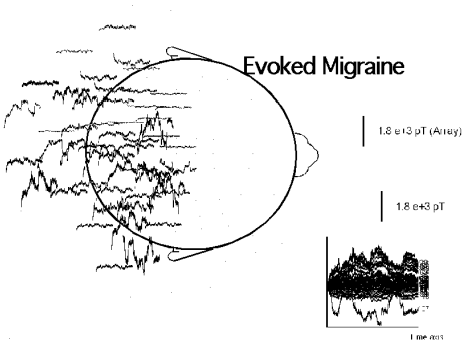

Fig 5. MEG signals during Visual stimulation of a migraine with aura subject.

DC shifts associated with an underlying neuronal disturbance were detectable outside of the cortical environment using non-invasive MEG. A characteristic signature of SCD-like events can be provided using MEG. Amplitude difference between spontaneous and evoked subjects arise due to dissimilar head diameters. Consequently the sensor-to-head distance varies. Complexities in interpreting the MEG signals that arise from an SCD event are due to the propagation patterns giving rise to cancellation of some of the magnetic fields.

The following points are important considerations for future DC MEG applications:

- These experiments increase the potential for using MEG to study the biophysics of migraine. A deeper understanding of the neurological disturbances linked to SCD-like events may be possible.
- Further studies utilizing the larger 148-channel neuromagnetometer array, will help us to obtain a more concise picture of what may be occurring in the cortex of migraine-with-aura patients
- Further analysis and mathematical modeling based on the contours of the cortex reconstructed from MRI scans will help to determine where in the cortex the DC MEG shifts arise.

References

[1] Cohen D : Steady fields of the body. In: Biomagnetism An interdisciplinary approach (SJ Williamson, GL Romani, L. Kaufman, I Modena Editors) Plenum Press: New York. pp. 327-340, 1982.

[2] Welch KMA, D'Andrea G, Tepley N, Barkley GL, Ramadan N : The concept of migraine as a state of central neuronal hyperexcitability. The Neurological Clinics Headache Issue.WB Saunders:Philidelphia, pp 817-82, 1990.

[3] Lauritzen M, Pathophysiology of the migraine aura; the spreading depression theory, Brain 117 (1994) 199-210.

[4] Saligram U, Burdette DE, Barkley GL, Moran JE, Tepley N : Measurement and quantification of interictal and postictal DC magnetic field shifts in unilateral temporal lobe epilepsy. In: Recent Advnaces in Biomagnetism: Proceedings of the 11th International Conference on Biomagnetism, (eds Yoshimoto T, Kotani M, Kuriki S, Karibe H, and Nakasato N) Tohoku University Press:Sendai, 1999.

[5] Chen Q, Chopp M, Chen H, Tepley N : Magnetoen cephaolgraphy of focal ischemia, Stroke 23(9):1299-1303, 1992.

[6] Vieth J, Kober H, Weise E, Daun A, Moeger A, Freidrich S, Pongratz H : Functional 3D localization of cerebrovascular accidents by magnetoencephalography (MEG), Neurology Research1992;14(2Suppl):132-4.

[7] Takanashi Y, Chopp M, Levine SR, Kim J, Moran JE, Tepley N, Chen Q, Barkley GL, Welch KMA: Magnetic fields associated with anoxic depolarisation in anethetized rats, Brain Research, 562:13-16, 1991.

[8] Hansen AJ, Zeuthen T. Extracellular ion concentration during spreading depression and ischemia in the rat brain cortex, Acta Physiol. Scand. 113 (1981) 437-445.

[9] Curio G, Erne SN, Burghoff M, Wolff KD Pilz A: Non-invasive neuromagnetic monitoring of nerve and muscle injury currents, Electroencpehalography and Clinical Neurophysiology 89:154-160, 1993.

[10] Cohen D: Detection and analysis of magnetic fields produced by bioelectric currents in humans. Journal of Applied Physics 40:10446-1048, 1969.

[11] Cohen D, Edelsack EA, and Zimmerman JE : Magneotcardiograms taken inside a shielded room with a superconducting point-contact mangetometer. Applied Physics Letters 16:278-280, 1970.

[12] Wübbeler G, Mackert BM, Armburst F, Burghoff M, Marx P, Curio G, Trahms L : Mesurement of near-DC Biomagnetic Fields of the head usinga horizontal modulation of the body postion. In: Recent Advnaces in Biomagnetism: Proceedings of the 11th International Conference on Biomagnetism, (eds Yoshimoto T, Kotani M, Kuriki S, Karibe H, and Nakasato N) Tohoku University Press:Sendai, 1999.

[13] Barkley GL, Tepley N, Nagel-Leiby S, Moran JE, Simkins RT, Welch KMA. Magnetoencephalograhic Studies of Migraine. Headache 30(7):428-434, 1990.

[14] Welch KMA : Migraine : A biobehavioral disorder. Archives of Neurology 44:323-327 , 1987.

[15] Barkely GL, Moran JE, Takanashi Y, Tepley N : Techniques for DC Magnetoencephaologography, Journal of Clinical Neurophysiology 8(2):189-199, 1991.

[16] Tepley N, Bowyer S, Clifton Y, Saligram U : A technique for sequential measurments of DC neuromagnetic, Electroencephaolgraphy and Clinical Neurophysioliology 99:16-18, 1996.

[17] Gardner-Medwin AR, Tepley N, Barkley GL, Moran J, Nagel Leiby S, Simkins RT, Welch KMA. Magnetic fields associated with spreading depression in anaesthetized rabbits. Brain Res 54Magnetic fields associated with SD: a model for the detection of migraine. Brain Research 442:185-190, 1988.

[19] Bowyer SM, Okada YC, Papuashvili N, Moran JE, Barkley GL, Welch KMA, Tepley N : Currents underlying MEG signals of spreading cortical depression in a rabbit model. In: Recent Advnaces in Biomagnetism: Proceedings of the 11th International Conference on Biomagnetism, (eds Yoshimoto T, Kotani M, Kuriki S, Karibe H, and Nakasato N) Tohoku University Press:Sendai, 1999.

[20] Bowyer SM, Tepley N, Papuashvili N, Kato S, Barkley GL, Welch KMA, Okada YC : Currents underlying MEG signals of spreading cortical depression in swine. In: Recent Advnaces in Biomagnetism: Proceedings of the 11th International Conference on Biomagnetism, (eds Yoshimoto T, Kotani M, Kuriki S, Karibe H, and Nakasato N) Tohoku University Press:Sendai, 1999.

Acknowledgments

Special thanks to Dr. N. Tepley for his help and suggestions with this manuscript. This research supported by NIH/NINDS Grants RO1-NS30914, and P50 NS32399.

Diagnosis of Myocardial Viability Based on Magnetocardiographic Recordings

Nowak H.[1], Leder U. [2], Pohl P.[2], Brauer H.[3], Tenner U.[4], Haueisen J. [1]

[1]JENASENSORIC, Jena, Germany
[2]Clinic of Internal Medicine, University of Jena, Jena, Germany
[3]University of Ilmenau, Ilmenau, Germany
[4]University of Ulm, Ulm, Germany
[5]Biomagnetic Centre, University of Jena, Jena, Germany

Introduction

From the 1960s through the 1970s and the 1980s magnetocardiography data were used predominantly for time domain and signal shape analysis of single leads or non-simultaneously obtained mapping data respectively [1]. This has provided insights into patient risk stratification and prognosis. In the 1990s, however, magnetocardiography began to play an increasingly important role in diagnosing and localising the sources of cardiac magnetic fields. This new application of inverse-solution-based analysis of magnetic fields has become known as Magnetic Source Imaging (MSI). In this respect, the development of source imaging techniques and multisensor devices [2] is advantageously interdependent.
Therefore, magnetocardiography developed as a new experimental discipline of functional imaging. The discipline has moved from no-model signal analysis to a broad emphasis on the functional localisation of cardiac electrical activity and characterisation of patients with known disease [3, 4]. Since that time, the application of new techniques of data analysis has evolved progressively, while the clinical relevance of currently available procedures is being assessed on an ongoing basis [5].
In this paper, following a brief introductory review from the clinical point of view, the major techniques of MSI of distributed cardiac electrical activity used in routine application at the Biomagnetic Centre Jena will be presented and discussed.

Coronary artery disease
Ischemic heart disease is usually due to obstruction of the coronary arteries, which in turn most commonly results from artherosclerosis. The importance of coronary artery disease in contemporary society is attested by the almost epidemic number of persons afflicted. It causes more deaths, disability, and economic loss in industrialised nations than any other group of diseases.
Myocardial infarctions may be divided into two major types: transmural infarcts, in which myocardial necrosis involves the full thickness of the ventricular wall, and subendocardial (nontransmural) infarcts, in which the necrosis involves the subendocardium, the intramural myocardium, or both without extending all the way through the ventricular wall. Eight to 10 days following infarction, the thickness of the cardiac wall in the area of the infarct is reduced as necrotic muscle is removed by mononuclear cells. A loss of functioning myocardium results. As a consequence of infarction, changes in left ventricular size, shape, and thickness involving both the infarcted and the noninfarcted segments of the ventricle often occur. These changes are referred to as "ventricular remodeling", a process that in turn can influence function and prognosis.
One of the most important developments in the treatment of patients with infarction consists of establishing reperfusion of ischemic heart muscle. It improves hemodynamics and decreases infarction size (the latter in early reperfusion).
Significant stenosis of one or more major epicardial arteries, which supply at least a moderate-sized area of viable myocardium, in a patient who has ischemia episodes, angina or major ventricular arrhythmia has to be treated by coronary revascularisation. Efforts to prevent and/or treat the disease have the potential for success. Diagnostic procedures are essential for the correct selection of patients and coronary vessels prior to revascularisation. In this respect it would be of great importance for the future of magnetocardiography to enter the field of assessment of myocardial viability.

Diagnostic procedure
The crucial problem in coronary artery disease refers to the identification of viable myocardium. Stunning and hibernation of myocardial segments may lead to reduced kinesis of viable tissue. Therefore, wall motion analysis fails to correctly diagnose viability. Additional procedures are required.
Myocardial infarction can become visualised by nuclear cardiology either as a "cold spot" or as a "hot spot". Cold spot imaging is based on perfusion defects, whereas the infarct can become visualised as a "hot spot" using a monoclonal antibody specific for intracellular myosin.
Since the gold standard in the diagnosis of myocardial viability (PET: combined perfusional/metabolic imaging) is not available everywere, stress-echocardiography or ^{201}Tl- or ^{99m}Tc-SestaMIBI stress imaging respectively are the most widely used standard procedures.

A precise localisation of myocardial infarction based on the standard ECG is not always possible. The accuracy of such a localisation is influenced, for example, by the distance of the electrode from the heart, which varies considerably among individuals. Therefore, additional anatomical constraints and the application of algorithms to solve the inverse problem of electrocardiography or magnetocardiography respectively are desirable.

Method

23 patients with prior myocardial infarction and 25 healthy subjects/patients without infarction were investigated. The presence of infarction (ECG, history, elevated blood level of cardiac enzymes) was proven by angiography. Fig. 1 displays an example of ECG and angiography of a patient suffering from an inferobasal-inferomedial aneurysm of the left ventricle.

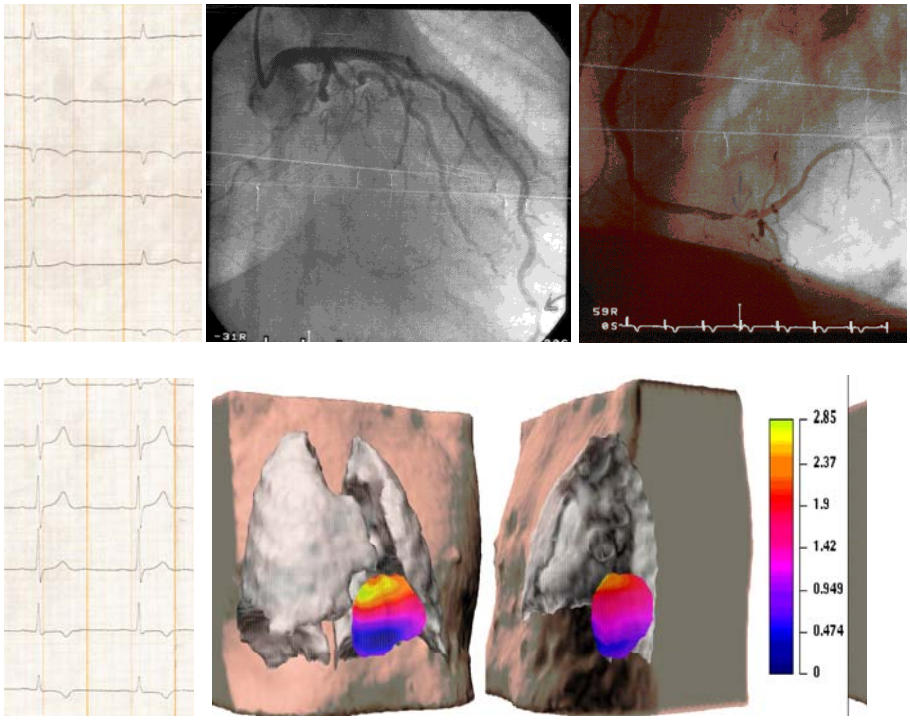

Figure 1: Top: ECG (Einthoven leads), angiogram (30° RAO, 60° LAO);
Bottom: ECG (Wilson leads), MSI (30° RAO, 60° LAO);
Inferobasal-inferomedial myocardial infarction

Magnetic field maps
Magnetocardiograms were taken using a multisensor device (Philips). The device consists of two sensor heads, each holding 31 sensors [6]. The recording time was set to 100 to 600 s (1000 Hz sampling rate). The sensor heads were tilted by about 30°. The coordinates of the torso relative to the multichannel system were determined by localising the center coordinates of 10 coilsets.

Magnetic resonance images
MRIs were taken with a 1.5 T machine (Philips Gyroscan® ACS II). Prior to investigation, coilsets were replaced by oil pills. A series of 40 to 60 transverse slices (5 mm thick, T1 weighted turbo field echo scan) were taken. The scan time window was placed in the late enddiastolic heart phase at R upstroke.
The data processing, i.e. segmentation of three-dimensional surfaces, calculation of current densities, and presentation of results was done with the software package Curry® [7]. The resulting stack of MRI slices was transformed into a three-dimensional dataset [8].

The surfaces required for volume conductor modeling were segmented by a threshold steered region growing algorithm.The following thinning procedure resulted in a reduced list of surface points. This list was used for the computation of a boundary element volume conductor model. The segmentation of the source structure (left ventricle) was done by hand using a freehand cursor brush in three zoomed orthogonal image planes. The left ventricular endocardial surface was divided into a grid of several hundred points of equal distance using a thinning algorithm. The list of myocardial point coordinates served as dipole positions for reconstruction. The overall time for MRI preparation took about one hour (30 minutes scan preparation and scan time, 30 minutes for 3D surface processing).

Current density images
Current density was calculated for a few hundred support points at the peak of the QRS complex. The reconstruction points were regularly spaced on the left ventricular endocardial surface with a mean distance of 5 mm. The current density had to satisfy the constraints of minimum norm least squares, lead field regularisation,

and noise regularisation. Noise regularisation was performed using the bend values of a L-curve. The resultant current density distribution was presented as a colour-coded surface plot of the left ventricle for the assessment of regional electrical activity. The localisation and extent of the area of low current density in the infarction patients were determined for seven segments of the left ventricle. Low current density was assumed for the currents below an arbitrarily defined value (1 mA/mm²). Localisation results were compared to ECG, echocardiography, scintigraphy, and left heart angiography.

Results

There were marked differences in mean current strength, localisation, and extent of areas of low current density between the infarction patients and the healthy subjects. Mean current densities of the patients turned out to be lower compared to the current densities of the healthy. A mean point distance of 5 mm for the generation of support point lists resulted in a standardised patch area of about 30 mm^2. According to the ventricular remodeling and enlargement after myocardial infarction, the number of points or currents respectively was considerably higher in patients. Nevertheless, the sum of all currents was lower in patients compared to the healthy subjects.
In table 1 MSI is compared to contrast angiography in the infarction group.

	Myocardial Segment - Infarction Patients						
Classi-fication	antero-basal	antero-medial	apical	infero-medial	infero-basal	septal	postero-lateral
pp	3	13	13	9	1	11	7
nn	15	5	7	9	14	7	12
pn	2	2	2	5	8	0	1
np	3	3	1	0	0	5	3
Σpp+nn	18	18	20	18	15	18	19
Σpn+np	5	5	3	5	8	5	4
pp	abnormal laevocardiography and abnormal MSI						
nn	normal findings for both procedures						
pn	abnormal angiography and normal MSI						
np	normal angiography and abnormal MSI						

Table 1 Comparison of angiography and MSI in 23 infarction patients (i.e. 7 segments in each patient, 161 segments overall)

In 23 infarction patients, the classifications of 126 out of 161 segments (78%) were in agreement (abnormal-abnormal or normal-normal respectively). 35 out of 161 segments (22%) had a different classification (abnormal-normal or normal-abnormal respectively). The interpretation of these findings will be discussed later on. The highest number of mismatch segments was found inferobasally.
Table 2 summarizes the results from 25 healthy subjects/patients without a history of myocardial infarction.

Error! Bookmark not defined. **Error! Bookmark not defined.**Classi-fication	Myocardial Segment - Non-Infarction Patients/Healthy						
	antero-basal	antero-medial	apical	infero-medial	infero-basal	septal	postero-lateral
n	2	2	0	4	5	6	6
p	23	23	25	21	20	19	19
Error! Bookmark not defined.n	normal MSI						
p	abnormal MSI						

Table 2: MSI in 25 normals/patients without infarction (7 segments in each normal/patient, 175 segments overall)

25 out of 175 Segments (14%) turned out to have an abnormal low current density. Note that segments located in an interior or nearly position again had the highest rate of abnormal MSI results.

Discussion

Despite the obstacle posed by the non-uniqueness of inverse solutions, we have shown that an estimation of the myocardial source activity in coronary artery disease can be achieved by a solution which minimizes the square of power integrated over a left ventricular surface.
Low regional current density turned out to be the hallmark of infarcted myocardial tissue in coronary artery disease. In this study there are several reasons for the mismatch of angiography-MSI. The interpretation of the coherence between regional wall motion and regional current density is limited by a lack of knowledge about the regional amount of viable myocardium. Because hypokinesis may occur in stunning and hibernating myocardium, as well as in myocardial infarction with varying degrees of myocardial fibrosis, reference procedures (PET, scintigraphy, endocardial catheter mapping) are required in future studies. Reversibility of wall motion abnormalities would be the way to differentiate underperfused but viable myocardium from myocardial scaring in a prospective study.
Assuming that MSI gives a true copy of regional electrical activity, the identification of hypokinetic but viable myocardium (pn-segments, Tab. 1) would become possible. Nevertheless, the results of this preparatory study should considered to be preliminary. Much work is to be done in this field.

Summary

Multisensor magnetocardiography archieved by sophisticated solutions of the inverse problem of electrocardiography may be of additional diagnostic value in clinical cardiology. The enormous hardware costs hinder the in-hospital application of magnetocardiography only in so far as the diagnostic outcome does not justify this expenditure. The non-invasive pre-interventional examination of patients suffering from coronary artery disease may provide an application of magnetic source imaging which is as fascinating as it is difficult.
Images of distributed cardiac source activity were obtained in 23 patients after myocardial infarction and in 25 patients/normals without a history of infarction. Constraints (minimum norm, lead field normalisation, noise regularisation, anatomical restriction) were used to obtain a unique solution. Current density was assigned to patches of the left ventricular endocardial surface. The resultant images were compared to regional wall motion in left ventriculography.
The vast majority of myocardial segments with wall motion abnormalities (hypokinesia, akinesia, dyskinesia) were identified by magnetic source imaging (low current density). However, in some segments (predominantly inferior) disagreement was found. The subjects without a history of infarction had only few segments with abnormal low current density.
The study demonstrates that inverse solutions aimed at current density calculations on realistic myocardial surfaces have the potential to identify and image electrical properties of the myocardium in coronary artery disease. However, further development of reconstruction algorithms and clinical studies including other reference procedures (PET, scintigraphy) are of paramount importance to the method.

References

[1] Siltanen, P., Magnetocardiography, In: Macfarlane, P.W., and Lawrie, T.D.V. Comprehensive Electrocardiology, New York, Pergamon Press, 1989: 1405-1438.

[2] Nowak, H. Biomagnetic Instrumentation, In: Andrä, W., and Nowak, H. Magnetism in Medicine, Berlin, WILEY-VCH, 1998: 88-135.

[3] Leder, U., Pohl, H.P., Michaelsen, S., Fritschi, T., Huck, M., Eichhorn, J., Müller, S., and Nowak, H. Noninvasive biomagnetic imaging in coronary disease based on individual current density maps of the heart, Int. J. Cardiol., 1998, 64: 83-92.

[4] Stroink, G., Moshage, W., and Achenbach, S. Cardiomagnetism, In: Andrä, W., and Nowak, H. Magnetism in Medicine, Berlin, WILEY-VCH, 1998: 136-189.

[5] Leder, U., Haueisen, J., Huck, M., and Nowak, H. Non-invasive imaging of arrhythmogenic left ventricular myocardium after infarction, THE LANCET, 1998, 352:1825.

[6] Dössel, O., David, B., Fuchs, M., Krüger, J., Lüdeke, K.M., and Wischmann, H.A. A 31-channel SQUID system for biomagnetic imaging, Appl. Supercond., 1993, 1 [10-12]: 1813-1825.

[7] Kullmann, W.H., and Fuchs, M. Integrated imaging of neuromagnetic reconstructions and morphological magnetic resonance data, Clin. Phys. Physiol. Meas., 1991, 12A: 37-41.

[8] Fuchs, M., Wischmann, H.A., Wagner, M., Krüger, J. Coordinate system matching for neuromagnetic and morphological reconstruction overlay, IEEE Trans. Biomed. Eng., 1995, 42: 416-420.

Acknowledgements

The authors would like to thank Ines Krummbein for providing MRI images, and Uwe Schulze for assistance during magnetocardiographic measurements. This work was supported by the German BMBF grant 13N664 and the Thuringian research grant B 301-9608

ERP mapping of brain activation during phonological processing

[1]Alice Mado Proverbio, [1]Stefania Lilli, Alberto Zani [2,1]

[1]Cognitive Electrophysiology Lab, Department of Psychology, University of Trieste, Trieste, Italy
[2]Cognitive Electrophysiology Lab, Istituto di Psicologia del CNR, Roma, Italy

Introduction

It is known that the first processing stage of visually presented words consists in the analysis of their physical characteristics as spatial frequency, orientation, color and dimensions at the primary visual area. The recognition of linguistic characters gifted of meaning (graphemic analysis) it would occur around 150 msec after the onset of the stimulus at the temporal occipital area (lingual gyrus and fusiform gyrus of left and right visual cortex) as shown by the magneto-encephalographic (MEG) study of Kuriki et al. (1988) [1]. With a PET study Petersen and colleagues (1990) [2] have identified in the medial left extra-striate cortex of occipital lobe the visual area specialized in the recognition of the graphic form of words (visual word form system). In this study a strong activation of this region was observed during the reading of words or pseudo-words (nonexistent words that obey to the rules of pronunciation of a date language), while such activation was being absent for the non-words (strings of illegible characters) or strings of false letters.
In the present study we investigated the neural basis of reading processing and phonological analysis by recording high density event-related potentials (ERPs) in healthy volunteers involved in a silent phonological decision task. Target stimuli were to be mentally recalled by participants on the basis of a short unique definition, and compared with a syllable presented in the visual modality. Subjects were instructed to make a decision about targets and syllable sounds by silently processing the sound dimensions of linguistic phonemes.

Methods

Subjects
Nine right-handed college students (4 males, 5 females) participated in our experiment. All had normal or corrected-to-normal vision and a mean age of 26 years. None of them was aware of the goal of our study.

Stimuli and procedure
High-resolution event-related potentials (ERPs) of the brain were recorded in healthy young volunteers during a phonological decision task. Participants were required to judge whether a visually presented three letters syllable was included or not in a target word by making a two-choices button-press. Syllables were randomly presented in upper case in the central visual field. Half of them were included in the target words at the beginning, in the middle, or in the final part. Their pronunciation was the same whether in isolation or within the word. Target words were not actually presented to subjects, but suggested by means of a unique definition visually presented on a computer screen.
Participants seated in a dimly lit, acoustically and electrically shielded cubicle at 114 cm from a TV screen. They were instructed to fixate a cross at the center of the screen and read a short definition which appeared for 2 sec in the upper part of central visual field. Immediately after, a question mark, which was used as a probe, was presented at the center of the screen for 750 to 1000 msec, and substituted right after by a trigram presented for 200 msec. Participants were instructed to to retrieve the target names, and to decide thereafter whether the syllable was part of the target by pressing as accurately and fast as possible a button for answer 'yes', and another one for answer 'no' with either the left or right hand.

EEG recording
EEG was continuously recorded from 30 scalp sites at a rate of 500 Hz and referenced to linked ears. Blinks and vertical eye movements were monitored with two electrodes placed below and above the right eye. Horizontal and vertical electro-oculograms were also monitored with electrodes placed at the outer canthi of the eyes. EEG signals were amplified with a band pass of 0.1-70 Hz. ERPs were averaged offline from 100 msec before to 1000 msec after probe presentation. The major ERP components were identified and measured automatically by a computer program and quantified by measuring peak latency and baseline-to-peak amplitude values.

Results

Figure 1 illustrates ERPs to the correct syllables (included in the thought word) and to the wrong ones (incompatible sounds with the thought word) recorded on the frontal (Fz) and parietal (Pz) electrode sites. Note that on the anterior brain area a negativity is manifested to the wrong syllables with two peaks toward 350 and 600 msecs, while on the back area the correct syllables produced a large positivity with two peaks around 340 (P300) and 520 (late positivity, LP). Since the participants had to answer to both the types of stimuli by pressing one of two keys to choice, the difference between the correct and incorrect conditions has to be imputed to the recognition of a phonological

incongruity between the sounds of the syllable and those of the words thought, which produces a phonological mismatch negativity similar to that found in the acoustical/phonetic modality.
ERPs to stems correctly judged as included in the target word displayed a large P300 component. Spatio-temporal mapping showed a large focus centered at central-parietal scalp areas. In contrast, ERPs to stems not included in the target words elicited a series of negative potentials, very likely reflecting the response to phonological incongruence. Spatio-temporal mapping of ERP waves showed that the effect of phonological incongruence on ERPs amplitude was evident as early as 185 msec centered over left and right lateral-occipital (OL/OR electrode sites, halfway between O1/O2 and T5/T6 electrode sites) areas. Neuroimaging CT scanning evidence is forthcoming to suggest that these sites fall on the extrastriate areas of the occipital lobes [3]. These high-temporal resolution ERPs indicate an early timing of activation for extrastriate regions during visually-coded phonological processing.

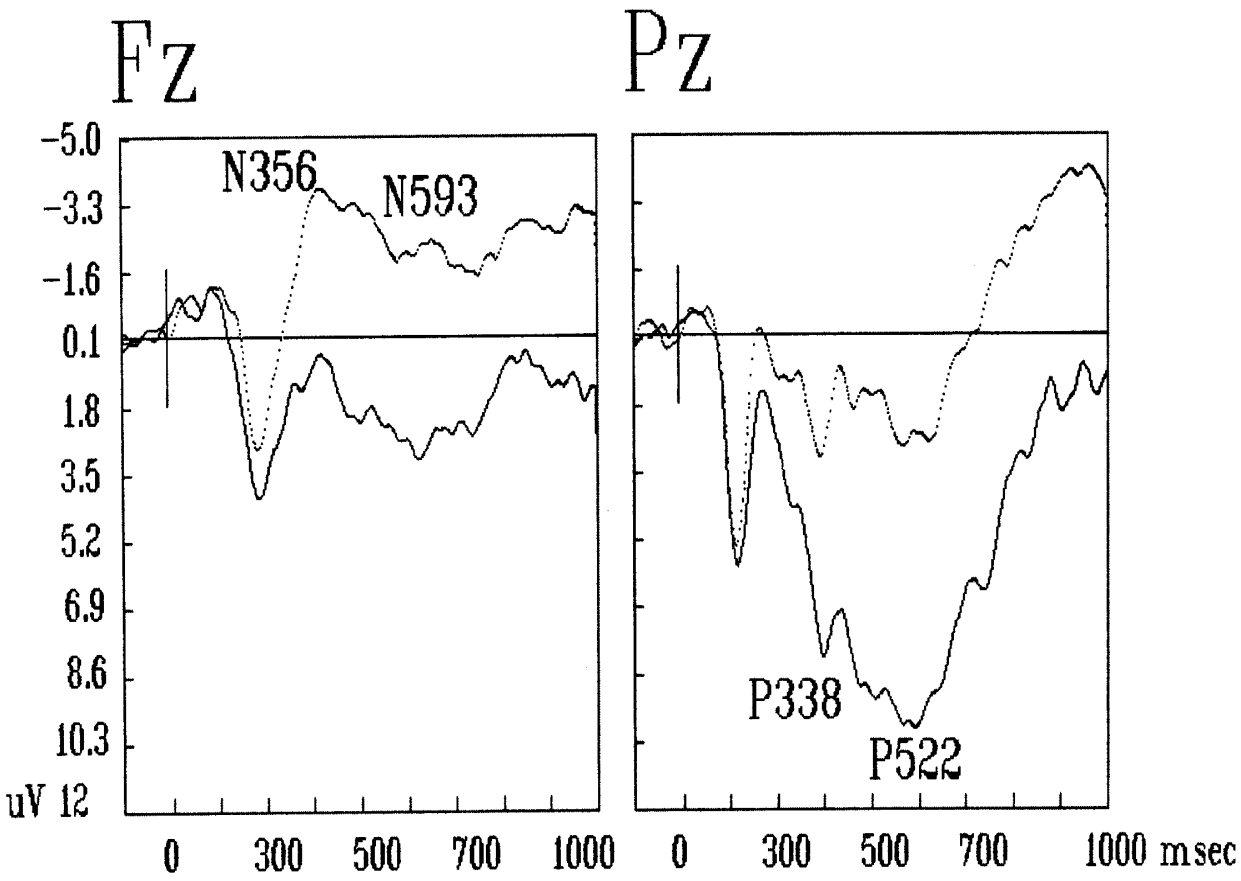

Figure 1. Grand-average ERPs to syllables included (solid line) or not included (dotted line) in the target word. ERPs were recorded at frontal (Fz) and parietal (Pz) midline sites.

Discussion

According to the available literature, the first stages of graphemic analysis and word recognition correspond to the arising of the evoked component N1 with a latency between 150 and 200. Subsequently, it is possible to identify at N2 level a stage of phonological information processing, i. e., related to the sounds of the language, both in the acoustic and visual modality. For instance in the ERP study of Connolly and Phillips (1994) [4] linguistic violations of acoustic phonemic type produced a negative response called phonological Mismatch Negativity (pMMN) around 270-300 msec of latency from the onset of the words.
In the present study, the ERPs showed a large negative response to the phonological incongruity at visual brain areas beginning from around 185 msec post-stimulus (see Figure 2a and 2b).
Overall, these data suggest that at a very early stage of linguistic analysis, phonological processing of simple word-stems may be carried out on the basis of a purely visual code, and that this coded processing is carried out by extra-striate regions of the occipital lobes of the brain, indicated by neuroimaging studies (PET) as the locus of word form system analysis [2].

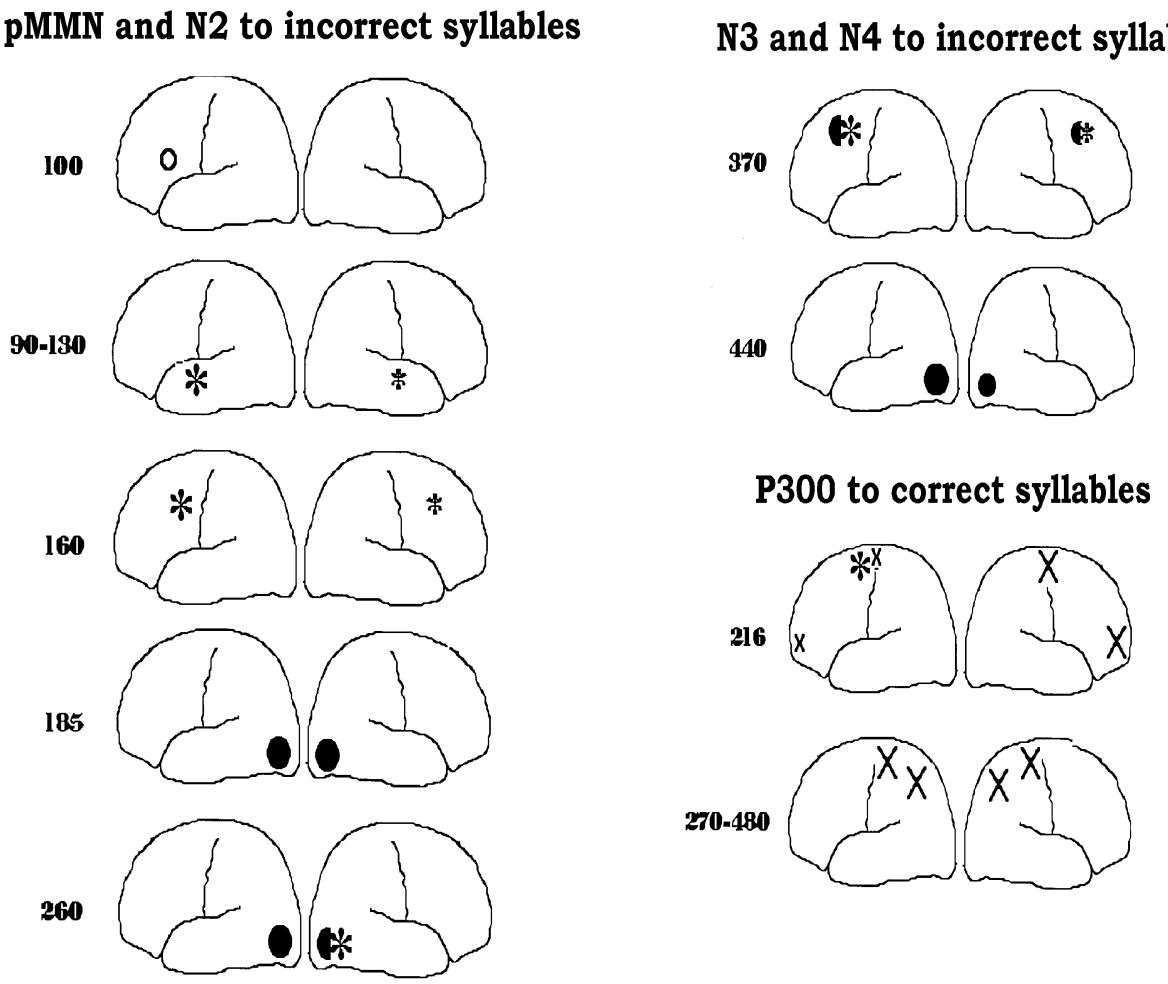

Figure 2a and 2b. Temporal series (latency in msec) of brain activation for left and right hemispheres as a function of phonological incongruence between target words and syllables. Symbols indicate the presence (or absence) of a brain response to the incongruence and the locus of effect recorded at scalp surface.

Empty circles.....no effect
Filled circles.....amplitude enhancement for N1,N2,N3,N4 components
** .....latency shortening*
X .....amplitude enhancement for P3 component.

References

[1] Kuriki, S., Takeuchi, F., and Hirata, Y., Neural processing of words in the human extrastriate visual cortex, Cogn. Brain Res., 1998, 6: 193-203.

[2] Petersen S.E., Fox, P.T., Posner, M.I., Mintun, M. and Raichle, M.E., Positron emission tomography studies of the processing of single words, J. Cognitive Neurosci.,1996,1:153-170.

[3] Homan, R.W., Herman J., and Purdy P., Cerebral location of international 10-20 system electrode placement, EEG and Clin. Neurophysiol., 1987, 66: 376-382.

[4] Connolly, J.F., and Phillips, N.A., Event-related potential components reflect phonological and semantic processing of the terminal word of spoken sentences, J. Cogn. Neurosci., 1994, 6: 256-266.

Acknowledgements

This research was funded by MURST grants to the lab of Cognitive Electrophysiology of Department of Psychology, University of Trieste.

Signal to Noise Improvement in fMRI Analysis

Erné S.N.[1], Müller H.-P.[1], Kammrath H.G.[1], Tomczak R.[2], Wunderlich A.[2]

[1]Central Institute for Biomedical Engineering, Ulm University, D-89069 Ulm, Germany
[2]Department for Diagnostic Radiology, University Clinic Ulm, D-89069 Ulm, Germany

Introduction

Functional human brain mapping is a rapidly expanding discipline. Non-invasive techniques can measure cerebral physiologic responses during neural activation [1]. During the last years interest in novel methods for mapping human brain function based on the technique of magnetic resonance imaging (MRI) has grown rapidly [2]. Functional MRI (fMRI) allows for the detection of slight physiological alterations, such as neuronal activation resulting in changes of blood flow, blood volume and blood oxygenation. These signal changes are related to changes in the concentration of deoxyhemoglobin which acts as an intravascular contrast agent for fMRI [3].
Therefore, fMRI methods can be designed that produce blood-oxygenation-level-dependent (BOLD) image contrast [4-6]. This method has a good spatial resolution, limited most likely only by the precision with which the autoregulatory mechanisms of the brain adjust blood flow in space to the metabolic demands of neuronal activity. Since fMRI is completely non-invasive using no contrast agent or ionizing radiation, repeated single-subject studies are becoming feasible.

Method

To evaluate the fMRI image series sophisticated algorithms and great computational power are needed to separate the physiological induced signals from artifacts resulting from patient movement or MRI detection techniques. Additionally, an improvement of the signal to noise ratio has to be reached. Variable visualization possibilities of the analysis results on the morphological background are necessary to allow for an interpretation of the results.
The Functional Analysis and Morphological Imaging Software (FAMIS) described in this work is to provide a contribution in all 3 fields. New analysis algorithms for motion correction as well as for functional analysis have been implemented. The results from analyzing fMRI data series with this software project can be visualized on a background obtained from the corresponding morphologic data.
The FAMIS consists of several modules (Fig. 1):

- A visualization module for the morphologic MRI data sets (Figs. 2-4). The module is easy to handle for the user and shows the morphologic data in two(2D)- and three(3D)-dimensional form. Of course, the visualization module can be used for fMRI data.
- A module for motion correction caused by shifting as well as by rotatory brain movements. General experience shows that it is a good advice to use motion correction as a prerequisite for the following cluster analysis.
- An algorithm to detect brain activation, that includes averaging of the fMRI data sets on the basis of the results of a cluster analysis. This cluster analysis identifies clusters of voxels that are exceptional by their time series as well as by their location and thus are special candidates for data averaging.
- Integration of functional results of the functional analysis to the morphologic environment.

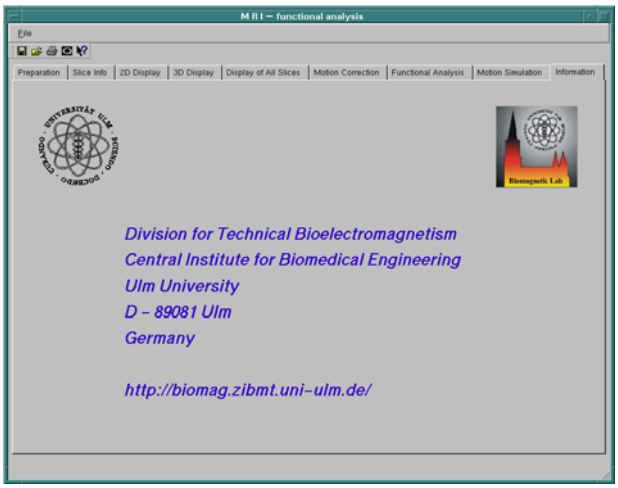

Fig. 1: Surface of the FAMIS.

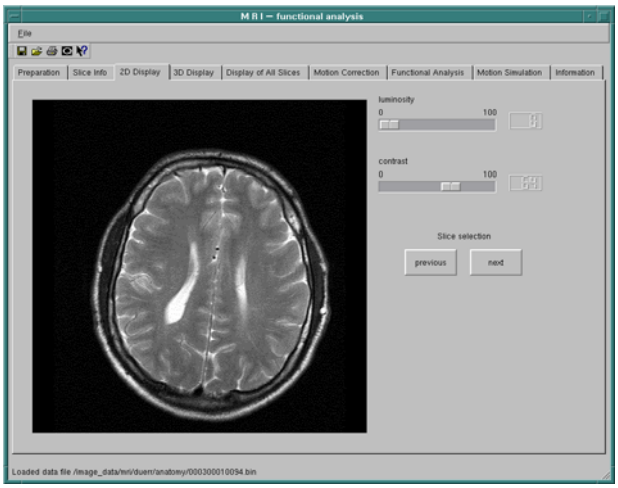

Fig. 2: 2D visualization.

For a validation of the algorithms simulation of rotational and shifting motions have been performed. The algorithms to detect brain activation have been compared to established analysis methods.

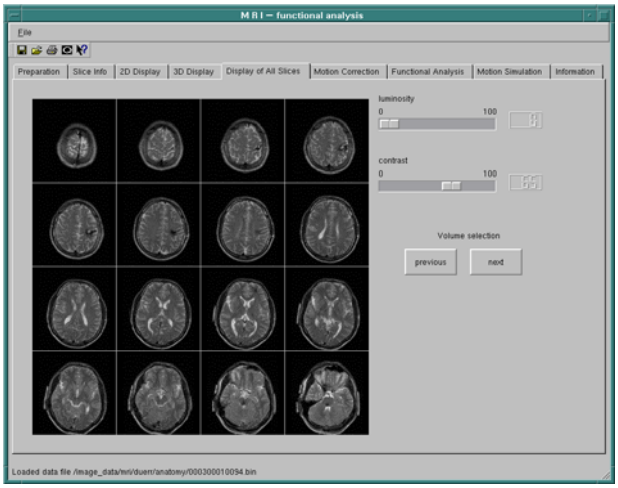

Fig. 3: Multislice visualization.

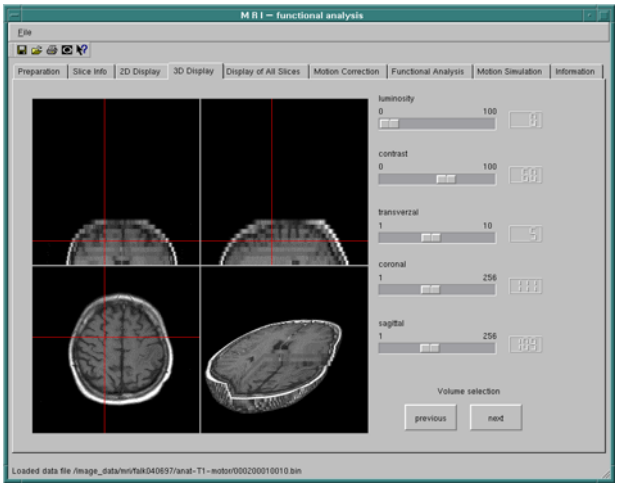

Fig. 4: 3D visualization.

Results

Motion correction

The motion correction is performed under the following assumptions: The brain is considered as a solid body that can move slightly with 6 degrees of freedom. There are no relative movements of single parts. The brain is not pulsating. The central slice of the 3D MRI data set acts as a reference slice with its contour acting as the reference for the motion correction. Next, the rotation and shifting matrices R and T are determined:

$$\vec{x}^{(2)} = \overrightarrow{\overrightarrow{R}\,x}^{(1)} + \vec{T} \qquad (1)$$

where $x^{(1)}$ and $x^{(2)}$ are the vectors of voxels of slice 1 or 2, respectively. These matrices minimize the error E between two central slices of subsequent recorded 3D volumes.

$$E = \sum_{i=1}^{N} (I_i^{(1)} - I_i^{(2)})^2 \longrightarrow \min \qquad (2)$$

N is the number of voxels in a slice, $I^{(1)}$ is the intensity of voxel i of the reference slice and $I^{(2)}$ the intensity of voxel i of the second slice, respectively.
Finally, this matrix is used for the transformation of the whole 3D data set. Thus, the motion correction is automatically performed and no interference of the analyst is necessary.
About 10 minutes is needed to calculate the motion correction for a set of 60 3D-volumes, each consisting of 16 slices (128x128 pixel) on a HP Workstation C160 series.

Motion Simulation

A further integrated part of the software is the motion simulation module. One original MRI brain volume is moved according to Eq. (1). Motions up to 2 pixels and 2° are possible.
One volume consisting of 16 slices, 128x128 pixels was copied 4 times and afterwards on each volume a motion was simulated separately. Then, the resulting volumes were motion corrected. The correction reveals the results summarized in Tab. 1. As a measure for the quality of the motion correction algorithm the reducing of the error E is used.

Trial no.	Δx	Δy	Δz	Δρ	Δθ	Δϕ	E
1	1	1	1	0°	0°	0°	317→0
2	0	0	0	1°	1°	1°	276→79
3	1	1	1	1°	1°	1°	285→82
4	2	2	0	1.5°	0°	0°	550→73

Tab. 1: Results from the motion simulation. The shifting is given in pixel values.

The simulations show that rotatory and shifting motions can be corrected at a large degree.

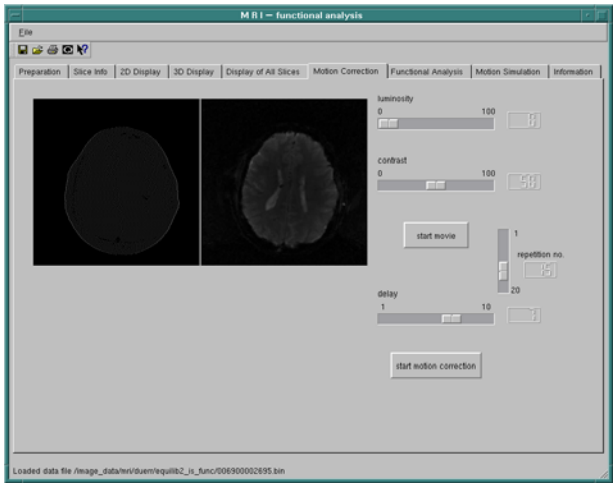

Fig. 5: Motion correction module including slice movie.

The results of the motion correction can be estimated by a visual inspection of a slice movie (Fig. 5).

Functional Analysis

To improve the signal to noise ratio averaging of fMRI data sets is performed over voxels which are assumed to belong to the same functional area. The groups of voxels to be averaged are defined by a hierarchical clustering procedure [5,6].

The noise reduction is obtained by averaging of voxels that are assumed to belong to the same activated morphologic region. The analysis is based on a cluster analysis that works with categorised data analysis. Here the similarity of the voxels is defined on the basis of several properties:

- Intensity of stimulus correlated signals.
- Correlation of the time course of the voxels.
- Geometrical distance (near voxels are more likely to belong to the same structure).
- Finally, the activation can be estimated either statistically (Kolmogorov-Smirnov test) or deterministic (amplitude of the stimulus correlated signals).

After clustering, a threshold is set to identify the group of voxels to be averaged and the spatial average is performed. After averaging, the amplitude of the signal of each voxel in phase with the stimulus on/off function is calculated.

As there exists no gold standard for judging the performance of fMRI analysis algorithms, we compared the results of a functional analysis with the results of a standard correlation analysis. Fig. 6 illustrates examples of fMRI analysis from a patient activating the left hand. The areas resulting from the functional analysis can be visualized on the background of the morphological data sets. The results of the functional analysis are colour coded and displayed on the background of the corresponding morphologic MRI images. The visual inspection shows a good coincidence. The clinical validity has to be proved in the future.

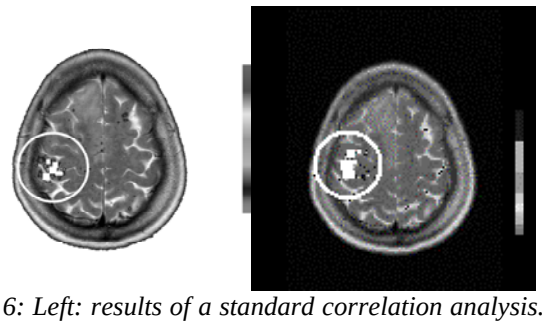

Fig. 6: Left: results of a standard correlation analysis. Right: results of the cluster algorithm. The picture is upside down due to different analysis programs.

Discussion

The FAMIS allows for an interactive visualization of the MRI data sets, for the fMRI data sets and of the results of the functional analysis on the morphological background The advantage of the motion correction algorithm is the user independent implementation for the correction of fMRI volumes due to rotatory patient movements or patient shift. Thus, reproducible results become feasible that can be received within a comparatively short time.

The similarity of the hemodynamic processes in the brain is obtained by a hierarchical clustering procedure. This algorithm is used for the signal to noise improvement and averaging of subsequently recorded fMRI volumes. The automation of the processing of the improvement of the signal to noise ratio by cluster analysis, provides a user-independent analysis of the data sets. Fast algorithms allow for the analysis of a large amount of MRI-based data sets within a comparatively short time. Other groups have developed further analysis algorithms for fMRI analysis based on clustering [7,9]. A comparison to these methods has to be performed.

References

[1] Toga, A.W., Mazziotta, J.C. Brain Mapping - The Methods, San Diego, Academic Press, 1996

[2] LeBihan, D. Diffusion and Perfusion Magnetic Resonance Imaging- Applications to Functional MRI, New York, Raven Press, 1995.

[3]. van Zijl P.C.M,.Eleff, S.M, Ulatowski, J.A., Oja, J.M.E., Ulug, A.M., Traystman, R.J., Kauppinen, R.A. Quantitative assessment of Blood Flow, Blood Volume and Blood Oxygenation effects in Functional Magnetic Resonance imaging, Nature Medicine 1998, 4: 159-167.

[4] Ogawa, S., Lee, T.M., Kay, A.R., Tank, D.W.. Brain Magnetic Resonance Imaging with Contrast Dependent on Blood Oxygenation. Proc. Natl. Acad. Sci. USA, 1990, 87: 9868-9872.

[5] Ogawa, S., Lee, T.M., Nayak. A.S., Glynn, P. Oxygenation-Sensitive Contrast in MRI of Rodent Brain at High Magnetic Fields. Magn. Res. Med., 1990, 14: 68-78.

[6] Ogawa, S., Lee, T.M., Barrara, B. The Sensitivity of Magnetic Resonance Image Signals of a Rat Brain to Changes in the Cerebral Venous Blood Oxygenation. Magn. Reson. Med., 1993, 29: 205-210.

[7] Baumgartner, R., Windischberger, C., Moser, E. Quantification in Functional Magnetic Resonance Imaging: Fuzzy Clustering vs. Correlation Analysis. Magn. Reson. Imaging, 1998, 16: 115-125.

[8] Erné, S.N., Trahms, L., Trontelj, Z. 1987 Clustering - A Novel Approach for Selected Averaging of Biomagnetic Signals In: *Biomagnetism `87* Atsumi, K., Kotani, M., Ueno, S., Katila, T., Wiliamson, S.J. eds. Tokyo Denki University Press, Tokyo 298-301.

[9] Baumgartner, R., Scarth, G., Teichtmeister, C., Somorjai, R., Moser, E. Fuzzy clustering of gradient-echo recalled functional MRI in the human Visual Cortex. Part I: Reproducibility. J. Magn. Reson. Imaging, 1997, 7: 1094-1101.

Physical Phantoms for Biomagnetic and Bioelectric Measurements

Tenner U.[1], Erné S.N.[1], Haueisen J.[2], Nowak H.[2], Brauer H.[3]

[1]University of Ulm, Ulm, Germany
[2]Friedrich-Schiller-University, Jena, Germany
[3]Technical University of Ilmenau, Ilmenau, Germany

Introduction

The interpretation of the measured, very weak magnetic fields generated by the electrically active organs requires special numerical techniques for localization and reconstruction of the sources. The state-of-the-art of the development of such methods is defined by inverse solution techniques which can reconstruct equivalent dipolar sources within more or less realistically shaped volume conductors. Due to the non-uniqueness of the inverse problem, source reconstruction is only possible under restricted conditions regarding volume conductors and sources. The use of physical phantoms might be helpful to validate the known inverse methods, to improve them or to develop a new one. In addition it is useful to perform magnetic and electrical measurements with physical phantoms under well-defined conditions to validate the models and to calibrate the measuring systems.
One advantage of physical phantom measurements over pure simulation studies, is that the former take into account real world influences such as environmental noise and 3-D positioning errors, thus providing an error estimation of the entire source reconstruction procedure. Current topics of research in bioelectromagnetism are algorithms for reconstruction of extended current sources by solving the inverse problem. The phantoms enables us to perform studies for testing different measuring systems and validating the localization algorithms.
In this paper we present an overview of the four different phantom models, conductivity compartments and five source modules developed in our group within the last three years. The phantoms were filled during measurements with NaCl solution. A special polymer membrane was used to model different conductive compartments in the thorax. The simplest source model is the current dipole which is a good approximation for focal sources. We developed five special source modules, that can be interchangeably fixed on a ground plate at a defined position at the interior back of the thorax phantom or in the head model. Four of the source modules consist of a set of multiple dipoles. The other module consists of an extended current source (butterfly source model) with variable position and orientation.
Magnetic Resonance Images (MRI) data of the physical phantom models were used to obtain geometric description of the volume conductor for the Boundary Element Method (BEM).

Tank model

We developed a tank model (340 mm, 310 mm, 190 mm) with octagonal cross section for basic studies. It consists of glass and has a plastic ground plate with holes for fixing several configurations of sources, inhomogeneities and electrodes for measuring the electrical potentials in space (Fig. 1).

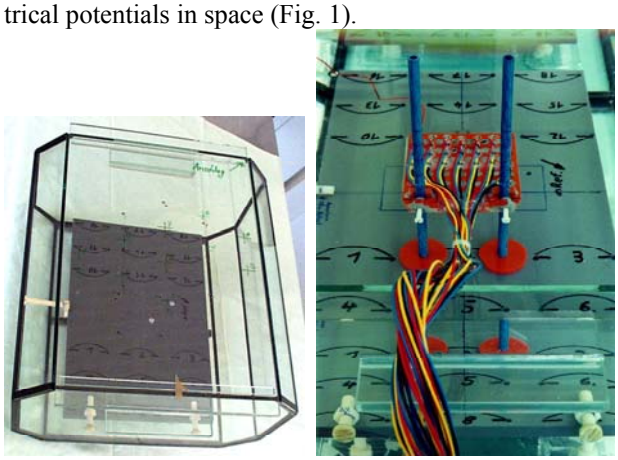

Figure 1: The tank model for basic biomagnetic and bioelectric measurements

We used the tank model for testing of our self designed extended sources and inhomogeneities. An extended current source model was realized by contacting the ends of twisted cooper wires with two thin rectangular plates of platin which were electrically isolated by a plastic cover. Another extended current source model was realized by creating a dipole array with 12 dipoles (Fig. 2).

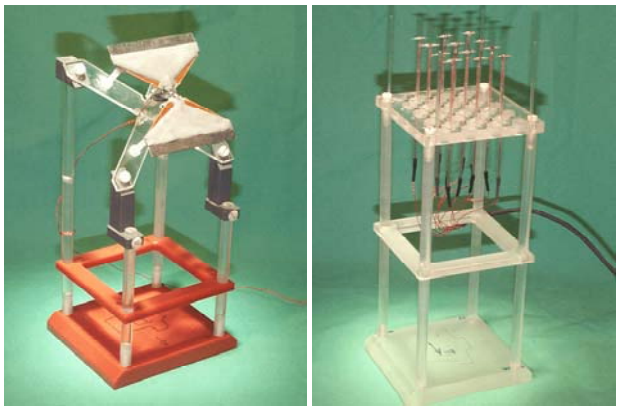

Figure 2: Modules with extended sources, butterfly source (left) and dipole array (right)

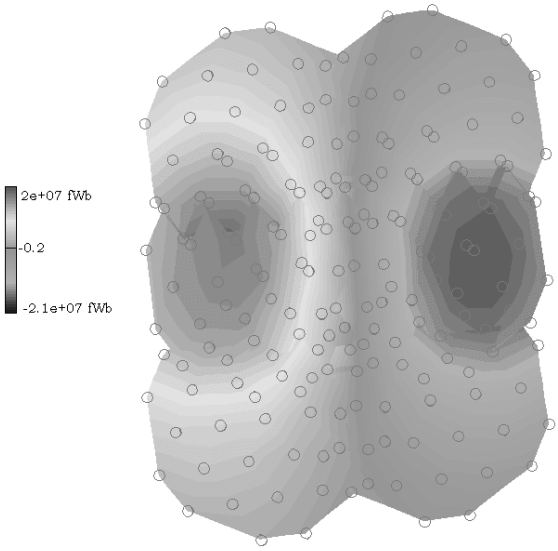

Figure 3: Magnetic field pattern generated by the extended source in the tank model measured with the 31-channel Philips SQUID system at the Biomagnetic Center Jena superimposing the 6 sensor positions and the butterfly source model

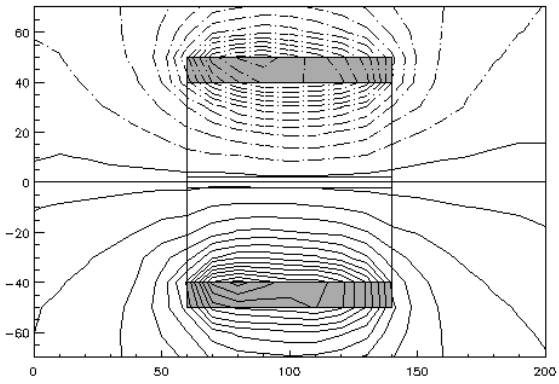

Figure 4: Electrical potential field measured 5 mm above the source plane

As an example the measurements of the butterfly source in the tank model are shown in Fig. 3 and Fig. 4. Measurements of the magnetic field (about 9 cm above the current source, Fig. 3) and of the electrical potential field in planes at different heights above the source (Fig. 4 shows the potential field in a distance of 5 mm to the source) confirm the expecting that the current is almost homogeneously distributed over the platin plates, i.e. this is really an extended source model [1]. Further, we used the butterfly source model in the realistic thorax phantom and in the head model for testing and validating the distributed source reconstruction algorithms [2].

Thorax phantom

The second model is a realistically shaped thorax phantom including 138 surface electrodes (Ag/AgCl) to perform magnetic field mapping (MFM) and body surface potential mapping (BSPM) simultaneously as well as to separate magnetic and electrical studies (Fig. 5).

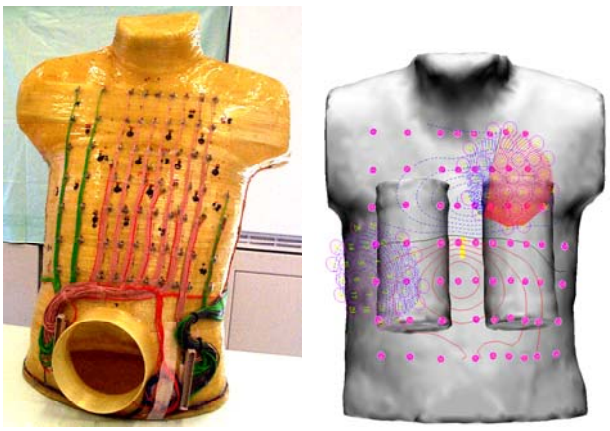

Figure 5: The physical thorax phantom and the inhomogeneous BEM model

The phantom was modeled with epoxy resin by reproducing the body surface of an young adult man. The relatively large filling neck allows the use of different biomagnetic sources and compartments having different conductivity's. A fastening installed on the back of the phantom enables easy and accurate installation and exchange of modules carrying different sources and inhomogeneities, respectively. The cables for the dipole sources can easily be inserted through the opening in the phantom. The firm installation of 138 electrodes (Ag/AgCl) enables a simultaneous recording of the electric field on the body surface for both the ECG (electrocardiogram) and the BSPM (Body Surface Potential Mapping). In order to obtain a representative result, we followed the NEMY-standard (Non-invasive Evaluation of the MYocardium) [3] with the installation of 120 electrodes.
The artificial lungs were modeled as two cylinders (Fig. 6). The cylinders consist of a plastic rack, and four circular and two rectangular ionic exchange-membranes. The membranes were fixed on the plastic rack to separate the compartments having different conductivity's. Partial compartments of different conductivity's were established by filling the artificial lung with varying NaCl concentrations [4]. In order to assess the influence of the membrane itself, we compared two measurement series, homogeneous torso without lung membranes and homogeneous torso with lung membranes, filled with the same NaCl concentration. Between these series we found mean localization differences for the longitudinal oriented dipoles of 0.025 mm and for the transversal oriented dipoles of 0.348 mm, respectively. This demonstrates that the membrane allows free ionic current flow while keeping the conductivity differences in the compartments.

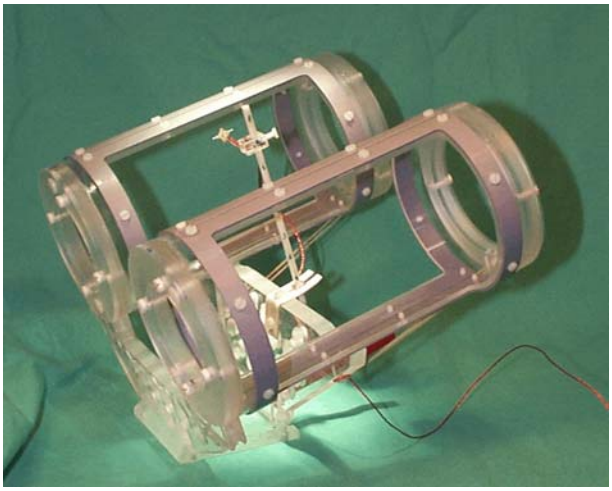

Figure 6: The plastic rack for the artificial lungs

Two dipole orientations were selected at seven different positions (depth): the first orientation longitudinal (craniocaudal) and the second orientation transversal (from right to left). Our main finding was that the accuracy of an estimated source location suffers from the inadequate modeling of the volume conductor, when the artificial lungs were not taken into account for modeling. In those cases both the calculated source location and calculated source strength were misestimated. Mislocalizations of up to 16 mm and wrong dipole strengths of up to 52 % were obtained. The calculations with the one compartment BEM model of combined MCG/ECG measurements for longitudinal oriented dipoles showed a larger localization error in depth than for transversal oriented dipoles, as the calculated longitudinal oriented dipole positions were too deep. The main error of the calculated moments is in the direction from the orientation of the dipole. The longitudinal oriented dipoles were too strong, and the transversal oriented dipoles were calculated too weak. We found that the dipole localization error and the calculated dipole strength error did not significantly depend on the dipole depth for longitudinal orientation, but for transversal orientation. The comparison of the maximum and minimum values of the magnetic field with and without artificial lungs for the transversal oriented dipoles shows an obvious influence from the artificial lungs. However, for the longitudinal oriented dipoles no such influence was observed. Also, for the electric potentials no such influence was observed. Additionally we checked the correlation coefficients between magnetic fields and electric potentials with and without artificial lungs. No influence of the artificial lungs was found for the correlation coefficient.
But the comparison of the maximum and minimum values of the magnetic fields with and without artificial lungs from the transversal oriented dipoles shows an obvious influence from the artificial lungs. For the magnetic fields from the longitudinal oriented dipoles and for all electric data no such trend was observed.
For a longitudinal oriented dipole a serious mislocalization in depth was found when omitting the artificial lungs in the BEM model. The dipole was localized on average 11.6 mm deeper than the actual dipole position. For both the transversal and the longitudinal oriented dipoles, the dipole strength deviates approximately 34 % when omitting the artificial lungs [4].

Spherical model

The third phantom is a spherical model with a diameter of 67 mm to characterize the minimum distance resolution between two dipole sources and validate the localization algorithms used in basic research of neuronal processes in animals. The volume conductor consists of two Perspex hemispheres. A special adjustment unit enables us to arrange two or more dipolar sources within 0.1 mm scale.

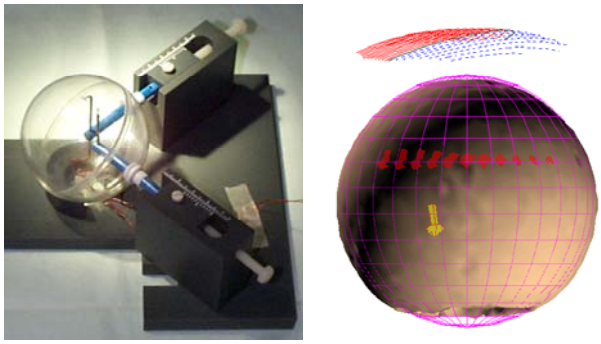

Figure 7: The spherical model with the special adjustment unit (left) and the BEM model (right)

For the verification of the single dipole localization algorithms we used the 31 channel Philips SQUID system. After the entire biomagnetic localization procedure (positioning the model, MCG measuring, creating BEM model from MRI) and by using the Simplex and Levenberg-Marquardt algorithm in the inverse calculations the localization error was less then 1 mm.
For the investigation of the spatiotemporal organization of neuronal processes in animals with the Magnetoencephalographie (MEG), a high temporal resolution (ms) as well as a reasonable spatial resolution of about 1 mm is necessary. We used the spherical model in order to determine the error for the localization of a single dipole and the resolution of multiple dipoles [5]. The investigation of a 16-channel-Micro-SQUID-MEG-system with a current dipole orientated tangential to the phantom surface produced the following spatial errors (x, y - horizontal plane, z - depth): systematic localization error e_x = 1.16 to 1.67 mm, e_y = -1.01 to -1.28 mm, e_z = -5.22 to -7.64 mm, standard deviation of the single measurements perpendicular to the dipole-axis s_{perp} = 0.05 to 0.22 mm, along to this axis s_{along} = 0.20 to 1.73 mm, in the depth s_z = 0.17 to 3.17 mm. The "goodness of fit" was better 95 %. The separation of two dipoles was still possible for parallel dipoles with a distance of $d_{parallel}$ = 0.03 mm and for those perpendicular orientated to each other with a distance of d_{perp} = 0.10 mm. The source localiza-

tion from the measured magnetic fields has been done by an algorithm of spatial filtering.

Head model

The fourth phantom is a head model consisting of a plastic cylinder with a rounded top for testing helmet systems (200 mm high, 115 mm diameter). The ground plate is designed in a way that the source modules of the thorax phantom can be used also in the head phantom.

Figure 8: The head model with a 8 dipole source module

This very recent development is now ready to be used in different helmet systems. The production of some copies of this model is planed.

Discussion

We realized a new physical model of an extended current source which can be used for both biomagnetic and bioelectric studies. Measurements of the magnetic field and the electrical potential field generated by this current source have clearly shown that this model can be used as an extended source model and hence, can be utilized for validating computer simulation methods.
Based on the results with the sphere model we conclude the MEG-system is able to achieve a resolution to investigate neuronal microstructures. The detected spatial errors could be related to positioning of the sensors in the cryostat vessel as well as external low frequency noise.
The ionic exchange-membrane does not disturb the free ionic current flow within the volume conductor. Thus, we conclude that the ionic exchange-membrane is well-suited for the construction of conductivity compartments in physical phantoms.
There are certain limitations in the application of our results to real patient data. First, our inhomogeneity modeling is restricted to cylinders, whereas the lungs are of complex shape. Second, in reality, dipoles usually are not longitudinal or transversal orientated. Thus, we believe that omission of the lungs in the forward model will result in a mixture of the different effects on the errors observed in this study. In other words, one would observe a certain instability of the inverse algorithm, where single localization results are not predictable. Nevertheless, this study gives an estimate of the order of the error in the source localization procedure.
The described physical phantoms has proved to be suitable for estimating the accuracy of biomagnetic measuring systems.

References

[1] Brauer, H., Tenner, U., Wiechmann, H., Ziolkowski, M., Haueisen, J., Nowak, H. and Leder, U., Verification of biomagnetic source reconstruction techniques by using a physical phantom, International Superconductive Electronics Conference, Second Circular (ISEC´97, June 25-28) Berlin, Germany, 1997, 338-340

[2] Brauer, H., Kosch, O., Ziolkowski, M., Tenner, U. and Haueisen, J., Rekonstruktion verteilter Stromquellen in einem Thoraxphantom mit Hilfe biomagnetischer Feldmessungen, 43. Int. Wiss. Kolloquium, TU Ilmenau, 1998, Proc., 3: 89-94

[3] Hoekema, R., Huiskamp, G. J. M., Oostendorp, T. F., Uijen, G. J. H., and van Oosterom, A., Lead system transformation for pooling of body surfacemap data a surface Laplacian approach, Journal of Electrocardiology, 1995, 28: 344 - 345

[4] Tenner, U., Haueisen, J., Nowak, H., Leder, U. and Brauer, H., Source localization in an inhomogeneous physical thorax phantom, Physics in Medicine and Biology, 1999, 44:

[5] Hagner, T., Eiselt, M., Giessler, F., Hansen, E., Haueisen, J. and Nowak, H., Hochauflösende Magnetoenzephalographie – Untersuchungen mit einem kleinvolumigen Phantom, 1999, 44: 38-45

Localization of somatosensory activity evoked by tactile and painful and non-painful electrical stimulation – A comparison using whole head magnetencephalography

Sterr, A., Kreyer, I., Elbert, T.

Department of Psychology, University of Konstanz, D-78457 Konstanz, Germany; Annette.Sterr@uni-Konstanz.de

Introduction

Noninvasive functional brain mapping and neuromagnetic source imaging in particular can uncover various aspects of somatotopy and functional organization of the human cortex. Functional cortical mapping gained particular importance for the investigation of cortical reorganization as a consequence of either cortical lesion or altered afferent input. Studies have mainly used electrical and tactile stimuli and to a lesser extent thermal or vibratory input. The different methods have different assets and drawbacks. Little research has been done to directly compare the various methods. Therefore it is unclear to what extent specific types of stimulation might reveal different aspects of functional organization and –possibly- different principles of reorganization.

Electrical stimulation below the pain threshold is the most common type of stimulation [9,2]. When applied to peripheral nerves, electrical stimuli evoke afferent volleys of compound action potentials that produce large and robust responses in the cortex. However, this stimulation induces simultaneous activation of a large number of *nerve fibers* with different conduction velocities thereby activating multiple regions in area SI [12]. In addition, they bypass the peripheral receptors and the most distal parts of the nerves.

Cutaneous electrical stimulation is another possibility to map the homuncular organization [6]. The electric current then activates *different cutaneous receptors* and therefore the evoked response is not receptor specific. Furthermore, a general problem with electrical stimuli is the occurrence of stimulus artifacts that might interfere with the evoked activity.

The most prominent advantage of tactile stimulation is the specific activation of mechanoreceptors with a *physiologically adequate* stimulus [7]. Tactile stimuli employ the "natural mechanism" of transforming mechanical energy into action potentials and eventually the activation of neurons in the central nervous system. Tactile stimulation methods employ air-puffs that are either applied directly to the skin [7] or can be used to expand a membrane which is fixated at the body surface [8]. Air-puff as well as the expansion of the membrane both lead to an indention of the skin that activates the mechanoreceptors. Compared to electrical stimuli, the tactile stimuli are less sharp in their temporal characteristics and the range of intensity is generally smaller. Consequently, tactile evoked activity seems to be weaker in amplitude.

Using a within-subjects design, we compared tactually (TL) electrically (EL) and in addition electrically pain-induced (PN) evoked magnetic fields (EFs) applied to either thumb (D1) or little finger (D5). The aim of the study was (1) to characterize discrepancies and similarities between the different EFs and their source localization and (2) to determine the magnitude of ipsilateral activation. We expected that TL- and EL – stimulation would lead to comparable results but that PN-stimulation should reveal different aspects of evoked activity.

Method

Five male student subjects (mean age: 30.6; STD: 9.9) participated in the study. All subjects were right handed as revealed by the Edinburgh Inventory (Oldfield, 1972). A 2x3 design comprising the experimental variables STIMULUS MODALITY (TL, EL & PN) and STIMULUS LOCATION (D1 & D5) was employed. From these variables six experimental conditions were derived (TL-D1, TL-D5, EL-D1, EL-D5, PN-D1, PN-D5). Conditions were presented block wise according to a fixed irregular order. In each block 250 trials were presented. The interval between stimulus onsets ranged randomly from 450 to 550 ms (rectangular distribution). TL stimulation consisted of a brief (30ms) superficial pressure stimulus applied by means of a standard pneumatic stimulator using a non painful stimulus intensity for all subjects [2, for more details].

Stimulus-Intensity	EL		PN	
	D1	D5	D1	D5
1	3.9	4.2	6.8	8.4
2	4	3.3	7.1	6.5
3	5.3	5	9.3	9.3
4	4.3	2.9	8.1	5.8
5	4.2	3.6	9	8.1

Table 1: Individual stimulus intensities for electrical non-painful (EL) and electrical painful (PN) stimulation applied to the right thumb (D1) and the right little finger (D5).

EL and PN stimuli were delivered with an electrode (3 mm long, 1mm in diameter) embedded in a plastic mount. Stimulus properties were defined as biphasic sinusoidal signals of 10 ms duration. Signal amplitudes

could be adjusted individually between 0 and 10 mA. In a pre-test session, sensation thresholds and pain thresholds for each participant were determined using the method of limits. The resulting thresholds were used to calculate the appropriate individual stimulus strengths for EL and PN stimulation. The average of both thresholds was used for EL. For PN the stimulus intensity of pain thresholds were multiplied by 1.5. Individual stimulus intensities are listed in table 1.

Magnetic fields were recorded in a magnetically shielded room using a 148-channel wholehead biomagnetometer (Magnes 2000, BTi, San Diego (CA). Data recording was performed in supine position with subjects lying their backs[2].

The frequency range was set to 0.1-200 Hz and data were sampled with 520.5 Hz. Stimulus locked epochs of 300 ms duration (151.21 ms pre-trigger & 147.85 post-trigger interval) were recorded and – after artifact rejection – averaged online to obtain condition-specific magnetic responses. The averaged evoked magnetic field data were digitally filtered using a second order 30 Hz low-pass filter. For baseline correction the average signal within 100 ms before stimulus onset was subtracted. Within the range of 30 – 80 ms after stimulus onset the first major pear was identified in each of the evoked waveforms. A single equivalent current dipole (ECD) (best fitting locale sphere) was fitted per each EF for two subsets of 37 channels (one for each hemisphere). The medians (11 data points centered at maximum signal strength) of the dipole moments and dipole locations for the peak in the signal power (root mean square across selected channels) were computed if the following criteria were met: (1) signal-to-noise-ratio > 3; (2) a goodness of fit of the ECD model to the measured field of 0.95. Analysis of variance and mean comparisons (t-tests) were calculated to determine significant effects.

The study was approved by the ethics committee of the University of Konstanz. Informed consent was signed by all participants prior to investigation.

Results

No obvious differences were observed between the waveforms elicited by TL, EL and PN stimulation for neither the thumb nor the little finger. This is demonstrated in figure 1, which illustrates the evoked responses in one subject.

Latencies differed for stimulus modalities ($F_{(2.4)}$=6.1; $p<0.05$) in that EL- and PN-latencies were shorter than TL-latencies (EL vs. TL: t=2.8, $p<0.05$; PN vs. TL: t=1.1, $p<0.05$; EL vs. PN: n.s.). This effect is illustrated in figure 2. The relative strengths of amplitudes (root mean squares across channels) and dipole moments between electrical and tactile stimulation was variable across subjects. However, PN-amplitudes turned out to be significantly higher then EL- amplitudes (t=3,2; $p<0.02$). During painful stimulation dipole strength was highest, but differences to EL and TL-stimulation were not significant.

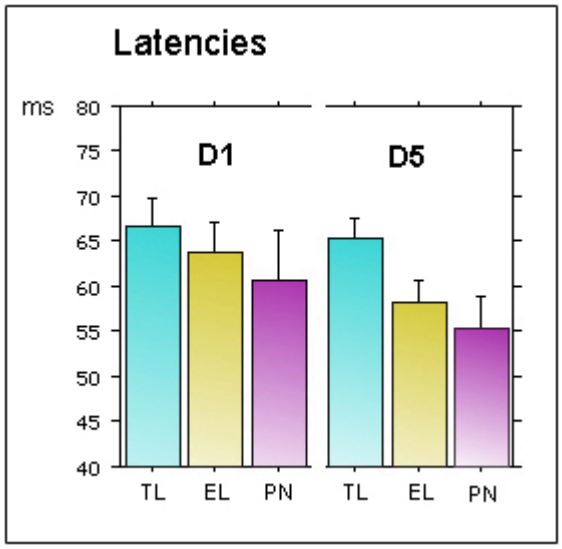

Figure 2: Latencies for all 3 stimulation methods applied to thumb (D1) and little finger (D5) of the right hand.

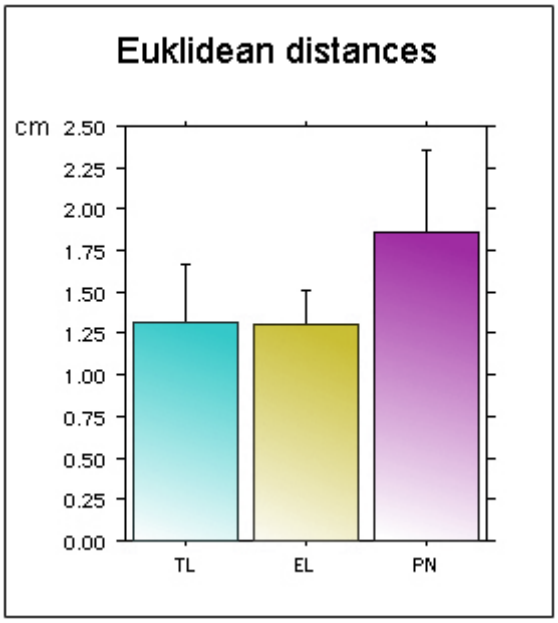

Figure 3 Euklidean distances for all 3 stimulation methods applied to thumb (D1) and little finger (D5) of the right hand.

For each stimulation method a somatotopic organization of the hand representation was observed in that D1 was located inferior (lateral) to D5. Euclidean dis-

[2]To avoid movements of the subjects during recording, we used a special mattress filled with fine plastic globes and air so that it could pick up the individual curvature of the subject's body. Then, the air was drawn form the mattress to provide a rigid but individually shaped base the subject was lying on. In addition, we used little cushions to secure the head position in the sensor.

tances between D1 and D5 were calculated to estimate the expansion of the hand representation. For TL- and EL-stimulation (TL: 1.35 ± 0.41 cm; EL: 1.31 ± 0.78 cm) Euclidean distances were the same. However with painful stimulation the Euclidean distance increased (PN: 1.89 ± 1.07 cm; $F_{(2,4)}$ =0.7; p=0.5, see figure 3). In some subjects right, ipsilateral activation was evident in the sensor layout for the electrical stimulation. However, it was impossible to model this ipsilateral component within the given latency range of 30-80 ms using the ECD model in any of the subjects.

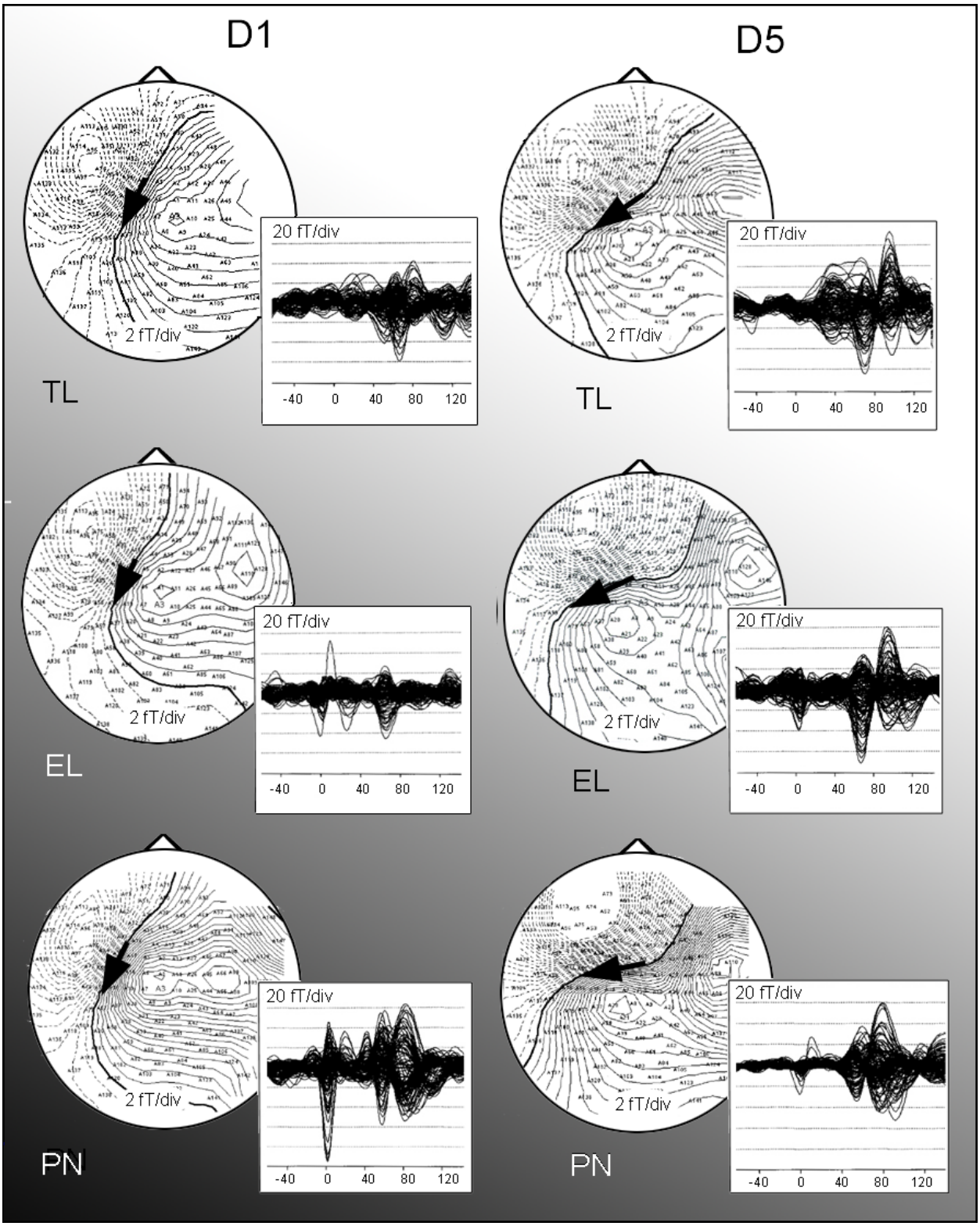

Figure 1: Contourplots and waveforms for tactile (TL), electrical non-painful (EL) and electrical painful (PN) stimuli applied to the right thumb (D1) and the right little finger (D5).

Discussion

The organization of primary sensory areas and its alterations serve as models in the field of clinical neuroplasticity. For investigations in humans, MEG-recordings have proven to be especially useful. Neuromagnetic source localization basically employs two classes of stimulation methods, electrical and tactile stimulation. Depending on the particular problem under investigation, each stimulation method has its advantages and disadvantages. The present experiment compared both methods in a within-subject design. Results suggest that tactile as well as non-painful electrically evoked fields do not produce systematically different locations or amplitudes. Furthermore, the somatotopic organization of the fingers in area 3b was depicted reliably by TL- as well as EL-stimulation. These results confirm former studies in which non-invasive mapping of the finger representations was shown with either tactile [5,11] or electrical evoked fields [1,9]. Our data further suggests that the localization of tactile as well as electrically evoked fields provide comparable estimations for the expansion of the hand representation. This was not the case for pain-evoked fields (PN stimulation), which lead to significantly larger Euclidean distances compared to both non-painful conditions. This difference between painful and non-painful stimulation suggests that the representation of painful stimuli evoked different aspects of somatotopic organization. Possibly, painful stimuli excite a larger neural network that is distributed across a larger region. This explanation could also account for the differences in amplitude, as the more widespread neural network would also include more neurons.

Latencies were found to be shorter when either painful or non-painful electrical stimuli were used. On average, latencies for tactile stimulation were 5 ms longer. This is consistent with the study of Forss et al., where differences in latencies between tactile air-puff stimulation and electrical nerve stimulation at the wrist amounted to 5.5-7.5 ms. The differences in latencies most likely do not indicate fascilitation of processing of electrically evoked responses but can be explained by the time the receptor needs to activate the sensory neurons.

We were unable to localize ipsilateral activation in any of the stimulation conditions. This observation is different from the report by Schnitzler et al., 1995 and Elbert et al., 1995. In some of our subjects, evoked activation was clearly visible over the ipsilateral hemisphere. But, if present at all, the evoked fields were quite small in amplitude, yielding a signal-to-noise ratio that was not sufficient for reliable source modeling. In sum our findings suggest, that pneumatic responses have longer latencies than electrically evoked fields, a finding that can be explained by the transduction time of the receptor. Otherwise these stimulation methods seem not to produce systematically different activities. Tactile as well as non-painful cutaneous electrical stimulation both allow a reliable description of aspects of the functional organization of the hand. However, given that our results are based on a small subject sample, greater subjects samples and more stimulation sites are necessary to detail these findings.

References

[1] Baumgartner, C., Sutherling, W. W., Di, S., Barth, D. S. Spatiotemporal modeling of cerebral evoked magnetic fields to median nerve stimulation. Electroencephalography and Clinical Neurophysiology, 1991, 79: 27-35.

[2] Elbert, T. (1998) Neuromagntism In: W. Andrä, H. Nowak. Magnetism in medicine, WO, J. Wiley & Sons, 1998, pp 190-262.

[3] Elbert, T., Flor, H., Birbaumer, N., Knecht, S., Hampson, S., Larbig, W., Taub,E. Extentive reorganization of the somatosensory cortex in adult humans after nervous system injury. NeuroReport, 1994, 5:2593-7.

[4] Elbert, T., Junghöfer, M., Scholz, B., Schneider, S. Separation of overlapping neuronal sources in the first and second somatosensory cortices. Brain Topography, 1995, 7: 275-282.

[5] Elbert, T., Sterr, A., Flor, H., Rockstroh, B, Knecht, S., Taub, E. Input-increase and input-decrease types of cortical reorganization after upper extremity amputation in humans. Exp. Brain Res., 1997, 117, 1: 161-164

[6] Forss, N., Jousmäki, V., Hari, R. Interaction between afferent input from fingers in human somatosensory cortex. Brain Research, 1995, 685: 68-76.

[7] Forss, N., Salmelin, R., Hari, R. Comparison of somatosensory evoked fields to airpuff and electric stimuli. Electroencephalography and Clinical Neurophysiology, 1994, 92:510-17.

[8] Gallen, C. C., Sobel, D. F., Lewine, J. D., Sanders, J. A., Hart, B. L., Davis, L. E., Orrison, W. W. Neuromagnetic mapping of brain function. Radiology,1993, 187: 863-7.

[9] Hari, R., Karhu, J., Hämäläinen, M., Knuutila, J., Salonen, O., Sams, M., Vilkman, V. Functional Organization of the first and second somatosensory cortices: a neuromagnetic study. European Journal of Neuroscience, 1993, 5: 724-34.

[10] Schnitzler, S., Salmelin, R., Salenius, S., Jousmäki, V., Hari, R. Tactile information from human hand reaches the ipsilateral cortex. Neuroscience Letters, 1995, 200:25-28.

[11] Sterr, A., Müller, M., Elbert, T., Rockstroh, R., Pantec, C., Taub,E. Perceptual correlates of changes in

cortical representations of fingers in blind mutli-finger readers. The Journal of Neuroscience, 1998,18:4417-23.

[12] Vanni, S., Rockstroh, R., Hari,R. Cortical sources of human short-latency somatosensory evoked fields to median and ulnar nerve stimuli. Brain Research, 373:25-33.

Acknowledgements

Work was supported by the Volkswagenstiftung and the Deutsche Forschungsgemeinschaft. We are grateful to Dr. Christian Wienbruch for technical assistance. Ursula Lommen and Dipl. Psych. Jürgen Kaufmann helped us with data recording.

INDEX BY AUTHORS

A

Avella C., 162

B

Bacharova L., 156
Bastiaansen M., 131
Beisteiner R., 120
Bonomo L., 112
Bowyer, S. M., 170
Brauer H., 174, 184
Breier, J. I., 70
Brunia C., 131
Burco F., 165

C

Chorvat D., 156
Constantinou, J., 70
Cunnington R., 116, 120

D

Dale, A. M., 53
Deecke L., 116, 120
Del Gratta C., 112
Della Penna S., 112
Donker D., 139
Dzemidzic M., 108, 123

E

Edlinger G., 131
Edward V., 120
Elbert, T., 188
Erdler M., 120
Erné, S. N., 152, 181, 184

F

Fahlbusch, R., 159
Fenici, R., 135
Ferretti A., 112
Fetzer J., 95
Fischer G., 95, 99, 147
Franciotti R., 112
Friston K. J., 87

G

Ganslandt O., 61, 159
Gartus A., 120
Grönemeyer D., 139

H

Hailer B., 139
Halgren E., 53
Hänninen H., 135, 143
Hashimoto I., 79
Haueisen J., 174, 184
Hren R., 104
Huiskamp G., 95

I

Ilmoniemi R. J., 48

J

Jazbinšek V., 104

K

Kamada K., 61
Kammrath H. G., 125, 181
Karhu, J., 74
Katila, T., 135, 143
Kober H., 61, 159
Korhonen, P., 135
Kreyer, I., 188

L

Lange S., 139
Lauerma K., 135, 143
Leder U., 174
Lesh M. D., 147
Lilli S., 162, 178
Lötjönen J., 135, 143
Lowe M. J., 108, 123
Lurito J. T., 108, 123

M

Mäkijärvi M., 135, 143
Mateasik A., 156
Mathews V. P., 108, 123
Miyashita Y., 127
Mlynash M., 147
Modre R., 95, 99, 147
Möller M., 61, 159
Moser E., 116, 120
Müller H. P., 152, 181

N

Nenonen J., 143

Neuper C., 131
Nimsky, C., 159
Nowak H, 174, 184

P

Papanicolaou A. C., 70
Peoppel D., 127
Pesola K., 135, 143
Peters M. J., 91
Pfurtscheller G., 131
Phillips C., 87
Phillips M. D., 108, 123
Pohl P., 174
Proverbio A. M., 162, 165, 178

R

Reddy G., 146, 147
Roberts T., 147
Roithinger F. X., 147
Romani G. L., 112
Rossini P. M., 112
Rucker W., 95
Rugg M. D., 87

R

Reddy G., 146, 147
Roberts T., 147
Roithinger F. X., 147
Romani G. L., 112
Rossini P. M., 112
Rucker W., 95
Rugg M. D., 87

S

Sakuma K., 79
Savoy R. L., 35
Sekihara K., 79, 127
Simos, P., 70
Sippens Groenewegen A., 147
Steiner P. R., 147
Sterr, A., 188
Stinstra J. G., 83
Streibl B., 120

T

Takala P., 143
Tartaro A, 112
Tenner U., 152, 174, 184
Tesche, C. D, 74
Tilg B., 95, 99, 147
Titomir L. I., 156
Toivonen L., 143
Tomczak R., 181
Torquati K., 112

V

van Burik M. J., 91
Van Leeuwen P., 139
Van Oosterom A., 24
Vieth J. B., 61, 159
Voipio-Pulkki L.M, 143

W

Wach P., 95, 99, 147
Windischberger C., 116, 120
Wunderlich A., 181

Z

Zani A., 162, 165, 178
Ziolkowski, M., 152
Zouridakis, G., 70